Title

Defining novel mechanisms that regulate phase separation of metabolic enzymes and stress granules

Permalink

Author

Begovich, Kyle

Publication Date

2019

UNIVERSITY OF CALIFORNIA SAN DIEGO

Defining novel mechanisms that regulate phase separation of metabolic enzymes and stress granules

A dissertation submitted in partial satisfaction of the requirements for the degree
Doctor of Philosophy

in

Biology

by

Kyle Begovich

Committee in charge:

Professor James Wilhelm, Chair
Professor Randolph Hampton
Professor Jens Lykke-Andersen
Professor Maho Niwa
Professor Gene Yeo

2019

This Dissertation of Kyle Begovich is approved, and it is acceptable in quality and from for publication on microfilm and electronically:

Chair

University of California San Diego

2019

DEDICATION

This work is dedicated to

my family,

friends,

colleagues,

and mentors

who have provided me with unconditional support

TABLE OF CONTENTS

LIST OF FIGURES

LIST OF TABLES

ACKNOWLEDGEMENTS

I would like to thank Dr. James Wilhelm for his supervision and imparting his wisdom on me to allow me to grow into the scientist that I am today. I have to thank you for taking a chance and hiring me as a staff research associate right out of college. Without that experience, I don’t know if I would have ever pulled the trigger on applying for Ph.D. programs. All his advice helped me stay course during my run toward obtaining a Ph.D. and at the same time, allow me to pursue other interesting questions in cell biology.

I would also like to acknowledge the members of my thesis committee: Dr. Jens Lykke-Andersen, Dr. Maho Niwa, Dr. Randy Hampton, and Dr. Gene Yeo. I cant thank you enough for all the scientific discussions during our committee meetings where you passed on your expertise and advice to guide me in the right direction. I couldn’t have done it without your guidance.

Additionally, I would like to thank Dr. Deborah Yelon for giving me the opportunity to explore zebrafish developmental biology. Coming into our collaboration, I had very little experience with developmental biology, but your patience and understanding was what I needed to bring me into a new field. I really appreciate you for making me feel like another member of your lab even though I wasn’t there full-time.

Words cant describe how immensely grateful I am to have worked with the members of the Wilhelm lab. I know I was able to thrive in this lab as you all welcomed me and was comfortable with my obnoxious and silly self. Charlongrat Noree is one of the kindest, selfless and hardworking people I’ve ever met, which makes me happy that we got to collaborate on a few projects. He was my first mentor in the lab and taught me all about yeast genetics and fluorescent microscopy. Risa Broyer has been a beacon of joy for me on tough days. I could always count on you for a good laugh even when you were doing a cleanse. She was also crucial for me learning how to perform cell culture. Elena Monfort-Prieto has been my lab mom the entire time I have been in the Wilhelm Lab. I can't thank her enough for being a good caretaker and also slapping some sense into me when I have gotten too crazy or in my head. I don't think I will ever find a coworker and friend like you in my future life. Michael Carver has been a tower of positivity. I'm glad you came along with your positive attitude and reminded me that science can be fun and exciting even in troubling times. I'm grateful for Sora Chee and her time and efforts in assisting me during my first few years of graduate school. Thank you to you all.

I would like to thank the participants of the HHMI Summer Institute whom I worked with for 4 summers at Woods Hole, MA. I know I complained a lot, but I'm so grateful for the friendships that we developed over complaining about Woods Hole and being stuck in PI paradise. Without your help and insight, I wouldn't have been able to push my research projects to new directions.

Additionally, I would like to thank the HHMI for funding me through the Gilliam Fellowship. Not only would I have not been able to travel to essential conferences without your support, I'm grateful for providing an inclusive environment to do research. Also I would like to thank my fellows for all the encouragement and fun you have given me over the past few years.

I would like to thank my UCSD Swim and Dive alumni and friends. They have all helped me get through some stressful and rough patches in my graduate career. They were always there to lend an ear to listen to any quarrels I had about school and life.

Most importantly, I want to thank my Mom, Dad and brother for all their unconditional support throughout my time as a Ph.D. student. This hasn't been the easiest 6 years for me and I couldn't have done it without you guys.

Chapter 2 is a manuscript submitted for publication. It may appear in Molecular Biology of the Cell. Noree, C., Begovich, K., Samilo, D., Broyer, R.M., Monfort-Prieto, E., Wilhelm, J.E. "A quantitative screen for metabolic enzyme structures reveals patterns of assembly across the yeast metabolic network." C. Noree is co-first author for this manuscript. D. Samilo and E. Monfort-Prieto helped create yeast strains used in this manuscript. R.M Broyer performed immunostaining experiments. J.E. Wilhelm helped write and edit this manuscript. The dissertation author is the primary experimenter and author on this paper.

Chapter 3 is a manuscript submitted for publication. It may appear in Molecular Cell. Begovich, K., Vu, A.Q., Yeo, G.W., Wilhelm, J.E. "Conserved metabolite regulation of stress granule assembly via AdoMet." Vu cultured iPSC-dervied motor neuron lines. All other experiments, imaging, data analysis, and writing this version of this manuscript were my responsibility. G.W. Yeo and J.E. Wilhelm helped edit/revise this manuscript. The dissertation author is the primary experimenter and author on this paper.

Chapter 4 is a manuscript submitted for publication. Begovich, K., Wilhelm, J.E. "An in vitro assembly system for yeast stress granules identifies roles for RNA nucleation and ATP." All experiments, imaging, data analysis and writing were my responsibility. J.E. Wilhelm helped edit/revise this manuscript. The dissertation author is the primary experimenter and author on this paper.

Appendix A is a manuscript in preparation and will be submitted for publication. Begovich, K., Yelon, D., J.E. Wilhelm. "PRPS polymerization is required for proper lens fiber organization in zebrafish." All experiments, imaging, data analysis and writing were my responsibility. D. Yelon and J.E. Wilhelm helped edit/revise this manuscript. The dissertation author is the primary experimenter and author on this paper.

Appendix B is a manuscript in preparation and will be submitted for publication. Begovich, K., Wilhelm, J.E. “AdoMet binding regulates stress granule-independent assembly and stress granule recruitment of Cys4.” The dissertation author is the primary experimenter and author on this paper.

VITA

2011	Bachelor of Science, University of California San Diego
2011-2013	Staff Research Associate, University of California San Diego
2014-2016	Teaching Assistant, University of California San Diego
2019	Doctor of Philosophy, University of California San Diego

PUBLICATIONS

Noree, C., Begovich, K., Samilo, D., Monfort-Prieto, E., Wilhelm, J.E. “A quantitative screen for metabolic enzyme structures reveals patterns of assembly across the metabolic network”. Manuscript submitted for publication (Molecular Biology of the Cell)

Begovich, K., Vu, A.Q., Yeo, G.W., Wilhelm, J.E. “Conserved metabolite regulation of stress granule assembly via AdoMet”. Manuscript submitted for publication (Molecular Cell)

Begovich, K., Wilhelm, J.E. “An in vitro system for stress granule assembly identifies roles for RNA nucleation and ATP.” Manuscript submitted for publication (Cell)

ABSTRACT OF THE DISSERTATION

Defining novel mechanisms that regulate phase separation of metabolic enzymes and stress granules

by

Kyle Begovich

Doctor of Philosophy in Biology

University of California San Diego, 2019

Professor James Wilhelm, Chair

Compartmentalization of biochemical processes is a central principle in cell biology. Traditionally, understanding spatial organization of reactions has focused on their localization to membrane-bound organelles. However, recent work has highlighted the ability of proteins and RNAs to dynamically partition into large, membrane-less condensates. Formation of these assemblies have been observed in both eukaryotes and prokaryotes suggesting that this could be an ancient mechanism utilized for compartmentalizing and regulating specific processes. This thesis focuses on identifying novel mechanisms that regulate the assembly of two classes of membrane-less condensates: metabolic enzymes and stress granules (SGs). First, we further expanded the list of metabolic enzymes capable of forming a filament or foci structure to 60 proteins. This expansion allowed us to determine that metabolic enzymes, which acted at branch points or highly connected nodes in the metabolic network, had a higher propensity to assemble into intracellular structures than other enzymes. Our analysis of the *de novo* purine biosynthesis pathway not only revealed that assembly is based on the hierarchical position in a pathway, but also that a subset of enzymes in this pathway localizes to SGs. These results led us to reexamine the hits from our screen and conduct a secondary screen for SG localization. In total, we identify 17 metabolic enzymes that are associated with SGs providing a connection between metabolic activity and post-transcriptional gene regulation. We find that the product of the SG-localized enzyme Sam1, AdoMet, regulates composition and frequency of acute and chronic nutrient stress-induced SGs. Furthermore, AdoMet blocks fusion of SGs in proliferating cancer cell lines while suppressing SG formation in motor neurons derived from patients with amyotrophic lateral sclerosis. With the goal of understanding the role of RNA-RNA interactions in SG formation, we developed a reconstitution system using yeast cytoplasmic extracts and *in vitro* transcribed RNA. Our *in vitro* assembled SGs mimicked *in vivo* SGs and advanced the knowledge of how ATP

levels regulate SG assembly, disassembly, morphology, and dynamics. Lastly, we find that building a canonical SG depends not only on the material state of a RNA, but also the composition of the RNA.

Chapter 1

Introduction

Principles of biochemical organization in cells

One of the key questions in cell biology is how cells organize and control complex biochemical processes over space and time in its crowded and diverse environment. Cells must compartmentalize specific reactions to prevent interference with other reactions and provide protection from changes in the surrounding environment. One mechanism to control spatiotemporal organization would be to concentrate reaction components to a confined space that partitions them away from others. In eukaryotic cells, membrane-bound organelles allow for specificity of pathways and provide a selective barrier to protect itself or the surrounding environment from potential damage. For example, harmful reactive species, which can damage the cytoplasm, are produced as a byproduct of reactions that occur in the mitochondria and peroxisome. However, the protective barrier of their membranes prevents diffusion into the cytoplasm to maintain homeostasis (Lenaz and Genova, 2009; Veenhuis et al., 2000). The membranous nature of these organelles can shield the components that reside within from changes in the surrounding cytoplasm like drops in pH levels.

The confinement of biochemistry to membrane-bound organelles raised the question if this is the only mechanism for localizing such processes. Despite the immense diversity of reactions, the cytoplasm has been largely taught as a “fluid, jelly-like substance” containing a mixture of protein, RNAs, and other macromolecules that lack any subcellular structure. The identification of the cytoskeleton provided insight that highly organized biochemistry can exist in the cytoplasm (Cooke and Murdoch, 1973; Higashi and Oosawa, 1965; Kirschner, 1986; Mitchison and Kirschner, 1984). Additionally, spherical, non-membrane bound components, like centrosomes, nucleoli, and Cajal bodies, support evidence for concentrated biochemistry and its relation to proper cellular functions (Gall, 2003; Pederson, 2011).

While most research has focused on compartmentalization in eukaryotes, it remained unclear if prokaryotes contained any similar mechanisms. The idea of the need for complex biochemical organization in bacteria was underappreciated for many years until the discovery of bacterial cytoskeletal proteins (Bi and Lutkenhaus, 1991; Jones et al., 2001). The bacterial cytoskeleton raises the question of how biochemistry was organized to originate early life. In the 1920s, biochemist Alexander Oparin proposed that life on Earth was derived by different types of coacervate droplets occuring in the primordial ocean (Bernal, 1967). Within these droplets, a gradual chemical evolution of carbon-based molecules could exist leading to life. This hypothesis argues that membrane-less organization of biochemistry is an ancient function of biology.

In support of the ideas from *The Origins of Life*, recent visual screens have revealed an explosion of novel intracellular structures, including RNA-protein granules, clusters of signaling proteins and metabolic enzymes (Anderson and Kedersha, 2006; Bethani et al., 2010; Narayanaswamy et al., 2009). While their formation follows similar mechanistic patterns, the functional consequences for their assembly varies from different networks as well as proteins within a defined network. Since these structures lack a membrane component, they have been classified as membrane-less organelles or biomolecular condensates (Banani et al., 2017). This thesis focuses on identifying novel mechanisms that regulate the assembly of two classes of biomolecular condensates: metabolic enzymes and a class of RNA-protein granules, known as stress granules (SGs).

Liquid-liquid phase separation

The lack of a membrane component for these biomolecular condensates raised the question of how they partition out from solution. Over the past decade, multiple reports have illuminated that many of these condensates assemble via liquid-liquid phase separation (LLPS) or demixing (Hyman et al., 2014; Shin and Brangwynne, 2017). LLPS is the process where two liquids demix into two separate phases based on homotypic and heterotypic interactions between the two liquids. A common household example of LLPS is the separation of oil and water after mixing salad dressing. Due to the physical properties of each liquid, mixing is prevented, as homotypic interactions will be favored over heterotypic interactions resulting in a two-phase state. This idea of LLPS has been well studied and characterized in polymer chemistry (Flory, 1942). Given the polymeric nature of proteins and nucleic acids, it makes sense that both can undergo demixing.

The first well-characterized example of a biomolecular condensate exhibiting properties of LLPS was the P granule, the germline granule in *C.elegans*. P granules are micron-sized assemblies of RNA-binding proteins and mRNA whose localization determines germline lineage (Wang and Seydoux, 2014). Time-lapse and tension microscopy analysis revealed that P granules were spherical, fused with each other and exhibited very fast internal rearrangement of components (Brangwynne et al., 2009). These results prompted further investigation that led to discovering that other types of RNA-protein granules (i.e. processing bodies, stress granules, promyelocytic bodies, and balbani bodies) exhibited similar properties to P granules (Shin and Brangwynne, 2017). Furthermore, the identification of LLPS promoting biomolecular condensates was not just specific to RNA-protein granules. Assembly of synaptic densities, membrane clusters, and signaling puncta also occurs by liquid demixing (Su et al., 2016; Zeng et al., 2016, 2018; Zhang et al., 2018). Additionally, LLPS contributes to the assembly of DNA and RNA condensates (Jain and Vale, 2017; Van Treeck et al., 2018)

Each type of condensate revealed common regulatory mechanisms that promote the demixing of their components. Proteins and RNAs found in biomolecular condensates are abundant in multivalent modules, which are elements that promote intra- and inter-molecular interactions (Han et al., 2012; Li et al., 2012; Nott et al., 2015). In polymer chemistry, multivalency promotes oligomerization and formation of higher-order structures required to obtain micron-sized assemblies. For proteins, demixing typically occurs via two modes of multivalent interactions: modular domains and/or intrinsically disordered regions (IDRs). Modular domain interactions, which are mediated through well-folded protein domains, have been implicated in the phase separation behavior of signaling pathways like actin-regulatory signaling pathway and T-cell activation (Li et al., 2012; Su et al., 2016). While IDRs lack a well-defined folding pattern, they contain repeat sequence elements that promote multivalent interactions (Su et al., 2016). Proteins found in RNA-granules are often enriched with IDRs and these domains alone are sufficient to drive demixing *in vitro* and *in vivo* (Lin et al., 2015; Reijns et al., 2008).

Despite the commonalities involved in the assembly of biomolecular condensates, the biological function associated with their formation differs. For example, concentrating APR2/3 complex into actin regulatory droplets dramatically increased actin polymerization rates (Li et al., 2012). Exclusion of phosphatases, but not kinases, from T cell receptor signaling clusters provides evidence that condensates can provide reaction specificity (Su et al., 2016). Conversely, sequestration of factors into biomolecular condensates can be used to downregulate the activity of proteins or RNA. Under cellular stress, translation factors and non-translating mRNA assemble into stress granules to decrease overall translational output (Protter and Parker, 2016). The association of heterochromatin with phase-separated human protein 1a droplets in

Drosophila embryos suggests that demixing can also be used to organize their interior space (Strom et al., 2017).

Spatial organization of metabolic enzymes

Homeostatic control of metabolism is essential for proper cell physiology under proliferative and non-proliferative conditions. Cells must be able to coordinate and regulate metabolic flux through various pathways in response to changing environments. This regulation has been taught through different mechanisms like allosteric regulation, post-translational modifications, and gene expression to regulate the enzymatic activity of metabolic enzymes. However, recent targeted visual and proteomic studies have highlighted the ability of metabolic enzymes to form filament or foci structures (Liu, 2010; Narayanaswamy et al., 2009; Noree et al., 2010). It is believed that their formation acts a mechanism to regulate metabolic flux, as their assembly is coordinated with specific growth conditions. One of the hallmark growth conditions for identifying metabolic enzyme assembly in yeast has been growth into stationary phase suggesting that nutrient deprivation is a key trigger for assembly. In support of this, removal of a specific metabolite from medium has been shown to trigger condensation. For example, removal of adenine or glucose was sufficient to form foci for purine biosynthetic enzyme Ade4 or glutamate synthetase (Gln1) in yeast, respectively (Narayanaswamy et al., 2009). These structures are highly dynamic assemblies as disassembly can be promoted by removal of the stress by replenishing cells with fresh medium or a specific metabolite (Narayanaswamy et al., 2009). Together, this argues that metabolic enzyme assembly represents a novel mechanism to maintain metabolic homeostasis.

Since nutrient deprivation is a major regulator of assembly, most of metabolic enzymes forming these structures are believed to be inactive storage depots. For instance, yeast pyruvate kinase, Cdc19, coalesces into inactive foci upon glucose starvation and heat shock (Saad et al., 2017). Additionally, yeast CTP synthetase assembles into filaments in response to end product inhibition, which suggests that enzyme inactivity drives polymerization (Noree et al., 2014). However, this assembly-inactivation correlation is not true for other metabolic enzymes. The mammalian Acetyl-CoA carboxylase and liver phosphofructokinase form polymers in response to enzyme activation (Hunkeler et al., 2018; Webb et al., 2017). The enzymatic state that drives assembly can also differ from organism to organism. In contrast to yeast CTP synthetase, polymerization of human CTP synthetase is coupled with enzyme activation (Lynch et al., 2017). Thus, targeted structure-function approaches must be used to determine which enzymatic state is associated with metabolic enzyme assembly for a given enzyme.

Due to their near identical morphologies, its been proposed that condensation of metabolic enzymes into higher order structures occurs via phase separation. While no liquid-like properties have been observed for metabolic enzymes, the mechanisms that drive their assembly are similar. Phosphorylation in Cdc19's IDR sequence mitigates multivalent interactions and promotes disassembly of Cdc19 (Saad et al., 2017). Protein modular domain interactions, via oligomerization, can also contribute to their polymeric state. Mutations that disrupt the olimerization interface of yeast CTP synthetase and glutamine synthetase block polymerization (Noree et al., 2014; Petrovska et al., 2014).

In addition to single enzyme assembly, condensate formation of multiple enzymes acting in consecutive steps in a pathway has also been observed. For example, removal of purines from media triggers the co-clustering of enzymes in the purine biosynthetic pathway, known as the purinsome (An et al., 2008). Assembly of the purinosome has been proposed to promote substrate channeling by localizing and concentrating reaction components to increase flux through the pathway. In support of this, glycolytic enzymes in yeast and *C.elegans* exhibit enhanced glycolytic activity upon co-assembly during hypoxic stress (Jang et al., 2016; Jin et al., 2017). However, its unknown what types of mechanisms regulate condensation in pathways where enzymes don't assemble in consecutive steps.

Mechanisms behind stress granules assembly

Stress granules (SGs) are phase-separated cytoplasmic assemblies of non-translating mRNPs that form in response to environmental stress (Protter and Parker, 2016). Like other biomolecular condensates, SGs assemble via different multivalent interactions that promote LLPS (Wheeler et al., 2016). Upon exposure to various stresses, polysomes disassociate from translating mRNAs that provide a scaffold to allow for protein-protein, protein-RNA, and RNA-RNA interactions. Newly exposed mRNA yields additional binding sites to recruit other RNA-binding proteins and allows for interaction between complimentary RNA sequences. Additionally, IDRs from proteins found in SGs can promote further protein-protein and protein-RNA interactions (Lin et al., 2015; Molliex et al., 2015). Together, these mechanisms increase the number of available mRNP interaction sites to promote LLPS. The sequestration of RNA-binding proteins and mRNAs away from polysomes into SGs provides a mechanism of stress-associated gene expression regulation.

With the growing appreciation and implication of SGs in neurodegenerative disease and cancer (Anderson et al., 2015; Li et al., 2013), much focus has been placed on understanding the composition and molecular mechanisms that regulate SG assembly. Recent proteomic and targeted approaches have illuminated that the composition of SGs is stress, cell-type, and organism-specific. Both yeast and mammalian stress granules contain markers found in pre-initiation complexes like Ded1/DDX3, eIF4E, eIF4G1, Pab1/PABPC, Pbp1/Ataxin-2, and

Pub1/TIA-1 along with ATPases, tRNA synthetases, and ribosome biogenesis factors (Jain et al., 2016). However, in yeast, azide-induced SGs contain other initiation factors like eIF4A/B whereas glucose deprivation-induced SGs lack these proteins (Buchan et al., 2011). In HeLa cells, localization of SF1 was observed in heat shock-induced SGs, but remained diffuse under exposure to arsenite (Markmiller et al., 2018). Additionally, the SG proteome becomes increasingly more diverse from yeast to humans (Farny et al., 2009; Jain et al., 2016). In support of this, certain stress granule markers like EIF3A and SRP68 were found exclusively in arsenite-induced SGs in HeLa and neural progenitor cells, respectively (Markmiller et al., 2018). This suggests that SGs may have different functions under different stresses or cell-types.

Initial proteomic data on SGs also revealed that SGs contain substructure (Jain et al., 2016). SGs are proposed to contain a solid, less dynamic core that is surrounded by a fluid, more dynamic phase. The idea of this two-phase system has been validated using structure illumination microscopy and immunostaining on isolated SG cores. While the exact assembly pathway of SGs is unknown, these results shed light onto which components reside in each phase.

In addition to i*n vivo* experimentation, biochemical efforts with recombinant SG proteins have provided insight into mechanisms that regulate SG assembly. *In vitro* studies have highlighted that SG proteins FUS, hnRNPA1, and TDP-43 can undergo LLPS *in vitro* (Conicella et al., 2016; Molliex et al., 2015; Patel et al., 2015). Furthermore, the IDRs of these proteins and other SG proteins alone are sufficient form droplets (Lin et al., 2015). IDR condensates have been show to recruit in other recombinant IDR proteins, suggesting that these approaches can be used to build SG-like assemblies *in vitro* (Lin et al., 2015). As these droplets mature over time, their morphology and dynamics is altered (Lin et al., 2015; Molliex et al., 2015; Patel et al., 2015). FRAP experiments reveal that exchange of internal components decrease in matured structures. This transition is also accompanied by the appearance of insoluble fibrous structures. Strengthening the connection between SGs and disease, amyotrophic later sclerosis (ALS)-associated mutations in FUS increase the propensity to demix and promote the formation of fibers at an accelerated rate (Kim et al., 2013; Patel et al., 2015). Thus, understanding the phase separation behavior of SG proteins *in vitro* can provide insight into potential targets for therapeutics.

SG function is not limited to just translational control as they also act as a triage centers for other classes of proteins. Sequestration of target of rapamycin complex 1 (TORC) into SGs represses its signaling activity (Takahara and Maeda, 2012; Wippich et al., 2013). Cells also utilize SG-quality control to dispose of misfolded proteins (REF). Consistent with SGs tying into other aspects of cell physiology, failure to form SGs results in reduced viability upon recovery (Orrù et al., 2016; Yang et al., 2014). Thus, identifying other processes that are regulated by SGs becomes an important task.

This thesis will focus on characterizing novel mechanisms that regulate the assembly of metabolic enzymes and SGs. In addition to identifying all the metabolic enzymes capable of forming intracellular structures, Chapter 2 will discuss the different modes of regulation and localization of metabolic enzyme filaments/foci in the *de novo* purine biosynthetic pathway. Chapter 3 of this thesis builds off the findings from Chapter 2 and identifies all the metabolic enzymes localized to chronic nutrient stress-induced SGs. Further, it will be revealed that metabolites from SG-localized enzymes can regulate assembly of SGs in yeast and human cells. Lastly, Chapter 4 explores the role of the RNA-RNA interactions in mediating stress granule assembly using a newly developed reconstitution system.

References

An, S., Kumar, R., Sheets, E.D., and Benkovic, S.J. (2008). Reversible Compartmentalization of de Novo Purine Biosynthetic Complexes in Living Cells. Science *320*, 103–106.

Anderson, P., and Kedersha, N. (2006). RNA granules. J. Cell Biol. *172*, 803–808.

Anderson, P., Kedersha, N., and Ivanov, P. (2015). Stress granules, P-bodies and cancer. Biochim. Biophys. Acta BBA - Gene Regul. Mech. *1849*, 861–870.

Banani, S.F., Lee, H.O., Hyman, A.A., and Rosen, M.K. (2017). Biomolecular condensates: organizers of cellular biochemistry. Nat. Rev. Mol. Cell Biol. *18*, 285–298.

Bernal, J.D. (1967). The origin of life (World Pub. Co.).

Bethani, I., Skånland, S.S., Dikic, I., and Acker-Palmer, A. (2010). Spatial organization of transmembrane receptor signalling. EMBO J. *29*, 2677–2688.

Bi, E., and Lutkenhaus, J. (1991). FtsZ ring structure associated with division in Escherichia coli. Nature *354*, 161–164.

Brangwynne, C.P., Eckmann, C.R., Courson, D.S., Rybarska, A., Hoege, C., Gharakhani, J., Jülicher, F., and Hyman, A.A. (2009). Germline P Granules Are Liquid Droplets That Localize by Controlled Dissolution/Condensation. Science *324*, 1729–1732.

Buchan, J.R., Yoon, J.-H., and Parker, R. (2011). Stress-specific composition, assembly and kinetics of stress granules in Saccharomyces cerevisiae. J. Cell Sci. *124*, 228–239.

Conicella, A.E., Zerze, G.H., Mittal, J., and Fawzi, N.L. (2016). ALS mutations disrupt phase separation mediated by -helical structure in the TDP-43 low complexity C-terminal domain. Struct. Lond. Engl. 1993 *24*, 1537–1549.

Cooke, R., and Murdoch, L. (1973). Interaction of actin with analogs of adenosinetriphosphate. Biochemistry *12*, 3927–3932.

Farny, N.G., Kedersha, N.L., and Silver, P.A. (2009). Metazoan stress granule assembly is mediated by P-eIF2α-dependent and -independent mechanisms. RNA *15*, 1814–1821.

Flory, P.J. Thermodynamics of High Polymer Solutions. 12.

Gall, J.G. (2003). The centennial of the Cajal body. Nat. Rev. Mol. Cell Biol. *4*, 975–980. Han, T.W., Kato, M., Xie, S., Wu, L.C., Mirzaei, H., Pei, J., Chen, M., Xie, Y., Allen, J., Xiao, G., McKnight, S.L. (2012). Cell-free Formation of RNA Granules: Bound RNAs Identify Features and Components of Cellular Assemblies. Cell *149*, 768– 779.

Higashi, S., and Oosawa, F. (1965). Conformational changes associated with polymerization and nucleotide binding in actin molecules. J. Mol. Biol. *12*, 843–865.

Hunkeler, M., Hagmann, A., Stuttfeld, E., Chami, M., Guri, Y., Stahlberg, H., and Maier, T. (2018). Structural basis for regulation of human acetyl-CoA carboxylase. Nature *558*, 470–474.

Hyman, A.A., Weber, C.A., and Jülicher, F. (2014). Liquid-Liquid Phase Separation in Biology. Annu. Rev. Cell Dev. Biol. *30*, 39–58.

Jain, A., and Vale, R.D. (2017). RNA Phase Transitions in Repeat Expansion Disorders. Nature *546*, 243–247.

Jain, S., Wheeler, J.R., Walters, R.W., Agrawal, A., Barsic, A., and Parker, R. (2016). ATPase-Modulated Stress Granules Contain a Diverse Proteome and Substructure. Cell *164*, 487–498.

Jang, S., Nelson, J.C., Bend, E.G., Rodríguez-Laureano, L., Tueros, F.G., Cartagenova, L., Underwood, K., Jorgensen, E.M., and Colón-Ramos, D.A. (2016). Glycolytic enzymes localize to synapses under energy stress to support synaptic function. Neuron *90*, 278-291.

Jin, M., Fuller, G.G., Han, T., Yao, Y., Alessi, A.F., Freeberg, M.A., Roach, N.P., Moresco, J.J., Karnovsky, A., Baba, M., Yates, J.R., Gitler, A.D., Inoki, K., Klionsky, D.J., Kim, J.K. (2017). Glycolytic Enzymes Coalesce in G Bodies under Hypoxic Stress. Cell Rep. *20*, 895–908.

Jones, L.J.F., Carballido-López, R., and Errington, J. (2001). Control of Cell Shape in Bacteria: Helical, Actin-like Filaments in Bacillus subtilis. Cell *104*, 913–922.

Kim, H.J., Kim, N.C., Wang, Y.-D., Scarborough, E.A., Moore, J., Diaz, Z., MacLea, K.S., Freibaum, B., Li, S., Molliex, A., Kanagaraj, A.P., Carter, R., Boylan, K.B., Wojtas, A.M., Rademakers, R., Pinkus, J.L., Greenberg, S.A., Trojanowski, J.Q., Traynor, B.J., Smith, B.N., Topp, S., Gkazi, A., Miller, J., Shaw, C.E., Kottlors, M., Kirschner, J., Li, Y.R., Ford, A.F., Gilter, A.D., Benatar, M., King, O.D., Kimonis, W.E., Ross, E.D., Weihl, C.C., Shorter, J., Taylor, J.P. (2013). Prion-like domain mutations in hnRNPs cause multisystem proteinopathy and ALS. Nature *495*, 467–473.

Kirschner, M. (1986). Beyond self-assembly: From microtubules to morphogenesis. Cell *45*, 329–342.

Lenaz, G., and Genova, M.L. (2009). Structural and functional organization of the mitochondrial respiratory chain: A dynamic super-assembly. Int. J. Biochem. Cell Biol. *41*, 1750–1772.

Li, P., Banjade, S., Cheng, H.-C., Kim, S., Chen, B., Guo, L., Llaguno, M., Hollingsworth, J.V., King, D.S., Banani, S.F., Russo, P.S., Jiang, Q.-X., Nixon, T., Rosen, M.K. (2012).

Phase Transitions in the Assembly of Multivalent Signaling Proteins. Nature *483*, 336–340.

Li, Y.R., King, O.D., Shorter, J., and Gitler, A.D. (2013). Stress granules as crucibles of ALS pathogenesis. J. Cell Biol. *201*, 361–372.

Lin, Y., Protter, D.S.W., Rosen, M.K., and Parker, R. (2015). Formation and Maturation of Phase-Separated Liquid Droplets by RNA-Binding Proteins. Mol. Cell *60*, 208–219.

Liu, J.-L. (2010). Intracellular compartmentation of CTP synthase in Drosophila. J. Genet. Genomics *37*, 281–296.

Lynch, E.M., Hicks, D.R., Shepherd, M., Endrizzi, J.A., Maker, A., Hansen, J.M., Barry, R.M., Gitai, Z., Baldwin, E.P., and Kollman, J.M. (2017). Human CTP synthase filament structure reveals the active enzyme conformation. Nat. Struct. Mol. Biol. *24*, 507–514.

Markmiller, S., Soltanieh, S., Server, K.L., Mak, R., Jin, W., Fang, M.Y., Luo, E.-C., Krach, F., Yang, D., Sen, A., Fulzele, A., Wozniak, J.M., Gonzalez, D.J., Kankel, M.W., Gao, F.-B., Bennett, E.J., Lecuyer, E., Yeo, G.E. (2018). Context- Dependent and Disease-Specific Diversity in Protein Interactions within Stress Granules. Cell *172*, 590-604.e13.

Mitchison, T., and Kirschner, M. (1984). Dynamic instability of microtubule growth. Nature *312*, 237.

Molliex, A., Temirov, J., Lee, J., Coughlin, M., Kanagaraj, A.P., Kim, H.J., Mittag, T., and Taylor, J.P. (2015). Phase Separation by Low Complexity Domains Promotes Stress Granule Assembly and Drives Pathological Fibrillization. Cell *163*, 123–133.

Narayanaswamy, R., Levy, M., Tsechansky, M., Stovall, G.M., O'Connell, J.D., Mirrielees, J., Ellington, A.D., and Marcotte, E.M. (2009). Widespread reorganization of metabolic enzymes into reversible assemblies upon nutrient starvation. Proc. Natl. Acad. Sci. *106*, 10147–10152.

Noree, C., Sato, B.K., Broyer, R.M., and Wilhelm, J.E. (2010). Identification of novel filament-forming proteins in Saccharomyces cerevisiae and Drosophila melanogaster. J. Cell Biol. *190*, 541–551.

Noree, C., Monfort, E., Shiau, A.K., and Wilhelm, J.E. (2014). Common regulatory control of CTP synthase enzyme activity and filament formation. Mol. Biol. Cell *25*, 2282–2290.

Nott, T.J., Petsalaki, E., Farber, P., Jervis, D., Fussner, E., Plochowietz, A., Craggs, T.D., Bazett-Jones, D.P., Pawson, T., Forman-Kay, J.D., Baldwin, A.J. (2015). Phase Transition of a

Disordered Nuage Protein Generates Environmentally Responsive Membraneless Organelles. Mol. Cell *57*, 936–947.

Orrù, S., Coni, P., Floris, A., Littera, R., Carcassi, C., Sogos, V., and Brancia, C. (2016). Reduced stress granule formation and cell death in fibroblasts with the A382T mutation of TARDBP gene: evidence for loss of TDP-43 nuclear function. Hum. Mol. Genet. *25*, 4473–4483.

Patel, A., Lee, H.O., Jawerth, L., Maharana, S., Jahnel, M., Hein, M.Y., Stoynov, S., Mahamid, J., Saha, S., Franzmann, T.M., Pozniakovski, A., Poser, I., Maghelli, N., Royer, L.A., Weigart, M., Meyers, E.W., Grill, S., Drechsel, D., Hyman, A.A., Alberti, S. (2015). A Liquid-to-Solid Phase Transition of the ALS Protein FUS Accelerated by Disease Mutation. Cell *162*, 1066–1077.

Pederson, T. (2011). The Nucleolus. Cold Spring Harb. Perspect. Biol. *3*, a000638.

Petrovska, I., Nüske, E., Munder, M.C., Kulasegaran, G., Malinovska, L., Kroschwald, S., Richter, D., Fahmy, K., Gibson, K., Verbavatz, J.-M., Alberti, S. (2014). Filament formation by metabolic enzymes is a specific adaptation to an advanced state of cellular starvation. ELife *3*.

Protter, D.S.W., and Parker, R. (2016). Principles and Properties of Stress granules. Trends Cell Biol. *26*, 668–679.

Reijns, M.A.M., Alexander, R.D., Spiller, M.P., and Beggs, J.D. (2008). A role for Q/N- rich aggregation-prone regions in P-body localization. J. Cell Sci. *121*, 2463–2472.

Saad, S., Cereghetti, G., Feng, Y., Picotti, P., Peter, M., and Dechant, R. (2017). Reversible protein aggregation is a protective mechanism to ensure cell cycle restart after stress. Nat. Cell Biol. *19*, 1202–1213.

Shin, Y., and Brangwynne, C.P. (2017). Liquid phase condensation in cell physiology and disease. Science *357*, eaaf4382.

Strom, A.R., Emelyanov, A.V., Mir, M., Fyodorov, D.V., Darzacq, X., and Karpen, G.H. (2017). Phase separation drives heterochromatin domain formation. Nature *547*, 241–245.

Su, X., Ditlev, J.A., Hui, E., Xing, W., Banjade, S., Okrut, J., King, D.S., Taunton, J., Rosen, M.K., and Vale, R.D. (2016). Phase separation of signaling molecules promotes T cell receptor signal transduction. Science *352*, 595–599.

Takahara, T., and Maeda, T. (2012). Transient Sequestration of TORC1 into Stress Granules during Heat Stress. Mol. Cell *47*, 242–252.

Van Treeck, B., Protter, D.S.W., Matheny, T., Khong, A., Link, C.D., and Parker, R. (2018). RNA self-assembly contributes to stress granule formation and defining the stress granule transcriptome. Proc. Natl. Acad. Sci. U. S. A. *115*, 2734–2739.

Veenhuis, M., Salomons, F.A., and Van Der Klei, I.J. (2000). Peroxisome biogenesis and degradation in yeast: A structure/function analysis. Microsc. Res. Tech. *51*, 584–600.

Wang, J.T., and Seydoux, G. (2014). P granules. Curr. Biol. CB *24*, R637–R638.

Webb, B.A., Dosey, A.M., Wittmann, T., Kollman, J.M., and Barber, D.L. (2017). The glycolytic enzyme phosphofructokinase-1 assembles into filaments. J. Cell Biol. *216*, 2305–2313.

Wheeler, J.R., Matheny, T., Jain, S., Abrisch, R., and Parker, R. Distinct stages in stress granule assembly and disassembly. ELife *5*.

Wippich, F., Bodenmiller, B., Trajkovska, M.G., Wanka, S., Aebersold, R., and Pelkmans, L. (2013). Dual Specificity Kinase DYRK3 Couples Stress Granule Condensation/Dissolution to mTORC1 Signaling. Cell *152*, 791–805.

Yang, X., Shen, Y., Garre, E., Hao, X., Krumlinde, D., Cvijović, M., Arens, C., Nyström, T., Liu, B., and Sunnerhagen, P. (2014). Stress Granule-Defective Mutants Deregulate Stress Responsive Transcripts. PLoS Genet. *10*, e1004763.

Zeng, M., Shang, Y., Araki, Y., Guo, T., Huganir, R.L., and Zhang, M. (2016). Phase Transition in Postsynaptic Densities Underlies Formation of Synaptic Complexes and Synaptic Plasticity. Cell *166*, 1163-1175.e12.

Zeng, M., Chen, X., Guan, D., Xu, J., Wu, H., Tong, P., and Zhang, M. (2018). Reconstituted Postsynaptic Density as a Molecular Platform for Understanding Synapse Formation and Plasticity. Cell *174*, 1172-1187.e16.

Zhang, Q., Huang, H., Zhang, L., Wu, R., Chung, C.-I., Zhang, S.-Q., Torra, J., Schepis, A., Coughlin, S.R., Kornberg, T.B., Shu, X. (2018). Visualizing Dynamics of Cell Signaling In Vivo with a Phase Separation-Based Kinase Reporter. Mol. Cell *69*, 334-346.e4.

Chapter 2

A quantitative screen for metabolic enzyme structures reveals patterns of assembly across the yeast metabolic network

Abstract

Despite the proliferation of proteins that can form filaments or phase-separated condensates, it remains unclear how this behavior is distributed over biological networks. We have found that 60 of the 440 yeast metabolic enzymes robustly form structures, including 10 that assemble within mitochondria. Additionally, the ability to assemble is enriched at branch points in several metabolic pathways. The assembly of enzymes at the first branch point in de novo purine biosynthesis is coordinated, hierarchical, and based on their position within the pathway, while the enzymes at the second branch point are recruited to RNA stress granules. Consistent with distinct classes of structures being deployed at different control points in a pathway, we find that the first enzyme in the pathway, PRPP synthetase, forms evolutionarily conserved filaments that are sequestered in the nucleus in higher eukaryotes. These findings provide a roadmap for identifying additional conserved features of metabolic regulation by condensates/filaments.

Introduction

One of the central problems of cell biology is how cells organize biochemical reactions in space and time. Traditionally, studies of this problem have focused on the compartmentalization of reactions within membrane compartments and organelles. Recently, however, there has been an increasing appreciation that the dynamic partitioning of proteins into novel non-membranous compartments can be used to regulate cytoplasmic processes such as signal transduction and RNA metabolism (Banani et al., 2017; Boeynaems et al., 2018). While the interaction domains and biophysical principles that govern the assembly and disassembly of signaling microclusters and RNA granules are increasingly well understood (Ditlev et al., 2018), it has remained unclear how these concepts might be deployed in other regulatory or biosynthetic networks.

Since many of the concepts, such as end product inhibition, that we rely upon to understand how biological networks are regulated were first described in metabolism (Adelberg and Umbarger, 1953; Gerhart and Pardee, 1962; Pardee and Yates, 1956; Srere, 1987), one might expect that the formation of non-membranous compartments might also play a critical role in regulating metabolic networks. Unfortunately, while studies have identified an increasing number of metabolic enzymes that are capable of forming biomolecular condensates and/or filaments, the connections between these structures and enzyme regulation has only been defined for a limited number of cases. For instance, end product inhibition by CTP has been found to trigger polymerization of bacterial CTP synthetase in an inactive conformation (Barry et al., 2014). Similarly, assembly of yeast glutamine synthetase results in its inactivation (Petrovska et al., 2014). Conversely, work on the mammalian Acetyl-CoA carboxylase and liver phosphofructokinase has found that enzyme polymerization and activation are intimately connected (Beaty and Lane, 1983a, b; Meredith and Lane, 1978; Webb et al., 2017). Thus, while metabolic enzyme condensates/filaments can be used to both activate and sequester enzymes, how such regulation is deployed throughout the metabolic network remains unclear.

The identification of metabolic enzyme condensates has also led to a renewed interest in whether these structures could be used to facilitate substrate channeling by partitioning multiple enzymatic steps of a pathway into clusters (Srere, 1987). For instance, the enzymes in the mammalian de novo purine biosynthetic pathway condense into a single structure, the purinosome, in response to purine limitation, mTOR signaling, and mitochondrial dysfunction (An et al., 2008; An et al., 2010; French et al., 2016). Similarly, hypoxic stress has been found to trigger the reorganization of glycolytic enzymes in yeast and *C. elegans* suggesting that clustering could enhance glycolytic activity in response to energy stress (Jang et al., 2016; Jin et al., 2017). Thus, distinct metabolic stresses can trigger metabolic enzymes to assemble into configurations that can facilitate pathway flux. However, it remains unclear whether the assembly of entire pathways into a common structure is a broadly deployed mechanism for regulating metabolic networks.

This lack of clarity is in spite of the fact that several biochemical and visual screens for proteins that form condensates and/or filaments have been conducted in *S. cerevisiae* in recent years (Chong et al., 2015; Mazumder et al., 2013; Narayanaswamy et al., 2009; Noree et al., 2010; O'Connell et al., 2014; Shen et al., 2016; Tkach et al., 2012). While, these screens have greatly expanded the number of proteins that form structures, these studies have failed to identify any rules or principles that govern which metabolic enzymes can form condensates/filaments and which do not. One possible reason for this failure is that the majority of visual screens have not quantitatively examined the frequency of structure formation across multiple growth conditions. Thus, enzymes that form structures in a small percentage of cells are on an equal footing with enzymes that robustly form structures in every cell potentially complicating any analysis. Similarly, the fact that biochemical screens for protein aggregation only detect partial overlap with visual screens suggests that these two methodologies might have different levels of sensitivity for condensate/filament formation (O'Connell et al., 2014). Thus, a screen that surveyed a variety of physiologically relevant growth conditions and measured the frequency of structure formation would provide a robust dataset for understanding the relationship between pathway architecture and enzyme condensate/filament formation.

Additionally, previous screens have not explored the relationship between enzyme assembly and the known compartmentalization of biochemical pathways into organelles, such as mitochondria. Given the importance of pathway compartmentalization in regulating metabolic flux, determining which compartmentalized enzymes form structures and whether they assemble inside or outside the compartment could reveal missed connections between pathway architecture and the ability of enzymes to form condensates/filaments.

In order to address both of these issues as well as expand the repertoire of metabolic enzymes capable of forming structures, we measured the frequency at which all 440 proteins in the yeast GFP strain collection with an annotated role in metabolism form condensates/filaments under three different growth conditions (log phase, post diauxic shift, and stationary phase). This screen identified 60 proteins capable of forming condensates or filaments in more than 10% of cells during at least one growth condition. This expanded the list of enzymes known to form condensates by 20. Our screen also identified 10 mitochondrial enzymes that form condensates within mitochondria at regions of high metabolic activity. Interestingly, we also identified several pathways where condensate formation was largely restricted to branch points in the metabolic network suggesting that condensate formation might regulate flux at decision points in a pathway. Consistent with this, we found that the assembly of enzymes at the first branch point in *de novo* purine biosynthesis is coordinated, hierarchical, and based on their position within the pathway, while the enzymes at the second branch point are recruited to RNA stress granules. We have also found that the first enzyme in the pathway, phosphoribosyl pyrophosphate (PRPP) synthetase, forms evolutionarily conserved filaments that are sequestered in the nucleus in higher eukaryotes arguing that while the ability to form structures may be conserved the regulatory role of the structures may diverge. Together, these results provide a framework for understanding the variety of ways metabolic enzyme condensates and filaments can be used to regulate the cellular metabolism.

Results

A systematic screen for metabolic enzymes that form intracellular structures.

There have been several screens to date that have identified metabolic enzymes that assemble into intracellular structures (Chong et al., 2015; French et al., 2016; Mazumder et al., 2013; Narayanaswamy et al., 2009; Noree et al., 2010; O'Connell et al., 2014; O'Connell et al., 2012; Shen et al., 2016; Tkach et al., 2012). However, many of these prior studies have focused on a single enzyme, pathway, or growth condition and often scored only the presence or absence of a structure in the population of cells. This has made it difficult to determine how many metabolic enzymes are capable of assembly, the diversity of growth conditions that trigger assembly, and whether assembly occurs broadly or is restricted to a subpopulation of yeast cells.

The goal of our screen was to quantitatively assess the ability of all 440 metabolic enzymes to form structures under three different growth conditions: log phase, post-diauxic shift (1 day), and stationary phase (5 days) (Figure 2.1A). Each of these growth conditions represents distinct metabolic conditions. During log phase, yeast cells grow and divide rapidly by fermentation of glucose present in the media. Upon glucose limitation, yeast enter the post-diauxic shift where they grow slowly and use the ethanol they produced during log phase. After ethanol and other nutrients have been utilized, cell division is dramatically reduced and cells enter stationary phase (Braun et al., 1996; Werner-Washburne et al., 1993).

By systematically identifying all of the enzymes that were capable of forming either foci or filaments and the frequency at which the structures formed, we hoped to identify any underlying principles governing which enzymes are capable of forming

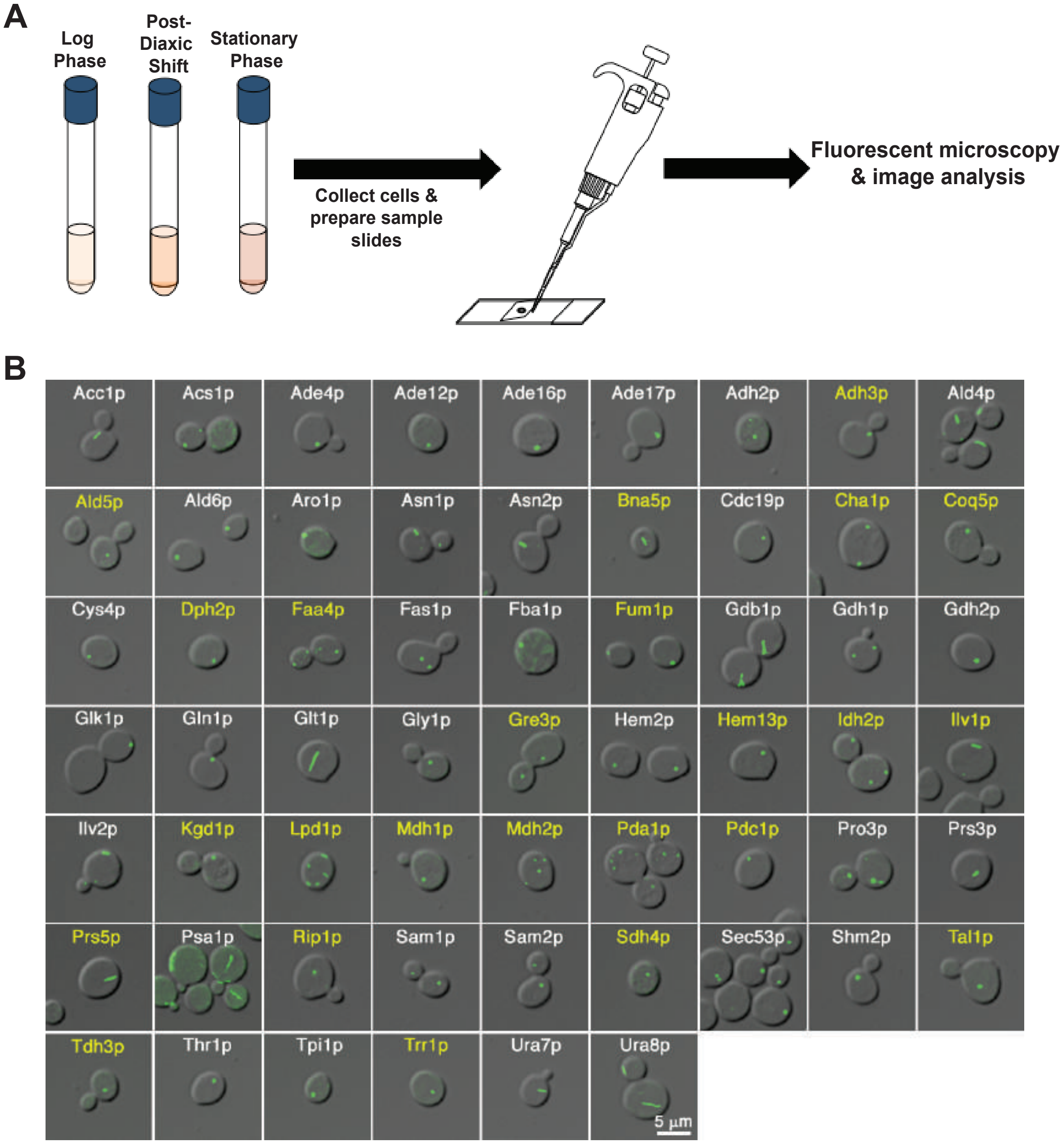

Figure 2.1. Screen of metabolic enzymes reveals 20 new proteins capable of assembly into foci or filaments (A) Schematic for screening the yeast GFP collection to identify all metabolic enzymes with the ability to form structures. Each strain was grown to log phase, post-diauxic shift, and stationary phase in YPD and fixed in 4% formaldehyde for 15 min at room temperature. Cells were washed and resuspended in 1M sorbitol prior to imaging. **(B)** Multiple growth conditions expand the list of metabolic enzymes forming assemblies. Representative images of metabolic enzymes capable of assembly into filaments or foci in greater than 10% of cells. Enzymes names highlighted in yellow represent previously unknown metabolic enzymes forming assemblies. Images were taken from the culture condition with the highest degree of assembly.

intracellular structures. Furthermore, since some GFP fusions cause aggregation in a small percentage of cells, we only included enzymes that formed structures in more than 10% of cells in our analysis. By these criteria, we have our screen has identified 60 metabolic enzymes that formed structures in more than 10% of cells under at least one growth condition (Table 2.1). Forty-seven of these metabolic enzymes formed foci-like structures while 11 assemble into discrete filaments (Figure 2.1B). Of these 11, we have identified three novel filament forming enzymes that have not been identified in previous screens: Bna5p, Prs3p, and Prs5p. While Bna5 encodes for kynureninase, Prs3p and Prs5p are subunits of yeast PRPP synthetase. The remaining 8 filament forming enzymes were also identified in previous screens of the yeast GFP strain collection: Acetyl-CoA carboxylase (Acc1p), asparagine synthetase (Asn1p, Asn2p), glycogen debranching enzyme (Gdb1p), glutamate synthase (Glt1p), GDP-mannose pyrophosphorylase (Psa1p) and CTP synthetase (Ura7p, Ura8p) (Noree et al., 2010; Petrovska et al., 2014; Shen et al., 2016). While all of these enzymes are capable of forming distinct filaments as assayed by pair-wise colocalization (Figure 2.2), 5 pairs of these filaments exhibit partial co-localization: Asn1p/Prs5p, Bna5p/Prs5p, Glt1p/Prs5p, Ura7p/Prs5p, and Gdb1p/Ura7p. This type of assembly is reminiscent of the stress-specific lateral assembly of CTP synthase filaments with IMP dehydrogenase filaments in mammalian cells (Carcamo et al., 2011; Chang et al., 2018; Keppeke et al., 2015). Thus, in addition to identifying 3 novel filament-forming metabolic enzymes our screen has also significantly broadened the number of metabolic filaments capable of lateral interactions providing a new window into this type of filament interaction.

Table 2.1. Metabolic enzymes identified to be capable of forming intracellular structures

Protein	Molecular function (SGD)	Pathways (SGD)	Cellular Components (SGD)	Abundance (% cells with structures)		
				Log	1-Day	5-Day
Acc1p	Acety-CoA carboxylase Biotin carboxylase	Fatty acid synthesis	Endoplasmic reticulum membrane Mitochondrion	19%	8%	37%
Acs1p	Acetate-CoA ligase	Acetate utilization Ethanol degradation	Cytoplasm Integral to membrane Mitochondrion	0%	4%	92%
Ade4p	Amidophosphoribosyltransferase	De novo biosynthesis of purine nucleotides	Cytoplasm	0%	18%	10%
Ade12p	Adenylsuccinate synthetase	De novo biosynthesis of purine nucleotides	Cytoplasm	0%	0%	44%
Ade16p	IMP cyclohydrolase Phosphoribosylaminoimidazolecarboxamide formyltransferase	De novo biosynthesis of purine nucleotides	Cytoplasm	0%	0%	42%
Ade17p	IMP cyclohydrolase Phosphoribosylaminoimidazolecarboxamide formyltransferase	De novo biosynthesis of purine nucleotides	Cytoplasm	0%	4%	33%
Adh2p	Alcohol dehydrogenase (NAD)	Ethanol degradation Glucose fermentation Isoleucine degradation Valine degradation	Cytoplasm	0%	0%	10%
Adh3p	Alcohol dehydrogenase (NAD)	Ethanol degradation Glucose fermentation Isoleucine degradation Valine degradation	Mitochondrial matrix Soluble fraction Mitochondrion	N/A	41%	4%
Ald4p	Aldehyde dehydrogenase (NAD) Aldehyde dehydrogenase [NAD(P)+]	Glucose fermentation	Mitochrondrial nucleoid Mitochondrion	59%	97%	94%
Ald5p	Aldehyde dehydrogenase [NAD(P)+]	Glucose fermentation	Mitochondrion	N/A	18%	11%
Ald6p	Aldehyde dehydrogenase [NAD(P)+]	Glucose fermentation	Cytoplasm Mitochondrion	0%	13%	66%
Aro1p	3-dehydroquinate dehydratase 3-dehydroquinate synthase Shikimate kinase	Chorismate biosynthesis Phenylalanine biosynthesis	Cytoplasm	0%	2%	16%
Asn1p	Asparagine synthase (glutamine-hydrolyzing)	Asparagine biosynthesis	Cytoplasm	0%	10%	90%
Asn2p	Asparagine synthase (glutamine-hydrolyzing)	Asparagine biosynthesis	Cytoplasm	0%	12%	92%
Bna5p	Kynureninase	De novo NAD biosynthesis	Cytoplasm Nucleus	0%	10%	80%
Cdc19p	Pyruvate kinase	Glucose fermentation Glycolysis	Cytoplasm	5%	43%	85%
Cha1p	L-serine ammonia-lyase L-threonine ammonia-lyase	L-serine degradation Threonine catabolism	Mitochondrial nucleoid Mitochondrion	0%	29%	5%
Coq5p	2-hexaprenyl-6-methoxy-1,4-benzoquinone methyltransferase	Ubiquinone biosynthesis	Mitochondrial matrix Mitochondrion	N/A	N/A	41%
Cys4p	Cysathionine beta-synthase	Cysteine biosynthesis from homocysteine Homocysteine degradation	Cytoplasm	3%	11%	20%
Dph2p	Unknown	Diphthamide biosynthesis	Cytoplasm	0%	0%	28%
Faa4p	Long-chain fatty acid-CoA ligase	Fatty acid oxidation	Lipid particle Cytoplasm	28%	61%	5%

Table 2.1. Metabolic enzymes identified to be capable of forming intracellular structures (continued)

Protein	Molecular function (SGD)	Pathways (SGD)	Cellular Components (SGD)	Abundance (% cells with structures)		
				Log	1-Day	5-Day
Fas1p	Palmitoyltransferase	Fatty acid biosynthesis Palmitate biosynthesis	Cytoplasm Fatty acid synthase complex Cytoplasm	0%	3%	26%
Fba1p	Fructose-bisphosphate aldolase	Gluconeogenesis Glucose fermentation Glycolysis	Mitochondrion Cytoplasm	0%	0%	15%
Fum1p	Fumurate hydratase	TCA cycle Aerobic respiration	Cytoplasm Mitochondrial matrix Mitochondrion	0%	13%	67%
Gdb1p	4-alpha-glucanotransferase	Glycogen catabolism	Cytoplasm Mitochondrion	0%	12%	39%
Gdh1p	Glutamate dehydrogenase (NADP+)	Glutamate biosynthesis	Nucleus Cytoplasm	0%	17%	12%
Gdh2p	Glutamate dehydrogenase (NADP+)	Glutamate degradation	Mitochondrion	19%	89%	95%
Glk1p	Glucokinase	Glucose fermentation Glucose-6-phosphate biosynthesis	Cytoplasm	22%	2%	25%
Gln1p	Glutamate-ammonia ligase	Glutamine biosythesis	Cytoplasm	5%	63%	86%
Glt1p	Glutamate synthase (NADH)	Glutamate biosynthesis from glutamine	Mitochondrion	24%	64%	98%
Gly1p	L-allo-threonine aldolase Threonine aldolase	Glycine biosynthesis from threonine	Cytoplasm	0%	11%	9%
Gre3p	Alditol:NADP+ 1-oxidoreductase	Xylose metabolism	Cytoplasm Nucleus	0%	10%	0%
Hem2p	Porphobilinogen synthase	Tetrapyrrole biosynthesis Heme and siroheme biosynthesis	Cytoplasm Nucleus	0%	12%	73%
Hem13p	Coproporhyrinogen oxidase	Heme biosynthesis	Cytoplasm	0%	15%	0%
Idh2p	Contributes to isocitrate dehydrogenase	TCA cycle Aerobic respiration	Mitochondrial matrix Mitochondrion	18%	58%	31%
Ilv1p	L-threonine ammonia-lyase	Isoleucine biosynthesis	Mitochondrion	43%	4%	1%
Ilv2p	Acetolactate synthase	Acetoin biosynthesis Isoleucine biosynthesis	Mitochrondrion	N/A	N/A	20%
Kgd1p	Oxoglutarate dehydrogenase	TCA cycle Aerobic respiration	Mitochodrial matrix Mitochondrial nucleoid Mitochondrion	47%	95%	100%
Lpd1	Dihydrolipoyl dehydrogenase	Folate biosynthesis	Mitochondrial nucleoid Mitochondrion	N/A	N/A	85%
Mdh1p	L-malate dehydrogenase	TCA cycle Aerobic respiration	Mitochondrial matrix Mitochondrion	N/A	N/A	12%
Pda1p	Pyruvate dehydrogenase	Pyruvate dehydrogenase complex	Mitochondrial nucleoid Mitochondrion	97%	96%	20%
Pdc1p	Pyruvate decarboxylase	Glucose fermentation Isoleucine degradation	Nucleus Cytoplasm	0%	0%	72%
Pro3p	Pyrroline-5-carboxylate reductase	Arginine degradation Proline biosynthesis	Cytoplasm	0%	12%	2%
Prs3p	Contributes to ribose phosphate diposphokinase	Histidine, purine, and pyrimidine biosynthesis	Cytoplasm	0%	6%	63%
Prs5p	Contributes to ribose phosphate diposphokinase	Histidine, purine, and pyrimidine biosynthesis	Cytoplasm	0%	40%	55%

Table 2.1. Metabolic enzymes identified to be capable of forming intracellular structures (continued)

Protein	Molecular function (SGD)	Pathways (SGD)	Cellular Components (SGD)	Abundance (% cells with structures) Log	1-Day	5-Day
Psa1p	Mannose-1-phosphate guanylyltransferase	Mannose biosynthesis	Cytoplasm	0%	23%	6%
Rip1p	Contribute to ubiquinol-cytochrome-c reductase	Aerobic respiration Electron transport chain	Mitochondrion	N/A	N/A	29%
Rnr4p	Ribonucleoside-diphosphate reductase	De novo biosynthesis of purine nucleotides	Cytoplasm Nucleus	2%	27%	80%
Sam1p	Methionine adenosyltransferase	S-adenosylmethionine biosynthesis	Cytoplasm	0%	19%	95%
Sam2p	Methionine adenosyltransferase	S-adenosylmethionine biosynthesis	Unknown	0%	11%	60%
Sdh4p	Contributes to succinate dehydrogenase	TCA cycle Electron transport chain	Mitochondrion	0%	12%	22%
Shm2p	Glycine hydroxymethyltransferase	Folate biosynthesis	Cytoplasm	19%	45%	27%
Sec53p	Phosphomannomutase	Mannose biosynthesis	Cytoplasm	0%	9%	41%
Tal1p	Sedoheptulose-7-phopshate:D-glyceraldehyde-3-phosphate glyveronetransferase	Non-oxidative branch of pentose phosphate pathway	Cytoplasm Nucleus	15%	58%	71%
Tdh3p	Glyceraldehyde-3-phosphate dehydrogenase	Gluconeogenesis Glucose fermentation Glycolysis	Cytoplasm Mitochondrion	0%	N/A	41%
Thr1p	Homoserine kinase	Threonine biosynthesis	Unknown	81%	78%	56%
Tpi1p	Triosephosphate isomerase	Glucose fermentation Glycolysis	Mitochondrion Cytoplasm	0%	3%	20%
Trr1p	Thioredoxin-disulfide reductase	Thioredoxin system	Cytoplasm	0%	13%	29%
Ura7p	CTP synthase	De novo biosynthesis of pyrimidine ribonucleotides	Cytoplasm	0%	9%	90%
Ura8p	CTP synthase	De novo biosynthesis of pyrimidine ribonucleotides	Cytoplasm	0%	6%	89%

Note: N/A = ambiguous, or signal is too dim, or too bright to distinguish structures from the background
Blue indicates metabolic enzymes with structures within the mitochondria

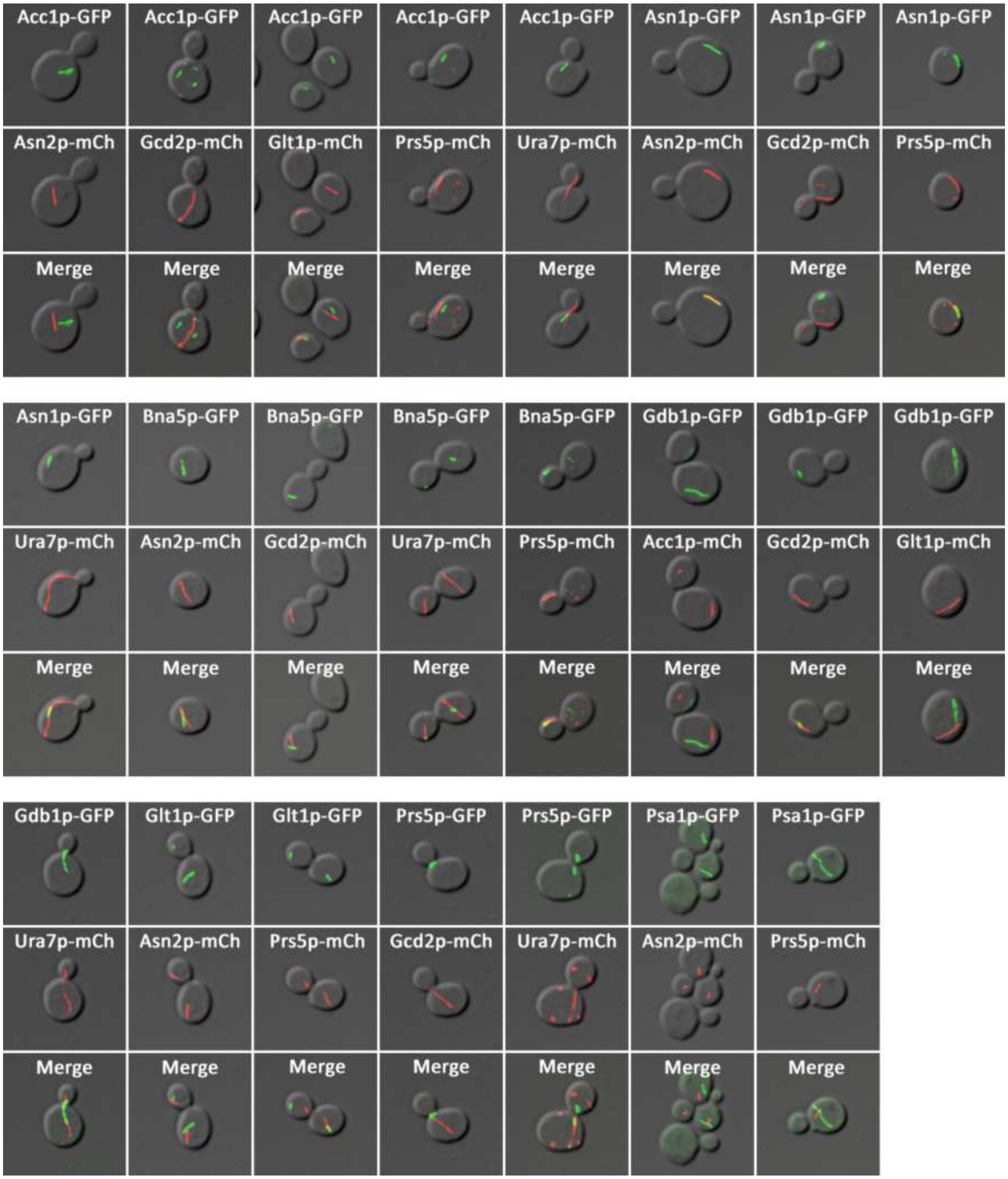

Figure 2.2. Pairwise colocalization reveals novel filament-forming proteins Dual fluorescent strains were grown to the time point where both structures were most abundant and fixed in 4% formaldehyde prior to imaging.

Analysis of our screen revealed 4 basic patterns of assembly: log phase restricted, stationary phase restricted, nutrient limited (restricted to both saturation and stationary phase), and constitutive. ~80% of the enzymes assemble solely when nutrients are limiting with the largest single category were those enzymes that assembled during both saturation and stationary phase (26/59) followed closely by enzymes that assemble only in stationary phase (17/59). Thus, while nutrient limitation is a major trigger for assembly across all metabolic pathways, the type of nutrient limitation (post diauxic shift vs stationary) is a key determinant in whether an individual enzyme will assemble.

Identification of metabolic enzymes that form structures within mitochondria

Previous screens of the yeast GFP strain collection for novel intracellular structures have focused largely on the presence or absence of a structure. However, there has been no systematic assessment of whether these enzyme structures are associated with organelles or other structures in the cell. This is particularly problematic since the compartmentalization of several metabolic pathways to mitochondria is a key organizing principle of metabolic biochemistry. Furthermore, the yeast metabolic enzyme, Ald4p, has recently been found to form structures within the mitochondria suggesting that a subset of metabolic enzymes might be forming within other compartments (Misonou et al., 2014; Noree, 2018). The fact that our screen identified 24 putative mitochondrial metabolic enzymes presented us with a unique opportunity to explore the extent of metabolic enzyme self-assembly within mitochondria. GFP yeast strains for each of the 24 hits from our screen which had a mitochondrial annotation were stained with MitoTracker to determine if the structures assembled inside or outside of mitochondria. (Table 2.1; Figure 2.3, Figure 2.4A). Ten of the enzymes formed discrete puncta within

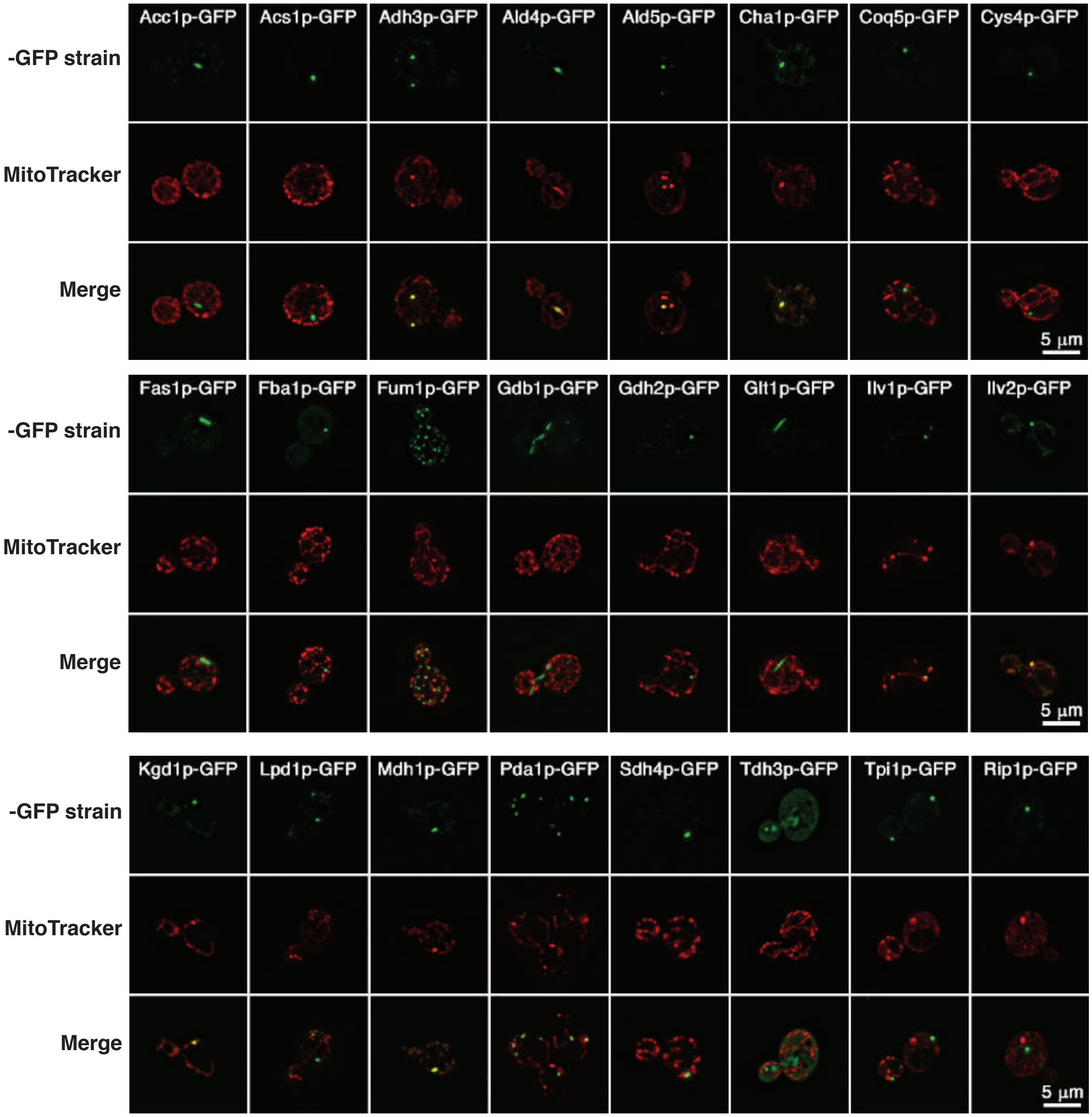

Figure 2.3. Mitotracker staining identifies metabolic enzymes forming structures in the mitochondria Ten of the twenty four mitochondrial annotated enzymes from our screen were able to form foci within the mitochondria. Cells expressing GFP-tagged metabolic enzymes were incubated with 0.1µM Mitotracker Red for 30 minutes. Cells were washed and then imaged immediately.

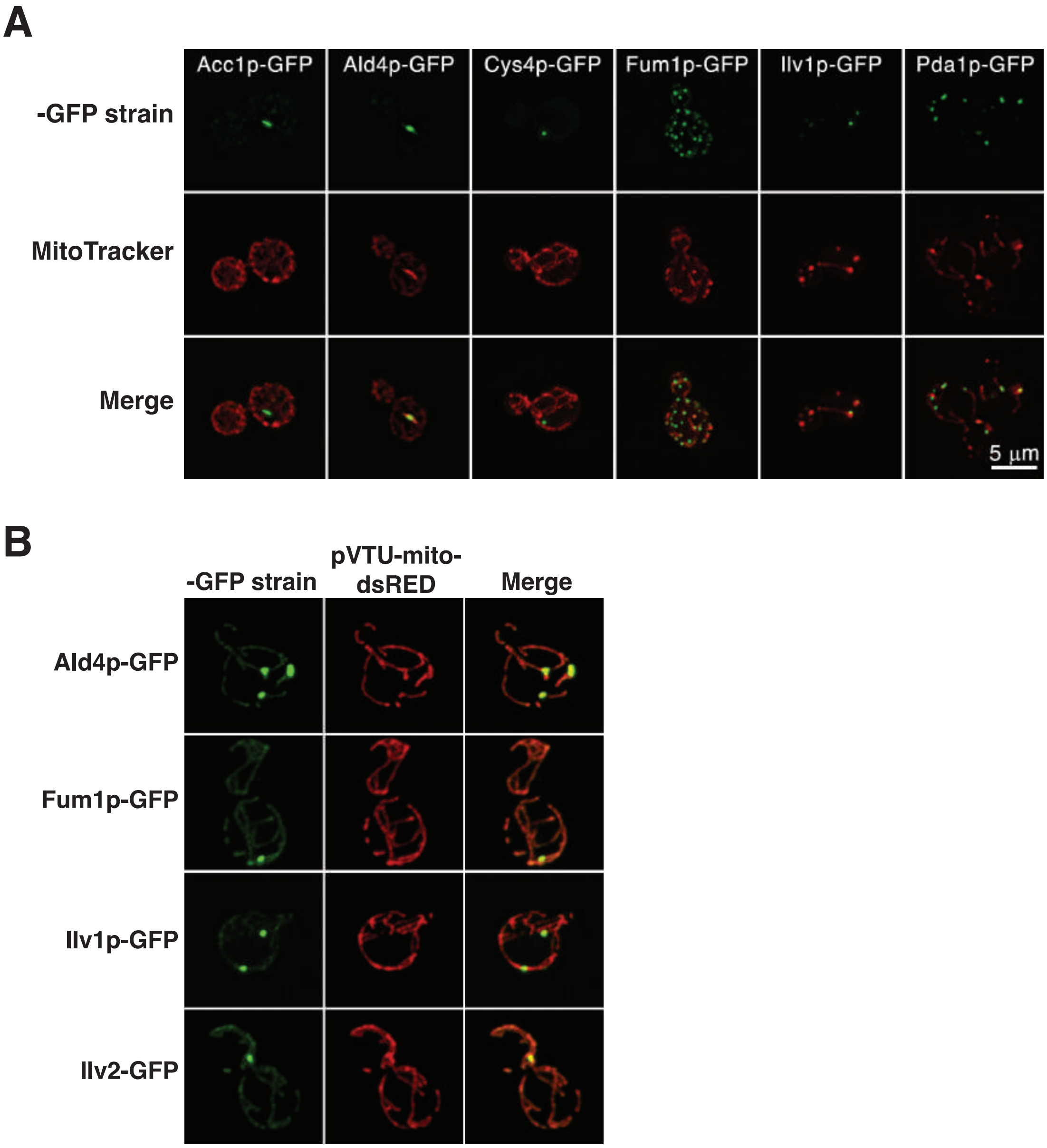

Figure 2.4. Metabolic enzymes can form discrete structures inside and/or outside of the mitochondria (**A**) Mitotracker staining reveals differential distribution of metabolic enzyme structures inside or outside of the mitochondria. Cells expressing GFP-tagged metabolic enzymes were incubated with 0.1µM Mitotracker Red for 30 minutes. Cells were washed and then imaged immediately. **(B)** Assembly of metabolic enzymes do not overlap with high density regions of mitochondria. Cells expressiong GFP- tagged metabolic enzymes were transformed with a plasmid containing a dsRed fluorescent protein attached to a mitochondrial targeting sequence (pVTU-mito-dsRED). Dual fluorescent strains were grown to either log phase (Ald4p) or post-diauxic shift (Fum1p, Ilv1p, Ilv2p) and imaged for colocalization.

the mitochondria and had annotations where the sole localization reported in the SGD was the mitochondria (Table 2.1). The remaining fourteen metabolic enzymes formed structures outside the mitochondria and were not studied further.

In the course of analyzing our MitoTracker staining, we noted that enzyme structures were often found at sites of high MitoTracker signal. Since MitoTracker import reflects mitochondrial activity, this suggested that either these enzymes were concentrated at regions of high respiratory activity or that enzymes accumulated at regions of high mitochondrial density. To distinguish between these two possibilities, we transformed a subset of our yeast GFP strains with a plasmid expressing dsRed fused to a mitochondrial targeting sequence. The distribution of these enzymes within the mitochondria was then examined under the growth conditions where foci formation is observed, either log phase (Ald4p) or post-diauxic shift (Fum1p, Ilv1p, Ilv2p). Our analysis revealed that the location of metabolic enzyme structures within mitochondria was not correlated with sites of high mitochondrial density suggesting that these enzymes might be accumulating in sites of high mitochondrial activity (Figure 2.4B).

One potential location for these structures is the nucleoid, which has long been known to be associated with metabolic enzymes. However, the number of structures that we observe are not consistent with the typical numbers of nucleoids present within the mitochondrial network under these growth conditions (Miyakawa, 2017; Miyakawa et al., 1984). Furthermore, when we compared the results from our screen with proteomic analysis of the nucleoids from yeast, we found that only 3 of the 10 metabolic enzymes that co-purified with nucleoids and were present in the GFP strain collection formed visible structures in our assay conditions (Miyakawa, 2017) (Figure 2.5). Thus, these enzymes are likely forming novel structures within mitochondria.

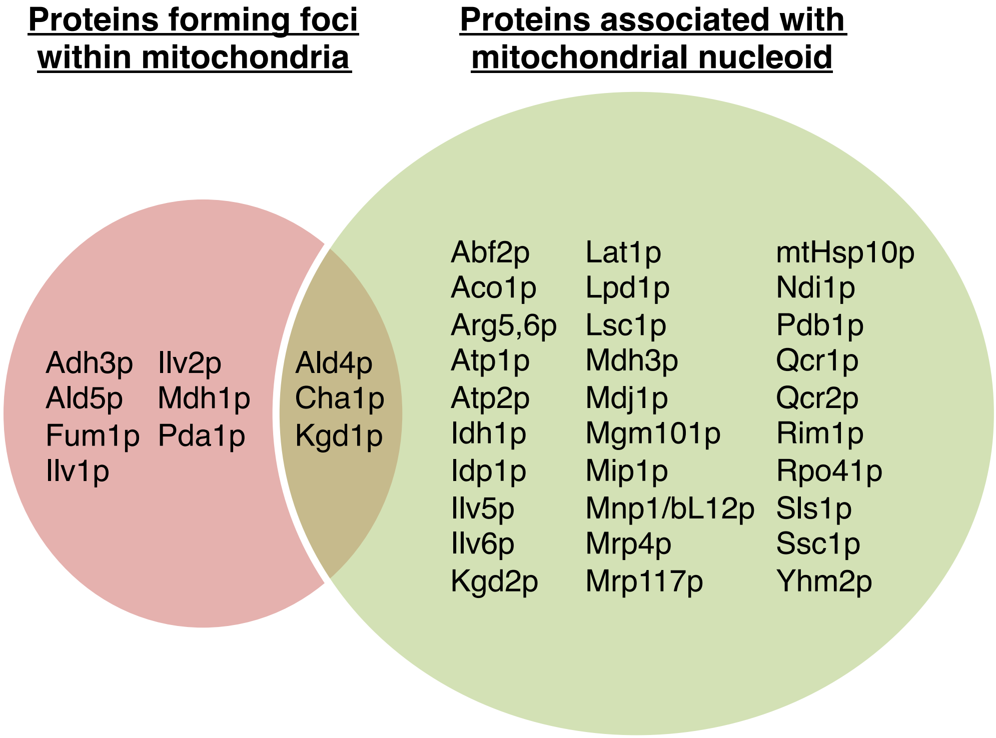

Figure 2.5. Only three mitochondrial proteins identified in our screen have association with the yeast mitochondrial nucleoid Venn diagram comparing the metabolic enzymes forming structures within the mitochondria and those proteins identified to be associated with the yeast mitochondrial nucleoid (Miyakawa, 2017).

Enzymes that act at nodes in the purine biosynthetic pathway assemble into distinct visible intracellular structures

The fact that our screen uncovered interactions between different metabolic filaments and identified enzymes that assemble within mitochondria suggested that there might be levels of metabolic enzyme organization and coordination that have been missed in previous screens. In order to address this, we focused on one well-studied pathway, *de novo* purine biosynthesis, to determine if there was any pattern to which enzymes formed structures and if the pattern of assembly was coordinated with pathway activity/regulation. We chose to use the de novo purine biosynthesis pathway for two reasons. First, a variety of studies of the *de novo* purine biosynthetic pathway in mammals identified a subset of enzymes assembled into a common structure in response to purine deprivation, the purinosome (Figure 2.6A) (An et al., 2008). Second, while multiple purine biosynthetic enzymes in yeast have been found to form enzyme structures, the fact that these structures did not form a classic "purinosome" suggested that another form of regulation might be operating in *S. cerevisiae* (Narayanaswamy et al., 2009; O'Connell et al., 2014). Thus, a more in depth analysis of this pathway in *S. cerevisiae* would allow us both to determine what aspects of enzyme organization, if any, are evolutionarily conserved and how assembly might be used to regulate metabolic flux through a pathway.

As part of this analysis, we rescreened all 21 proteins that comprise the *de novo* purine biosynthetic pathway for the ability to assembly into intracellular structures, the frequency with which these structures form, and the growth conditions that triggered assembly using the yeast GFP strain collection. For each enzyme, the percentage of cells with GFP-labeled structures was determined in triplicate for four different growth conditions: log phase growth and cultures grown to 1 day (post-diauxic shift), 3 days (transitional), or 5 days (stationary phase). Our

Figure 2.6. Enzymes in the *de novo* purine biosynthetic pathway assemble with different kinetics (A) Schematic of the *de novo* purine biosynthetic pathway with yeast orthologs in blue on the left and mammalian orthologs in green on the right. Abbreviations for intermediate metabolites and catalytic enzymes: R5P = Ribose-5-phosphate; PRPP = 5-Phosphoribosylpyrophosphate; PRA = 5- phosphoribosylamine; GAR = 5-phosphoribosylglycineamide; FGAR = 5'-phosphoribosyl- *N*- formylglycinamide; FGAM = 5'-phosphoribosyl-*N*-formylglycinamidine; AIR = 5'-phosphoribosyl-5- aminoimidazole; CAIR = 5'- phosphoribosyl-4-carboxy-5-aminoimidazole; SAICAR = 5'- phosphoribosyl-4-(N-succinocarboxamide)-5-aminoimidazole; AICAR = 5-amino-4- imidazolecarboxamide ribotide; FAICAR = 5-formamido-1-(5-phosphoribosyl)-imidazole-4- carboxamide; IMP = inosine- 5'-monophosphate; XMP = xanthosine-5'-phosphate; GMP = guanosine-5'- phosphate; GDP = guanosine-5'-diphosphate; SAMP = adenylosuccinate; AMP = adenosine-5'- phosphate; ADP = adenosine-5'-diphosphate; Prs1-5p = phosphoribosylpyrophosphate synthetase; Ade4p = amidophosphoribosyltransferase; Ade5,7p = GAR synthetase/AIR synthetase; Ade8p = GAR transformylase; Ade6p = FGAM synthetase; Ade2p = AIR carboxylase; Ade1p = SAICAR synthase; Ade16/17p = IMP cyclohydrolase; Ade12p = Adenylosuccinate synthetase; Ade13p = adenylosuccinate lyase; Adk2p = mitochondrial GTP:AMP phosphotransferase; Adk1p = adenylate kinase; Imd2-4p = IMP dehydrogenase; Gua1p = GMP synthetase; Guk1p = guanylate kinase; PPAT = PRPP amidotransferase; TrifGART = trifunctional glycinamide ribonucleotide (GAR) transformylase; GARS = GAR synthase; GAR Tfase = GAR transformylase; AIRS = aminoimidazole ribonucleotide (AIR) synthase; FGAMS = formylglycinamidine ribonucleotide (FGAM) synthase; PAIC = phosphoribosylaminoimidazole carboxylase; CAIRS = carboxyaminoimidazole ribonucleotide (CAIR) synthase; SAICARS = succinylaminoimidazolecarboxamide ribonucleotide (SAICAR) synthase; ASL = adenylosuccinate lyase; ATIC = AICAR transformylase/IMP cyclohydrolase; AICAR Tfase = aminoimidazolecarboxamide ribonucleotide (AICAR) transformylase ; IMPCH = IMP cyclohydrolase (**B)** Assembly of PRPP synthetase subunits is enriched for Prs3p and Prs5p. GFP-tagged versions of the PRPP synthetase proteins (Prs1p, Prs2p, Prs3p, Prs4p, Prs5p) were grown in YPD to log phase, 1 day, 3 day, and 5 day time points and assayed for assembly formation. Representative images are shown below. **(C)** Only enzymes located at branch points (Ade4p and Ade16/17p) assemble into foci. GFP tagged versions of purine biosynthetic enzymes acting in middle of the pathway were grown in identical conditions as indicated in (B) and assayed for assembly formation. Representative images are shown below. **(D)** Ade12p is the only enzyme forming foci in the ADP production branch. GFP tagged versions of purine biosynthetic enzymes involved in ADP production were grown in identical conditions as indicated in (B) and assayed for assembly formation. Representative images are shown below. **(E)** All subunits of the IMPDH complex assemble into foci. GFP tagged versions of purine biosynthetic enzymes involved in GDP production were grown in identical conditions as indicated in (B) and assayed for assembly formation. Representative images are shown below. Data is represented as mean of at least three independent experiments; error bars indicate SEM. Images were taken from the culture condition with the highest degree of assembly.

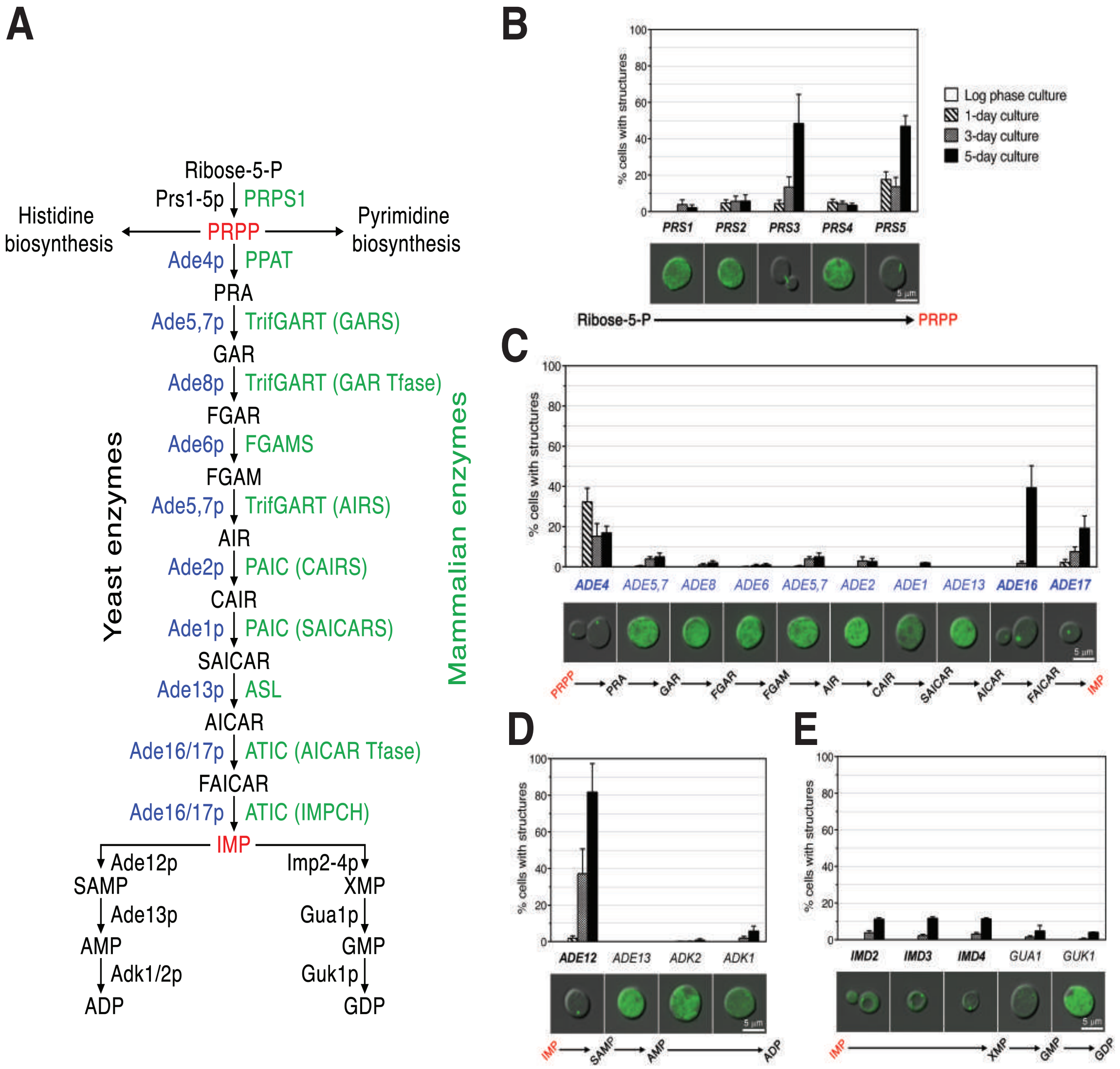
A
Ribose-5-P
Prs1-5p
PRPS1
Histidine biosynthesis
PRPP
Pyrimidine biosynthesis
Ade4p
PPAT
PRA
Ade5,7p
TrifGART (GARS)
GAR
Ade8p
TrifGART (GAR Tfase)
FGAR
Ade6p
FGAMS
FGAM
Ade5,7p
TrifGART (AIRS)
AIR
Ade2p
PAIC (CAIRS)
CAIR
Ade1p
PAIC (SAICARS)
SAICAR
Ade13p
ASL
AICAR
Ade16/17p
ATIC (AICAR Tfase)
FAICAR
Ade16/17p
ATIC (IMPCH)
IMP
Ade12p
SAMP
Ade13p
AMP
Adk1/2p
ADP
Imp2-4p
XMP
Gua1p
GMP
Guk1p
GDP
Yeast enzymes
Mammalian enzymes
B
% cells with structures
100
80
60
40
20
0
PRS1
PRS2
PRS3
PRS4
PRS5
5 µm
Ribose-5-P
PRPP
Log phase culture
1-day culture
3-day culture
5-day culture
C
% cells with structures
100
80
60
40
20
0
ADE4
ADE5,7
ADE8
ADE6
ADE5,7
ADE2
ADE1
ADE13
ADE16
ADE17
5 µm
PRPP
PRA
GAR
FGAR
FGAM
AIR
CAIR
SAICAR
AICAR
FAICAR
IMP
D
% cells with structures
100
80
60
40
20
0
ADE12
ADE13
ADK2
ADK1
5 µm
IMP
SAMP
AMP
ADP
E
% cells with structures
100
80
60
40
20
0
IMD2
IMD3
IMD4
GUA1
GUK1
5 µm
IMP
XMP
GMP
GDP

quantitative analysis found that twelve of the 21 proteins involved in *de novo* purine biosynthesis displayed little if any assembly behavior (i.e. structures in <6% of cells in at least one growth condition) (Figure 2.6B-D; Table 2.2). This list included Ade5,7p and Ade2p which previous screens identified as forming foci (Narayanaswamy et al., 2009; O'Connell et al., 2014), but which form foci only at low frequency under our growth conditions (4.95% -Ade5,7p; 2.98% - Ade2p). In contrast, nine of the proteins showed a high level of assembly with most forming structures in 30-80% of cells under at least one growth condition (Figure 2.6B-D; Table 2.2). These nine proteins that form structures represent five distinct purine biosynthetic enzymes: PRPP synthetase (Prs3p, Prs5p), PRPP amidotransferase (Ade4p), 5-amino-4-imidazolecarboxamide ribonucleotide transformylase/IMP cyclohydrolase (Ade16/17p), adenylosuccinate synthase (Ade12p) and inosine monophosphate (IMP) dehydrogenase (Imd2-4p). Interestingly, four of these five enzymes that form foci at high frequency are known to be highly regulated by feedback inhibition and allosteric control consistent with a role in flux control (Holmes et al., 1974; Rebora et al., 2001; Smith, 1998; Switzer and Sogin, 1973; Van der Weyden and Kelly, 1974; Wyngaarden, 1976). Additionally, all of these enzymes are found at branchpoints/nodes in the purine biosynthetic pathway and many enzymes that were found in the mammalian purinosome did not assemble to a significant degree in yeast. We also confirmed that the assembly behavior of these 9 proteins was independent of the GFP tag and that the GFP tag did not cause auxotrophy in the cases where this could be examined (Figure 2.7). Thus, these structures are not due to the GFP tag or protein denaturation.

The fact that these enzymes are assembling at branch points within a given pathway raised the question of whether or not this is a feature common to multiple metabolic pathways. Consistent with the *de novo* purine biosynthetic pathway, we found that enzymes that can form

Table 2.2. Summary of structure formation frequency of yeast enzymes involved in purine biosynthesis

Biological process	Protein	% Cells with structures (Average ± SEM)			
		Log-phase	1-day	3-day	5-day
PRPP biosynthesis	**Prs1p-GFP**	0.00 ± 0.00	0.00 ± 0.00	3.84 ± 2.65	2.17 ± 1.55
	Prs2p-GFP	0.00 ± 0.00	4.72 ± 1.75	5.64 ± 2.82	5.77 ± 3.40
	Prs3p-GFP	0.00 ± 0.00	4.38 ± 1.92	13.41 ± 5.63	48.34 ± 16.09
	Prs4p-GFP	0.00 ± 0.00	5.08 ± 1.75	4.34 ± 1.43	3.48 ± 1.11
	Prs5p-GFP	0.00 ± 0.00	17.60 ± 4.20	13.61 ± 5.07	46.79 ± 5.86
IMP biosynthesis	**Ade4p-GFP**	0.00 ± 0.00	32.28 ± 6.79	15.26 ± 6.25	16.89 ± 3.30
	Ade5,7p-GFP	0.00 ± 0.00	0.43 ± 0.24	3.93 ± 1.16	4.95 ± 1.97
	Ade8p-GFP	0.00 ± 0.00	0.00 ± 0.00	0.91 ± 0.73	2.01 ± 1.02
	Ade6p-GFP	0.00 ± 0.00	0.14 ± 0.14	0.62 ± 0.62	0.96 ± 0.75
	Ade5,7p-GFP	0.00 ± 0.00	0.43 ± 0.24	3.93 ± 1.16	4.95 ± 1.97
	Ade2p-GFP	0.00 ± 0.00	0.00 ± 0.00	2.98 ± 1.97	2.63 ± 1.49
	Ade1p-GFP	0.00 ± 0.00	0.00 ± 0.00	0.00 ± 0.00	1.99 ± 0.20
	Ade13p-GFP	0.00 ± 0.00	0.00 ± 0.00	0.00 ± 0.00	0.00 ± 0.00
	Ade16p-GFP	0.00 ± 0.00	0.00 ± 0.00	1.78 ± 1.03	39.29 ± 10.97
	Ade17p-GFP	0.00 ± 0.00	2.25 ± 1.45	7.57 ± 2.42	19.16 ± 6.14
AMP/ADP biosynthesis	**Ade12p-GFP**	0.00 ± 0.00	1.94 ± 1.27	37.21 ± 13.52	81.70 ± 15.60
	Ade13p-GFP	0.00 ± 0.00	0.00 ± 0.00	0.00 ± 0.00	0.00 ± 0.00
	Adk2p-GFP	0.00 ± 0.00	0.13 ± 0.13	0.16 ± 0.16	0.80 ± 0.80
	Adk1p-GFP	0.00 ± 0.00	0.00 ± 0.00	1.92 ± 1.02	5.80 ± 2.65
GMP/GDP biosynthesis	**Imd2p-GFP**	0.00 ± 0.00	0.00 ± 0.00	3.78 ± 1.21	11.17 ± 0.86
	Imd3p-GFP	0.00 ± 0.00	0.00 ± 0.00	2.21 ± 0.76	11.65 ± 0.88
	Imd4p-GFP	0.00 ± 0.00	0.00 ± 0.00	3.10 ± 0.82	11.37 ± 0.61
	Gua1p-GFP	0.00 ± 0.00	0.00 ± 0.00	1.42 ± 0.73	4.83 ± 2.95
	Guk1p-GFP	0.00 ± 0.00	0.00 ± 0.00	0.42 ± 0.42	4.02 ± 0.24

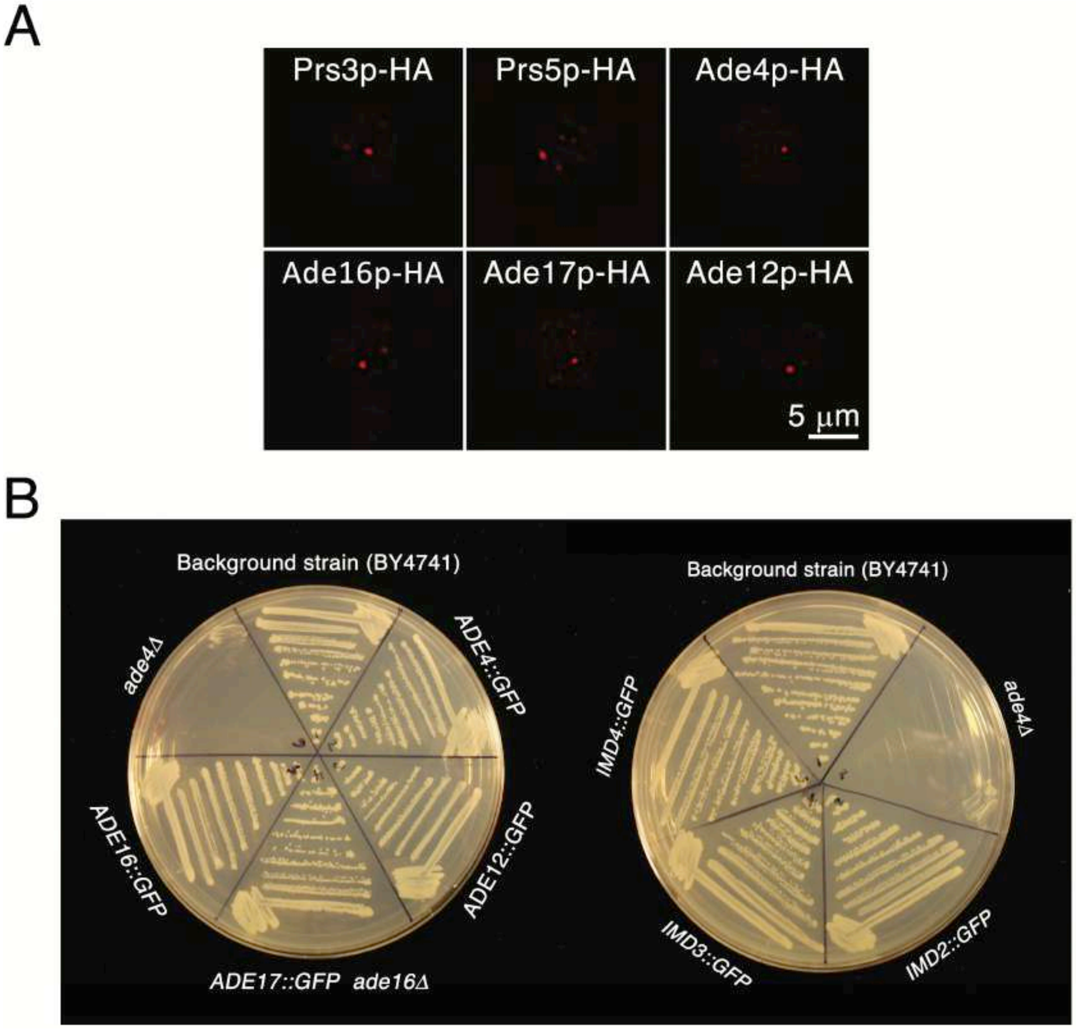

Figure 2.7. Assembly of purine enzymes is not GFP-dependent and the GFP-tagged enzymes are functional (A) Structure formation of purine biosynthetic enzymes is not due to GFP aggregation. Yeast cells expressing HA-tagged purine biosynthetic enzymes were grown in YPD for 5 days and indirect immunofluorescence was performed using an anti-HA antibody. **(B)** GFP-tagged strains do not interfere with functionality of the metabolic enzyme. Yeast strains were tested by streaking them out on adenine dropout plates. *ADE17::GFP ade16Δ* is able to grow on the adenine dropout plate, confirming that GFP does not affect the function of Ade17p. Yeast *ade4Δ* is used as a negative control as it cannot grow on the plate without adenine supplement.

structures are found at highly connected portions of glycolysis pathway, glutamate biosynthetic pathway, and the methionine/cysteine biosynthetic pathway (Figure 2.8). This suggests that spatial reorganization of metabolic enzymes might be used to coordinate flux through competing branches of particular pathways in response to nutrient limitation.

Higher order assembly is not used for substrate channeling or to coordinate activity at distinct nodes

Our finding that the only enzymes that form structures at high frequency are those that act at nodes in the *de novo* purine biosynthetic pathway suggested three potential novel modes of regulation. First, the enzymes at nodes could co-assemble to route products down specific pathways via substrate channeling. Second, the enzymes that act at different nodes could co-assemble in order to facilitate feedback inhibition. Third, pathway flux might not be regulated via co-assembly of enzymes in this pathway. In order to distinguish between these possibilities, we performed pair-wise co-localization experiments between the enzymes that act at the first committed step in *de novo* purine biosynthesis (Prs3p, Prs5p, and Ade4p) as well as those that act the second major branchpoint in the pathway, which are involved with generation and conversion of IMP into either GTP or ATP (Ade16p, Ade17p, Ade12p, and Imd4p). For each set of enzymes, one protein was tagged with GFP while the second was tagged with mCherry (Figure 2.9). We only observed colocalization when enzymes acted at the same step: Prs3p and Prs5p (Figure 2.9A), which are both subunits of PRPP synthetase, and Ade16p and Ade17p, which are isozymes of the bifunctional 5-aminoimidazole-4-carboxamide ribonucleotide transformylase/IMP cyclohydrolase (Figure 2.9B). These results argue that the assembly of these enzymes into large structures is not a strategy for substrate channeling, since enzymes that act on different steps are not found in the same structure.

Figure 2.8. Position within a pathway can determine the ability of self-assembly
(A) Representative images of metabolic enzymes involved in glycolysis and glucose fermentation pathways. Images were taken from the culture condition with the highest degree of assembly. **(B)** Schematic of the glycolysis and glucose fermentation pathway. Metabolic enzymes that form intracellular structures are highlighted in red. Abbreviations: Glk1p = glucokinase, Hxk1p/Hxk2p = hexokinase, Pgi1p = glucose-6-phosphate isomerase, Pfk1p/Pfk2p = phosphofructokinase, Fba1p = aldolase, Tpi1 = triosephosphate isomerase, Tdh1p/Tdh2p/Tdh3p = glyceraldehyde-3-phosphate dehydrogenase, Pgk1p = 3-phosphoglycerate kinase, Gpm1p = phosphoglycerate mutase, Eno1p/Eno2p = enolase, Cdc19p = pyruvate kinase, Pdc1p = pyruvate decarboxylase, Adh2p/Adh3p = alcohol dehydrogenase, Ald4p/Ald5p/Ald6p = aldehyde dehydrogenase. **(C)** Representative images of metabolic enzymes involved in the glutamate biosynthetic pathway. Images were taken from the culture condition with the highest degree of assembly. **(D)** Schematic of glutamate biosynthetic pathway. Metabolic enzymes that form intracellular structures are highlighted in red. Abbreviations: NH_3 = ammonia, Gln1p = glutamine synthetase, Glt1p = glutamate synthase, Gdh1p/Gdh2p/Gdh3p = NADP-dependent glutamate dehydrogenase. **(E)** Representative images of metabolic enzymes involved in methionine and cysteine biosynthesis. Images were taken from the culture condition with the highest degree of assembly. **(F)** Schematic of methionine and cysteine biosynthesis. Metabolic enzymes that form intracellular structures are highlighted in red. Abbreviations: Met6p = Cobalamin-independent methionine synthase, Cys4p = cystathionine beta-synthase, Cys3p = cystathionine gamma-lyase, Sam1p/Sam2p = S- adenosylmethionine synthetase

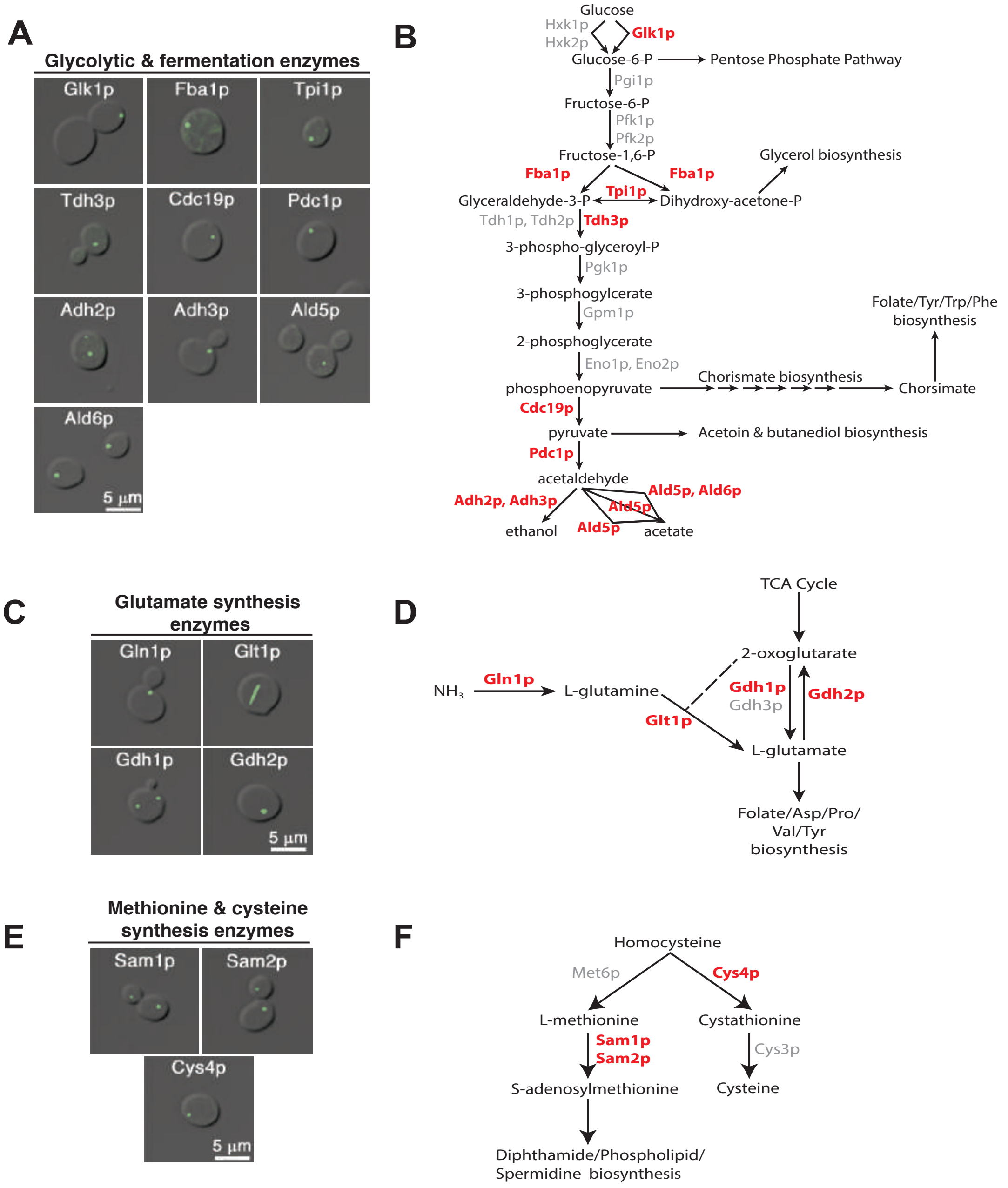
A
Glycolytic & fermentation enzymes
Glk1p
Fba1p
Tpi1p
Tdh3p
Cdc19p
Pdc1p
Adh2p
Adh3p
Ald5p
Ald6p
5 µm
B
Glucose
Hxk1p
Hxk2p
Glk1p
Glucose-6-P
Pentose Phosphate Pathway
Pgi1p
Fructose-6-P
Pfk1p
Pfk2p
Fructose-1,6-P
Glycerol biosynthesis
Fba1p
Fba1p
Tpi1p
Glyceraldehyde-3-P
Dihydroxy-acetone-P
Tdh1p, Tdh2p
Tdh3p
3-phospho-glyceroyl-P
Pgk1p
3-phosphogylcerate
Folate/Tyr/Trp/Phe biosynthesis
Gpm1p
2-phosphoglycerate
Eno1p, Eno2p
Chorismate biosynthesis
phosphoenopyruvate
Chorsimate
Cdc19p
pyruvate
Acetoin & butanediol biosynthesis
Pdc1p
acetaldehyde
Ald5p, Ald6p
Adh2p, Adh3p
Ald5p
ethanol
Ald5p
acetate
C
Glutamate synthesis enzymes
Gln1p
Glt1p
Gdh1p
Gdh2p
5 µm
D
TCA Cycle
2-oxoglutarate
NH$_3$
Gln1p
L-glutamine
Gdh1p
Gdh3p
Gdh2p
Glt1p
L-glutamate
Folate/Asp/Pro/Val/Tyr biosynthesis
E
Methionine & cysteine synthesis enzymes
Sam1p
Sam2p
Cys4p
5 µm
F
Homocysteine
Met6p
Cys4p
L-methionine
Cystathionine
Sam1p
Sam2p
Cys3p
S-adenosylmethionine
Cysteine
Diphthamide/Phospholipid/Spermidine biosynthesis

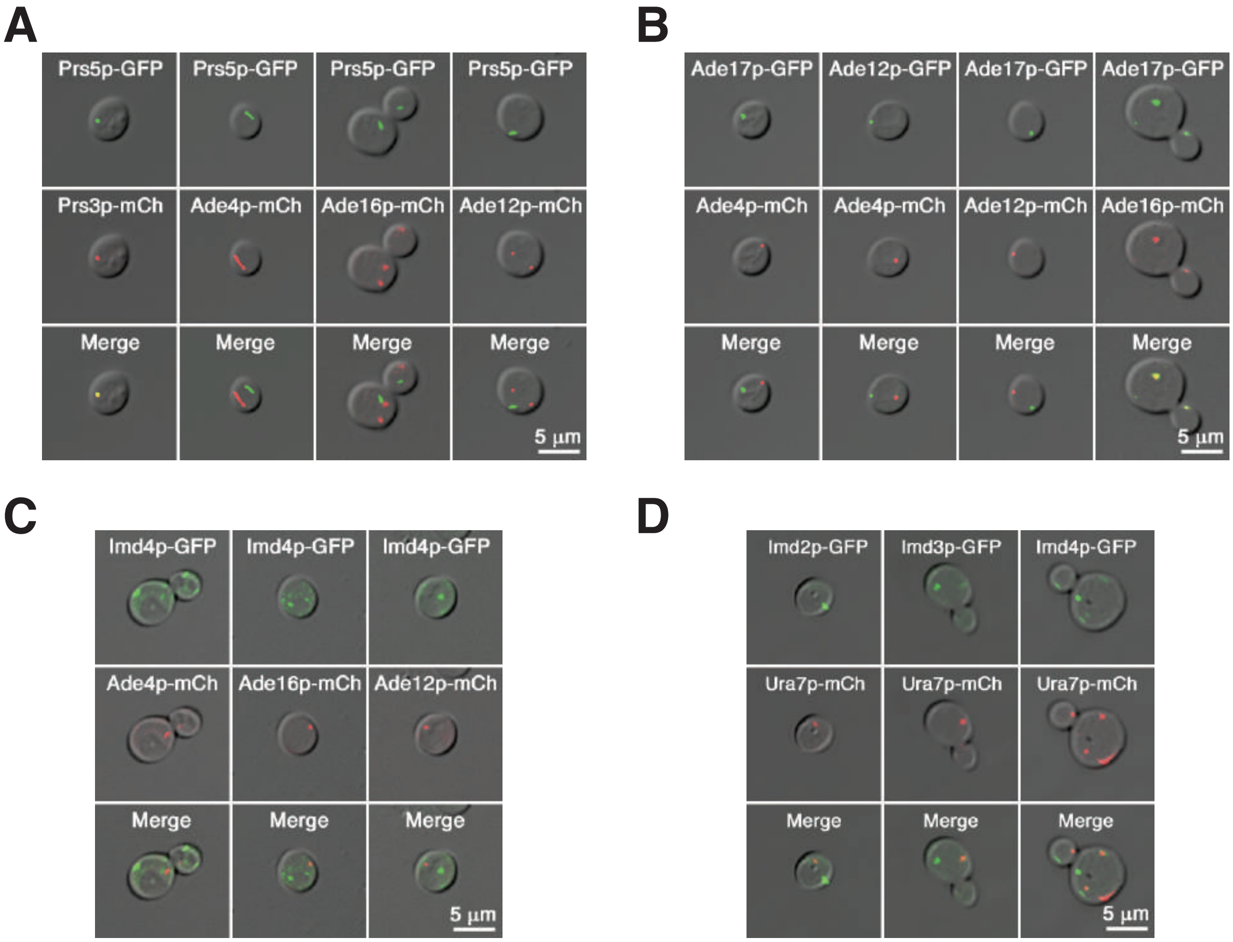

Figure 2.9. Only intracellular structures formed by metabolic enzymes performing the same reaction colocalize with each other.
(A) Prs5p does not colocalize with any downstream enzyme in the *de novo* purine biosynthetic pathway. Dual fluorescent strains were grown to 5 days in YPD for imaging. **(B)** Only Ade16p and Ade17p foci show colocalization with each other. Growth conditions were identical to those indicated in (A). **(C)** Imd4p fails to colocalize with its upstream enzyme (Ade4p, Ade16p) or its cross-pathway enzyme (Ade12p). Growth conditions were identical to those indicated in (A). **(D)** Unlike in other eukaryotes, IMP dehydrogenase (Imd2-4p) does not colocalize with CTP synthetase (Ura7p). Growth conditions were identical to those indicated in (A).

We next examined the possibility that enzymes acting at different nodes within the same or competing pathways might co-assemble to facilitate coordinated regulation. First, we used pair-wise co-localization experiments to determine if there were any enzymes that acted at the first decision point in *de novo* purine biosynthesis that co-assembled with enzymes at the second decision point. Ade4p, which acts at the first committed step of *de novo* purine biosynthesis, showed no co-localization with any of the enzymes (Ade17p, Ade12p, and Imd4p) that act at the second decision point in the pathway (Figure 2.9B). Thus, the enzymes from the two major nodes of this pathway do not co-assemble with each other. We also explored the possibility that enzymes that form intracellular structures and whose products are known to cross-regulate each other might co-assemble to facilitate the balancing of flux through different parts of the metabolic network.

Since the downstream products of Ade12p and Imd2/3/4p cross regulate each other to ensure the balanced synthesis of ATP and GTP, we tested whether these enzymes co-assemble to facilitate pathway balancing. We observed no co-localization of these enzymes arguing that the formation of these structures is not necessary for coordinating the activity of the different branches of the *de novo* purine biosynthetic pathway (Figure 2.9C). We also extended this analysis to coordination between purine and pyrimidine biosynthesis. Since CTP synthetase (Ura7p) is a highly studied metabolic polymer and is allosterically activated by GTP, the downstream product of Imd2/3/4p, we examined whether Ura7p and Imd2/3/4p structures co-localized (Carcamo et al., 2011; Ingerson-Mahar et al., 2010; Levitzki and Koshland, 1972; Liu, 2010; Noree et al., 2010). Ura7p filaments were not associated with any of the structures formed by Imd2p, Imd3, or Imd4p (Figure 2.9D). Thus, while the ability of metabolic enzymes in the *de novo* purine biosynthetic pathway to form structures is restricted to those enzymes that act at key decision points in the pathway, there appears to be no co-assembly to facilitate regulation within or between different pathways. Together, this argues the role of these enzyme structures in flux control does not occur via a substrate channeling mechanism.

A subset of purine biosynthetic enzymes are components of RNA granules

Since the assembly of metabolic enzymes within the *de novo* purine biosynthetic pathway does not appear to be a mechanism for substrate channeling, we considered other ways these enzyme structures might impact metabolic flux. One way to control flux through a pathway is by modulating the levels of rate limiting enzymes in the cytoplasm (Jin et al., 2017; Saad et al., 2017). It was recently shown that yeast pyruvate kinase, Cdc19p, was recruited into RNA granules upon carbon starvation to regulate its enzymatic activity highlighting a new localization pattern for controlling metabolic flux (Saad et al., 2017). Since many RNA granules form in the cytoplasm under the same conditions that cause metabolic enzymes to assemble, we examined the possibility if any purine biosynthetic enzymes had similar crosstalk with these structures. In order to explore this possibility, we evaluated the localization pattern of the enzymes in purine biosynthesis that form structures for co-localization with either RNA stress granules (Ded1p-mCherry) and/or processing bodies (Edc3p-mCherry). Prs3p and Prs5p were excluded from these studies since they form filaments that are clearly distinct from RNA granules. While Ade4p and Ade12p showed little (<5%) localization with either RNA granule marker when yeast are grown to stationary phase, the vast majority of Ade16p (91%) and Ade17p (90%) co-localized with the stress granule marker, Ded1p (Figure 2.10A; Table 2.3). Furthermore, the remaining Ade16p (8%) and Ade17p (9%) structures appear to be processing bodies as measured by co-localization with the processing body marker Edc3p-mCherry (Figure 2.10B; Table 2.3). Thus, while

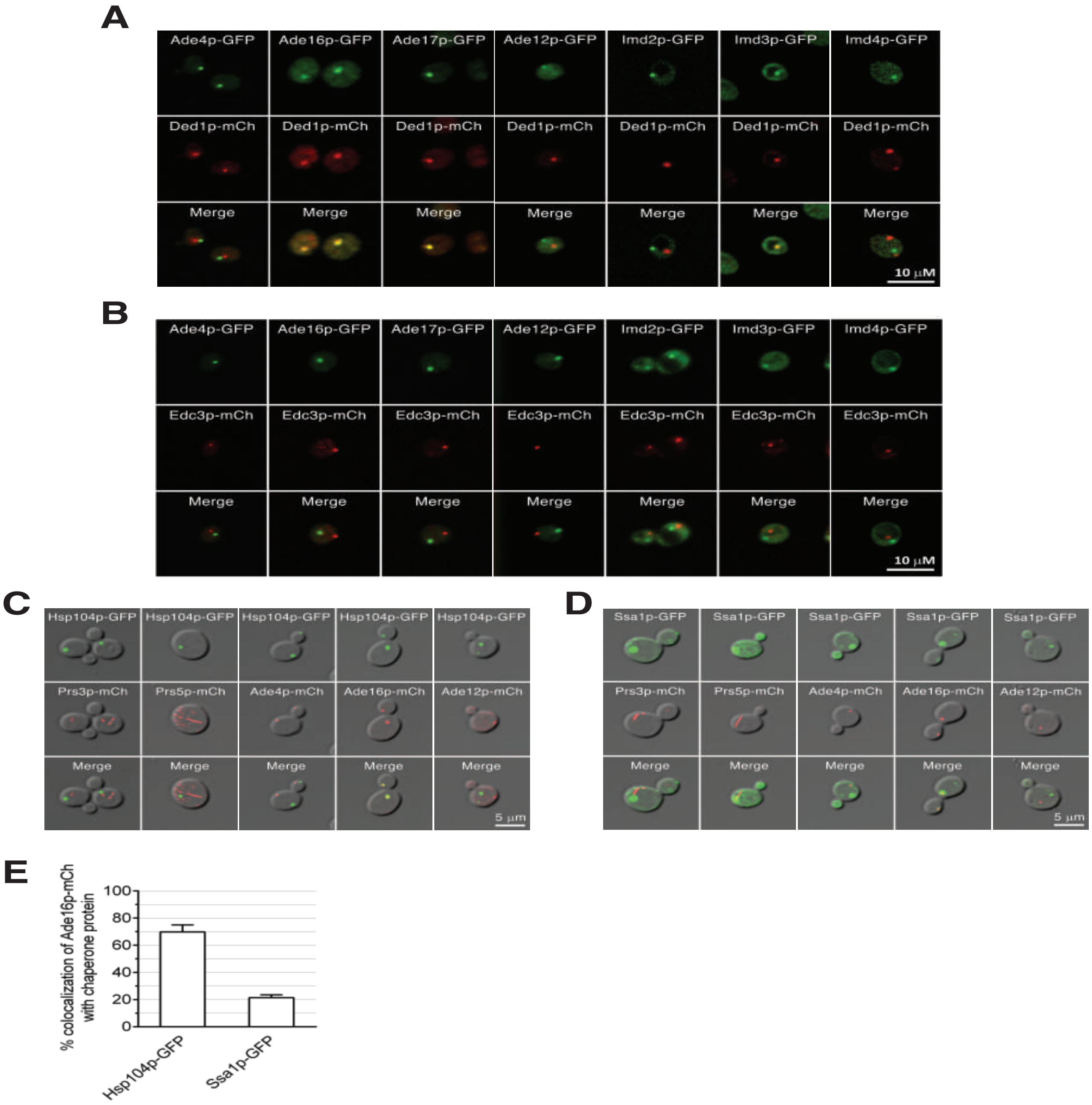

Figure 2.10. Ade16p, Ade17p and Imd3p are recruited to stress granules
(A) Ade16p, Ade17p, and Imd3p display high levels of colocalization with the stress granule marker, Ded1p. Dual fluorescent strains were grown in YPD to 5 days, with the exception of Ade4p-GFP, which was examined at 1 day. **(B)** All enzymes in the purine biosynthetic pathway showed no colocalization with the processing body marker, Edc3p. Growth conditions were identical to those indicated in (A). **(C)** Ade16p also colocalizes with known stress granule associated chaperone, Hsp104p. Growth conditions were identical to those indicated in (A). **(D)** Ade16p colocalizes with known stress granule associated chaperone, Ssa1p. Growth conditions were identical to those indicated in (A). **(E)** Quantification of colocalization of Ade16p with chaperones Hsp104p and Ssa1p. Data is represented as mean of at least three independent experiments; error bars indicate SEM.

Table 2.3. Summary of colocalization frequency of GFP-tagged protein with mCherry-tagged Ded1p or mCherry-tagged Edc3p

Protein	% of GFP foci that colocalize with Ded1p-mCherry	% of GFP foci that colocalize with Edc3p-mCherry
ADE4::GFP	2.95 ± 0.71	4.31 ± 0.39
ADE16::GFP	91.10 ± 1.86	8.11 ± 1.29
ADE17::GFP	90.29 ± 0.63	9.58 ± 1.84
ADE12::GFP	5.25 ± 1.20	4.96 ± 0.66
IMD2::GFP	13.09 ± 1.58	6.67 ± 0.98
IMD3::GFP	34.68 ± 3.89	7.30 ± 1.48
IMD4::GFP	15.99 ± 2.73	6.67 ± 1.01

stationary phase is a trigger for all four enzymes to assemble, only Ade16/17p, is specifically recruited to RNA granules.

We also observed a higher degree of colocalization of Imd3p with stress granules compared to Imd2p and Imd4p (Figure 2.10A-B; Table 2.3). The recruitment of one subunit of the IMP dehydrogenase complex to stress granules suggests that Imd3p possesses a potential novel function involved in RNA metabolism, whereas the other subunits do not. To further validate the presence of metabolic enzymes in stress granules, we scored for the colocalization of two associated chaperones, Hsp104p and Ssa1p, and found overlap of these foci with Ade16p (Figure 2.10C-E, Table 2.4). Surprisingly, Ade16/17p and Imd3p also lack the prion-like domains that typically play a role in recruitment of proteins to stress granules suggesting that they are recruited via a novel mechanism. Thus, Ade16/17p and Imd3p are novel components of stress granules and their association suggests a potential role in post-transcriptional gene regulation and metabolism.

Specific subunits of PRPP synthetase polymerize under distinct growth conditions

Since only a subset of purine enzymes are localized to RNA granules, we next explored other mechanisms for controlling pathway activity such as the sequestration of essential subunits into a structure. Yeast PRPP synthetase presents an excellent case study for such a possibility due to its unusual subunit architecture. While PRPP synthetases in other organisms are homo-oligomeric, no single yeast Prs protein can form a functional enzyme and only certain hetero-oligomeric combinations of the five Prs proteins are enzymatically active. Our initial screen identified that two subunits (Prs3p, and Prs5p) were capable of filament formation and co-localize to the same structure (Fig 2.8A). Interestingly, all of the enzymatically active combinations of Prs subunits contain either Prs3p or Prs5p, but not both. Thus, these two

Table 2.4. Summary of colocalization frequency of Ade16p-mCherry and GFP-tagged chaperone proteins

	with Hsp104p-GFP	**with Ssa1p-GFP**
% colocalization of Ade16p-mCherry	69.89 ± 5.19	21.48 ± 2.01

subunits appear to delineate distinct forms of PRPP synthetase, a conclusion that is supported by the fact that *PRS3Δ* and *PRS5Δ* are synthetically lethal with each other (Hernando et al., 1999; Hernando et al., 1998).

If selective polymerization of Prs3p and Prs5p is a mechanism for regulating PRPP synthetase activity, we would expect that the assembly/dissassembly of each subunit might be triggered by distinct growth conditions. To test this, we examined whether a brief 30 min shift into fresh media could trigger the disassembly of Prs3p and/or Prs5p filaments in yeast grown to stationary phase. This shift caused the rapid disassembly of both Prs3p and Prs5p filaments while the protein levels of both proteins remained constant. Furthermore, 30 min shifts to YP alone caused no disassembly of Prs3p and Prs5p filaments (Figure 2.11A; Table 2.5). As a result, we focused our attention on the role of glucose in triggering disassembly of these filaments. Both Prs3p and Prs5p filaments disassemble in response to either the addition of fresh glucose to the culture or a 30-minute shift to 2% glucose. Thus, the disassembly of both types of filaments is regulated by glucose.

Since addition of glucose triggers disassembly of Prs3p and Prs5p filaments, we predicted that removal of glucose from log phase cultures would trigger assembly. Interestingly, the assembly Prs3p and Prs5p showed a differential response to glucose removal. While Prs3 and Prs5 do not show any structures during logarithmic growth, a 30-minute shift to media lacking glucose was sufficient to trigger Prs5p filament formation in ~90% cells, but did not trigger Prs3p assembly (Figure 2.11B; Table 2.6). Thus, two different subunits of PRPP synthetase in yeast, Prs5p and Prs3p, form filaments under distinct conditions: Prs3p assembles only in stationary phase while Prs5p assembles in response to acute glucose limitation and stationary phase. Because glucose can directly generate the substrate for PRPP synthetase, ribose-5-

Figure 2.11. Coordinated structure formation of Prs5p and Ade4p controls pathway flux **(A)** Prs3p, Prs5p, and Ade4p structures disassemble in response to the presence of fresh glucose. Cells expressing GFP-tagged purine biosynthetic enzymes were grown in YPD for 5 days, except for *ADE4::GFP* strain (1 day), and then shifted into the indicated media and incubated for 30 min at 30°C and visualized immediately. Protein levels were determined by western blot analysis and were normalized to no treatment samples (indicated below blots). **(B)** Prs5p and Ade4p have distinct triggers for structure formation. Yeast cells expressing GFP-tagged purine biosynthetic enzymes were grown to log phase in complete SD media, shifted into the indicated media for 30 min at 30°C, and counted immediately. **(C)** Deletion of downstream enzymes of Ade4p lead to increased structure formation of Ade4p. Wild-type and mutant cells expressing Ade4p-GFP were grown in YPD for 1 day at 30°C and scored for structure formation. Protein levels were determined by western blot analysis and were normalized to the wild-type strain (indicated below blots). **(D)** Loss of feedback inhibition increases foci formation of Ade4p. Cells expressing wild-type Ade4p-GFP and Ade4p(K333Q)-GFP were grown to log phase in YPD and cells were scored for frequency of structure formation. Protein levels were determined by western blot analysis and were normalized to the wild-type strain (indicated below blots). Data is represented as mean of at least three independent experiments; error bars indicate SEM. **(E)** Model for the coordinating activities of Prs5p and Ade4p with regulated structure assembly statuses is illustrated.

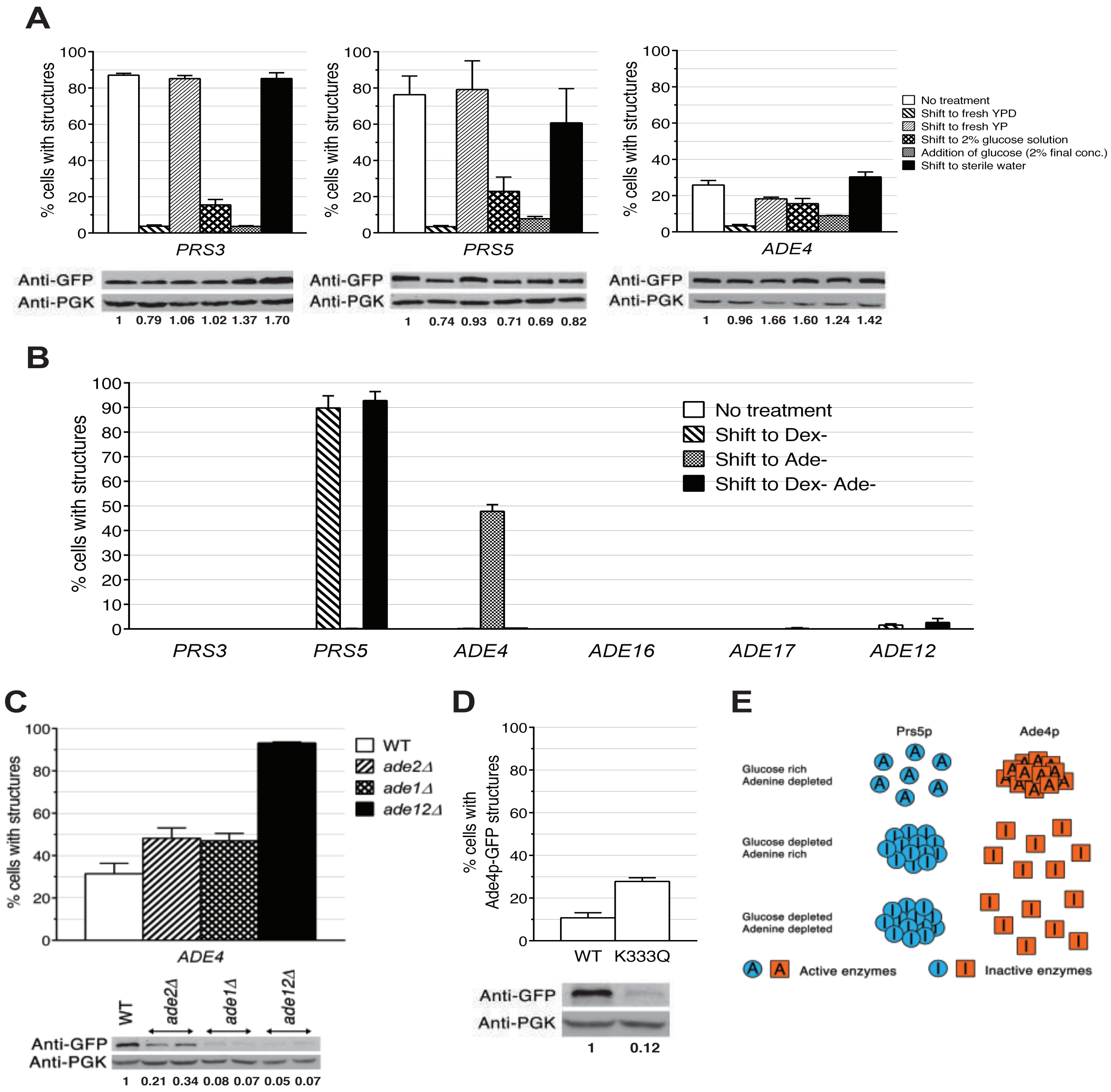
A
% cells with structures
100
80
60
40
20
0
PRS3
PRS5
ADE4
No treatment
Shift to fresh YPD
Shift to fresh YP
Shift to 2% glucose solution
Addition of glucose (2% final conc.)
Shift to sterile water
Anti-GFP
Anti-PGK
1 0.79 1.06 1.02 1.37 1.70
1 0.74 0.93 0.71 0.69 0.82
1 0.96 1.66 1.60 1.24 1.42
B
% cells with structures
100
90
80
70
60
50
40
30
20
10
0
No treatment
Shift to Dex-
Shift to Ade-
Shift to Dex- Ade-
PRS3
PRS5
ADE4
ADE16
ADE17
ADE12
C
% cells with structures
WT
ade2Δ
ade1Δ
ade12Δ
ADE4
Anti-GFP
Anti-PGK
1 0.21 0.34 0.08 0.07 0.05 0.07
D
% cells with Ade4p-GFP structures
WT
K333Q
Anti-GFP
Anti-PGK
1
0.12
E
Prs5p
Ade4p
Glucose rich
Adenine depleted
Glucose depleted
Adenine rich
Glucose depleted
Adenine depleted
Active enzymes
Inactive enzymes

Table 2.5. Summary of structure formation frequency of yeast GFP strains treated with different conditions

Protein	No treatment	Shift to fresh YPD	Shift to fresh YP	Shift to 2% glucose solution	Addition of glucose (2% final conc.)	Shift to sterile water
Prs3p-GFP	87.059 ± 0.991	3.743 ± 0.722	85.184 ± 1.676	15.488 ± 2.988	3.666 ± 0.376	85.189 ± 3.175
Prs5p-GFP	76.287 ± 10.344	3.396 ± 0.635	79.136 ± 15.858	22.916 ± 7.842	7.790 ± 1.216	60.735 ± 18.937
Ade4p-GFP	25.831 ± 2.535	3.297 ± 0.769	18.232 ± 0.905	15.592 ± 2.837	8.896 ± 0.172	30.320 ± 2.704
Ade16p-GFP	35.406 ± 9.359	1.119 ± 0.556	27.084 ± 10.315	0.942 ± 0.471	1.433 ± 0.803	29.714 ± 8.252
Ade17p-GFP	16.440 ± 2.475	5.323 ± 1.322	15.662 ± 4.397	4.201 ± 0.942	3.527 ± 1.209	22.286 ± 3.611
Ade12p-GFP	89.648 ± 7.729	1.184 ± 0.280	71.703 ± 5.603	1.160 ± 0.582	2.601 ± 1.336	71.673 ± 25.561
Imd2p-GFP	10.597 ± 0.585	1.561 ± 0.237	1.272 ± 0.170	2.221 ± 0.306	1.305 ± 0.099	4.373 ± 0.596
Imd3p-GFP	9.788 ± 0.424	1.380 ± 0.372	1.682 ± 0.307	1.785 ± 0.534	1.120 ± 0.296	5.450 ± 0.333
Imd4p-GFP	10.459 ± 0.537	1.309 ± 0.170	1.862 ± 0.562	1.825 ± 0.183	1.461 ± 0.410	7.259 ± 0.639

Table 2.6. Summary of structure formation frequency of yeast GFP strains upon induction by glucose and/or adenine depletion

Protein	No treatment	Shift to Dex-	Shift to Ade-	Shift to Dex- and Ade-
Prs3p-GFP	0.00 ± 0.00	0.00 ± 0.00	0.00 ± 0.00	0.00 ± 0.00
Prs5p-GFP	0.00 ± 0.00	89.82 ± 4.93	0.12 ± 0.12	92.78 ± 3.71
Ade4p-GFP	0.00 ± 0.00	0.12 ± 0.12	47.81 ± 2.69	0.37 ± 0.00
Ade16p-GFP	0.00 ± 0.00	0.00 ± 0.00	0.00 ± 0.00	0.00 ± 0.00
Ade17p-GFP	0.00 ± 0.00	0.00 ± 0.00	0.00 ± 0.00	0.25 ± 0.25
Ade12p-GFP	0.00 ± 0.00	1.56 ± 0.53	0.00 ± 0.00	2.67 ± 1.59

phosphate, via the pentose phosphate pathway, this result suggests that substrate availability could regulate polymerization of Prs3p and Prs5p (Zimmer, 1992).

Ade4p assembly is regulated by end-product inhibition

Given our results with PRPP synthetase, we next examined the disassembly behavior of the other purine biosynthetic enzymes that form structures. In all cases, a brief 30 min shift to fresh YPD caused elimination of all of the structures with no change in protein level (Figure 2.11A, Figure 2.12). Additionally, shifting to YP had little to no effect on the disassembly of any of the purine biosynthetic structures (Figure 2.11A, Figure 2.12; Table 2.5). This suggested that glucose might regulate the disassembly of all of the structures in the de novo purine biosynthetic pathway. The addition of either fresh glucose to the culture or a 30-minute shift to 2% glucose caused Ade16/17p, Ade12p, and Imd2-4p structures to disassemble without a change in protein level; however, Ade4p structures remained intact (Figure 2.12; Table 2.5). Additionally, we found that acute removal of glucose does not trigger the assembly of any other purine biosynthetic enzyme other than Prs5p (Figure 2.11B). Thus, only Prs5p and Ade4p structures showed assembly/disassembly behavior that was distinct from the other enzymes in the pathway.

Given this result, we focused our attention on whether acute removal of adenine from the growth media could trigger purine biosynthetic enzymes to assemble. We focused on the response to adenine limitation for two reasons. First, adenine removal would be predicted to increase flux though the de novo purine biosynthetic pathway; thus, enzymes that assemble would be likely to be doing so in response to increased activity. Second, recent work on Ade4p suggested that removal of adenine for 2 hours caused Ade4p to assemble into structures in a translation-dependent manner raising the possibility that Ade4p structures form due to increased

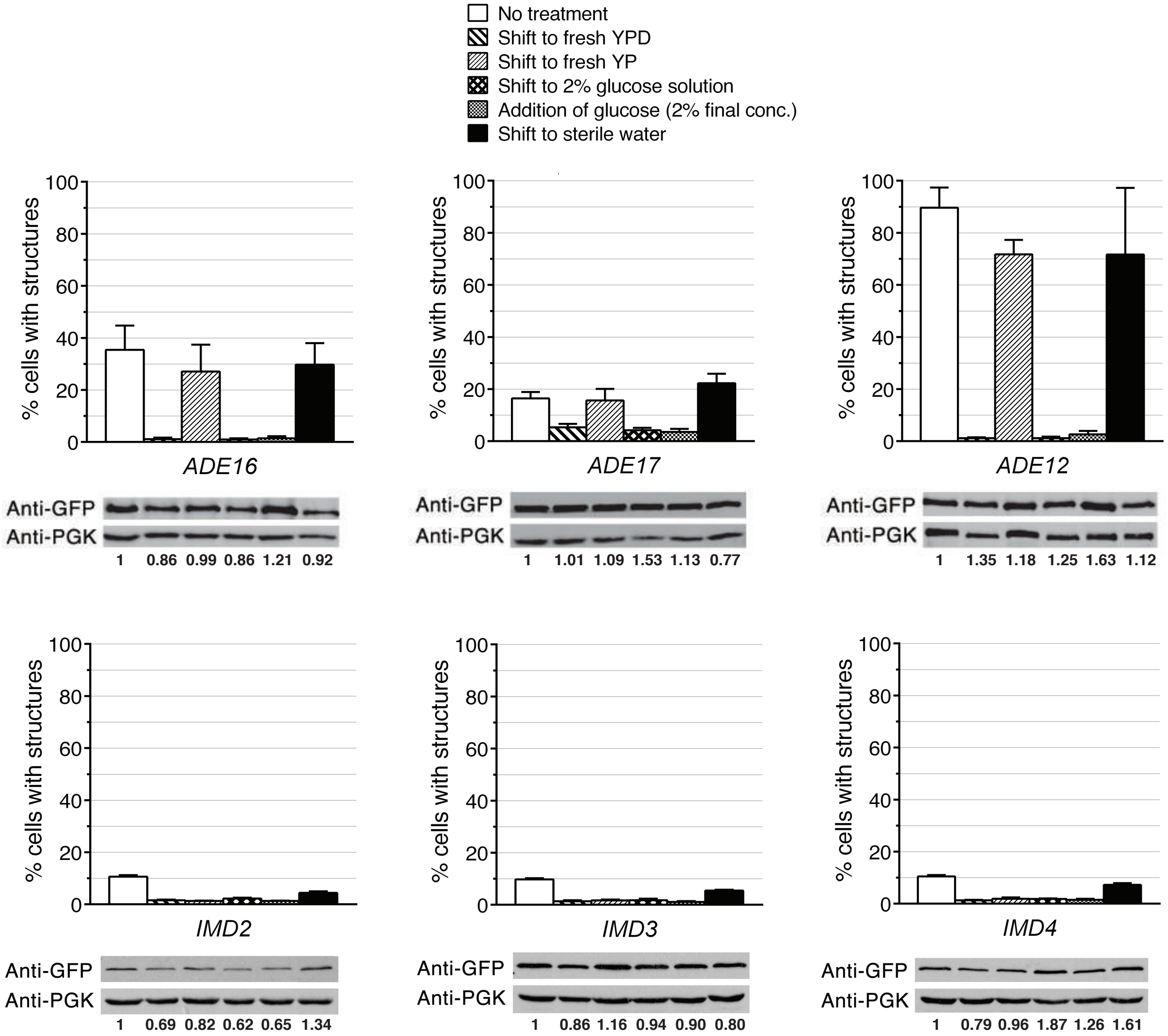

Figure 2.12. Disassembly of downstream acting purine enzymes is carbon-dependent. Addition of fresh media with glucose is able to disassemble all purine biosynthetic enzymes. Cells expressing GFP-tagged purine biosynthetic enzymes were grown in YPD for 5 days and then shifted into the indicated media and incubated for 30 min at 30°C and visualized immediately. Protein levels were determined by western blot analysis and were normalized to no treatment samples (indicated below blots)

protein levels in response to adenine deprivation (Narayanaswamy et al., 2009; O'Connell et al., 2014).

To identify purine biosynthetic enzymes that formed adenine responsive structures, strains were grown to log phase and then shifted to Ade- media for 30 minutes. Only Ade4p assembled (48% of cells) and no change in Ade4p protein levels were observed (Figure 2.11B; Table 2.6). These results suggested that Ade4p formed structures in response to increased enzyme/pathway activity.

While adenine removal is a potent driver of Ade4p assembly, it was unclear what metabolic changes might be triggering the assembly of Ade4p structures. The transcriptional regulation of purine biosynthetic genes is known to respond to the elevated levels of the metabolic intermediate 5-aminoimidazole-4-carboxamide ribonucleotide (AICAR) that occur when flux through the pathway decreases (Pinson et al., 2009). In order to explore whether Ade4p assembly might be responding to changes in metabolite levels, we assayed the effect of deleting different enzymes in *de novo* purine biosynthesis on the assembly of Ade4p foci. Interestingly, Ade4p assembly differed from the transcriptional regulation of the *ADE* genes in that deletion of enzymes that act upstream of AICAR biosynthesis (*ADE1* and *ADE2*) as well as those that act downstream (*ADE12*) increased the number of Ade4p foci when cultures were grown to 1 day (Pinson et al., 2009; Rebora et al., 2001) (Figure 2.11C). While all three deletions caused an increase in Ade4p foci as compared to wild type, the magnitude of the response differed between the different mutations. Deletion of either *ADE1* or *ADE2* caused a 1.5-fold increase in Ade4p foci as compared to wild type, while deletion of *ADE12*, which acts downstream of IMP biosynthesis, caused a 3-fold increase in Ade4p foci with almost all cells (93%) possessing Ade4p structures (Figure 2.11C; Table 2.7). Given that disruption of ATP

Table 2.7. Summary of structure formation frequency of Ade4p-GFP upon deletion of ADE2, ADE1, and ADE12

Gentoype	**% cells with Ade4p-GFP structures**
WT	31.42 ± 4.88
***ade2*Δ**	48.18 ± 4.86
***ade1*Δ**	47.04 ± 3.51
***ade12*Δ**	93.18 ± 0.50

and GTP synthesis (*ade1Δ* and *ade2Δ*) or solely ATP synthesis (*ade12Δ*) display increased Ade4p structures suggests that decreases and/or imbalances of the amount of end products of the pathway to regulate its Ade4p assembly.

Our epistasis analysis of Ade4p assembly is consistent with the fact that Ade4p activity is regulated by ATP and/or GTP levels via a feedback inhibition mechanism (Rebora et al., 2001). To investigate whether Ade4p foci formation is responsive to feedback inhibition, we leveraged previous structural and biochemical studies of *E. coli* amidophosphoribosyltransferase, the orthologue of Ade4p, which identified K326Q as a mutation that confers resistance to feedback inhibition without affecting enzyme activity (Zhou et al., 1993). In order to assess the role of feedback inhibition on Ade4p assembly, we introduced the equivalent mutation (K333Q) into the chromosomal *ADE4* gene in yeast and measured the frequency of structure formation for Ade4p(K333Q)-GFP as compared to wild type when cells are grown to log phase. The Ade4p(K333Q)-GFP strain displayed a 2.6-fold increase in the percentage of cells with structures as compared to WT consistent with increased enzyme activity driving Ade4p assembly (Figure 2.11D; Table 2.8). Thus, while Prs5p subunits are sequestered in an inactive filament, Ade4p assembles under conditions that either decrease end product inhibition or necessitate increased pathway flux.

The assembly of Ade4p and Prs5p is coordinately regulated

If the ability of metabolic enzymes to assemble into filaments and foci is a mechanism for controlling pathway flux, one would expect that assembly/disassembly of different enzymes in the same pathway would be highly coordinated. Consistent with this, we have found that acute glucose removal triggers down regulation of PRPP synthetase activity via Prs5p sequestration, but does not cause activation of Ade4p and the assembly of Ade4p

Table 2.8. Summary of structure formation frequency of WT vs K333Q Ade4p-GFP

	% cells with Ade4p-GFP structures
WT	10.73 ± 2.42
K333Q	27.80 ± 1.73

into structures (Figure 2.11A-B). Interestingly, the converse is also true - acute adenine removal causes activation of Ade4p and the formation of Ade4p structures, but does not cause the inactivation of PRPP synthetase by Prs5p polymerization (Figure 2.11B). While these observations are consistent with coordinated regulation of enzyme assembly, regulation of assembly via glucose and adenine could be occurring independently of each other. If Prs5p polymerization and Ade4p assembly were truly coordinately regulated, one would predict that removal of both glucose and adenine would cause Prs5p to assemble and would block the assembly of Ade4p. This is due to the fact that there is no reason to activate Ade4p, even in the absence of adenine, if the upstream enzymes are inactivated or down regulated. Consistent with this prediction, only Prs5p forms structures when shifted to media lacking both glucose and adenine (Figure 2.11B). Thus, the assembly of Prs5p and Ade4p is coordinately regulated and the hierarchy of assembly reflects their relative position in the *de novo* purine biosynthetic pathway (Figure 2.11B).

The assembly of PRPP synthetase is evolutionarily conserved

The coordinate regulation of Prs5p and Ade4p assembly raised the question of whether the ability of these enzymes to form structures is evolutionarily conserved. Previous work on the mammalian ortholog of Ade4p, PPAT, found that it was recruited to purinosomes in response to purine depravation. This suggested that activation of PPAT/Ade4p via recruitment to an intracellular structure might be evolutionarily conserved. However, the unusual subunit architecture of yeast PRPP synthetase suggested that polymerization might be unique to the yeast enzyme. The active forms of yeast PRPP synthetase are assembled from unique combinations of the 5 *PRS* gene products (Hove-Jensen, 2004). This allows the potential down-regulation of enzyme activity by sequestering an essential subunit via polymerization. However, mammalian

PRPP synthetases are homo-hexameric, suggesting that this type of regulation might not exist in higher eukaryotes (Li et al., 2007). In order to test whether the PRPP synthetase filament formation is evolutionarily conserved, we immunostained Drosophila ovaries, rat hippocampal neurons, and human primary culture fibroblasts for PRPP synthetase. In all three cases, we found that PRPP synthetase forms filaments in the nucleus under normal growth conditions (Figure 2.13A-C). Thus, the ability of PRPP synthetase to form filaments is evolutionarily conserved.

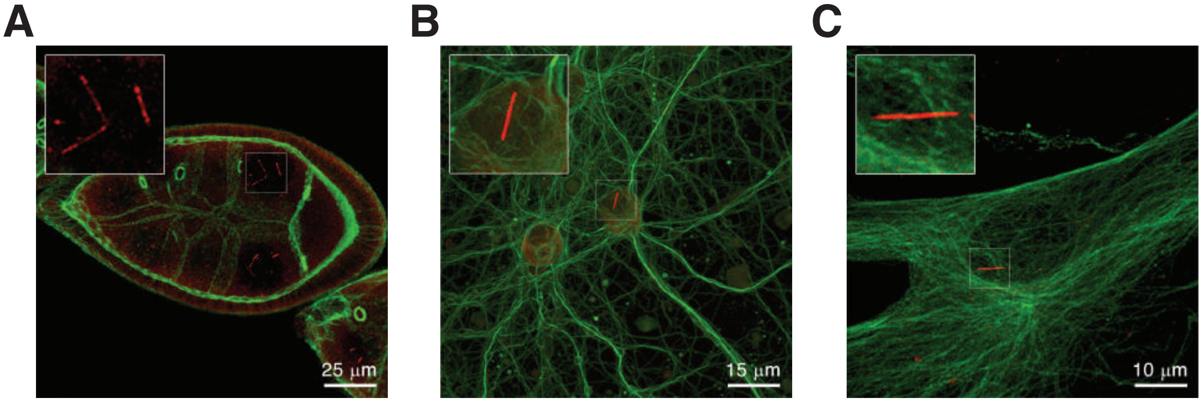

Figure 2.13. Filament formation of PRPP synthetase is evolutionarily conserved
Conservation of PRPP synthetase into filaments observed in *Drosophila* egg chambers (**A**), rat neurons (**B**), and human fibroblasts (**C**). The insert at the top left corner of each image is 3x magnified of the original image. PRPP synthase is stained with anti-PRPS1 (Covance) (in red), and tubulin is detected with anti-tubulin-FITC (Sigma) (in green).

Discussion

Regulation of metabolic networks by self-assembling enzymes

There have been several proposed roles for metabolic enzymes assembling into supra-molecular complexes. End product inhibition by CTP is a trigger for bacterial CTP synthetase to polymerize in an inactive state arguing that the formation of these complexes can be used to buffer the amount of free, active enzyme (Barry et al., 2014). In contrast, acetyl Co-A carboxylase forms filaments as part of its activation mechanism arguing that polymerization might facilitate cooperative activation of the enzyme (Beaty and Lane, 1983b; Meredith and Lane, 1978). In addition to playing roles in activation and inactivation of single enzymes, multiple enzymes of the de novo purine biosynthetic pathway co-assemble into a single structure, the purinosome, arguing that these structures might also play a role in accelerating pathway flux via substrate channeling. While these studies have supported a variety of regulatory roles for metabolic enzyme structures, it has remained unclear whether this type of regulation is just an idiosyncratic feature of particular enzymes or if there are rules that determine where in a metabolic network this type of regulation is deployed.

Our visual screen of the yeast GFP strain collection identified 60 metabolic enzymes that are capable of forming structures. In contrast to other previous screens of the yeast GFP strain collection, we assayed multiple different growth conditions and measured the extent of structure formation in the population of cells. Our analysis revealed that assembly of metabolic enzymes was often associated with locations within a pathway where either their substrate or product is highly connected with other parts of the metabolic network. This selective positioning could be important in times of growth and stress where reorganization of enzymes could promote and inactivate enzyme activity to ensure coordination of metabolites.

This conclusion is supported by our in depth analysis of the Prs5p and Ade4p assembly in the *de novo* purine biosynthetic pathway. If enzyme polymerization/assembly were a mechanism for controlling pathway activity, we would expect the formation of these structures to be coordinately regulated - there is no need to activate a downstream enzyme if the upstream enzymes have been inactivated. The fact that the assembly of Prs5p into an inactive polymer occurs when glucose is limiting, while the Ade4p foci form when the pathway is activated in response to a lack of adenine provided a unique opportunity to test this mechanism of pathway regulation. Our observation that when yeast are acutely deprived of both glucose and adenine, Prs5p polymerizes while Ade4p remains dispersed within the cytoplasm argues that these structures are coordinately controlled and that there is a hierarchy to their formation: inactivation of upstream steps (i.e. Prs5p) blocks the activation of downstream steps (i.e. Ade4p).

Previous reports have supported the notion that assembly of consecutive enzymes in a metabolic pathway acts as a mechanism to facilitate flux through a pathway via substrate channeling. However, we found little support for substrate channeling from our screen. Consistent with a lack of a yeast equivalent of the mammalian purinosome, our global analysis did not identify entire pathways comprised of enzymes that formed structures. This was particularly true in glycolysis where we found that none of the enzymes that form structures act at on consecutive steps of the pathway. Instead, the glycolytic enzymes that were capable of assembly either generated or consumed highly connected metabolites in the pathway. Given that many of the intermediates derived from glycolysis fuel other pathways like amino acid or lipid biosynthesis, the assembly of a subset of glycolytic enzymes into these structures may provide a mechanism for ensuring the efficient utilization of carbon sources by gating flux through multiple branching pathways. Furthermore, the set of glycolytic enzymes that form structures may be adaptive to specific stresses since the enzymes we identified do not substantially overlap with those found to be localized to RNA granules in response to hypoxic stress (Jin et al., 2017).

Stress granules and filaments as potential sites of metabolic enzyme cross-regulation

Interestingly, while we find little evidence for assembly of enzymes acting in consecutive step of a metabolic pathway, we did find limited co-localization of enzymes between enzymes in different pathways in two situations we examined. First, we found five pairs of metabolic enzyme filaments (Figure 2.2) that interacted with each other in addition to forming separate filaments. Interestingly, prior to our screen only two metabolic enzyme filaments were known to interact with each other: IMP dehydrogenase and CTP synthetase. The lateral interaction between these two enzyme filaments in response to specific stresses has been proposed to help balance CTP and GTP biosynthesis in mammals (Carcamo et al., 2011; Liu, 2016). However, we found that this interaction is not conserved since none of the IMP dehydrogenases (Imp2-4p) in yeast form filaments. Interestingly, filaments comprised of the yeast CTP synthetase, Ura7p, do interact with filaments comprised of the Prs5p subunit of PRPP synthetase. The interaction between filaments comprised of enzymes that act at the top of purine biosynthesis and the bottom of pyrimidine biosynthesis suggests that the regulatory possibilities proposed for IMPDH and CTPS in mammals might also occur in yeast, but with different sets of enzymes. While the potential regulatory interactions between the remaining pairs of interacting filaments remains unclear, the results of our screen provide a basis for future studies for defining the structural basis for how distinct enzyme filaments can interact.

Ironically, the other example of enzyme co-localization that we observed was yeast IMP dehydrogenase co-assembling with two other enzymes that act at the second branch point of the *de novo* purine biosynthetic pathway. Instead of forming autonomous structures like Prs5 and

Ade4, these three enzymes are recruited to stress granules. This observation suggests that recruitment of IMP dehydrogenase into enzyme regulatory structures might be a recurring theme in evolution, but that the nature of the structure (filament vs stress granule) may vary from species to species. Additionally, the localization of metabolic enzymes to stress granules suggests that not all metabolic enzyme structures are comprised solely of metabolic enzymes and that they could play roles in integrating metabolic regulation with the control of other cellular pathways. RNA granules are known to recruit and regulate the activity of components of particular signaling pathways (Shah et al., 2014; Zhang et al., 2016). Given that the identity of which glycolytic enzymes are recruited to RNA granules varies depending on the stress, it is possible that RNA granule recruitment provides a route for differentially regulating metabolic pathways in response to translational, oxidative, and/or nutrient stresses (Jin et al., 2017)).

Alternatively, there has been increasing interest in the possibility that certain metabolic enzymes can act as RNA binding proteins to regulate gene expression post-transcriptionally. This interest has been driven by results from global screens for RNA binding proteins that identified a large number of metabolic enzymes as well as previous studies of the TCA cycle enzyme aconitase (Castello et al., 2012; Castello et al., 2016; Liao et al., 2016; Mitchell et al., 2013; Scherrer et al., 2010). Aconitase is an Fe-S cluster enzyme, however when iron limitation leads to failure to form an Fe-S cluster, it is an RNA binding protein that regulates the translation and stability of mRNAs for key iron uptake genes, such as transferrin (Eisenstein, 2000; Haile et al., 1992). While only Imd3p has been identified as a RNA binding proteins in global screens, the localization of these three purine biosynthetic enzymes to stress granules implies that they could have secondary functions similar to other moonlighting enzymes like aconitase (Mitchell et al., 2013). Future studies directed at identifying the complete set of metabolic enzymes that localize to stress granules and determining whether stress granules act site for integrating stress with metabolic activity or if the localization reflects additional moonlighting roles for a subset of metabolic enzymes will help resolve this question.

Conservation of metabolic enzyme assembly

CTP synthetase filament formation was simultaneously discovered in bacteria, *D. melanogaster*, *S. cerevisiae*, and humans. This suggested that the ability of metabolic enzymes to assemble into structures might be broadly conserved across species. However, the fact that the purinosome is not conserved from yeast to mammals argued that there may not a simple one-to-one correspondence between enzyme structures in different species. The results of our screen provide a robust foundation for comparing assembly behavior across species. For instance, our screen identified 10 metabolic enzymes that form structures within mitochondria. These 10 metabolic enzyme structures do not appear to be localized to nucleoids or other known mitochondrial structures based on their distribution. Thus, in addition to identifying a novel example of sub-organellar organization, these 10 enzymes provide a starting point for identifying metabolic enzymes in bacteria that may form structures comparable to those of CTP synthetase.

Similarly, our screen is likely to be useful in identifying metabolic enzyme assemblies in higher eukaryotes as evidenced by our discovery that the ability of PRPP synthetase to form filaments is conserved from yeast to humans. Furthermore, our observation that PRPP synthetase forms filaments in the nuclei of mammalian cells while in *S. cerevisiae*, the filaments are comprised of inactive subunits that polymerize in the cytoplasm argues that assembly might be conserved, but the purpose and location of the structure might vary greatly between species. Given that many inborn errors in metabolism display oddly tissue specific phenotypes that are difficult to explain in light of the known biochemical function of the enzyme, future comparative studies that leverage the results of our screen could provide insights into whether enzyme assembly behavior contributes to the pathophysiology of some of these diseases.

Materials and Methods

Yeast Strains and Media

Yeast strains used in this study are listed in Table 2.9. Briefly, all strains were grown at 30°C in YPD (2% peptone, 1% yeast extract, 2% dextrose) unless otherwise indicated. Strains with GFP tagged proteins were from the yeast GFP collection (Howson et al., 2005).

Yeast GFP Collection Screen

Yeast strains were grown in 5 mL liquid YPD at 30°C with shaking for the indicated time points. Cells were fixed by adding 100 µl of 37% w/v formaldehyde to 1 ml of yeast liquid culture and incubated on a rotating platform for at least 15 min at room temperature. Cells were then washed once with sterile water and resuspended in 1M sorbitol prior to counting and imaging. Structure formation was quantitated by counting the total number of cells and the number of cells with structures from at least 250 cells and reported as a percentage of cells with structures.

Construction of Yeast Strains

Generation of mCherry/GFP strains

Plasmids pBS34 (mCherry/KanMX6) or pBS35 (mCherry/HygromycinB) were used to generate mCherry-tagging cassettes via PCR and transformed into the appropriate GFP background strain. The positive clones were validated by PCR and fluorescence microscopy. In all cases, the primers were designed according to established protocols (http://depts.washington.edu/yeastrc/pages/pBS34.html), except that 10 additional nucleotides were added to the homology sequence to the gene of interest in order to improve the efficiency of homologous recombination.

Table 2.9. List of yeast strains used in this study

Strain	**Genetic background**	**Reference**
BY4741	*MATa his3Δ1 leu2Δ0 met15Δ0 ura3Δ0*	Dharmacon
PRS1::GFP-His3MX6	BY4741	GFP collection
PRS2::GFP-His3MX6	BY4741	GFP collection
PRS3::GFP-His3MX6	BY4741	GFP collection
PRS4::GFP-His3MX6	BY4741	GFP collection
PRS5::GFP-His3MX6	BY4741	GFP collection
ADE1::GFP-His3MX6	BY4741	GFP collection
ADE2::GFP-His3MX6	BY4741	GFP collection
ADE4::GFP-His3MX6	BY4741	GFP collection
ADE5::GFP-His3MX6	BY4741	GFP collection
ADE6::GFP-His3MX6	BY4741	GFP collection
ADE7::GFP-His3MX6	BY4741	GFP collection
ADE8::GFP-His3MX6	BY4741	GFP collection
ADE12::GFP-His3MX6	BY4741	GFP collection
ADE13::GFP-His3MX6	BY4741	GFP collection
ADE16::GFP-His3MX6	BY4741	GFP collection
ADE17::GFP-His3MX6	BY4741	GFP collection
ADK1::GFP-His3MX6	BY4741	GFP collection
ADK2::GFP-His3MX6	BY4741	GFP collection
IMD2::GFP-His3MX6	BY4741	GFP collection
IMD3::GFP-His3MX6	BY4741	GFP collection
IMD4::GFP-His3MX6	BY4741	GFP collection
GUA1::GFP-His3MX6	BY4741	GFP collection
GUK1::GFP-His3MX6	BY4741	GFP collection
ade2Δ:KanMX6; ADE4::GFP-His3MX6	BY4741	This study
ade1Δ:KanMX6; ADE4::GFP-His3MX6	BY4741	This study
ade12Δ:KanMX6; ADE4::GFP-His3MX6	BY4741	This study
ADE4::GFP-KanMX6	BY4741	This study
ADE4(K333Q)::GFP-KanMX6	BY4741	This study
ADE4::3HA-KanMX6	BY4741	This study
ADE12::3HA-KanMX6	BY4741	This study
ADE16::3HA-KanMX6	BY4741	This study
ADE17::3HA-KanMX6	BY4741	This study
PRS3::3HA-KanMX6	BY4741	This study

Table 2.9. List of yeast strains used in this study (continued)

PRS5::3HA-KanMX6	BY4741	This study
PRS3::mCherry-KanMX6; PRS5::GFP-His3MX6	BY4741	This study
ADE4::mCherry-KanMX6; PRS5::GFP-His3MX6	BY4741	This study
ADE12::mCherry-KanMX6; PRS5::GFP-His3MX6	BY4741	This study
ADE16::mCherry-KanMX6; PRS5::GFP-His3MX6	BY4741	This study
ADE4::mCherry-KanMX6; ADE17::GFP-His3MX6	BY4741	This study
ADE4::mCherry-KanMX6; ADE12::GFP-His3MX6	BY4741	This study
ADE12::mCherry-KanMX6; ADE17::GFP-His3MX6	BY4741	This study
ADE16::mCherry-KanMX6; ADE17::GFP-His3MX6	BY4741	This study
ADE4::mCherry-KanMX6; IMD4::GFP-His3MX6	BY4741	This study
ADE12::mCherry-KanMX6; IMD4::GFP-His3MX6	BY4741	This study
ADE12::mCherry-KanMX6; IMD4::GFP-His3MX6	BY4741	This study
URA7::mCherry-KanMX6; IMD2::GFP-His3MX6	BY4741	This study
URA7::mCherry-KanMX6; IMD3::GFP-His3MX6	BY4741	This study
URA7::mCherry-KanMX6; IMD4::GFP-His3MX6	BY4741	This study
DED1::mCherry-HphNT1; ADE4::GFP-His3MX6	BY4741	This study
DED1::mCherry-HphNT1; ADE12::GFP-His3MX6	BY4741	This study
DED1::mCherry-HphNT1; ADE16::GFP-His3MX6	BY4741	This study
DED1::mCherry-HphNT1; ADE17::GFP-His3MX6	BY4741	This study
DED1::mCherry-HphNT1; IMD2::GFP-His3MX6	BY4741	This study
DED1::mCherry-HphNT1; IMD3::GFP-His3MX6	BY4741	This study
DED1::mCherry-HphNT1; IMD4::GFP-His3MX6	BY4741	This study
EDC3::mCherry-HphNT1; ADE4::GFP-His3MX6	BY4741	This study
EDC3::mCherry-HphNT1; ADE12::GFP-His3MX6	BY4741	This study
EDC3::mCherry-HphNT1; ADE16::GFP-His3MX6	BY4741	This study
EDC3::mCherry-HphNT1; ADE17::GFP-His3MX6	BY4741	This study
EDC3::mCherry-HphNT1; IMD2::GFP-His3MX6	BY4741	This study
EDC3::mCherry-HphNT1; IMD3::GFP-His3MX6	BY4741	This study

Table 2.9. List of yeast strains used in this study (continued)

EDC3::mCherry-HphNT1; IMD4::GFP-His3MX6	BY4741	This study
ADE4::mCherry-KanMx6; HSP104::GFP-His3MX6	BY4741	This study
ADE12::mCherry-KanMx6; HSP104::GFP-His3MX6	BY4741	This study
ADE16::mCherry-KanMx6; HSP104::GFP-His3MX6	BY4741	This study
PRS3::mCherry-KanMx6; HSP104::GFP-His3MX6	BY4741	This study
PRS5::mCherry-KanMx6; HSP104::GFP-His3MX6	BY4741	This study
ADE4::mCherry-KanMx6; SSA1::GFP-His3MX6	BY4741	This study
ADE12::mCherry-KanMx6; SSA1::GFP-His3MX6	BY4741	This study
ADE16::mCherry-KanMx6; SSA1::GFP-His3MX6	BY4741	This study
PRS3::mCherry-KanMx6; SSA1::GFP-His3MX6	BY4741	This study
PRS5::mCherry-KanMx6; SSA1::GFP-His3MX6	BY4741	This study

Generation of HA-tagged strains

The 3HA-KanMX6 cassette was PCR amplified from pFA6a-3HA-kanMX6 in the same manner as the mCherry cassettes and transformed into yeast strain, BY4741, using the lithium acetate/PEG method (Ito et al., 1983). Positive clones were verified by PCR and indirect immunofluorescence.

Construction of Ade4p feedback inhibition resistant yeasts

The full-length *ADE4* coding sequence was amplified from genomic DNA isolated from yeast strain BY4741 using primers that introduced a *Sal*I site at the start of the gene and *Sma*I site at the end of the gene. The *ADE4* coding sequence was then subcloned into pFA6a-GFP-kanMX6 upstream of the GFP cassette. Site directed mutagenesis was then used to introduce the K333Q mutation into *ADE4* in the pFA6a-*ADE4*-GFP-kanMX6 plasmid (primers available on request). After the K333Q mutation was verified by sequencing, the *ade4*(K333Q)-GFP-kanMX6 cassette was PCR amplified with primers containing 50 bp upstream of the *ADE4* start codon and 50 bp downstream of the *ADE4* stop codon. The PCR product was then transformed into yeast strain BY4741 using the lithium acetate/PEG method (Ito et al., 1983). Transformants were selected on YPD agar plate containing G418 (400 μg/mL), and verified by sequencing.

Yeast Strains for Epitasis Studies

Strains from the GFP collection (*MATa his3Δ1 leu2Δ0 met15Δ0 ura3Δ0*) were crossed to specific strains from the yeast knockout collection (*MATα his3Δ1 leu2Δ0 lys2Δ0 ura3Δ0*; gift from Maho Niwa, UC San Diego). The crosses were plated onto YPD plates and re-streaked onto Met$^-$/Lys$^-$ double-dropout plates to select for diploid cells. Single colonies were then inoculated into 2 ml YPD, incubating for 8 hours at 30ºC. The cells were washed and resuspended in 1 ml Spo-UL media (0.1% yeast extract; 1% potassium acetate; 0.05% dextrose;

0.002% leucine, 0.004% uracil), and grown for 5-6 days on a rotator at room temperature. Tetrads were then digested with 200 U/ml zymolase (Zymo Research) and micro-dissected into single cells onto YPD plates followed by growth at 30ºC for 48 hours. Colonies were gridded onto YPD plates and grown overnight. The master plate was then replica plated onto either $G418^+$ YPD or SC-His drop out plates and grown overnight. Each haploid was genotyped by PCR or growth on selective media to ensure the presence of the GFP, the deletion, and the markers of our standard strain background (*his3Δ1 leu2Δ0 met15Δ0 ura3Δ0)*.

MitoTracker staining

GFP-tagged strains were grown to either log phase or 1 day in YPD at 30°C with shaking. Mitotracker Red (Life Technologies) was added to the culture to a final concentration of 0.1 μM and incubated at room temperature on a rotatory platform in the dark for 30 minutes. Cells were then washed once and resuspended in 1M sorbitol and imaged immediately.

Fluorescence Microscopy and Image Analysis

Images from the screening the Yeast GFP collection, Mitotracker Red, and colocalization experiments were acquired using a DeltaVision® system with an Olympus IX70 microscope, Olympus PlanApo 60X/1.40 Oil objective, and SoftWoRx™ software version 2.5 (Applied Precision). Images for mitochondrial staining using the pVTU-mito-dsRed plasmid as well as RNA granule colocalization were taken using a Zeiss Axiovert 200M fluorescent microscope equipped with a CSU-X1 spinning disk (Yokogawa), an iChromeMLE laser source (Toptica Photonics) and μManager version 1.4 software. For each acquisition, a 2μm Z-stack was taken with slices at 0.25μm intervals using the 40X (or 100X for intensity ratio determination) objective.

For colocalization experiments, cells were then grown to stages where formation of the GFP-tagged structure was highest and then fixed in 4% formaldehyde (with the exception of *IMD2::GFP*, *IMD3::GFP*, and *IMD4::GFP*) prior to imaging. For RNA granule and chaperone colocalization experiments, images were taken and then analyzed on ImageJ and colocalization was determined by examining each confocal slice image. Independent experiments were repeated at least 3 times for graphing (mean ± SEM).

Protein Extraction and Western Blotting

Whole cell extracts were prepared via NaOH extraction according to (Kushnirov, 2000). Briefly, 2.5 OD600 cells were harvested and resuspended in 0.1N NaOH and incubated at room temperature for 5 minutes. Following centrifugation, cell pellets were resuspended in 2x Sample Buffer and subsequently boiled for 5 minutes at 95°C. Cell lysates were then resolved by 10% SDS-PAGE. Proteins were transferred to a nitrocellulose membrane (GE Amersham) by electro-blotting (Owl HEP-1, Thermo Scientific). Then standard protocol for Western blot was performed. To detect GFP-tagged proteins, 1:5,000 rabbit anti-GFP (Torrey Pines Biolabs Inc.) was used as a primary antibody and 1:10,000 ECL^{TM} donkey anti-rabbit IgG, horseradish peroxidase-linked whole antibody (GE Healthcare UK Limited) as a secondary antibody. For internal loading control detection, 1:10,000 mouse anti-3-phosphoglycerate kinase (yeast) IgG_1 monoclonal antibody (Invitrogen) was used as a primary antibody and 1:2,500 ECL^{TM} sheep anti-mouse IgG, horseradish peroxidase-linked whole antibody (GE Healthcare UK Limited) as a secondary antibody.

Media Shift Experiments

For disassembly experiments, yeast strains were grown in YPD at 30°C shaking for the indicated amount of days and subsequently washed once and resuspended into new media (YPD, YP, 2% glucose, or water). Cells were then incubated for 30 min at 30°C with rocking and immediately imaged. Cells were also taken for protein extraction followed by western blot analysis.

For assembly experiments, yeast strains were grown in SD media to log phase and washed once with new media (SD, SD lacking glucose, SD lacking adenine, or SD lacking glucose and adenine) and resuspended in appropriate media. Cells were incubated for 30 min at 30°C with rocking and immediately imaged. All experiments were independently repeated 3 times and illustrated as percentage of cells with visible structures (mean ± SEM).

Yeast Indirect Immunofluorescence

Indirect immunofluorescence was performed as previously described (Noree et al., 2010).

Generation of anti-PRPS1 antibody

The full-length coding region of PRPS1 was cloned into pProEx-Htc and expressed as an N-terminal 6xHis-tagged fusion protein in BL21 (DE3) *Escherichia coli*. Soluble His-PRPS1 was purified using a Ni-nitrilotriacetic acid affinity column, eluted with imidazole, and injected into rabbits (antiserum production by Covance). The antiserum was purified against 6xHis-PRPS1 protein on a CnBr-activated sepharose 4B (GE Healthcare) column.

PRPS1 Immunostaining

Immunostaining and microscopy for *Drosophila* egg chambers were performed as previously described (Wilhelm et al., 2003). Immunostaining and microscopy for rat neurons was performed as previously described (Noree et al., 2010). For fibroblast staining, primary fibroblasts (R. Naviaux, University of California, San Diego) were plated on coverslips and cultured for 5 days at 37°C and 5% CO_2 in MEM (Invitrogen) supplemented with 10% Fetal Bovine Serum (Cellgro), 1% L-glutamine (Invitrogen), and 1% Penicillin Streptomycin

(Invitrogen). Fibroblasts were fixed by incubating in 4% Paraformaldehyde in PBS for 20 minutes. The coverslips were then rinsed with 1X PBS then followed by two 5-minute washes in 1X PBS. The cells were incubated for 17 minutes at room temperature in permeabilization solution (PBS with 1% goat serum and 0.5% TritonX-100) followed by three 5-minute washes in blocking solution (PBS and 1% goat serum). The coverslips were incubated overnight at 4°C in primary antibody diluted in blocking solution. The cells were washed twice for 5 minutes using blocking solution then incubated for 2 hours at room temperature in secondary antibody diluted in blocking solution. The secondary antibody was then aspirated to incubate for 10 minutes in DAPI diluted in blocking solution, then rinsed quickly, followed by three 5-minute washes in blocking solution. This was followed by a quick wash in water. The coverslips were mounted using Vectashield (Vector Laboratories) and images using laser confocal microscope (TCS SP5; Leica). The following antibodies were used for immunostaining: α-PRPS1 (1:300, this manuscript), α-Tubulin-FITC (1:150, Sigma), and α-rabbit AlexaFluor 568 (Invitrogen) secondary antibody.

Acknowledgements

We would like to thank Douglass Forbes comments on this manuscript and Susanne Rafelski for the gift of the pVTU-mito-dsRed plasmid. This work was supported by the HCIA program of HHMI.

Chapter 2 is a manuscript submitted for publication. It may appear in Molecular Biology of the Cell. Noree, C., Begovich, K., Samilo, D., Broyer, R.M., Monfort-Prieto, E., Wilhelm, J.E. “A quantitative screen for metabolic enzyme structures reveals patterns of assembly across the yeast metabolic network”. C. Noree is co-first author for this manuscript. D. Samilo and E. Monfort-Prieto helped create yeast strains used in this manuscript. R.M Broyer performed immunostaining experiments. J.E. Wilhelm helped write and edit this manuscript. The dissertation author is the primary experimenter and author on this paper.

References

Adelberg, E.A., and Umbarger, H.E. (1953). Isoleucine and valine metabolism in Escherichia coli. V.alpha-Ketoisovaleric acid accumulation. J Biol Chem *205*, 475-482.

An, S., Kumar, R., Sheets, E.D., and Benkovic, S.J. (2008). Reversible compartmentalization of de novo purine biosynthetic complexes in living cells. Science *320*, 103-106.

An, S., Kyoung, M., Allen, J.J., Shokat, K.M., and Benkovic, S.J. (2010). Dynamic regulation of a metabolic multi-enzyme complex by protein kinase CK2. J Biol Chem *285*, 11093-11099.

Banani, S.F., Lee, H.O., Hyman, A.A., and Rosen, M.K. (2017). Biomolecular condensates: organizers of cellular biochemistry. Nat Rev Mol Cell Biol *18*, 285-298.

Barry, R.M., Bitbol, A.F., Lorestani, A., Charles, E.J., Habrian, C.H., Hansen, J.M., Li, H.J., Baldwin, E.P., Wingreen, N.S., Kollman, J.M*.,* Gitai, Z. (2014). Large-scale filament formation inhibits the activity of CTP synthetase. Elife *3*, e03638.

Beaty, N.B., and Lane, M.D. (1983a). Kinetics of activation of acetyl-CoA carboxylase by citrate. Relationship to the rate of polymerization of the enzyme. J Biol Chem *258*, 13043-13050.

Beaty, N.B., and Lane, M.D. (1983b). The polymerization of acetyl-CoA carboxylase. J Biol Chem *258*, 13051-13055.

Boeynaems, S., Alberti, S., Fawzi, N.L., Mittag, T., Polymenidou, M., Rousseau, F. Schymkowitz, J., Shorter, J., Wolozin, B., Van Den Bosch, L*.,* Tompa, P., Fuxreiter, M. (2018). Protein Phase Separation: A New Phase in Cell Biology. Trends Cell Biol *28*, 420-435.

Braun, E.L., Fuge, E.K., Padilla, P.A., and Werner-Washburne, M. (1996). A stationary-phase gene in Saccharomyces cerevisiae is a member of a novel, highly conserved gene family. J Bacteriol *178*, 6865-6872.

Carcamo, W.C., Satoh, M., Kasahara, H., Terada, N., Hamazaki, T., Chan, J.Y., Yao, B., Tamayo, S., Covini, G., von Muhlen, C.A*.,* Chan, E.K.L. (2011). Induction of cytoplasmic rods and rings structures by inhibition of the CTP and GTP synthetic pathway in mammalian cells. PLoS One *6*, e29690.

Castello, A., Fischer, B., Eichelbaum, K., Horos, R., Beckmann, B.M., Strein, C., Davey, N.E., Humphreys, D.T., Preiss, T., Steinmetz, L.M*.,* Krijgsveld, J., Hentze, M.W. (2012). Insights into RNA biology from an atlas of mammalian mRNA-binding proteins. Cell *149*,1393-1406.

Castello, A., Fischer, B., Frese, C.K., Horos, R., Alleaume, A.M., Foehr, S., Curk, T., Krijgsveld, J., and Hentze, M.W. (2016). Comprehensive Identification of RNA-Binding Domains in Human Cells. Mol Cell *63*, 696-710.

Chang, C.C., Keppeke, G.D., Sung, L.Y., and Liu, J.L. (2018). Inter-filament interaction between IMPDH and CTPS cytoophidia. FEBS J.

Chong, Y.T., Koh, J.L., Friesen, H., Duffy, S.K., Cox, M.J., Moses, A., Moffat, J., Boone, C., and Andrews, B.J. (2015). Yeast Proteome Dynamics from Single Cell Imaging and Automated Analysis. Cell *161*, 1413-1424.

Ditlev, J.A., Case, L.B., and Rosen, M.K. (2018). Who's In and Who's Out-Compositional Control of Biomolecular Condensates. J Mol Biol.

Eisenstein, R.S. (2000). Iron regulatory proteins and the molecular control of mammalian iron metabolism. Annu Rev Nutr *20*, 627-662.

French, J.B., Jones, S.A., Deng, H., Pedley, A.M., Kim, D., Chan, C.Y., Hu, H., Pugh, R.J., Zhao, H., Zhang, Y., Huang, T.J., Fang, Y., Zhuang, X., Benkovic, S.J. (2016). Spatial colocalization and functional link of purinosomes with mitochondria. Science *351*, 733-737.

Gerhart, J.C., and Pardee, A.B. (1962). The enzymology of control by feedback inhibition. J Biol Chem *237*, 891-896.

Haile, D.J., Rouault, T.A., Tang, C.K., Chin, J., Harford, J.B., and Klausner, R.D. (1992). Reciprocal control of RNA-binding and aconitase activity in the regulation of the iron-responsive element binding protein: role of the iron-sulfur cluster. Proc Natl Acad Sci USA *89*, 7536-7540.

Hernando, Y., Carter, A.T., Parr, A., Hove-Jensen, B., and Schweizer, M. (1999). Genetic analysis and enzyme activity suggest the existence of more than one minimal functional unit capable of synthesizing phosphoribosyl pyrophosphate in Saccharomyces cerevisiae. J Biol Chem *274*, 12480-12487.

Hernando, Y., Parr, A., and Schweizer, M. (1998). PRS5, the fifth member of the phosphoribosyl pyrophosphate synthetase gene family in Saccharomyces cerevisiae, is essential for cell viability in the absence of either PRS1 or PRS3. J Bacteriol *180*, 6404-6407.

Holmes, E.W., Pehlke, D.M., and Kelley, W.N. (1974). Human IMP dehydrogenase. Kinetics and regulatory properties. Biochim Biophys Acta *364*, 209-217.

Hove-Jensen, B. (2004). Heterooligomeric phosphoribosyl diphosphate synthase of Saccharomyces cerevisiae: combinatorial expression of the five PRS genes in Escherichia coli. J Biol Chem *279*, 40345-40350.

Howson, R., Huh, W.K., Ghaemmaghami, S., Falvo, J.V., Bower, K., Belle, A., Dephoure, N., Wykoff, D.D., Weissman, J.S., and O'Shea, E.K. (2005). Construction, verification and experimental use of two epitope-tagged collections of budding yeast strains. Comp Funct Genomics *6*, 2-16.

Ingerson-Mahar, M., Briegel, A., Werner, J.N., Jensen, G.J., and Gitai, Z. (2010). The metabolic enzyme CTP synthase forms cytoskeletal filaments. Nat Cell Biol *12*, 739-746.

Ito, H., Fukuda, Y., Murata, K., and Kimura, A. (1983). Transformation of intact yeast cells treated with alkali cations. J Bacteriol *153*, 163-168.

Jang, S., Nelson, J.C., Bend, E.G., Rodriguez-Laureano, L., Tueros, F.G., Cartagenova, L., Underwood, K., Jorgensen, E.M., and Colon-Ramos, D.A. (2016). Glycolytic Enzymes Localize to Synapses under Energy Stress to Support Synaptic Function. Neuron *90*, 278-291.

Jin, M., Fuller, G.G., Han, T., Yao, Y., Alessi, A.F., Freeberg, M.A., Roach, N.P., Moresco, J.J., Karnovsky, A., Baba, M., Yates, J.R., Gitler, A.D., Inoki, K., Klionsky, D.J., Kim, J.K. (2017). Glycolytic Enzymes Coalesce in G Bodies under Hypoxic Stress. Cell Rep *20*, 895-908.

Keppeke, G.D., Calise, S.J., Chan, E.K., and Andrade, L.E. (2015). Assembly of IMPDH2-based, CTPS-based, and mixed rod/ring structures is dependent on cell type and conditions of induction. J Genet Genomics *42*, 287-299.

Kushnirov, V.V. (2000). Rapid and reliable protein extraction from yeast. Yeast *16*, 857- 860.

Levitzki, A., and Koshland, D.E., Jr. (1972). Role of an allosteric effector. Guanosine triphosphate activation in cytosine triphosphate synthetase. Biochemistry *11*, 241- 246.

Li, S., Lu, Y., Peng, B., and Ding, J. (2007). Crystal structure of human phosphoribosylpyrophosphate synthetase 1 reveals a novel allosteric site. Biochem J *401*, 39-47.

Liao, Y., Castello, A., Fischer, B., Leicht, S., Foehr, S., Frese, C.K., Ragan, C., Kurscheid, S., Pagler, E., Yang, H., Krijgsveld, J., Hentze, M.W., Preiss, T. (2016). The Cardiomyocyte RNA-Binding Proteome: Links to Intermediary Metabolism and Heart Disease. Cell Rep *16*, 1456-1469.

Liu, J.L. (2010). Intracellular compartmentation of CTP synthase in Drosophila. J Genet Genomics *37*, 281-296.

Liu, J.L. (2016). The Cytoophidium and Its Kind: Filamentation and Compartmentation of Metabolic Enzymes. Annu Rev Cell Dev Biol *32*, 349-372.

Mazumder, A., Pesudo, L.Q., McRee, S., Bathe, M., and Samson, L.D. (2013). Genome-wide single-cell-level screen for protein abundance and localization changes in response to DNA damage in S. cerevisiae. Nucleic Acids Res *41*, 9310-9324.

Meredith, M.J., and Lane, M.D. (1978). Acetyl-CoA carboxylase. Evidence for polymeric filament to protomer transition in the intact avian liver cell. J Biol Chem *253*, 3381-3383.

Misonou, Y., Kikuchi, M., Sato, H., Inai, T., Kuroiwa, T., Tanaka, K., and Miyakawa, I. (2014). Aldehyde dehydrogenase, Ald4p, is a major component of mitochondrial fluorescent inclusion bodies in the yeast Saccharomyces cerevisiae. Biol Open *3*, 387-396.

Mitchell, S.F., Jain, S., She, M., and Parker, R. (2013). Global analysis of yeast mRNPs. Nat Struct Mol Biol *20*, 127-133.

Miyakawa, I. (2017). Organization and dynamics of yeast mitochondrial nucleoids. Proc Jpn Acad Ser B Phys Biol Sci *93*, 339-359.

Miyakawa, I., Aoi, H., Sando, N., and Kuroiwa, T. (1984). Fluorescence microscopic studies of mitochondrial nucleoids during meiosis and sporulation in the yeast, Saccharomyces cerevisiae. J Cell Sci *66*, 21-38.

Narayanaswamy, R., Levy, M., Tsechansky, M., Stovall, G.M., O'Connell, J.D., Mirrielees, J., Ellington, A.D., and Marcotte, E.M. (2009). Widespread reorganization of metabolic enzymes into reversible assemblies upon nutrient starvation. Proc Natl Acad Sci U S A *106*, 10147-10152.

Noree, C. (2018). Extramitochondrial Assembly of Mitochondrial Targeting Signal Disrupted Mitochondrial Enzyme Aldehyde Dehydrogenase. Sci Rep *8*, 6186.

Noree, C., Sato, B.K., Broyer, R.M., and Wilhelm, J.E. (2010). Identification of novel filament-forming proteins in Saccharomyces cerevisiae and Drosophila melanogaster. J Cell Biol *190*, 541-551.

O'Connell, J.D., Tsechansky, M., Royal, A., Boutz, D.R., Ellington, A.D., and Marcotte, E.M. (2014). A proteomic survey of widespread protein aggregation in yeast. Mol Biosyst *10*, 851-861.

O'Connell, J.D., Zhao, A., Ellington, A.D., and Marcotte, E.M. (2012). Dynamic reorganization of metabolic enzymes into intracellular bodies. Annu Rev Cell DevBiol *28*, 89-111.

Pardee, A.B., and Yates, R.A. (1956). Control of pyrimidine biosynthesis in Escherichia coli by a feed-back mechanism. J Biol Chem *221*, 757-770.

Petrovska, I., Nuske, E., Munder, M.C., Kulasegaran, G., Malinovska, L., Kroschwald, S., Richter, D., Fahmy, K., Gibson, K., Verbavatz, J.M., Alberti, S. (2014). Filament formation by metabolic enzymes is a specific adaptation to an advanced state of cellular starvation. Elife.

Pinson, B., Vaur, S., Sagot, I., Coulpier, F., Lemoine, S., and Daignan-Fornier, B. (2009). Metabolic intermediates selectively stimulate transcription factor interaction and modulate phosphate and purine pathways. Genes Dev *23*, 1399-1407.

Rebora, K., Desmoucelles, C., Borne, F., Pinson, B., and Daignan-Fornier, B. (2001). Yeast AMP pathway genes respond to adenine through regulated synthesis of a metabolic intermediate. Mol Cell Biol *21*, 7901-7912.

Saad, S., Cereghetti, G., Feng, Y., Picotti, P., Peter, M., and Dechant, R. (2017). Reversible protein aggregation is a protective mechanism to ensure cell cycle restart after stress. Nat Cell Biol *19*, 1202-1213.

Scherrer, T., Mittal, N., Janga, S.C., and Gerber, A.P. (2010). A screen for RNA-binding proteins in yeast indicates dual functions for many enzymes. PLoS One *5*, e15499.

Shah, K.H., Nostramo, R., Zhang, B., Varia, S.N., Klett, B.M., and Herman, P.K. (2014). Protein kinases are associated with multiple, distinct cytoplasmic granules in quiescent yeast cells. Genetics *198*, 1495-1512.

Shen, Q.J., Kassim, H., Huang, Y., Li, H., Zhang, J., Li, G., Wang, P.Y., Yan, J., Ye, F., and Liu, J.L. (2016). Filamentation of Metabolic Enzymes in Saccharomyces cerevisiae. J Genet Genomics *43*, 393-404.

Smith, J.L. (1998). Glutamine PRPP amidotransferase: snapshots of an enzyme in action. Curr Opin Struct Biol *8*, 686-694.

Srere, P.A. (1987). Complexes of sequential metabolic enzymes. Annu Rev Biochem *56*, 89-124.

Switzer, R.L., and Sogin, D.C. (1973). Regulation and mechanism of phosphoribosylpyrophosphate synthetase. V. Inhibition by end products and regulation by adenosine diphosphate. J Biol Chem *248*, 1063-1073.

Tkach, J.M., Yimit, A., Lee, A.Y., Riffle, M., Costanzo, M., Jaschob, D., Hendry, J.A., Ou, J., Moffat, J., Boone, C., Davis, T.N., Nislow, C., Brown, G.W. (2012). Dissecting DNA damage response pathways by analysing protein localization and abundance changes during DNA replication stress. Nat Cell Biol *14*, 966-976.

Van der Weyden, M.B., and Kelly, W.N. (1974). Human adenylosuccinate synthetase. Partial purification, kinetic and regulatory properties of the enzyme from placenta. J Biol Chem *249*, 7282-7289.

Webb, B.A., Dosey, A.M., Wittmann, T., Kollman, J.M., and Barber, D.L. (2017). The glycolytic enzyme phosphofructokinase-1 assembles into filaments. J Cell Biol *216*, 2305-2313.

Werner-Washburne, M., Braun, E., Johnston, G.C., and Singer, R.A. (1993). Stationary phase in the yeast Saccharomyces cerevisiae. Microbiol Rev *57*, 383-401.

Wyngaarden, J.B. (1976). Regulation of purine biosynthesis and turnover. Adv Enzyme Regul *14*, 25-42.

Zhang, B., Shi, Q., Varia, S.N., Xing, S., Klett, B.M., Cook, L.A., and Herman, P.K. (2016). The Activity-Dependent Regulation of Protein Kinase Stability by the Localization to P-Bodies. Genetics *203*, 1191-1202.

Zhou, G., Charbonneau, H., Colman, R.F., and Zalkin, H. (1993). Identification of sites for feedback regulation of glutamine 5-phosphoribosylpyrophosphate amidotransferase by nucleotides and relationship to residues important for catalysis. J Biol Chem *268*, 10471-10481.

Zimmer, H.G. (1992). The oxidative pentose phosphate pathway in the heart: regulation, physiological significance, and clinical implications. Basic Res Cardiol *87*, 303-316.

Chapter 3

Conserved metabolite regulation of stress granule assembly via AdoMet

Abstract

Stress granules (SGs) are evolutionarily conserved condensates of ribonucleoproteins that assemble in response to metabolic stresses. Because aberrant SG formation is associated with amyotrophic lateral sclerosis (ALS), understanding the connection between metabolic activity and SG composition can provide therapeutic insights into neurodegeneration. Here, we identify 17 metabolic enzymes recruited to yeast SGs in response to physiological growth stress. Furthermore, the product of one of these enzymes, AdoMet, is a regulator of SG assembly and composition. Decreases in AdoMet levels increase SG formation, while chronic elevation of AdoMet produce SG remnants lacking proteins associated with the 5'end of transcripts. Interestingly, acute elevation of AdoMet blocks SG formation in yeast and motor neurons. Treatment of ALS-derived motor neurons with AdoMet also suppresses the formation of TDP-43 positive SGs, a hallmark of ALS. Together these results argue that AdoMet is an evolutionarily conserved regulator of SG composition and assembly, with therapeutic potential in neurodegeneration.

Introduction

Cells deploy a variety of mechanisms in order to fine tune biochemical processes in response to environmental stressors. One of these mechanisms is the formation of stress granules (SGs) - evolutionarily conserved, cytoplasmic condensates comprised of non-translating messenger ribonucleoproteins (mRNPs) (Panas et al., 2016; Protter and Parker, 2016). SGs assemble in response to a variety of nutrient and metabolic stresses and are believed to provide a mechanism for coupling metabolic stress to post-transcriptional gene regulation (Kedersha et al., 2002; Khong et al., 2017; Panas et al., 2016; Protter and Parker, 2016). Furthermore, SGs act as centers to regulate cell signaling outputs and protein folding highlighting SGs as global integrators of the stress response (Arimoto et al., 2008; Harding et al., 2000; Kedersha et al., 2013; Wippich et al., 2013). SGs are transient and require tight regulation of assembly-disassembly for cell function and viability. Consistent with this, disruption of SG formation decreases cell survival when the stress is removed (Eisinger-Mathason et al., 2008; Kim et al., 2012; Kwon et al., 2007; Orru et al., 2016; Yang et al., 2014).

In addition to their role in integrating the cellular stress response, SGs have been implicated in a variety of neurodegenerative disorders. Mutations in the SG components FUS and HNRNPA2B1, as well as TARDBP (encoding TDP-43) have been linked to amyotrophic lateral sclerosis (ALS) and frontotemporal dementia (FTD) (Kim et al., 2013; Kwiatkowski et al., 2009; Martinez et al., 2016; Sreedharan et al., 2008; Vance et al., 2009). Interestingly, pathogenic mutations in these genes all cluster in regions that encode low complexity sequences (LCSs) or intrinsically disordered regions (IDRs) (Chen-Plotkin et al., 2010; Ryan et al., 2018; Shang and Huang, 2016). These pathogenic IDR and LCS domains drive recruitment of the proteins into SGs and alter the dynamics and composition of SGs that form in response to the altered protein

(Kato et al., 2012; Kim et al., 2013; Ling et al., 2013; Murakami et al., 2015; Patel et al., 2015; Ryan et al., 2018). Consequently, dysregulation in SG dynamics in ALS patients results in accumulation of atypical cytoplasmic, SG-like protein aggregates in dying neurons of the brain and spinal cord. Furthermore, accumulation of cytoplasmic TDP-43 in aberrant motor neuron SGs is considered a hallmark of ALS (Bentmann et al., 2012; Blokhuis et al., 2013; Farg et al., 2013; Keller et al., 2012; Kim et al., 2013; Liu-Yesucevitz et al., 2010). These results argue that understanding how SGs assemble in response to metabolic or nutrient stresses is critical both for understanding the pathophysiology of ALS and FTD as well as developing treatment strategies focused on disrupting the formation of aberrant SGs.

The current model for SG formation is that cellular stresses promote liquid-liquid phase separation (LLPS) of mRNPs via different multivalent interactions (Banani et al., 2017; Jain et al., 2016; Van Treeck et al., 2018; Wheeler et al., 2016). For instance, stress-induced disassociation of polysomes from translating mRNAs is thought to create a scaffold that can drive LLPS in two complementary ways (Panas et al., 2016; Protter and Parker, 2016). First, the exposure of sequences within the mRNA allows RNA-RNA interactions to help drive LLPS. Additionally, the recruitment of proteins with IDRs or LCSs to the exposed transcript can drive LLPS via protein-protein interactions. Together these two mechanisms can greatly increase the number of mRNP interaction sites driving LLPS and SG formation. Consistent with this model, altering the protein levels of SG components or post-translational modifications within IDRs or LCSs of SG proteins have been shown to regulate these protein-protein interactions and thus, SG assembly (Hilliker et al., 2011; Hofweber et al., 2018; Swisher and Parker, 2010; Tsai et al., 2016; Tsai et al., 2017).

Given the linkage between SGs and several neurodegenerative diseases, the composition of the SG proteome has been a subject of intense focus in order to identify potential therapeutic targets. Unfortunately, large-scale biochemical studies have found that SG composition is not only stress-specific, but also organismal and cell type specific (Jain et al., 2016; Markmiller et al., 2018). Furthermore, these studies also revealed that SGs contain two distinct phases: a solid-like core and a dynamic surrounding shell (Jain et al., 2016; Markmiller et al., 2018). While different mass spectrometry techniques have helped identify which components reside within each phase, the relative role of SG core proteins and shell proteins in SG formation and pathogenesis remains unclear.

Despite the fact that SGs formation and composition is stress specific, there has been surprisingly little exploration of the connections between metabolism and SG assembly. To date, only a few metabolic enzymes have been shown to localize to stress granules via proteomic and/or targeted studies. This deficit is likely due to the limited number of stress conditions that have been used in SG proteomic studies. Similarly, only one metabolite from intermediate metabolism, acetyl-CoA, has been implicated in regulating stress granule formation (Rollins et al., 2017). Thus, the identification of metabolic enzymes that are recruited to SGs in a stress specific manner would identify new linkages between SG formation and metabolism as well as provide a novel set of potential therapeutic targets for ALS and FTD.

In this report, we have identified 17 metabolic enzymes that are recruited to yeast SGs in a stress specific manner. Interestingly, AdoMet, the product of one these enzymes, is a regulator of SG assembly and composition. The regulation of yeast SG formation by AdoMet is biphasic with chronic changes altering SG composition and acute elevation of AdoMet suppressing SG assembly. Additionally, acute elevation of AdoMet also suppresses SG formation in motor neurons, demonstrating conserved metabolite regulation of SG assembly from yeast to humans. The suppressive effect of AdoMet on SG formation also occurs in iPSC-derived motor neurons from ALS patients. Most provocatively, AdoMet also blocks the recruitment of cytoplasmic TDP-43 to remnant SGs in this cell culture model of ALS, arguing that AdoMet can modify the pathogenic accumulation of SG material. Together these results argue that metabolic activity controls both the composition and extent of SG formation and provide a framework for the identification of lead compounds that can modify or suppress SG formation.

Results

A subset of metabolic enzymes preferentially localize to SGs

While SGs are known to assemble in response to a variety of nutrient and metabolic stresses, little remains known how metabolic activity is linked to SG formation. Given that a number of metabolic enzymes self-organize into structures under conditions that also trigger SGs and Processing bodies (P-bodies) formation suggests potential interactions between metabolic structures and RNA granule formation. Consistent with this, three metabolic enzymes in the *de novo* purine biosynthetic pathway were recently discovered to localize to SGs upon growth to stationary phase (Noree et al, submitted). To explore the extent of metabolic enzyme recruitment to SGs, we screened all 34 known metabolic enzymes that form cytoplasmic foci for recruitment to either SGs and/or P-bodies. Each metabolic enzyme was endogenously tagged with GFP and the extent of enzyme recruitment to RNA granules was assayed at either 1 day or 5 days of growth using Ded1-mCherry (SG marker) or Edc3-mCherry (P-body marker) expressed from its endogenous locus (Figure 3.1). This screen identified 17 new metabolic enzymes that exhibited greater than 15% co-localization with either type of RNA granule (Figure 3.1, Table 3.1). While all 17 enzymes preferentially localized to SGs compared to P-bodies, three enzymes (Gly1, Gre3, Pro3) were also enriched in P-bodies. These results significantly broaden the number of metabolic enzymes recruited to SGs beyond those identified by prior proteomic and targeted studies.

Our screen also revealed two distinct patterns of SG recruitment. 10 metabolic enzymes were recruited directly to SGs. However, 7 enzymes had the ability to form structures independent of SGs suggesting that this class of enzymes might form structures that are in turn recruited to SGs. Consistent with this interpretation, enzymes in this class such as Cys4 and

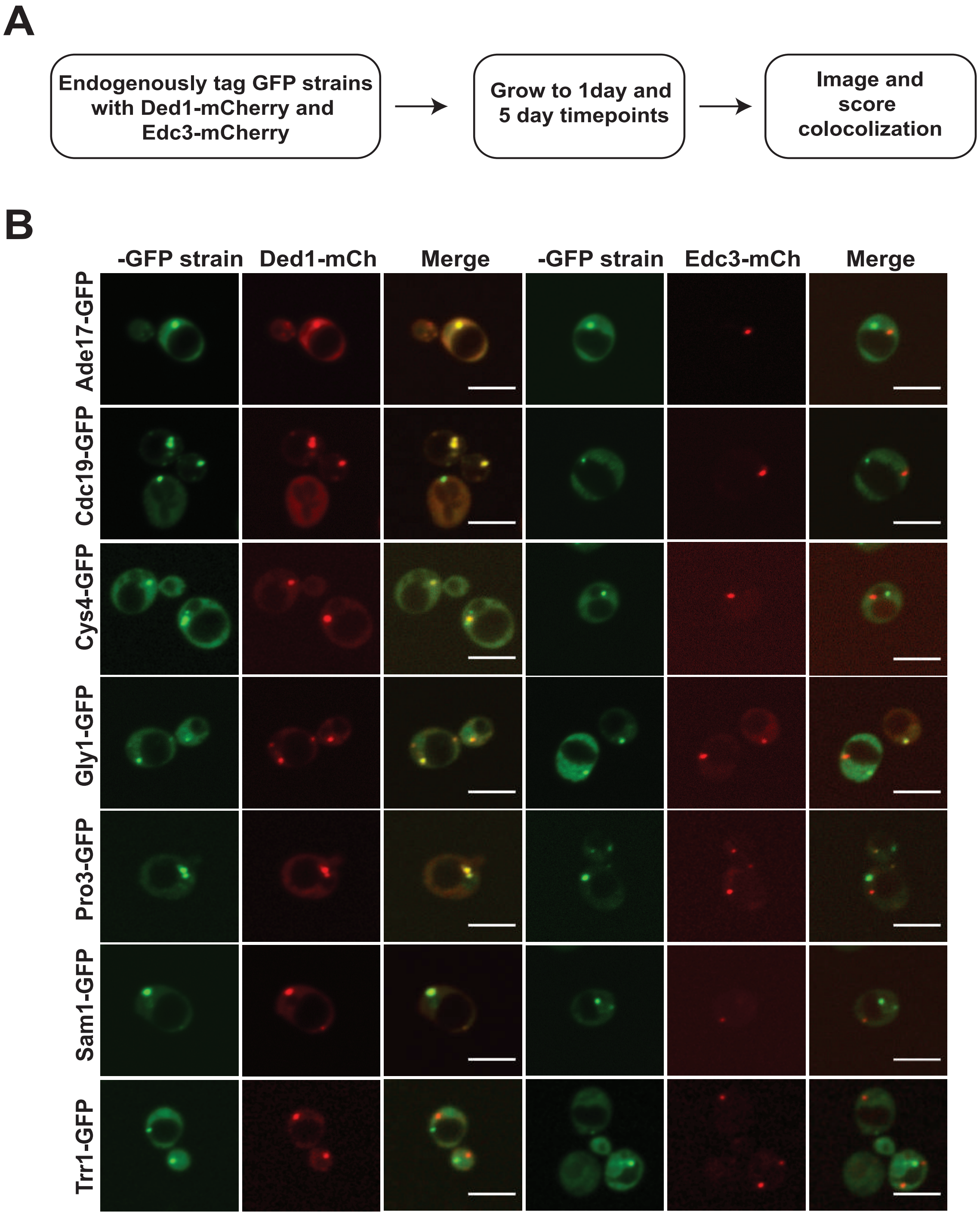

Figure 3.1. Metabolic enzymes localize to RNA granules during late growth stages
(A) Schematic illustrating workflow for RNA granule screen. **(B)** Representative fluorescent images of cells expressing GFP tagged metabolic enzymes and mCherry tagged Ded1 (Stress Granules) or Edc3 (P-bodies) from either 1-day or 5-day time points. Scale bar: 5μm

Table 3.1. Colocalization analysis of hits from RNA granule screen

		1 Day			5 Days		
Protein	**Molecular function**	**Percent cells with foci**	**Ded1::mCherry colocalization**	**Edc3::mCherry cololcalization**	**Percent cells with foci**	**Ded1::mCherry colocalization**	**Edc3::mCherry cololcalization**
Ade16	IMP cyclohydrolase Phosphoribosylamino imidazolecarboxamide formyltransferase	0%	0 ± 0%	0 ± 0%	42%	91.10 ± 1.86	8.11 ± 1.29
Ade17	IMP cyclohydrolase Phosphoribosylamino imidazolecarboxamide formyltransferase	5%	0 ± 0%	0 ± 0%	33%	90.29 ± 0.63	9.58 ± 1.84
Ald6	Aldehyde dehyrogenase	13%	60.10 ± 6.11	4.23 ± 0.86	66%	49.01 ± 2.41	1.87 ± 0.31
Cdc19	Pyruvate kinase	34%	4.71 ± 2.49	1.53 ± 0.79	85%	48.04 ± 5.06	3.38 ± 1.11
Cys4	Cystathionine beta-synthase	11%	5.56 ± 1.33	0.71 ± 0.44	30%	60.24 ± 7.1	4.69 ± 0.7
Dph2	Unknown	0%	0 ± 0%	0 ± 0%	28%	45.51 ± 6.79	2.26 ± 0.69
Gdh1	Glutamate dehydrogenase	17%	74.31 ± 1.51	4.18 ± 1.13	40%	49.17 ± 8.05	2.32 ± 0.59
Gly1	L-allo-threonine aldolase Threonine aldolase	11%	82.26 ± 1.81	16.42 ± 1.17	75%	29.76 ± 6.48	6.76 ± 0.66
Gre3	Alditol:NADP+ 1-oxidoreductase D-xylose:NADP reductase Glucose 1-dehydrogenase	10%	45.87 ± 4.25	22.44 ± 1.04	60%	75.63 ± 1.08	8.78 ± 1.41
Hem2	Porphobilinogen synthase	12%	17.03 ± 2.12	4.05 ± 1.31	73%	18.89 ± 3.92	5.07 ± 1.11
Hem13	Coproporphyrinogen oxidase	15%	70.81 ± 2.49	6.79 ± 1.07	5%	0 ± 0	0 ± 0
Imd3	IMP dehydrogenase	0%	0 ± 0	0 ± 0	10%	34.86 ± 3.89	7.3 ± 1.46
Pro3	Pyrroline-5-carboxylate reductase	11%	73.40 ± 8.20	24.53 ± 5.90	50%	89.09 ± 1.81	8.08 ± 1.92
Sam1	Methionine adenosyltransferase	19%	85.22 ± 1.01	9.90 ± 1.21	65%	84.96 ± 2.41	12.47 ± 1.81
Sam2	Methionine adenosyltransferase	13%	78.65 ± 1.69	9.07 ± 1.14	60%	80.93 ± 2.9	8.7 ± 1.03
Shm2	Glycine hydroxymethyltransferase	45%	3.28 ± 0.81	0 ± 0	27%	13.77 ± 2.29	1.01 ± 0.51
Tpi1	Triosephosphate isomerase	4%	0 ± 0	0 ± 0	20%	19.03 ± 4.23	2.01 ± 0.62

Cdc19 show a decline in the number of independent structures over time while the amount of enzyme present in SGs increases (Table 3.1).

Given the role of intrinsically disordered regions (IDRs) and low complexity sequences (LCSs) in targeting proteins to RNA granules, we also examined whether any of these motifs were present and/or enriched in either class of SG associated metabolic enzymes. 12 out of the 17 enzymes localized to SGs were predicted to contain an IDR and/or LCS; however, these motifs were found at an equal frequency amongst the 17 enzymes in our screen that were not recruited to RNA granules (Table 3.2 and 3.3). Thus, neither the ability to be recruited to a SG nor the pattern of recruitment can be predicted by the presence or absence of IDRs or LCSs. Furthermore, only 3 of our SG associated enzymes have been annotated as having RNA binding activity by high throughput screens (Table 3.2) arguing the majority of these enzymes are not recruited to SGs via RNA. Together, these results suggest that recruitment of metabolic enzymes to RNA granules occurs via novel, uncharacterized mechanisms.

The metabolic enzyme Sam1 is a stress specific component of SGs

Recruiting metabolic enzymes to SGs represents potential way to couple SG assembly to changes in metabolic activity/stress. If this were the case, one might expect that the recruitment of metabolic enzymes to SGs would be stress specific. While our screen focused on standard growth stresses, including growth to post-diauxic shift (1 day) or growth to stationary phase (5 days) in rich medium, most studies of SGs focus on the effects of acute energy stresses on log phase cells. This raised the possibility that this set of metabolic enzymes had been missed in prior studies of SGs due to the fact that their recruitment is stress-specific. In order to test this possibility, we examined whether one of the enzymes identified in our screen the S-adenosylmethionine synthetase, Sam1 (Figure 2.1B, Figure 2.2A-B), is recruited to SGs in

Table 3.2. Domain analysis of hits from RNA granule screen

Protein	IDR? (IUPRED)	LCS? (SEG)	RNA binding? (SGD)	SG proteome? (Jain et al 2016)
Ade16	-	252-263	N	N
Ade17	-	252-263	N	N
Ald6	15-17, 40-57, 87-88	-	N	N
Cdc19	23-26, 93-99, 101-105, 372-377	375-389	N	N
Cys4	1-12, 57-78	21-36, 85-94, 190-204	Y*	Y
Dph2	417-434, 458-471, 500-519, 521-534	109-122	N	N
Gdh1	60-61, 362-363	100-118	N	N
Gly1	-	-	N	N
Gre3	-	-	Y**	N
Hem2	1-2	161-172, 236-248	N	N
Hem13	1-19, 38-61, 86-99, 313-314	-	N	N
Imd3	108-109, 432-433	202-213	Y*	N
Pro3	53-55	194-208	N	N
Sam1	105-112	256-270	N	Y
Sam2	169-172, 175-177	258-272	N	Y
Shm2	24-29	301-312	N	N
Tpi1	-	-	N	N

*(Mitchell et al., 2013)
**(Scherrer et al., 2010)

Table 3.3. Domain analysis of non-hits from RNA granule screen

Protein	IDR? (IUPRED)	LCS? (SEG)	RNA binding? (SGD)	SG proteome? (Jain et al 2016)
Acs1	1-37, 39-46, 57-61, 77-78, 239-240	296-303, 588-602	N	N
Ade4	-	-	N	N
Ade12	132-139, 248-261, 283-284, 286-287, 290-291	127-138	N	N
Adh2	22-24	63-79, 173-186	N	N
Faa4	9-13, 17-27, 212-213, 693-694	-	N	Y
Fas1	44-49, 51-53, 325-327, 339-340, 352-356, 1114-1115, 1195-1197, 1556-1557, 1677-1678	1105-1123, 1462-1473	N	N
Fba1	142-143, 182-194, 314-317	-	N	N
Imd2	108-109, 432-433	-	Y*	N
Imd4	433-434	-	Y*	N
Mdh2	1-4	12-41	N	N
Pdc1	187-188, 561-562	415-428	N	N
Rnr4	-	-	N	N
Sec53	147-148, 150-152	-	N	Y
Tal1	1-14, 37-39, 50-51	218-230	N	N
Tdh3	-	179-201	Y**	N
Thr1	41-42, 46-54, 174-182, 184-185, 187-196, 356-357	104-122	N	N
Trr1	53-55, 63-66, 69-70	-	N	N

* (Mitchell et al., 2013)
**(Shen et al., 2014)

response to acute energy stresses. In addition to its high colocalization with SGs, we also chose Sam1 as our follow up candidate since its substrates and products (methionine, ATP, AdoMet) are highly utilized and connected to multiple metabolic pathways. While Ded1-positive SGs readily formed in log phase yeast that were treated with sodium azide, ethanol, or shifted to media lacking glucose, Sam1-GFP remained diffuse under all of these conditions (Figure 2.2C-D). Since all of these stresses were acute energy stresses, we also tested the effects of translational stress on Sam1 recruitment to SGs. Given the role of methionine in translation initiation, we reasoned that acute methionine limitation may also trigger SG assembly. Sam1 catalyzes the ATP-dependent conversion of methionine to S-adenosylmethionine (AdoMet) (Figure 2.2A), thus methionine limitation might be expected to trigger both SG assembly and regulate Sam1 activity and/or recruitment to SGs. While shifting log phase yeast to media lacking methionine robustly triggered the assembly of Ded1-containing SGs, the SGs failed to recruit Sam1 (Figure 2.2C-D). Thus, methionine limitation constitutes a previously unidentified trigger for SG assembly; however, it is not a trigger for Sam1 recruitment to SGs.

Given these results, we next explored whether we could bypass the stress-specific recruitment of SGs by manipulating the levels of SG components. Overexpression of particular SG components can nucleate SG assembly in the absence of an external stress (Hilliker et al., 2011; Swisher and Parker, 2010). For instance, overexpression of either Ded1 or Pbp1 triggers the assembly of SGs in unstressed log phase cells (Figure 2.2E-F). However, these SGs fail to recruit Sam1. Thus, merely triggering the aggregation of SG proteins is insufficient to recruit Sam1. Since Sam1 has a short LCS motif typical of SG nucleators, we also tested whether overexpression of Sam1 could trigger SG assembly. Overexpression of Sam1 in log phase yeast did not cause protein aggregation or trigger SG formation (Figure 2.2E-F). Thus, Sam1 does not

Figure 3.2. Recruitment of Sam1 to stress granules is stress specific
(A) Schematic representation of methionine biosynthesis/recycling pathway in *S.cerevisae*. **(B)** Quantification of percentage of cells with Sam1-GFP foci and Ded1-GFP foci at different growth stages. Data is presented as average ± SEM of three independent replicates. **(C)** Quantification of logarithmically growing strains expressing Ded1-GFP or Sam1-GFP upon exposure to different acute stresses. Data is presented as average ± SEM of three independent replicates. **(D)** Representative fluorescent images from Figure 3.2C. **(E)** Quantification of logarithmically growing strains with GFP tagged Ded1 or Sam1 and overexpressing nucleator stress granule proteins (Ded1 or Pbp1) or Sam1. Data is presented as average ± SEM of three independent replicates. **(F)** Representative fluorescent images from Figure 3.2E. **(G)** Quantification of logarithmically growing strains expressing Ded1-GFP or Sam1-GFP upon a 10 minute heat shock at 46°C. Data is presented as average ± SEM of three independent replicates. **(H)** Representative fluorescent images from Figure 3.2G. **(I)** Representative fluorescent images of Sam1 colocalization with stress granules under heat shock conditions. Scale bars in **(D)**, **(F)**, **(H)**, and **(I)** are 5µm.

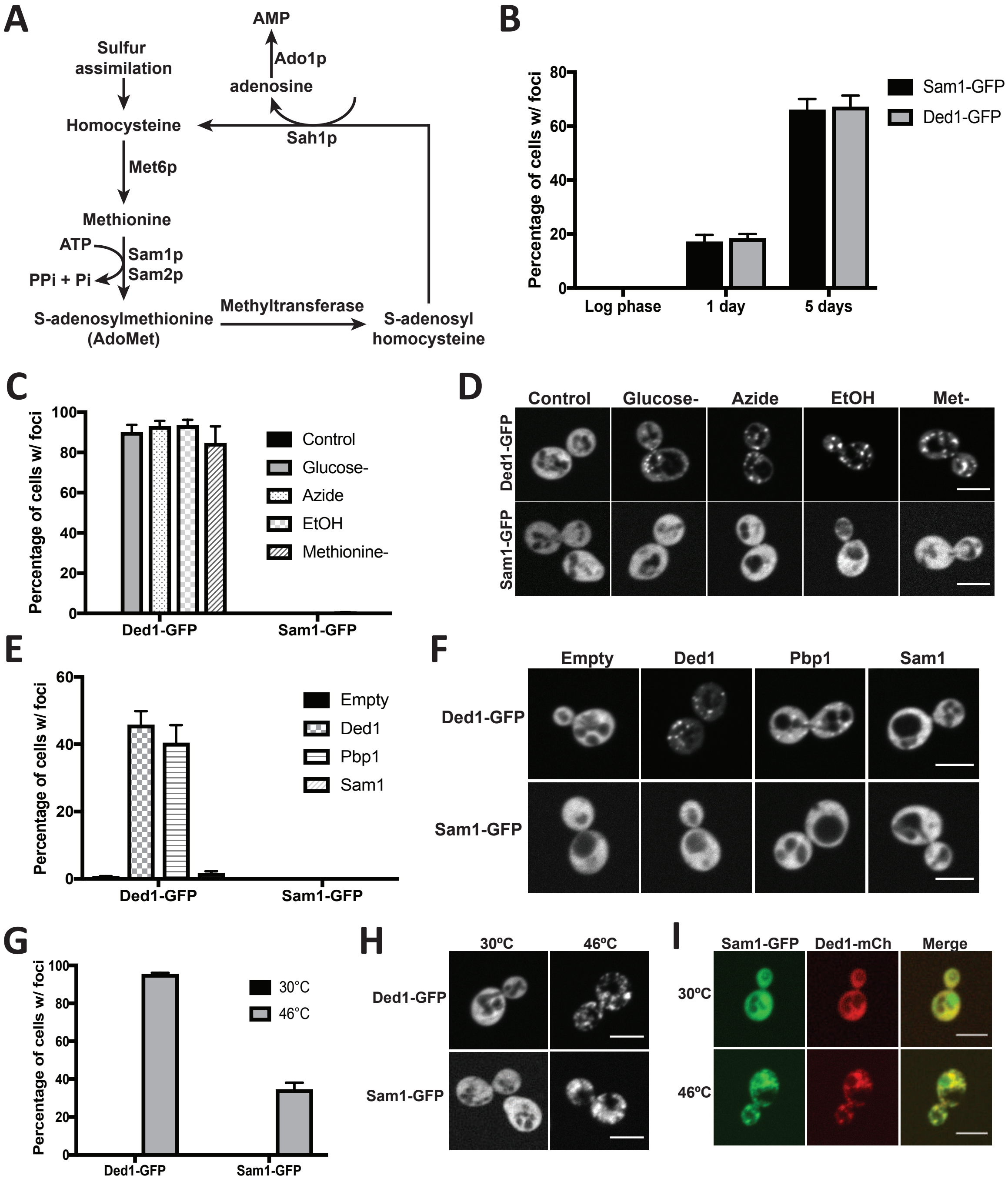
A
AMP
Ado1p
Sulfur assimilation
adenosine
Homocysteine
Sah1p
Met6p
Methionine
ATP
Sam1p
Sam2p
PPi + Pi
S-adenosylmethionine (AdoMet)
Methyltransferase
S-adenosyl homocysteine
B
Percentage of cells w/ foci
80
60
40
20
0
Log phase
1 day
5 days
Sam1-GFP
Ded1-GFP
C
Percentage of cells w/ foci
100
80
60
40
20
0
Ded1-GFP
Sam1-GFP
Control
Glucose-
Azide
EtOH
Methionine-
D
Control
Glucose-
Azide
EtOH
Met-
Ded1-GFP
Sam1-GFP
E
Percentage of cells w/ foci
60
40
20
0
Ded1-GFP
Sam1-GFP
Empty
Ded1
Pbp1
Sam1
F
Empty
Ded1
Pbp1
Sam1
Ded1-GFP
Sam1-GFP
G
Percentage of cells w/ foci
100
80
60
40
20
0
Ded1-GFP
Sam1-GFP
30°C
46°C
H
30ºC
46ºC
Ded1-GFP
Sam1-GFP
I
Sam1-GFP
Ded1-mCh
Merge
30ºC
46ºC

have a high propensity to aggregate in vivo. Consistent with this, we also found that Sam1 was only recruited to only 30% of SGs formed in response to heat shock while the majority of the protein remained diffused (Figure 2.2G-I). Together, these results argue Sam1 is a stress-specific component of SGs, but it is not capable of nucleating SGs on its own.

Decreased AdoMet levels triggers SG assembly and Sam1 recruitment

The localization of Sam1 in a stress specific manner to SGs suggests that the products of Sam1 might play a role in modulating SG assembly. In order to test this possibility, we leveraged previous structure function studies of the *E. coli* ortholog of Sam1, MetK, to design a set of mutations that disrupts the enzyme's activity (Taylor and Markham, 1999, 2000). While each mutation resulted in a decrease in enzymatic activity of MetK, we utilized mutants that would disrupt enzyme tetramerization (C91Y), ATP hydrolysis (D121N) or have no additional effect (K252M) (Figure 3.3A). Each mutation was introduced into the endogenous *SAM1* locus and assayed for its effects on SG formation.

All three *SAM1* inactivating mutations caused a 3-fold increase in SG formation that were positive for two SG markers (Ded1 and Pbp1) and three metabolic enzymes (Sam1, Sam2, and Ade17) (Figure 3.4A). Interestingly, both the C91Y and K252M mutations displayed no defects in Sam1p recruitment while the ATP hydrolysis mutant, D121N, significantly reduced Sam1 localization to SGs (Figure 3.3B-C). Sam2's recruitment to SGs was also disrupted in the *SAM1* D121N allele, whereas Ade17, Ded1, and Pbp1 remained unaffected (Figure 3.3D-E). These results argue that the inactivation of Sam1, rather than disruption of its localization to SGs, is responsible for the increase in SG formation observed in all three *SAM1* mutations.

A potential way for Sam1 to regulate SG assembly would be by controlling the levels of various SG components. While the effects of Sam1 inactivation on Sam1 protein levels are allele

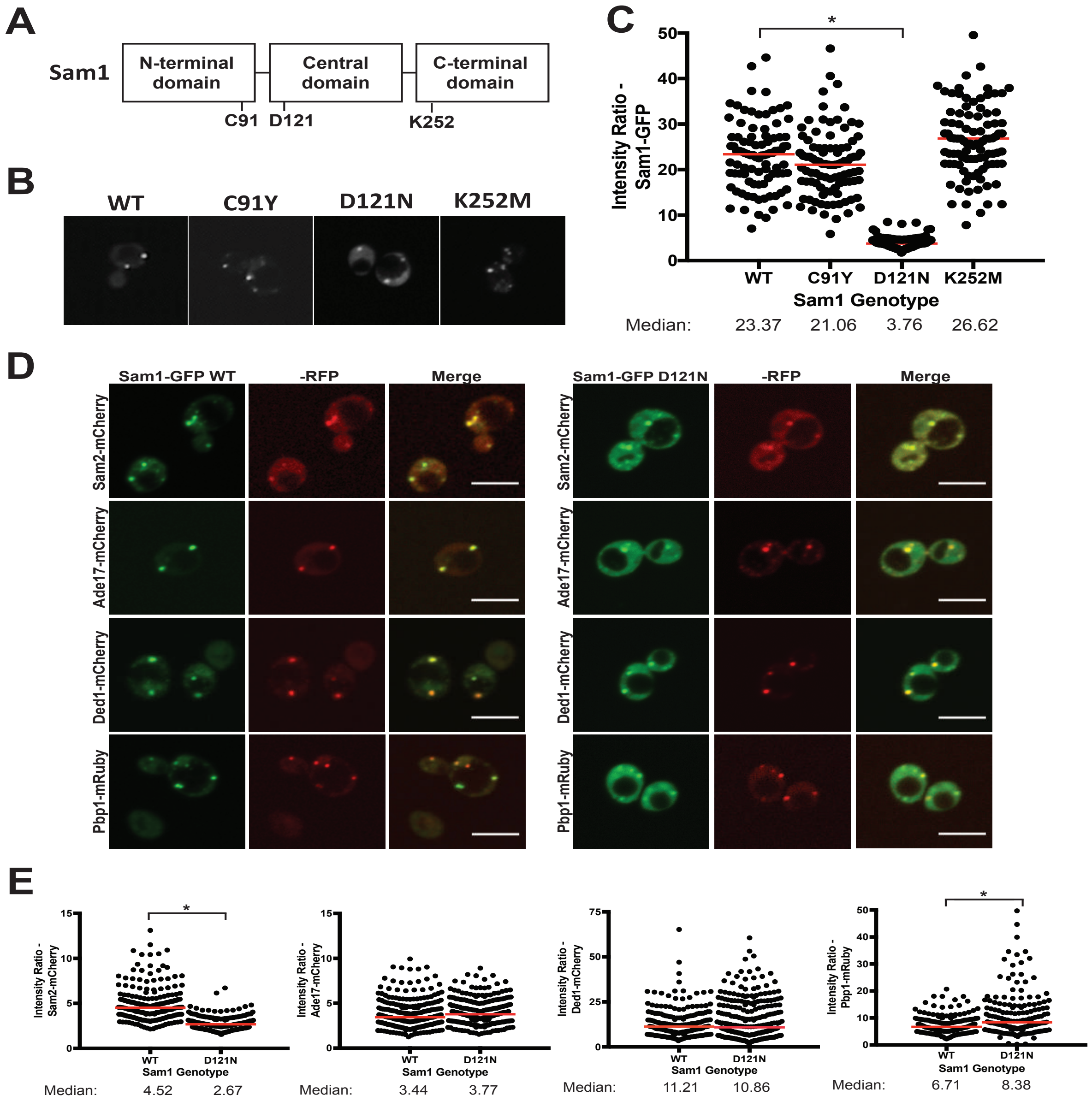

Figure 3.3. Mutation in the ATP binding domain of Sam1 inhibit recruitment of Sam1 and Sam2 to stress granules

(A) Schematic illustration of Sam1 protein showing positions of each domain and where point mutations reside. **(B)** Representative fluorescent images of cells expressing WT or mutant Sam1-GFP from the endogenous locus. **(C)** Dot plot displaying foci-to-cytoplasm ratios for Sam1-GFP in WT and mutant alleles. **(D)** Representative fluorescent images of cells expressing WT or D121N Sam1-GFP and RFP-tagged Sam2, Ade17, Ded1 or Pbp1 from the endogenous locus. **(E)** Dot plot displaying foci-to-cytoplasm ratios for RFP-tagged Sam2, Ade17, Ded1, and Pbp1 in WT and Sam1 D121N backgrounds. Scale bars in **(B)** and **(D)** are 5μM, * indicates $P<0.05$.

Figure 3.4. Decreased AdoMet levels result in increased stress granule formation
(A) Quantification of cells with foci from 1-day cultures expressing WT or mutant Sam1-GFP alleles along with RFP-tagged metabolic enzymes (Sam2, Ade17) and stress granule markers (Ded1, Pbp1). Data is presented as average ± SEM of three independent replicates. **(B)** Western blot analysis from strains used in Figure 3.4A at 1 day time point. **(C)** Quantification of proteins levels from Figure 3.4B. Data is presented as average ± SEM of three independent replicates. **(D)** Quantification of mRNA levels using qPCR analysis from WT and mutant Sam1 alleles. Data is presented as average ± SEM of three independent replicates. **(E)** Quantification of cells with foci from 1-day cultures expressing WT or mutant Sam1-GFP alleles and Ded1-mCherry supplemented with or without 250μM AdoMet. Data is presented as average ± SEM of three independent replicates. **(F)** Western blot analysis from strains used in Figure 3.4E at 1 day time point. **(G)** Quantification of proteins levels from Figure 3.4E. Data is presented as average ± SEM of three independent replicates. * indicates $P<0.05$.

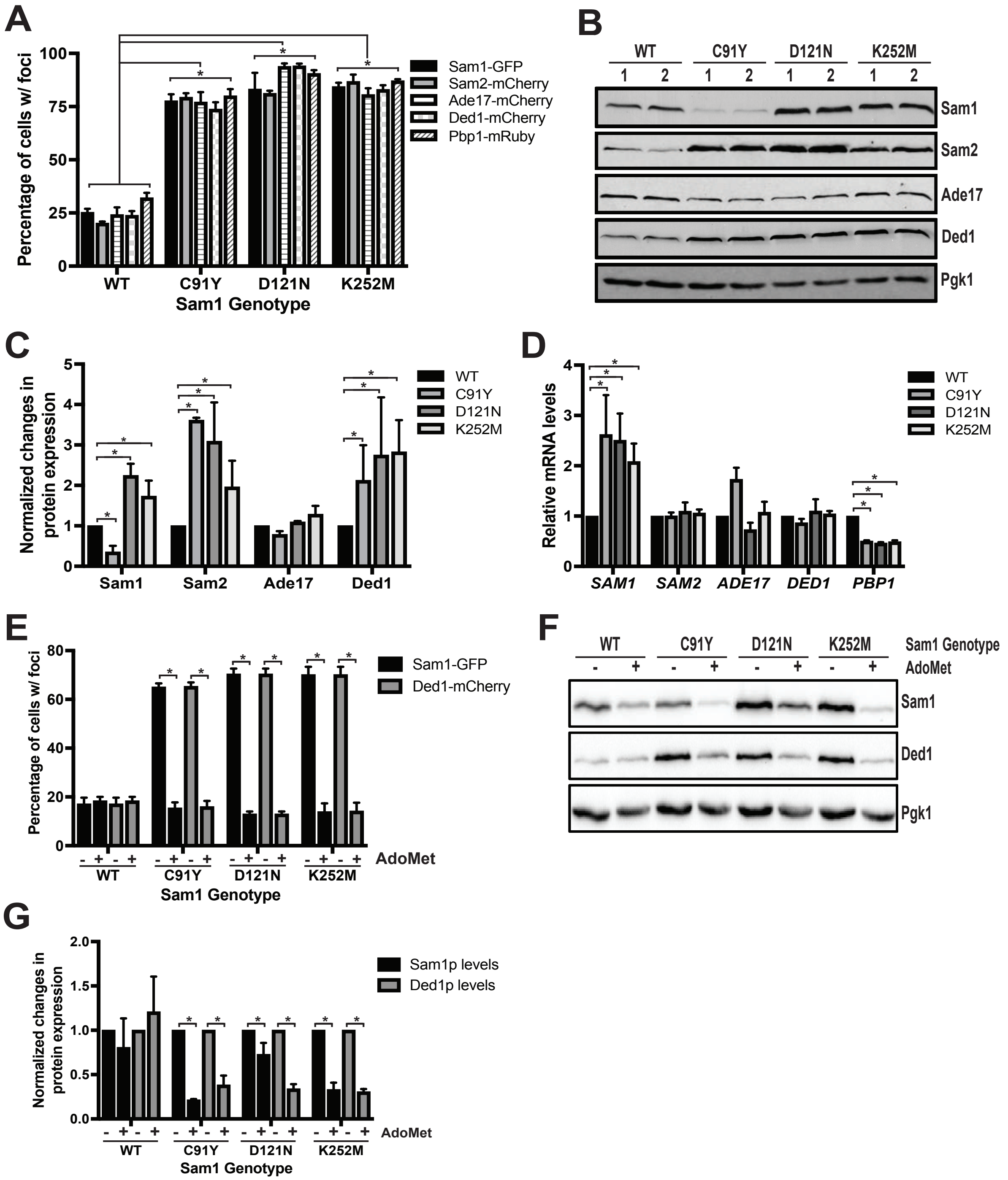
A
Percentage of cells w/ foci
100
75
50
25
0
WT
C91Y
D121N
K252M
Sam1 Genotype
Sam1-GFP
Sam2-mCherry
Ade17-mCherry
Ded1-mCherry
Pbp1-mRuby
*
B
WT
C91Y
D121N
K252M
1 2 1 2 1 2 1 2
Sam1
Sam2
Ade17
Ded1
Pgk1
C
Normalized changes in protein expression
5
4
3
2
1
0
Sam1
Sam2
Ade17
Ded1
WT
C91Y
D121N
K252M
D
Relative mRNA levels
4
3
2
1
0
SAM1
SAM2
ADE17
DED1
PBP1
WT
C91Y
D121N
K252M
E
Percentage of cells w/ foci
80
60
40
20
0
Sam1-GFP
Ded1-mCherry
- + - +
AdoMet
WT
C91Y
D121N
K252M
Sam1 Genotype
F
WT
C91Y
D121N
K252M
Sam1 Genotype
- + - + - + - +
AdoMet
Sam1
Ded1
Pgk1
G
Normalized changes in protein expression
2.0
1.5
1.0
0.5
0.0
Sam1p levels
Ded1p levels
- + - +
AdoMet
WT
C91Y
D121N
K252M
Sam1 Genotype

dependent, all three *SAM1* mutations caused a ~2.5 fold increase in Ded1 levels and a 2 to 4 fold increase in Sam2 protein, but had no effect on Ade17 levels (Figure 3.4B-C). However, this increase in Ded1 protein levels was not due to transcriptional upregulation (Figure 3.4D). Since overexpression of Ded1 can trigger SG assembly during log phase, this result suggested that one of the ways that Sam1 activity controls SG formation is via Ded1 levels at growth to 1 day in a post-transcriptional manner.

One way that the levels of the SG nucleator, Ded1, could be coupled to Sam1 activity is via the levels of AdoMet. If this were the case, exogenous AdoMet would be predicted to restore the SG formation in *SAM1* mutations to wild type levels. To test this, we supplemented cultures of wild type and mutant *SAM1* strains with 250 μM AdoMet and assayed its effects on SG formation and Ded1 protein levels when grown for 24 hours. In wild type strains, exogenous AdoMet had no effect on the expression level of Ded1 or on the frequency of SG formation as indicated by Sam1-GFP and Ded1-mCherry (Figure 3.4E-F). In contrast, AdoMet treatment restored protein levels of Ded1 and the frequency of SG formation to wild type levels for all three *SAM1* loss-of-function mutations. These results argue that decreases in AdoMet increase SG formation that is likely due to the increase in Ded1 protein levels.

Prolonged AdoMet accumulation disrupts SG assembly

AdoMet regulated SG accumulation under the same growth stress that triggers the recruitment of Sam1. This suggested that AdoMet might have an autoregulatory role in SG assembly when cells are grown under chronic nutrient stress. If this were true, one would expect that increase in AdoMet levels might block or greatly reduce SG formation at growth to 1 day. However, because AdoMet uptake is glucose-dependent, our ability to increase AdoMet levels above normal is limited at the 1-day time point. As a result, we applied a genetic approach to manipulating AdoMet levels. Deletion of *ADO1* has been previously found to increase AdoMet levels by 7-fold at 1 day growth compared wild type. This suggested that deletion of *ADO1* might suppress SG formation. Consistent with this, deleting *ADO1* almost completely blocked the formation of Ded1-containing SGs. (Figure 3.5A).

One potential mechanism for the effect of *ado1Δ* on SGs is that increasing AdoMet levels at this time point decreases Ded1 expression. Consistent with this interpretation, we found that deletion of *ADO1* decreases protein levels of Ded1 by 40%. (Figure 3.5B-C). Furthermore, the decrease in Ded1 protein levels occurred despite *DED1* mRNA levels increasing by 50% in *ado1Δ* strains (Figure 3.5D). Consistent with transcript levels from Sam1 inactivation strains, this argues that the effect of AdoMet on Ded1 expression is post-transcriptional. Additionally, even though Ded1 is a substrate for arginine methyltransferase, Hmt1, the post-transcriptional effects we observe are not mediated by Hmt1 or its target residues in Ded1 arguing that these effects occur via a novel AdoMet controlled pathway (Erce et al., 2013; Low et al., 2013) (Figure 3.6A-B).

The striking effect of elevated AdoMet levels on Ded1 expression raised the possibility that AdoMet might be regulating composition and/or composition of multiple RNA granule components at growth to 1 day. In order to test this possibility, we examined the effects of *ado1Δ* on the localization of two P-body markers, Edc3 and Dcp2, as well as five additional SG proteins, eIF4E, eIF4G1, Pab1, Pbp1, and Pub1. Deletion of *ADO1* has no effect on P-body formation (Figure 3.6C-D). Thus, *ado1Δ* strains do not have a generalized defect in RNA granule assembly. In contrast to its effect on P-bodies, *ado1Δ* had selective effects on the recruitment of proteins to SGs. Pab1, Pbp1, and Pub1 were all recruited normally into SGs in the *ado1Δ* strain (Figure 3.5A). Thus, *ado1Δ*-mediated down regulation of Ded1 does not eliminate SGs

Figure 3.5. 5'UTR mRNA-associated stress granule proteins are not recruited to stress granules under high AdoMet levels under growth to 1 day.
(A) Quantification and representative fluorescent images of WT and *ado1Δ* strains with GFP-tagged stress granule proteins at 1 day time point. Data is presented as average ± SEM of three independent replicates. **(B)** Western blot analysis of strains used in Figure 3.5A at 1 day time point. **(C)** Quantification of proteins levels from Figure 3.5B. Data is presented as average ± SEM of three independent replicates. **(D)** Quantification of mRNA levels using qPCR analysis from WT and *ado1Δ* strains. Data is presented as average ± SEM of three independent replicates. **(E)** Quantification and representative fluorescent images of logarithmically growing WT and *ado1Δ* strains expressing Ded1-GFP under acute stress. Data is presented as average ± SEM of three independent replicates. **(F)** Quantification and representative fluorescent images of logarithmically growing WT and *ado1Δ* strains expressing Ded1-GFP under heat shock conditions. Data is presented as average ± SEM of three independent replicates.
Scale bars in **(A)**, **(E)**, and **(F)** are 5µm, * indicates $P<0.05$.

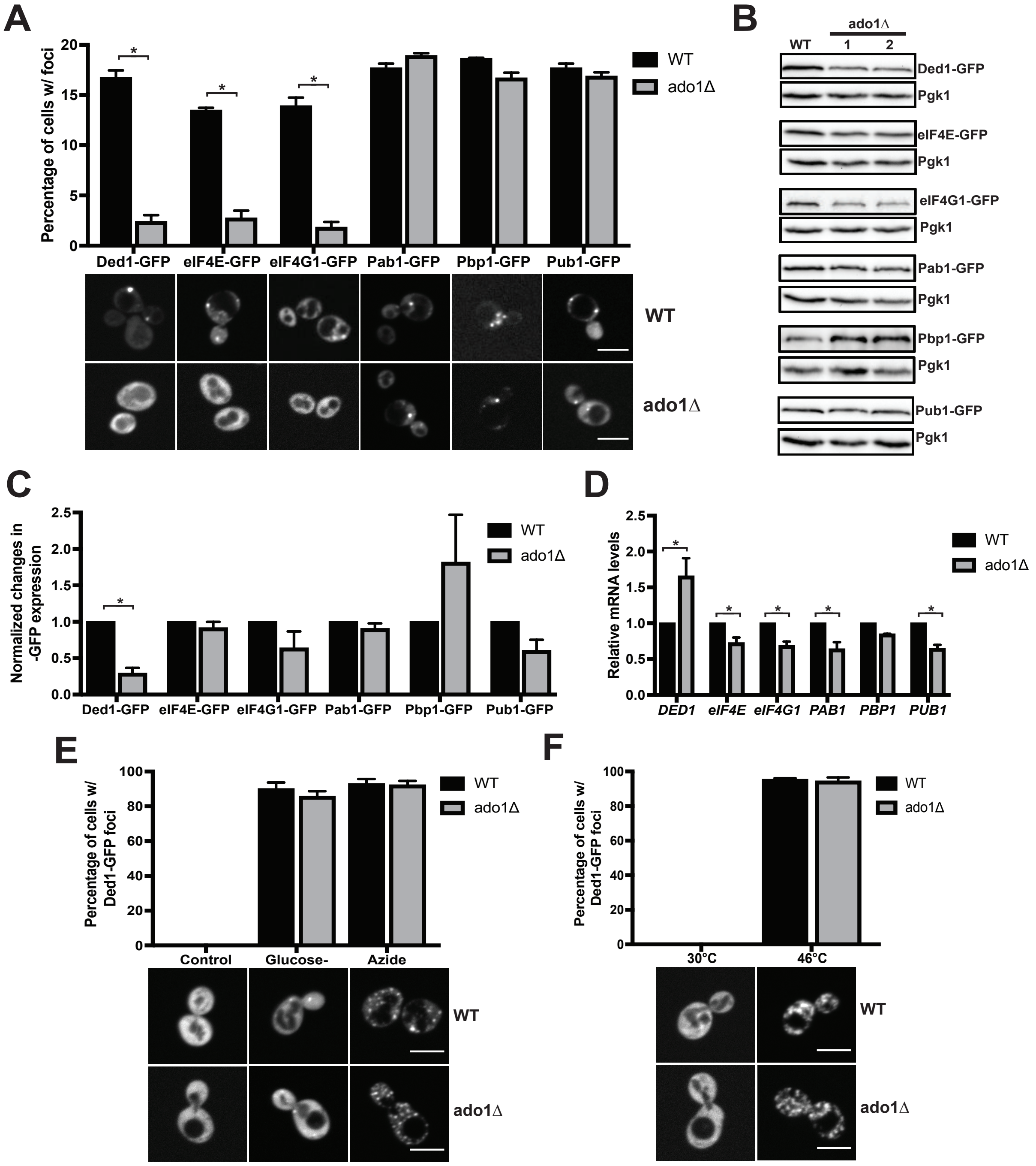
A
Percentage of cells w/ foci
20
15
10
5
0
*
*
*
WT
ado1Δ
Ded1-GFP
eIF4E-GFP
eIF4G1-GFP
Pab1-GFP
Pbp1-GFP
Pub1-GFP
WT
ado1Δ
B
ado1Δ
WT
1
2
Ded1-GFP
Pgk1
eIF4E-GFP
Pgk1
eIF4G1-GFP
Pgk1
Pab1-GFP
Pgk1
Pbp1-GFP
Pgk1
Pub1-GFP
Pgk1
C
Normalized changes in -GFP expression
2.5
2.0
1.5
1.0
0.5
0.0
*
WT
ado1Δ
Ded1-GFP
eIF4E-GFP
eIF4G1-GFP
Pab1-GFP
Pbp1-GFP
Pub1-GFP
D
Relative mRNA levels
2.5
2.0
1.5
1.0
0.5
0.0
*
*
*
*
*
WT
ado1Δ
DED1
eIF4E
eIF4G1
PAB1
PBP1
PUB1
E
Percentage of cells w/ Ded1-GFP foci
100
80
60
40
20
0
WT
ado1Δ
Control
Glucose-
Azide
WT
ado1Δ
F
Percentage of cells w/ Ded1-GFP foci
100
80
60
40
20
0
WT
ado1Δ
30°C
46°C
WT
ado1Δ

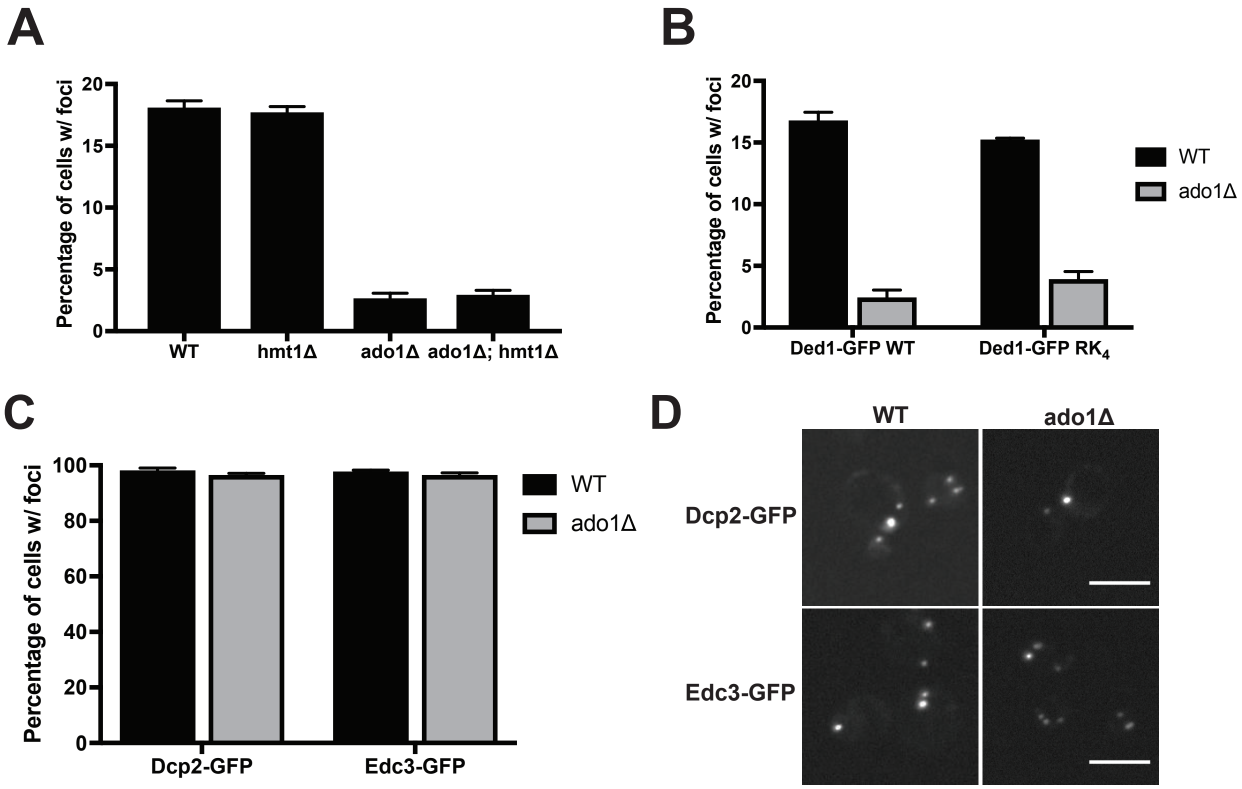

Figure 3.6. Stress granule phenotype in *ado1Δ* strain is independent of P-body formation or arginine methylation
(A) Quantification of cells with Ded1-GFP foci in WT, *hmt1Δ*, *ado1Δ*, and *ado1Δ;hmt1Δ* background strains at 1-day time point. Data is presented as average ± SEM of three independent replicates. **(B)** Quantification of cells with foci in WT and *ado1Δ* backgrounds expressing either WT or RK$_4$ Ded1-GFP. Data is presented as average ± SEM of three independent replicates. **(C)** Quantification of cells with foci for P-body markers (Dcp2 and Edc3) in WT and *ado1Δ* background strains at 1-day time point. Data is presented as average ± SEM of three independent replicates. **(D)** Representative images from Figure 3.6A. Scale bar: 5μM

completely. In contrast, *ado1Δ* largely blocked the recruitment of eIF4E and eIF4G1 to SGs (Figure 3.5A). Furthermore, the loss of eIF4E and eIF4G1 is not due to decrease expression of either protein arguing that deletion of *ADO1* blocks the recruitment of both proteins to SGs (Figure 3.5B-C). Together, these results argue that AdoMet levels regulate the recruitment of a subset of SG proteins at growth to 1 day.

If Sam1 participated in a feedback loop regulating SG assembly at growth to 1 day, one might expect that alterations in AdoMet levels would regulate Sam1 recruitment to SGs. To test this possibility, we examined the localization of 4 metabolic enzymes (Sam1, Ade17, Cdc19, and Cys4) in an *ado1Δ* strain background. Sam1 and Ade17 both failed to form foci when *ADO1* was deleted (Figure 3.7A). In contrast, Cdc19 and Cys4 both formed foci at normal levels. Unlike Ded1, protein levels of all 4 proteins were unchanged or elevated by the deletion of *ADO1* (Figure 3.7B-C). Furthermore, Cdc19 and Cys4 foci both colocalized with Pbp1-mRuby in *ado1Δ* strains indicating that the structures are SG remnants. (Figure 3.7D-G). Thus, AdoMet levels regulate the recruitment of a subset of metabolic enzymes to SG at growth to 1 day, including the enzyme that synthesizes AdoMet, Sam1.

AdoMet supplementation suppresses acute stress induced SG assembly

Since the recruitment of metabolic enzymes to SGs is specific at growth to 1 day, we next investigated whether deleting *ADO1* has effects on the assembly of SGs regardless of the stress. Shifting yeast to media lacking glucose, treatment with sodium azide, or heat shock, all triggered Ded1-SG assembly at the same frequency in wild type and *ado1Δ* strains (Figure 3.5E-F). This suggested that either the effect of AdoMet on SG assembly was stress specific or that the levels of AdoMet in log phase *ado1Δ* strains were insufficient to trigger the effects. In order to explore

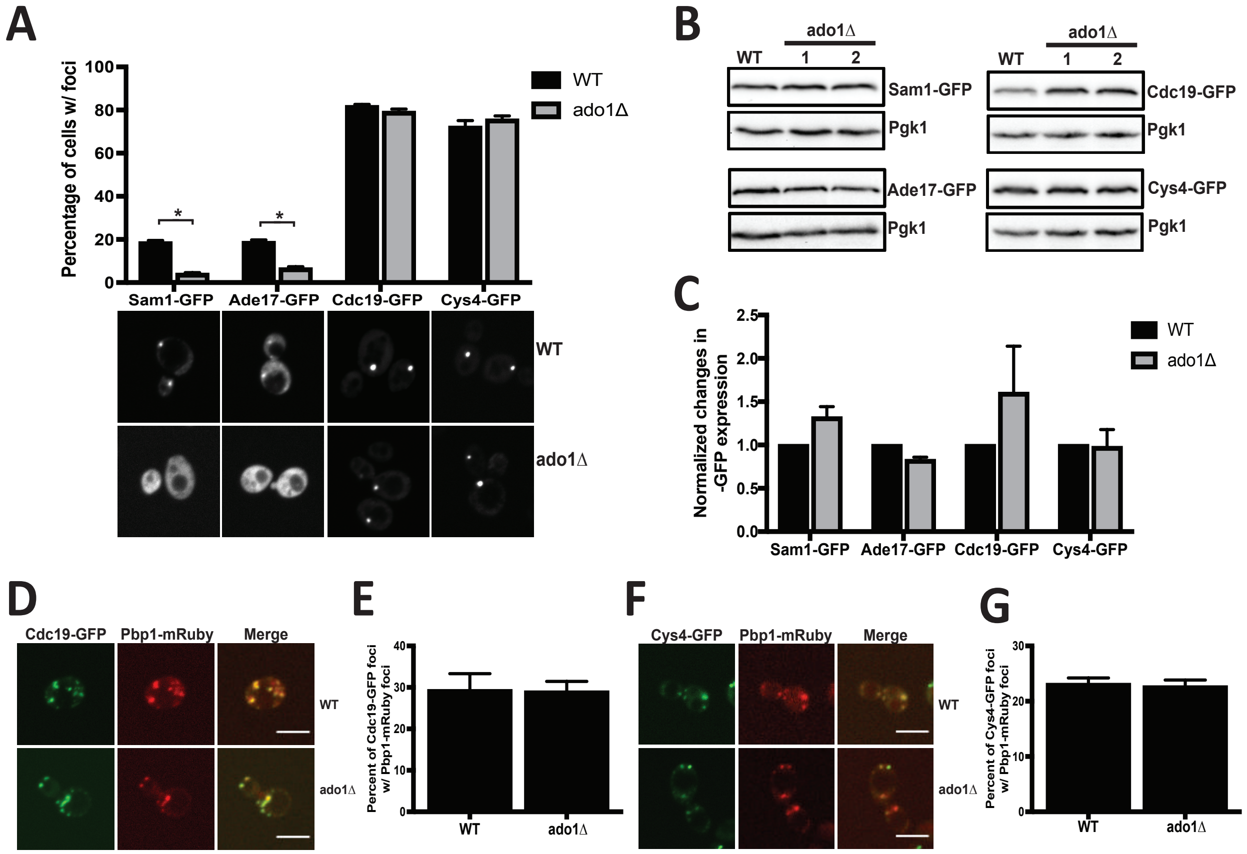

Figure 3.7. High AdoMet levels prevent recruitment of Sam1 and Ade17 to stress granules **(A)** Quantification and representative fluorescent images of WT and *ado1Δ* strains with GFP-tagged metabolic enzymes at 1 day time point. Data is presented as average ± SEM of three independent replicates. * indicates $P<0.05$. **(B)** Western blot analysis of strains used in Figure 3.7A at 1 day time point. **(C)** Quantification of proteins levels from Figure 3.7B. Data is presented as average ± SEM of three independent replicates. **(D)** Representative fluorescent images of WT or *ado1Δ* strains expressing Cdc19-GFP and Pbp1-mRuby at 1 day time point. **(E)** Quantification of the degree of colocalization of Cdc19-GFP foci to Pbp1-mRuby foci in WT and *ado1Δ* strains. Data is presented as average ± SEM of three independent replicates. **(F)** Representative fluorescent images of WT or *ado1Δ* strains expressing Cys4-GFP and Pbp1-mRuby at 1 day time point. **(E)** Quantification of the degree of colocalization of Cys4-GFP foci to Pbp1-mRuby foci in WT and *ado1Δ* strains. Data is presented as average ± SEM of three independent replicates. Scale bars in **(A)**, **(D)**, and **(F)** are 5μM.

the second possibility, we grew wild type yeast in media supplemented with 250μM AdoMet and then subsequently treated them azide. AdoMet treatment caused a reduction in the percentage of cells with foci and foci per cell as assayed with four different SG markers, Ded1, eIF4G1, Pab1, and Pub1 (Figure 3.8A-C). Interestingly, unlike the effects we observed in *ado1Δ* strains, AdoMet treatment had no effect on the protein level of Ded1 or the other SG proteins we used as markers (Figure 3.8D). Additionally, AdoMet mediated SG suppression was not dependent on Hmt1p arginine methylation (Figure 3.8E-G). This suggests that AdoMet is playing a critical role in suppressing SG assembly independent of protein levels or arginine methylation.

AdoMet's ability to suppress azide-induced SGs raised the question of whether it could suppress SG assembly upon other canonical stresses. Shifting AdoMet supplemented cultures to media lacking glucose prevented SG assembly (Figure 3.9A-B). However, we observed no difference in heat shock-induced SGs when cultures were grown with exogenous AdoMet (Figure 3.9C-D). Thus, while AdoMet treatment suppresses SGs that form in response to acute energy stress, heat shock-induced SG assembly occurs via a different pathway.

One possible way that AdoMet might suppress SG assembly is via an effect on translation. SGs are thought to form in response to reduced translation triggered via a variety of stresses (Panas et al., 2016; Protter and Parker, 2016). This leads to transcript release from polysomes enabling *trans* RNA-RNA, RNA-protein, and protein-protein interactions to nucleate SGs. This release step is believed to be critical for SG formation since treatment with cycloheximide can prevent SG formation (Wheeler et al., 2016). If AdoMet acted at the level of translation, we would predict that polysome traces would still be intact in AdoMet supplemented cultures when cells are exposed to azide. However, polysomes are absent in both azide treated cells and cells that were grown with AdoMet prior to azide treatment (Figure 3.8H). Thus,

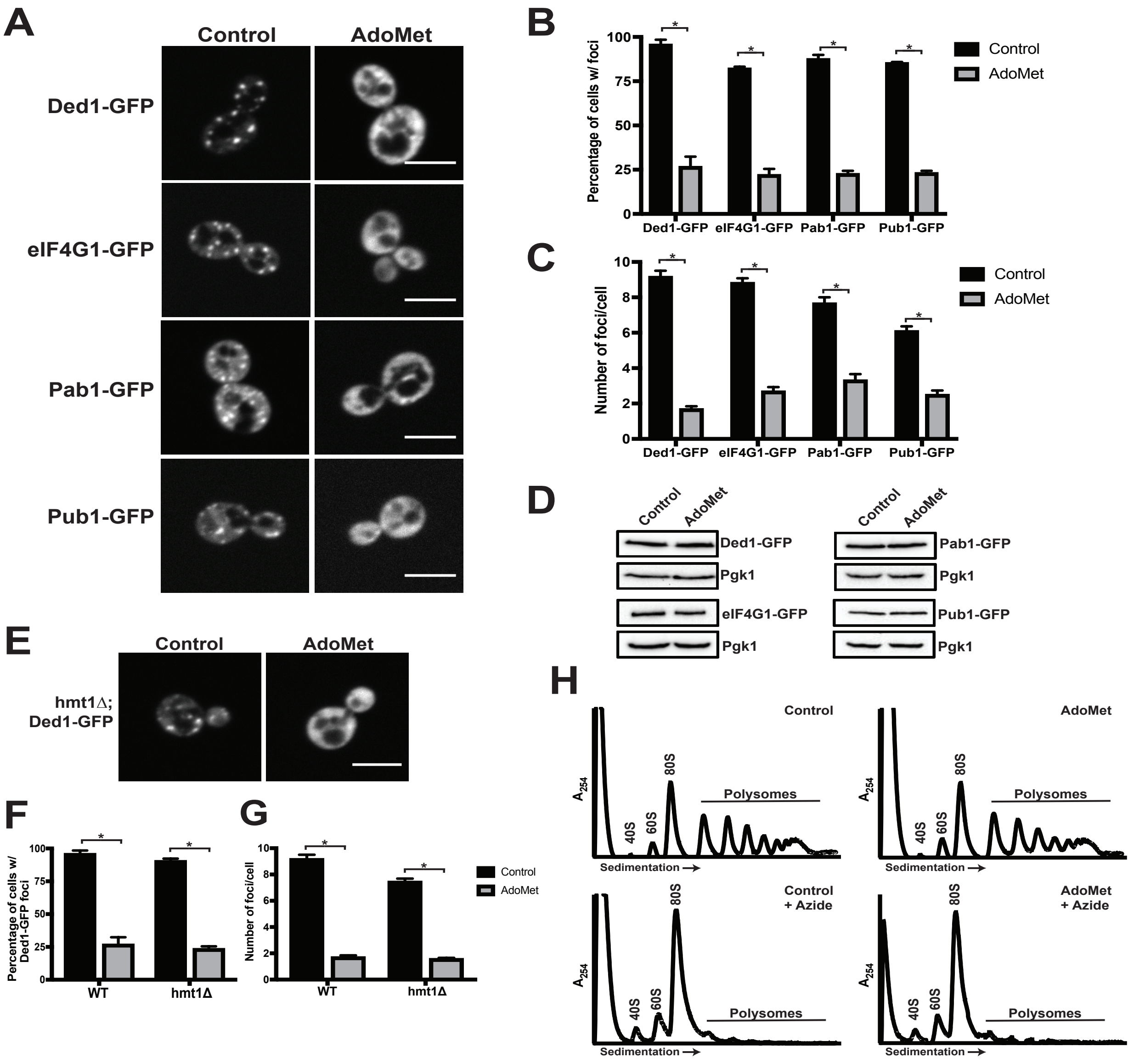

Figure 3.8. Exogenous AdoMet suppresses acute stress-induced stress granules
(A) Representative fluorescent images of logarithmically growing with (AdoMet) or without (Control) 250μM AdoMet WT strains expressing GFP tagged stress granule proteins upon azide treatment. **(B)** Quantification of cells with foci from Figure 3.8A. Data is presented as average ± SEM of three independent replicates. **(C)** Quantification of the number of foci/cell from Figure 3.8A. Data is presented as average ± SEM of three independent replicates. **(D)** Western blot analysis from strains used in Figure 4A. **(E)** Representative fluorescent images of WT and *hmt1Δ* strains expressing Ded1-GFP upon azide treatment. **(F)** Quantification of cells with foci from Figure 3.8E. Data is presented as average ± SEM of three independent replicates. **(G)** Quantification of the number of foci/cell from Figure 3.8E. Data is presented as average ± SEM of three independent replicates. **(H)** Polysome traces from logarithmically growing strains with or without 250μM AdoMet under unstressed or azide treated conditions.
Scale bars in **(A)** and **(E)** are 5μm, * indicates P<0.05.

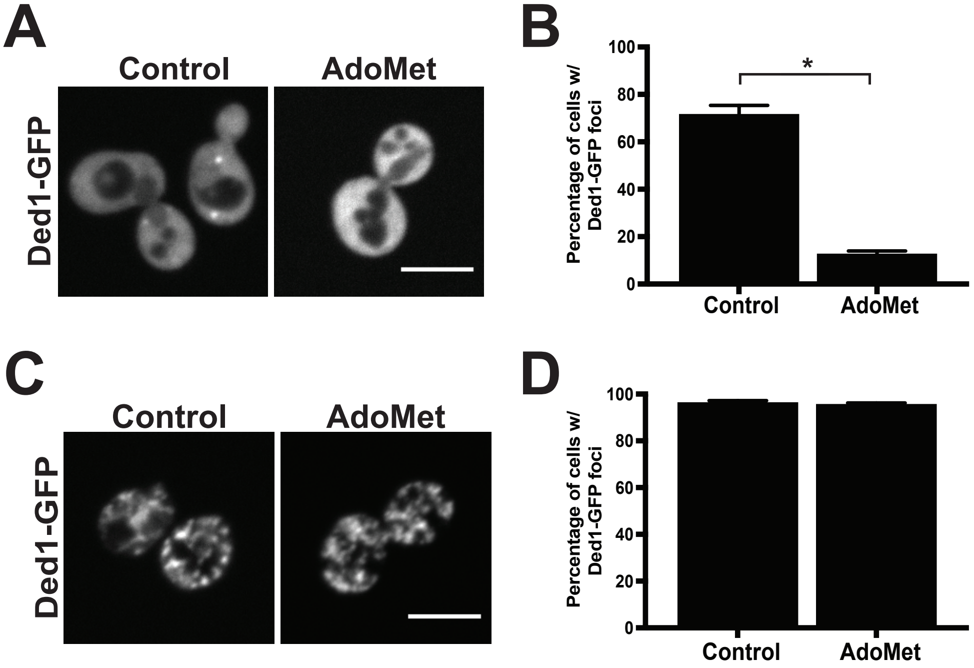

Figure 3.9. AdoMet-mediated stress granule suppression is specific to azide and glucose deprivation, but not heat shock

(A) Representative fluorescent images of logarithmically growing with (AdoMet) or without (Control) 250µM AdoMet strains expressing Ded1-GFP upon glucose deprivation. **(B)** Quantification of cells with foci from Figure 3.9A. Data is presented as average ± SEM of three independent replicates. **(C)** Representative fluorescent images of logarithmically growing with (AdoMet) or without (Control) 250µM AdoMet strains expressing Ded1-GFP upon heat shock. **(D)** Quantification of cells with foci from Figure 3.9C. Data is presented as average ± SEM of three independent replicates. Scale bars in **(A)** and **(C)** are 5µM, * indicates $P<0.05$.

AdoMet plays a role in regulating SG assembly downstream of the inhibition of translation. Together these results argue that AdoMet has two distinct effects on yeast SGs: an acute effect that suppresses SG formation and a late growth stage effect that alters the expression of Ded1 and the recruitment of a subset of SG proteins.

AdoMet affects SG fusion in cultured mammalian cells

While AdoMet is an abundant, conserved metabolite, the assembly pathway for SGs differs between yeast and mammalian cells. Yeast SGs assemble via accretion/enlargement of an initial nucleation event (Wheeler et al., 2016). In contrast, mammalian SGs form via the fusion of many small SGs (Ivanov et al., 2003). This difference in dynamics suggested that the regulation of SG assembly by AdoMet might be specific to yeast. In order to test this possibility, we focused on the effects of AdoMet on SGs that form in response to acute stress as opposed to chronic stress due to the lack of a stationary phase-like stress in mammalian cells that could induce SGs. Pretreatment of HeLa cells with 4mM AdoMet prior to oxidative stress with 500μM sodium arsenite caused an increase in the number of small SGs (+AdoMet) compared to cells without pretreatment (-AdoMet) (Figure 3.10A-C). AdoMet treatment had no effect on the expression level of either G3BP1 or DDX3 arguing that the changes we observe are not secondary to global changes in the levels of SG components (Figure 3.10D).

Since the composition of mammalian SGs varies depending on the type of stress and the cell type, we next explored whether AdoMet affected the dynamics of SGs that form in response to proteotoxic stress (MG132) or translational stress (RocA, rocaglamide). Interestingly, pre-treatment of HeLa cells with AdoMet also caused an increase in SG number and a decrease in SG size for both proteotoxic and translational stress (Figure 3.10E-J). This argued that, in HeLa cells, AdoMet treatment disrupts a step in SG formation that is independent of the stress that

Figure 3.10. AdoMet supplementation regulates stress granule assembly in HeLa cells
(A) Representative immunofluorescence images stained for DDX3 and G3BP1 of HeLa cells under unstressed and 500µM $NaAsO_2$-treated conditions. HeLa cells were treated with or without 4mM AdoMet for 3 hours prior to addition of $NaAsO_2$ for 1 hour. **(B)** Boxplot displaying the number of stress granules/cell from Figure 3.10A. Plotted values are a compilation of three independent experiments. **(C)** Boxplot displaying quantification of the average stress granule size from Figure 3.10A. Plotted values are a compilation of three independent experiments. **(D)** Western blot analysis from HeLa cell lysates of AdoMet-treated and AdoMet-untreated cells. Values represent normalized protein levels of AdoMet-treated to untreated samples. **(E)** Representative immunofluorescence images stained for DDX3 and G3BP1 of HeLa cells under 100µM MG132-treated conditions. HeLa cells were treated with or without 4mM AdoMet for 3 hours prior to addition of MG132 for 2 hours. **(F)** Boxplot displaying the number of stress granules/cell from Figure 3.10E. Plotted values are a compilation of three independent experiments. **(G)** Boxplot displaying the average stress granule size from Figure 3.10E. Plotted values are a compilation of three independent experiments. **(H)** Representative immunofluorescence images stained for DDX3 and G3BP1 of HeLa cells under 2µM RocA-treated conditions. HeLa cells were treated with or without 4mM AdoMet for 3 hours prior to addition of RocA for 2 hours. **(I)** Boxplot displaying the number of stress granules/cell from Figure 3.10H. **(J)** Boxplot displaying the average stress granule size from Figure 3.10H. Scale bars in **(A)**, **(E)**, and **(H)** are 10µm, * indicates $P<0.05$.

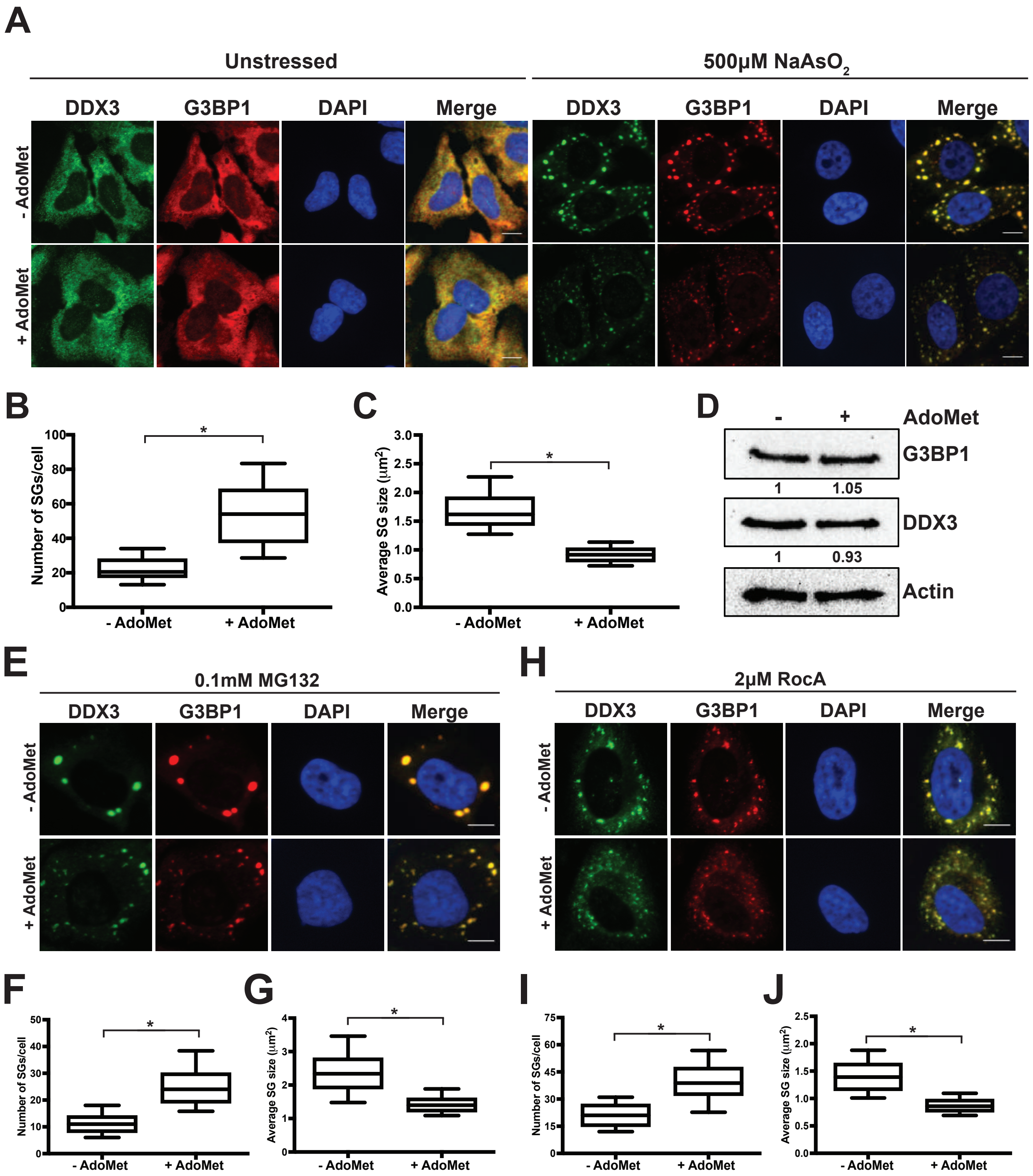
A
Unstressed
500μM NaAsO2
DDX3
G3BP1
DAPI
Merge
- AdoMet
+ AdoMet
B
Number of SGs/cell
0
20
40
60
80
100
*
- AdoMet
+ AdoMet
C
Average SG size (μm2)
0.0
0.5
1.0
1.5
2.0
2.5
3.0
*
- AdoMet
+ AdoMet
D
-
+
AdoMet
G3BP1
1
1.05
DDX3
1
0.93
Actin
E
0.1mM MG132
DDX3
G3BP1
DAPI
Merge
- AdoMet
+ AdoMet
H
2μM RocA
DDX3
G3BP1
DAPI
Merge
- AdoMet
+ AdoMet
F
Number of SGs/cell
0
10
20
30
40
50
*
- AdoMet
+ AdoMet
G
Average SG size (μm2)
0
1
2
3
4
*
- AdoMet
+ AdoMet
I
Number of SGs/cell
0
15
30
45
60
75
*
- AdoMet
+ AdoMet
J
Average SG size (μm2)
0.0
0.5
1.0
1.5
2.0
2.5
*
- AdoMet
+ AdoMet

initiates SG formation. Further, we tested whether AdoMet's effect was cell-type specific. AdoMet treatment on U2OS cells yielded similar effects to HeLa cells on arsenite-induced SGs (Figure 3.11A-C). Surprisingly, pretreatment with AdoMet suppressed the formation of SGs in response to RocA in U2OS cells (Figure 3.11D-F). These results argue that cell type differences might modulate both SG formation and the response to AdoMet.

With the majority of stresses on AdoMet treated cells producing many small SGs, these results suggested that AdoMet treatment might be disrupting the fusion step in SG formation. If this were the case, the number and size of SGs would be relatively constant throughout the duration of the stress for AdoMet pretreated cells while the number of SGs would fall and their size would increase due to SG fusion in untreated cells. As predicted, the number of SGs decreased in untreated cells over the course of one hour after arsenite treatment while the number of SG in AdoMet treated cells remained largely constant (Figure 3.12A). Similarly, we observed that the average size of SGs increased one hour after arsenite treatment while the average size of SGs in AdoMet-treated cells remained largely constant (Figure 3.12B). Consistent with this, AdoMet treatment does not affect the extent of eIF2a phosphorylation after arsenite treatment, arguing that AdoMet is not buffering oxidative stress or disrupting the earliest steps in SG formation (Figure 3.12C-D).

Since SG fusion is microtubule dependent (Ivanov et al., 2003), we also examined whether the effect of AdoMet was dependent on the microtubule cytoskeleton (Ivanov et al., 2003). AdoMet treatment does not cause an obvious defect in microtubule organization in HeLa cells (Figure 3.12E). Additionally, AdoMet treatment caused a decrease in SG size and an increase in the number of SGs even in cells that were treated with the microtubule depolymerizing drug, Nocodazole (Figure 3.12E-F). SG formation and recruitment of specific

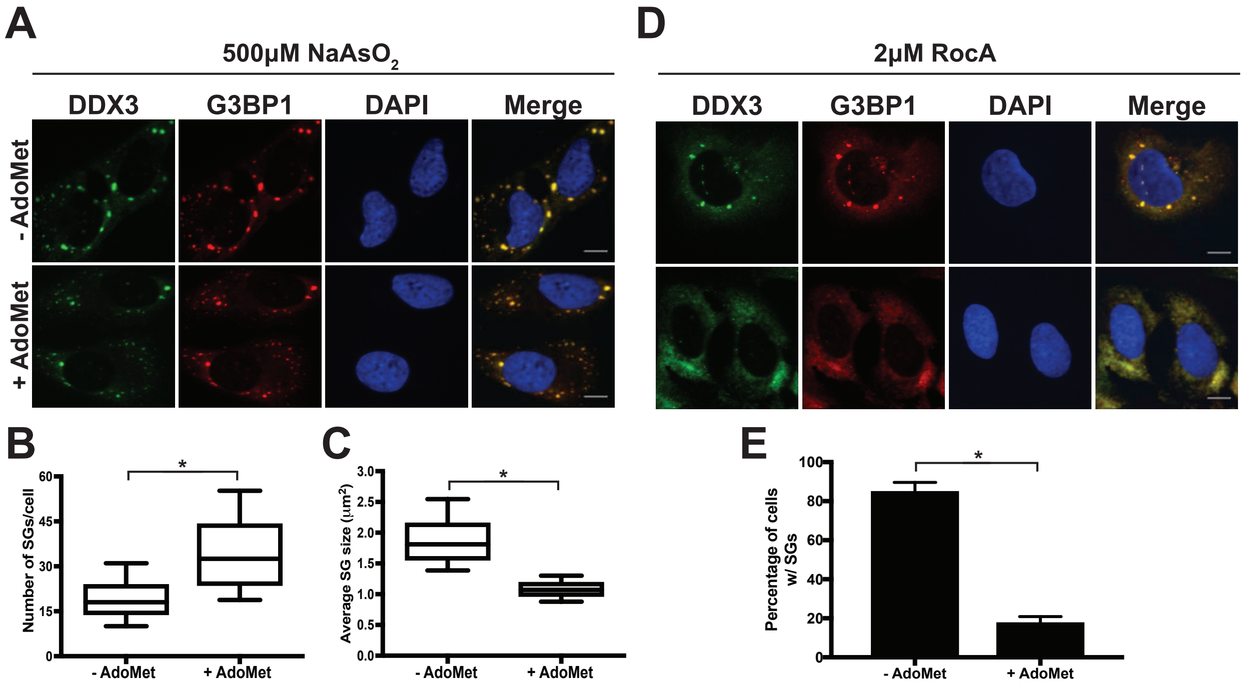

Figure 3.11. Stress granule assembly is disrupted in AdoMet-treated U2OS cells
(A) Representative immunofluorescence images stained for DDX3 and G3BP1 in U2OS cells under 500μM NaAsO$_2$-treated conditions. U2OS cells were treated with or without 4mM AdoMet for 3 hours prior to addition of NaAsO$_2$ for 1 hour. **(B)** Boxplot displaying the number of stress granules/cell from Figure 3.11A. Plotted values are a compilation of three independent experiments. **(C)** Boxplot displaying quantification of the average stress granule size from Figure 3.11A. Plotted values are a compilation of three independent experiments. **(D)** Representative immunofluorescence images stained for DDX3 and G3BP1 in U2OS cells under 2μM RocA-treated conditions. U2OS cells were treated with or without 4mM AdoMet for 3 hours prior to addition of RocA for 2 hours. **(E)** Quantification of cells containing stress granules from Figure 3.11D. Data is presented as average ± SEM of three independent replicates. Scale bars in **(A)** and **(D)** are 10μM, * indicates $P<0.05$.

Figure 3.12. Stress granules are unable to properly fuse in AdoMet-treated HeLa cells
(A) Boxplots depicting the number of stress granules/cell at the indicated time points after addition of 500µM $NaAsO_2$ from AdoMet-treated (+ AdoMet) and AdoMet-untreated (-AdoMet) HeLa cells. Plotted values are a compilation of three independent experiments. **(B)** Boxplots depicting the average stress granule size at the indicated time points after addition of 500µM $NaAsO_2$ from AdoMet-treated (+ AdoMet) and AdoMet-untreated (-AdoMet) HeLa cells. Plotted values are a compilation of three independent experiments. **(C)** Western Blot analysis of HeLa cell lysates from the indicated time points after the addition of 500µM $NaAsO_2$ from AdoMet-treated (+ AdoMet) and AdoMet-untreated (-AdoMet) cells. **(D)** Quantification of proteins levels from Figure 3.12C. Data is presented as average ± SEM of three independent replicates. **(E)** Representative immunofluorescence images stained for Tubulin and G3BP1 in HeLa cells under 500µM $NaAsO_2$-treated conditions. HeLa cells were treated with or without 4mM AdoMet for 3 hours and then DMSO or 5µM Nocodazole for two hours prior to addition of $NaAsO_2$. Scale bar: 10µM. **(F)** Boxplot displaying the number of stress granules/cell from Figure 3.12E. Plotted values are a compilation of three independent experiments. **(G)** Boxplot displaying quantification of the average stress granule size from Figure 3.12E. Plotted values are a compilation of three independent experiments. * indicates $P<0.05$.

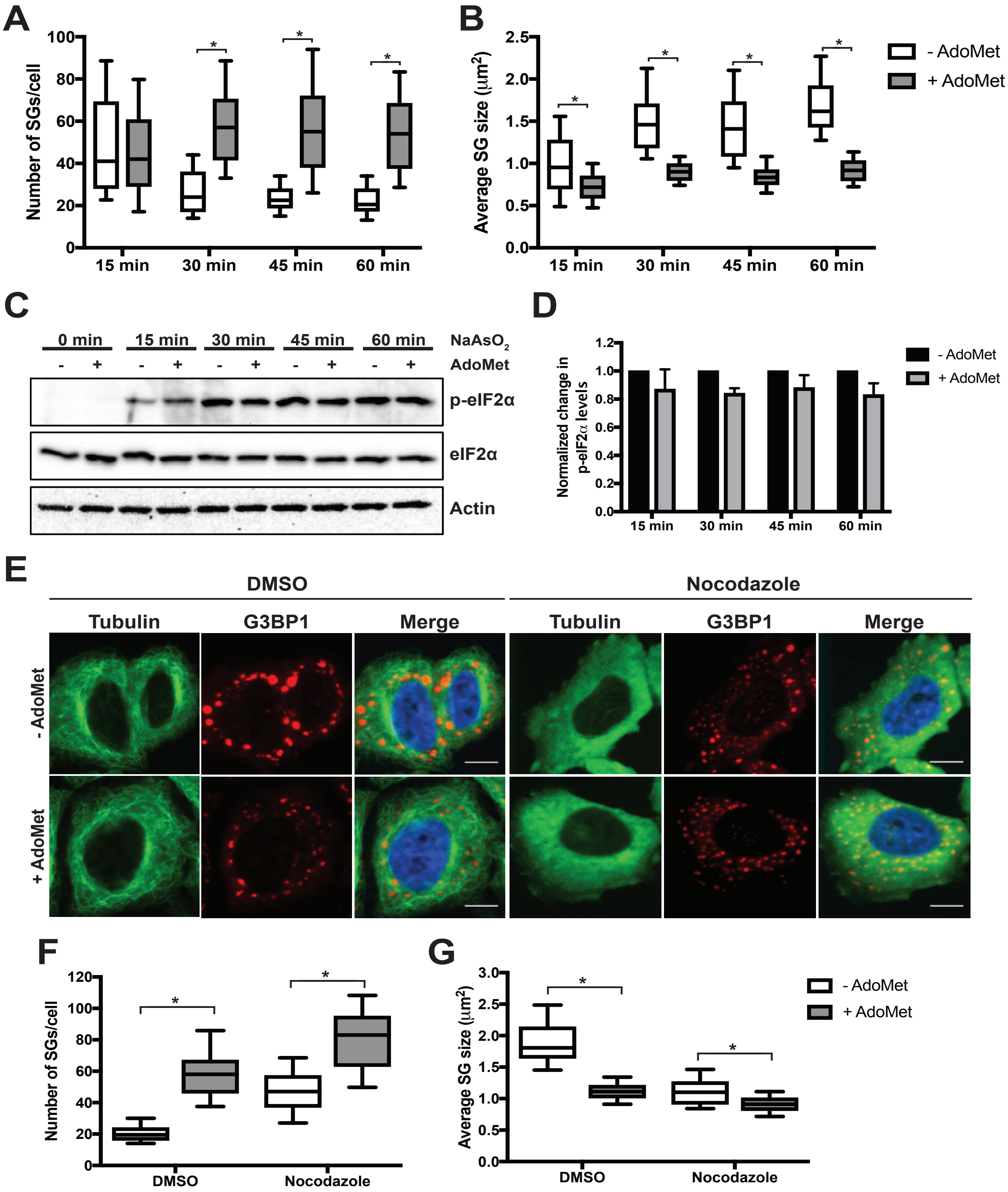
A
Number of SGs/cell
0
20
40
60
80
100
15 min
30 min
45 min
60 min
*
B
Average SG size (μm²)
0.0
0.5
1.0
1.5
2.0
2.5
15 min
30 min
45 min
60 min
- AdoMet
+ AdoMet
C
0 min
15 min
30 min
45 min
60 min
NaAsO₂
AdoMet
- +
p-eIF2α
eIF2α
Actin
D
Normalized change in p-eIF2α levels
0.0
0.2
0.4
0.6
0.8
1.0
1.2
15 min
30 min
45 min
60 min
- AdoMet
+ AdoMet
E
DMSO
Nocodazole
Tubulin
G3BP1
Merge
- AdoMet
+ AdoMet
F
Number of SGs/cell
0
20
40
60
80
100
120
DMSO
Nocodazole
G
Average SG size (μm²)
0.0
0.5
1.0
1.5
2.0
2.5
3.0
DMSO
Nocodazole
- AdoMet
+ AdoMet

SG components is also regulated by arginine methylation within RGG domains. Interestingly, we also found that effects of AdoMet on SG organization still occur in the presence of the methyltransferase inhibitor, AdOx (Figure3.13). Thus, the effects of AdoMet on SGs occur independently of microtubules and the majority of methyltransferases.

AdoMet reduces SG formation in iPSC-derived motor neurons

Since both cell type and stress appeared to modulate the effects of AdoMet, we sought to test the effects of AdoMet on SG formation in cells where misregulation of SGs is linked to disease. Recent genetic studies have identified amyotrophic lateral sclerosis (ALS)-linked mutations in several RNA binding proteins (RBPs) that are either found in or regulate SGs, including TDP-43 and FUS (Kim et al., 2013; Kwiatkowski et al., 2009; Martinez et al., 2016; Sreedharan et al., 2008; Vance et al., 2009). These mutations often alter the propensity for the proteins to phase separate and provoke protein aggregation (Kato et al., 2012; Kim et al., 2013; Ling et al., 2013; Murakami et al., 2015; Patel et al., 2015; Ryan et al., 2018). Neurons that contain these mutated RBPs and are continuously exposed to a lifetime of stress are thought to accumulate insoluble, pathological inclusions that contain many SG proteins. To test the effect of AdoMet on SG dynamics in ALS-associated motor neurons, we differentiated motor neurons using our previously established protocol (Martinez et al., 2016) from iPSC lines derived from patients with ALS-associated mutations in either TDP-43 (N352S) or FUS (R521G). The effects of AdoMet on arsenite- and puromycin-induced SGs were then examined, compared to control motor neurons from iPSC lines derived by a genetically related, but unaffected family member and an unrelated healthy individual. AdoMet treatment reduced both the number of SG/cell as well as the total SG area/cell in both stresses (Figure 3.14A-D). Thus, AdoMet disrupts SG formation in motor neurons and the effect is independent of the stress, unlike HeLa and U2OS

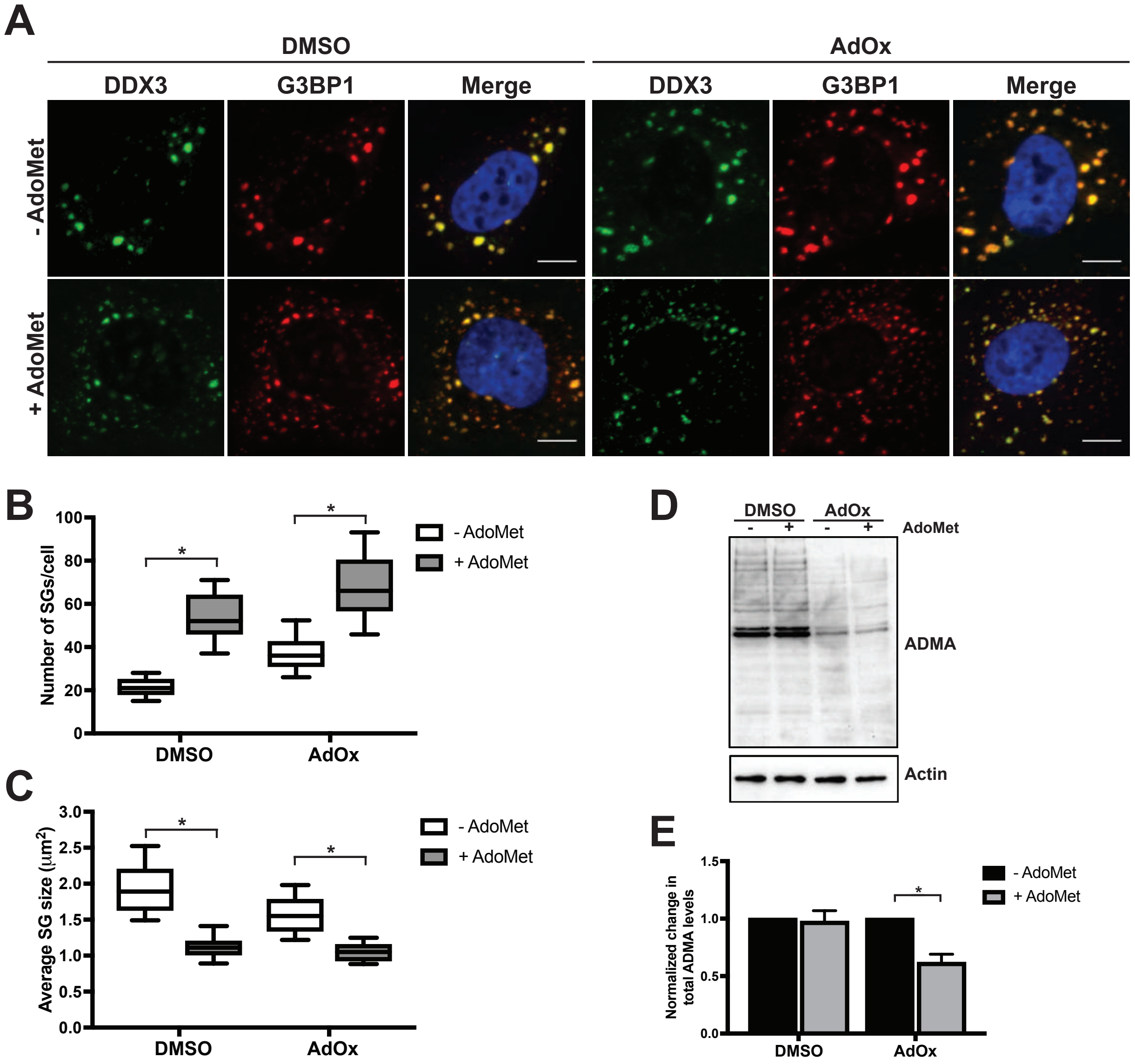

Figure 3.13. AdoMet's effect on stress granule is not linked to protein methylation
(A) Representative immunofluorescence images stained for DDX3 and G3BP1 in HeLa cells under 500μM NaAsO$_2$-treated conditions. HeLa cells were treated with DMSO or 20μM AdOx for 48 hours followed by the addition of 4mM AdoMet for 3 hours before arsenite stress. Scale bar: 10μM. **(B)** Boxplot displaying the number of stress granules/cell from Figure 3.13A. Plotted values are a compilation of three independent experiments. **(C)** Boxplot displaying quantification of the average stress granule size from Figure 3.13A. Plotted values are a compilation of three independent experiments. **(D)** Western blot analysis from HeLa cell lysates that were treated with DMSO or 20μM AdOx followed by addition of 4mM AdoMet. **(E)** Quantification of total ADMA levels from Figure 3.13D. Data is presented as average ± SEM of three independent replicates. * indicates P<0.05.

Figure 3.14. AdoMet reduces stress granule formation in iPSC-derived motor neurons and reduce TDP-43 accumulation in stress granules

(A) Representative immunofluorescence images of control iPSC-derived motor neuron (MN) lines and ALS-associated TDP-43 N352S and FUS R521G mutant iPSC-derived motor neuron lines stained for TDP-43 and G3BP1 exposed to 250μM $NaAsO_2$. Motor neurons were pretreated with or without 4mM AdoMet for 3 hours prior to addition of sodium arsenite. **(B)** Boxplots displaying quantification of the number of stress granules/cell and total stress granule area from Figure 3.14A. Plotted values are a compilation of three independent experiments. **(C)** Representative immunofluorescence images of control iPSC-derived motor neuron (MN) lines and ALS-associated TDP-43 N352S and FUS R521G mutant iPSC-derived motor neuron lines stained for TDP-43 and G3BP1 exposed to 5μg/ml puromycin. Motor neurons were pretreated with or without 4mM AdoMet for 3 hours prior to addition of puromycin. **(D)** Boxplots displaying quantification of the number of stress granules/cell and total stress granule area from Figure 3.14C. Plotted values are a compilation of three independent experiments. **(E)** Representative immunofluorescence images of wildtype iPSC-derived motor neuron lines stained for Ataxin 2, G3BP1, and TDP-43 exposed to 5μg/ml puromycin. Motor neurons were pretreated with or without 4mM AdoMet for 3 hours prior to addition of puromycin. Scale bars in **(A)**, **(C)**, and **(E)** are 10μM. * indicates $P<0.05$.

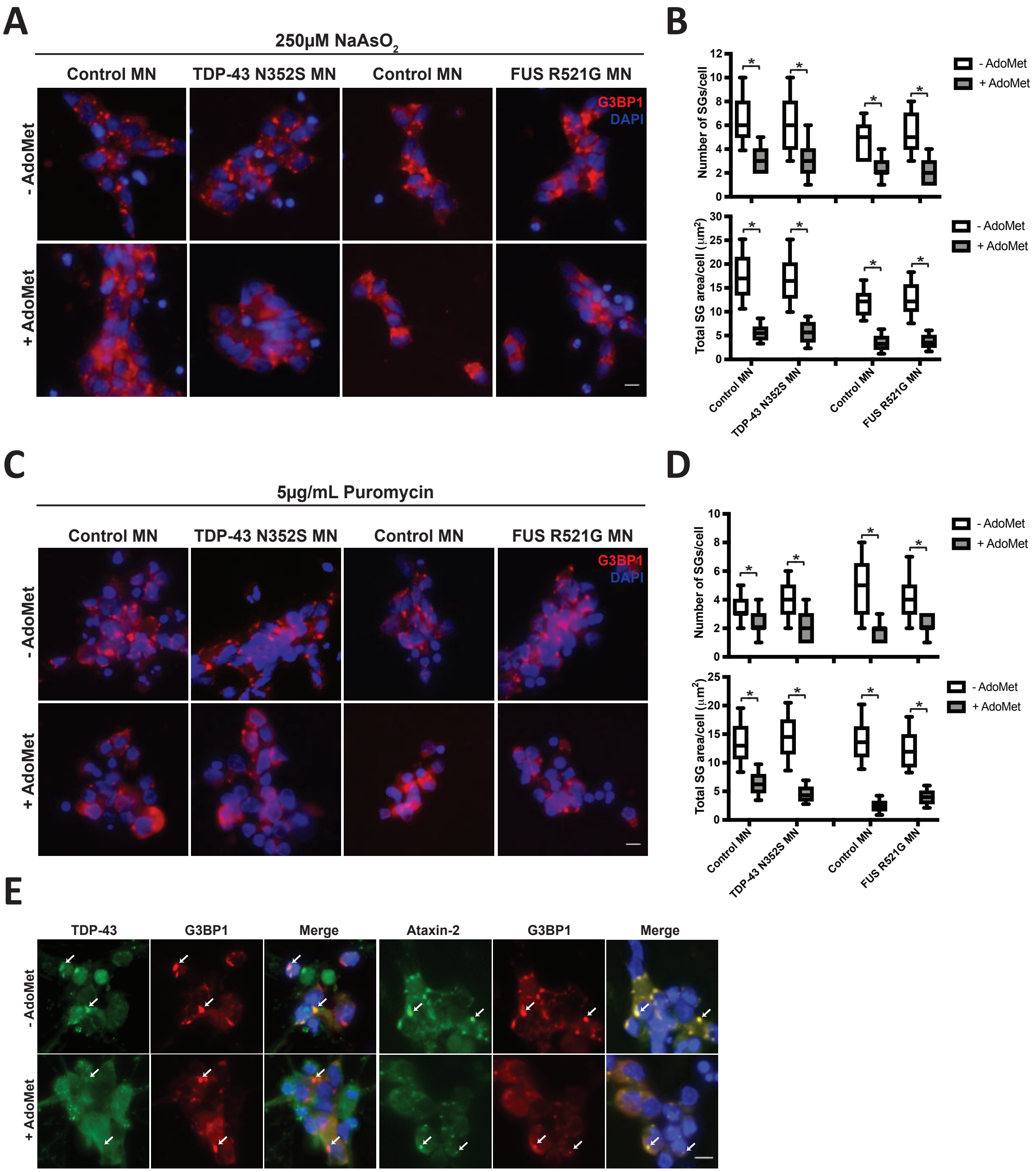
A
250μM NaAsO2
Control MN
TDP-43 N352S MN
Control MN
FUS R521G MN
G3BP1
DAPI
- AdoMet
+ AdoMet
B
Number of SGs/cell
Total SG area/cell (μm2)
- AdoMet
+ AdoMet
*
Control MN
TDP-43 N352S MN
Control MN
FUS R521G MN
C
5μg/mL Puromycin
Control MN
TDP-43 N352S MN
Control MN
FUS R521G MN
G3BP1
DAPI
- AdoMet
+ AdoMet
D
Number of SGs/cell
Total SG area/cell (μm2)
- AdoMet
+ AdoMet
*
Control MN
TDP-43 N352S MN
Control MN
FUS R521G MN
E
TDP-43
G3BP1
Merge
Ataxin-2
G3BP1
Merge
- AdoMet
+ AdoMet

cells.

A hallmark of ALS includes the mislocalization of nuclear TDP-43 to cytoplasmic inclusions in spinal motor neurons of ALS patients (Bentmann et al., 2012; Blokhuis et al., 2013; Farg et al., 2013; Keller et al., 2012; Kim et al., 2013; Liu-Yesucevitz et al., 2010). As a result, we next examined if AdoMet treatment affected TDP-43 recruitment to SGs in addition to decreasing the number of SGs that form. Interestingly, the SGs that form in response to puromycin fail to recruit TDP-43 when the iPSC-derived motor neurons are pre-treated with AdoMet. This effect was specific to TDP-43 as recruitment of Ataxin-2 to SGs was unaffected in AdoMet-pretreated iPSC-derived motor neurons (Figure 3.14E). Thus, in addition to decreasing SG formation, AdoMet treatment also decreases the recruitment of TDP-43 to SGs that form in response to stress.

Discussion

SGs are believed to play a critical role in modulating gene expression programs in response to environmental and nutrient stresses. However, it has been unclear how changes in cellular activity regulate stress granule formation and composition. Our finding that Sam1 is recruited to yeast stress granules in response to a specific nutrient stress and that the product of Sam1, AdoMet, regulates stress granule formation in both yeast and human cells suggests that the connections between metabolism and SG assembly might be broader than previously believed.

Stress specific recruitment of metabolic enzymes to SGs

Recent work on the SG proteome suggests that SG composition can vary depending on the cell type and the nature of the stress (Markmiller et al., 2018). Since many of the stresses that trigger SG assembly are thought to alter metabolic activity, either directly or indirectly, one might expect metabolic enzymes to be a common component of SGs. However, few metabolic enzymes have been identified in proteomic and targeted studies of *S. cerevisiae* SGs (Jain et al., 2016; Markmiller et al., 2018; Saad et al., 2017). Our identification of 17 metabolic enzymes that are recruited to SGs in response to physiological nutrient stresses, but are not recruited to SGs in response to multiple acute stresses argues that SG composition is tailored to the nature of the stress and that chronic stresses might require reorganization of the metabolic network.

This result also helps to explain why no metabolic enzymes have been identified in previous proteomic studies of mammalian SGs. All of the stresses that are traditionally used to induce mammalian stress granule, such as sodium azide, do not trigger the recruitment of metabolic enzymes to yeast SGs. Thus, one might expect to only observe metabolic enzymes in SG that assemble in response to the mammalian equivalent of a stationary phase nutrient stress.

Future studies directed at defining physiological nutrient stresses that induce SGs in mammalian cells would likely expand the connections between the SG proteome and metabolism.

Given that the recruitment of metabolic enzymes to SGs in yeast is stress specific, one might expect that additional targeting mechanisms might be used for this class of proteins. Consistent with this, the metabolic enzymes recruited to SGs are not enriched in either IDR or LCS sequences relative to metabolic enzymes that are not targeted to SGs. Furthermore, the majority of the SG associated metabolic enzymes do not possess a predicted RNA binding domain and have not been identified in high throughput screens as RNA binding proteins. Thus, it is likely that neither the presence of IDR or LCS sequences is sufficient to target these metabolic enzymes to SGs and that the recruitment mechanism likely to involve additional stress-specific interaction domains.

Biphasic AdoMet regulation of yeast SG assembly

The stress specific recruitment of metabolic enzymes suggested a novel route to identify metabolic pathways that might play a role in regulating SG assembly. Our focus on the product of Sam1, AdoMet, has uncovered unexpected parallels between how metabolites regulate metabolism and SG formation/composition. Metabolite regulation of metabolic pathway activity is biphasic. Critical metabolites can directly regulate enzyme activity over short time scales, but they also cause changes in the expression profile of a pathway when the metabolite is present or absent for long periods of time. Interestingly, we observe a similar two-phase regulation of SG formation and composition by AdoMet.

Brief treatments of log phase yeast with AdoMet were able to block SG formation in response to acute stresses without affecting expression levels of SG proteins. In contrast, genetic manipulations that caused sustained alterations in AdoMet levels affected the expression of the stress granule nucleator, Ded1. For instance, mutations in SAM1 that decrease AdoMet production increase Ded1 protein levels. Since overexpression of Ded1 is known to trigger SG assembly, the increase in SG formation when AdoMet levels fall is likely due to its effect on Ded1 expression. Conversely, the deletion of *ADO1* in diauxic phase cultures causes an increase in AdoMet levels and a reduction in both Ded1 protein levels and its localization to SGs. Interestingly, this effect on Ded1 expression was post-transcriptional since *ado1Δ* strains had elevated DED1 transcript levels even though the levels of Ded1 protein were decreased. Furthermore, aspects of this control loop might be conserved from yeast to humans since protein levels of human ortholog of Ded1, DDX3, have also been shown to be sensitive to AdoMet levels in Huh7 cells (Schroder et al., 2012).

These changes in SG composition in response to sustained elevation of AdoMet are not limited to Ded1. SGs in *ado1Δ* strain SGs also lacked other 5' UTR mRNA-associated proteins including eIF4G1 and eIF4E, while SG proteins associated with the 3' UTR of mRNA (ie Pab1, Pbp1, and Pub1) where unaffected. Additionally, SGs in *ado1Δ* strains were defective in recruiting Sam1 and Ade17. However, none these recruitment defects were due to a decrease in protein expression. Thus, sustained increases in AdoMet levels can selectively block recruitment of a subset of SG components in addition to downregulating Ded1. Together these results argue that AdoMet acts at short time scales to suppress stress granule formation, while chronic increases in AdoMet modify the SG proteome by affecting both the expression and recruitment of SG components. Recent work has also identified acetyl-CoA as a candidate small molecule regulator of SGs; however, its mechanism of action is unclear (Rollins et al., 2017). Future studies of how acetyl-CoA regulates SG assembly at short and long time scales will help determine if biphasic regulation is a common feature of metabolite regulation of yeast SG formation.

While the molecular targets of AdoMet at either time scale are unclear, our initial characterization suggests that it does not act via protein methylation. Deletion of the Ded1 methyltransferase, HMT1, did not block the effect of elevated AdoMet levels. Similarly, treatment of mammalian cells with the broad-spectrum methyltransferase inhibitor, AdOx, did not block the effect of AdoMet on SGs. These experiments raise the possibility that AdoMet might disrupt SG formation by altering RNA methylation. While mRNAs with m^6A modifications are recruited into SGs (Anders et al., 2018; Wang et al., 2015), it remains to be determined if the levels of mRNA methylation can alter the dynamics of SG formation.

Conservation of AdoMet-mediated SG regulation in mammalian cells

While yeast and mammalian SGs share a significant overlap in their proteome, not all aspects of composition and regulation are conserved. For instance, mammalian SGs mature by the fusion of small SGs into larger SGs, while fusion-based maturation has not been observed in yeast (Ivanov et al., 2003; Wheeler et al., 2016). Despite these differences, yeast and mammalian SGs are both regulated by AdoMet. Treatment of either yeast or iPSC-derived motor neurons with AdoMet suppressed arsenite-induced SG formation in both cell types arguing that AdoMet is a conserved small molecule regulator of SGs.

Interestingly, while the acute effects of AdoMet on yeast and iPSC-derived motor neurons are comparable, AdoMet treatment had distinct effects on SG formation in cancer derived cell lines. Treatment of HeLa cells with AdoMet prior to oxidative, proteotoxic, and translational stress resulted in SGs that were greater in number and smaller in size. This suggests that AdoMet treatment disrupts SG fusion in cancer derived cell lines rather than blocking SG formation. Furthermore, this effect is microtubule-independent arguing that AdoMet treatment is disrupting a novel step in the SG fusion process. One possible reason that AdoMet treatment causes disrupts different steps in SG formation in HeLa cells as compared to iPSC-derived motor neurons is that cancer cell lines and non-dividing primary cells have distinct metabolic profiles. Future studies examining how basal cell metabolism alters AdoMet's effects on SG formation will likely provide new insights into what makes particular cells sensitive or resistant to stress.

Most provocatively, AdoMet treatment suppressed SG formation in iPSC-derived motor neurons that expressed mutated forms of TDP-43 and FUS found in ALS patients. AdoMet was effective in blocking SG assembly in these disease models even though these mutated forms of TDP-43 and FUS have an increased propensity to phase separate (Ling et al., 2013; Mackenzie et al., 2017; Murakami et al., 2015; Patel et al., 2015). Thus, aberrant, pathogenic SGs are just as sensitive to AdoMet treatment as normal SGs. This argues that AdoMet acts at a step in SG formation that is common to both the conventional SG assembly pathway and the pathways used by aggregation prone variants of TDP-43 and FUS. Furthermore, the few SGs that form in mutant motor neurons pre-treated with AdoMet fail to recruit TDP-43. Thus, the ability of AdoMet to suppress the formation of pathological SGs argues that pathways that control either AdoMet levels or the SG response to AdoMet presents an exciting and tractable therapeutic approach for ALS and other neurodegenerative diseases.

Materials and Methods

Experimental Model and Subject Details

All yeast experiments were carried out in *Saccharomyces cerevisiae* budding yeast in the BY4741 background. All yeast strains were grown at 30°C unless otherwise indicated in either YPD medium (1% yeast extract, 2% peptone, 2% dextrose) or synthetic defined medium (0.17% yeast nitrogen base without ammonium sulfate or amino acids, 0.5% ammonium sulfate, amino acids, 2% glucose).

The HeLa-S3 cell line is derived from human female cervical adenocarcinoma tissue and the U2OS cell line is derived from human female osteosarcoma tissue. Both HeLa and U2OS cell lines were maintained in DMEM (Gibco), 10% fetal bovine serum (Corning), and 1% penicillin/streptomycin (Gibco) at 37°C and 5%CO_2 in a humidified incubator.

Adult human primary fibroblasts carrying TARDBP (N352S) mutation and a control individual were obtained by Dr. John Ravits (University of California, San Diego). Primary fibroblasts were cultured in DMEM supplemented with 10% fetal bovine serum, NEAA, and l-glutamine at 37°C and 5%CO_2 in a humidified incubator. To generate iPSCs, fibroblasts were transduced with Cytotune iPS Sendai Reprogramming Kit, according to manufacturer's protocol (Invitrogen). Human iPSC line carrying ALS-associated FUS (R521G) mutation was previously reprogrammed from primary fibroblast obtained by Franca Cambia, Edward Kasarskis, and Haining Zhu (University of Kentucky), as described (Kapeli et al., 2016). All iPSCs were maintained on Matrigel-coated plates (BD Biosciences) in mTeSR1 growth media (Stem Cell Technologies) at 37°C and 5% CO_2 in a humidified incubator. Colonies were expanded by clump-passaging using enzyme-free dissociation buffer (EDTA). Informed consent was obtained from all individuals prior to sample collection. The use of patient fibroblast for research was approved by the University of California, San Diego Institutional Review Board.

Plasmids and Strains

Plasmids from this work were generated by standard molecular biology techniques and verified by sequencing (Eton Bioscience).

A complete list of strains used in this study is listed in Table 3.4. All yeast strains were derived from a parent strain with the genotype MATa his3Δ1 leu2Δ0 met15Δ0 ura3Δ0 (BY4741). Generation of endogenous GFP-tagged strains and gene disruption was created using standard PCR-mediated techniques. Strains from the GFP collection were used as background strains for the production of dual-fluorescent tagged strains used in RNA granule screen. For all other experiments, newly made strains were generated using BY4741 (Dharmacon) as the parental strain.

Ded1-GFP and Sam1-GFP variants were introduced into their respective endogenous loci by PCR amplifying cassettes that contained the coding sequence of Ded1-GFP or Sam1-GFP, a kanamycin resistance marker, and a 50bp sequence homologous to downstream of their respective stop codons. These cassettes were introduced into yeast using standard yeast transformation protocols. Genomic DNA was extracted from resulting transformants and the loci were PCR amplified and sequenced to verify the presence of the correct mutation.

Preparation of Samples for Yeast Microscopy

For acquiring images from RNA granule screen, cells were grown in YPD at 30°C for 1 day and 5 days and fixed prior to imaging. Briefly, 0.1mL 37% formaldehyde

Table 3.4. List of yeast strains used in this study

Name	Genetic background	Reference
BY4741	MATa his3Δ1 leu2Δ0 met15Δ0 ura3Δ0	Dharmacon
Ade17-GFP, Ded1-mCherry	BY4741, ADE17-GFP::HIS, DED1-mCherry::HphNT1	This study
Ade17-GFP, Edc3-mCherry	BY4741, ADE17-GFP::HIS, EDC3-mCherry::HphNT1	This study
Cdc19-GFP, Ded1-mCherry	BY4741, CDC19-GFP::HIS, DED1-mCherry::HphNT1	This study
Cdc19-GFP, Edc3-mCherry	BY4741, CDC19-GFP::HIS, EDC3-mCherry::HphNT1	This study
Cys4-GFP, Ded1-mCherry	BY4741, CYS4-GFP::HIS, DED1-mCherry::HphNT1	This study
Cys4-GFP, Edc3-mCherry	BY4741, CYS4-GFP::HIS, EDC3-mCherry::HphNT1	This study
Gly1-GFP, Ded1-mCherry	BY4741, GLY1-GFP::HIS, DED1-mCherry::HphNT1	This study
Gly1-GFP, Edc3-mCherry	BY4741, GLY1-GFP::HIS, EDC3-mCherry::HphNT1	This study
Pro3-GFP, Ded1-mCherry	BY4741, PRO3-GFP::HIS, DED1-mCherry::HphNT1	This study
Pro3-GFP, Edc3-mCherry	BY4741, PRO3-GFP::HIS, EDC3-mCherry::HphNT1	This study
Sam1-GFP, Ded1-mCherry	BY4741, SAM1-GFP::HIS, DED1-mCherry::HphNT1	This study
Sam1-GFP, Edc3-mCherry	BY4741, SAM1-GFP::HIS, EDC3-mCherry::HphNT1	This study
Trr1-GFP, Ded1-mCherry	BY4741, TRR1-GFP::HIS, DED1-mCherry::HphNT1	This study
Trr1-GFP, Edc3-mCherry	BY4741, TRR1-GFP::HIS, EDC3-mCherry::HphNT1	This study
Sam1-GFP WT, Sam2-mCherry	BY4741, SAM1-GFP (WT)::KanMX6, SAM2-mCherry::HphNT1	This study
Sam1-GFP C91Y, Sam2-mCherry	BY4741, SAM1-GFP (C91Y)::KanMX6, SAM2-mCherry::HphNT1	This study
Sam1-GFP D121N, Sam2-mCherry	BY4741, SAM1-GFP (D121N)::KanMX6, SAM2-mCherry::HphNT1	This study
Sam1-GFP K252M, Sam2-mCherry	BY4741, SAM1-GFP (K252M)::KanMX6, SAM2-mCherry::HphNT1	This study
Sam1-GFP WT, Ade17-mCherry	BY4741, SAM1-GFP (WT)::KanMX6, ADE17-mCherry::HphNT1	This study
Sam1-GFP C91Y, Ade17-mCherry	BY4741, SAM1-GFP (C91Y)::KanMX6, ADE17-mCherry::HphNT1	This study
Sam1-GFP D121N, Ade17-mCherry	BY4741, SAM1-GFP (D121N)::KanMX6, ADE17-mCherry::HphNT1	This study
Sam1-GFP K252M, Ade17-mCherry	BY4741, SAM1-GFP (K252M)::KanMX6, ADE17-mCherry::HphNT1	This study
Sam1-GFP WT, Ded1-mCherry	BY4741, SAM1-GFP (WT)::KanMX6, DED1-mCherry::HphNT1	This study
Sam1-GFP C91Y, Ded1-mCherry	BY4741, SAM1-GFP (C91Y)::KanMX6, DED1-mCherry::HphNT1	This study

Table 3.4. List of yeast strains used in this study (continued)

Sam1-GFP D121N, Ded1-mCherry	BY4741, SAM1-GFP (D121N)::KanMX6, DED1-mCherry::HphNT1	This study
Sam1-GFP K252M, Ded1-mCherry	BY4741, SAM1-GFP (K252M)::KanMX6, DED1-mCherry::HphNT1	This study
Sam1-GFP WT, Pbp1-mRuby2	BY4741, SAM1-GFP (WT)::KanMX6, PBP1-mRuby2::NatMX6	This study
Sam1-GFP C91Y, Pbp1-mRuby2	BY4741, SAM1-GFP (C91Y)::KanMX6, PBP1-mRuby2::NatMX6	This study
Sam1-GFP D121N, Pbp1-mRuby2	BY4741, SAM1-GFP (D121N)::KanMX6, PBP1-mRuby2::NatMX6	This study
Sam1-GFP K252M, Pbp1-mRuby2	BY4741, SAM1-GFP (K252M)::KanMX6, PBP1-mRuby2::NatMX6	This study
Ade17-GFP	BY4741, ADE17-GFP::HphNT1	This study
Cdc19-GFP	BY4741, CDC19-GFP::HphNT1	This study
Cys4-GFP	BY4741, CYS4-GFP::HphNT1	This study
Ded1-GFP	BY4741, DED1-GFP::HphNT1	This study
Dcp2-GFP	BY4741, DCP2-GFP::HphNT1	This study
Edc3-GFP	BY4741, EDC3-GFP::HphNT1	This study
eIF4G1-GFP	BY4741, EIF4G1-GFP::HphNT1	This study
eIF4E-GFP	BY4741, EIF4E-GFP::HphNT1	This study
Pab1-GFP	BY4741, PAB1-GFP::HphNT1	This study
Pub1-GFP	BY4741, PUB1-GFP::HphNT1	This study
Pbp1-GFP	BY4741, PBP1-GFP::HphNT1	This study
Sam1-GFP	BY4741, SAM1-GFP::HphNT1	This study
Ade17-GFP, ado1Δ	BY4741, ADE17-GFP::HphNT1, ado1Δ::NatMX6	This study
Cdc19-GFP, ado1Δ	BY4741, CDC19-GFP::HphNT1, ado1Δ::NatMX6	This study
Cys4-GFP, ado1Δ	BY4741, CYS4-GFP::HphNT1, ado1Δ::NatMX6	This study
Ded1-GFP, ado1Δ	BY4741, DED1-GFP::HphNT1, ado1Δ::NatMX6	This study
Dcp2-GFP, ado1Δ	BY4741, DCP2-GFP::HphNT1, ado1Δ::NatMX6	This study
Edc3-GFP, ado1Δ	BY4741, EDC3-GFP::HphNT1, ado1Δ::NatMX6	This study
eIF4G1-GFP, ado1Δ	BY4741, EIF4G1-GFP::HphNT1, ado1Δ::NatMX6	This study
eIF4E-GFP, ado1Δ	BY4741, EIF4E-GFP::HphNT1, ado1Δ::NatMX6	This study
Pab1-GFP, ado1Δ	BY4741, PAB1-GFP::HphNT1, ado1Δ::NatMX6	This study
Pub1-GFP, ado1Δ	BY4741, PUB1-GFP::HphNT1, ado1Δ::NatMX6	This study
Pbp1-GFP, ado1Δ	BY4741, PBP1-GFP::HphNT1, ado1Δ::NatMX6	This study
Sam1-GFP, ado1Δ	BY4741, SAM1-GFP::HphNT1, ado1Δ::NatMX6	This study
Ded1-GFP, hmt1Δ	BY4741, DED1-GFP::HphNT1, hmt1Δ::KanMX6	This study
Ded1-GFP, hmt1Δ, ado1Δ	BY4741, DED1-GFP::HphNT1, ado1Δ::NatMX6, hmt1Δ::KanMX6	This study
Ded1-GFP	BY4741, DED1-GFP::KanMX6	This study
Ded1-GFP RK4	BY4741, DED1-GFP (R51K, R62K, R87K, R578K)::KanMX6	This study
Ded1-GFP, ado1Δ	BY4741, DED1-GFP::KanMX6, ado1Δ::NatMX6	This study
Ded1-GFP RK4, ado1Δ	BY4741, DED1-GFP (R51K, R62K, R87K, R578K)::KanMX6, ado1Δ::NatMX6	This study
Cdc19-GFP, Pbp1-mRuby2	BY4741, CDC19-GFP::HphNT1, PBP1-mRuby2::NATMX6	This study
Cdc19-GFP, Pbp1-mRuby2, ado1Δ	BY4741, CDC19-GFP::HphNT1, PBP1-mRuby2::NATMX6, ado1Δ::KanMX6	This study
Cys4-GFP, Pbp1-mRuby2	BY4741, CYS4-GFP::HphNT1, PBP1-mRuby2::NATMX6	This study

Table 3.4. List of yeast strains used in this study (continued)

Cys4-GFP, Pbp1-mRuby2, ado1Δ	BY4741, CYS4-GFP::HphNT1, PBP1-mRuby2::NATMX6, ado1Δ::KanMX6	This study

was added to 1mL of culture and rotated for 15 min at RT. Fixed cells were then spun down and washed with water before resuspending in 1M Sorbitol. Cells were stored for up 1 week at 4°C or imaged immediately. For the remaining experiments, live cell imaging was used. Cells were grown in indicated medium at 30°C to either log phase or 1 day time point and spun down. Samples were concentrated in their existing medium and cells were imaged immediately.

Heat shock, sodium azide, glucose deprivation, and ethanol shock were carried out as described previously with methionine deprivation under similar conditions. Briefly, cells were grown in indicated medium (YPD or SD) overnight at 30°C and then back diluted into fresh medium to an OD600 of 0.2 and grown at 30°C to log phase. For heat shock experiments, cells were transferred to a water bath set at 46°C or remained at 30°C for 10 minutes. For NaN_3 experiments, yeast cultures were treated with 0.5% NaN_3 or water for 30 minutes at 30°C prior to imaging. For glucose deprivation experiments, cells were collected and washed in 30°C pre-warmed medium lacking glucose (YP or SD Glu-) followed by resuspension again in 30°C pre-warmed medium lacking glucose. Cells were then placed back at 30°C for 30 minutes and then imaged immediately prior to imaging. For ethanol shock, yeast cultures were collected and washed in 30°C pre-warmed SD medium with ethanol (SD EtOH 6%) as its sole carbon source followed by resuspension again in 30°C pre-warmed SD medium with ethanol. Cells were placed black at 30°C for 30 minutes and imaged immediately. For methionine deprivation experiments, cells were collected and washed with 30°C pre-warmed SD medium lacking methionine followed by resuspension again in 30°C pre-warmed SD medium lacking methionine. Cells were placed back at 30°C for 30 minutes and imaged immediately.

For AdoMet supplemented experiments, yeast cultures were grown overnight in YPD medium at 30°C and then back diluted into YPD with 250µM AdoMet (Sigma Aldrich). Cells were then grown to the desired time point.

RNA Isolation and qPCR

Total RNA was obtained by harvesting 40 OD600 units of cells from the 1 day time point and resuspending pellets in RNA lysis buffer (10mM EDTA, 50mM NaOAc pH 5.5). Next, SDS was added to a final volume of 1%. Samples were then subjected to a series of hot acid phenol/chloroform, acid phenol/chloroform, and chloroform extractions followed by precipitation. 5µg of RNA were taken to create cDNA using SuperScript III First-Strand Synthesis System (Invitrogen) following the manufacture's protocol. Quantitative PCR (qPCR) was performed using SYBR Green PCR Master Mix (Applied Biosystems). The relative levels of transcripts were calculated using the (ΔΔCt) method and normalized to *PGK1*.

Polysome Profile Analysis

200mLs of wild-type cells (BY4741) were grown to log phase (OD600 ~ 0.5) in YPD medium with or without 250µM AdoMet (Sigma Aldrich) at 30°C. Once cells reached log phase, the 200mL culture was split into two flasks containing 100mLs each and one was treated with 0.05% sodium azide for 30 min at 30°C. Prior to harvesting, cells were treated with 100µg/ml cyclohexamide (Sigma Aldrich) and allowed to shake for an additional 2 minutes at 30°C. Cultures were then spun down for 5 min at 4,000rpm at 4°C and the pellet was washed and resuspended in 1.5mL ice-cold Polysome Lysis Buffer (20mM Tris-HCl pH 8.0, 140mM KCl, 1.5mM $MgCl_2$, 100µg/ml cyclohexamide and 1% TritonX-100). An equal volume of acid-washed glass beads were added to the resuspensions and lysis was performed by vortexing samples for 30 seconds for a total of 8 times with 1 minute of recovery on ice in between cycles.

Lysates were then cleared by centrifuging samples for 5 min at 2,000 rpm at 4°C. The supernatant was recovered and then spun for 10 minutes at 14,000 rpm at 4°C. The supernatant was colleceted and A_{260} values were determined using a NanoDrop Spectrophotometer. 50 A_{260} units were then loaded onto a 10-50% linear sucrose gradient and centrifuged for 3 hours at 35,000rpm at 4°C. Gradients were collected from the top using a Biocomp Nano Fractionator which continuously measure A_{254} values to generate polysome traces.

Generation of iPSC-derived Motor Neurons

Human motor neurons (MN) were differentiated from iPSC as previously described (Markmiller et al., 2018). Briefly, immediately before differentiation, iPSCs were passaged with Accutase (Stemcell Technologies) and grown as a monolayer on feeder-free plates in mTeSR1. Once the cells reached >90% confluency, medium was changed daily with N2B27 medium (DMEM/F12 + GlutaMAX (Life Technologies), 1% N-2 supplement, 2% B-27 supplement (Thermo Fisher Scientific), 200µM ascorbic acid (Sigma-Aldrich), and 1% Penicillin/Streptomycin) and supplemented with 1µM Dorsomorphin dihydrochloride, 10µM SB431542, and 4µM CHIR99021 (Tocris) for 6 days. From day 7 to 18, cells were fed daily with N2B27 medium supplemented with 1µM Dorsomorphin dihydrochloride, 10µM SB431542, 200nM Smoothened Agonist (SAG, Tocris), and 1.5µM retinoic acid (RA, Sigma). On day 18, cells were dissociated using Accutase and transferred to plates coated first with 0.001% w/v poly-D-lysine hydrobromide (PDL) and poly-L-ornithine (PLO, Sigma) overnight, followed by an overnight incubation of 20ug/ml laminin (Life technologies) at 37°C, 5% CO_2. The dissociated cells were seeded in N2B27 medium supplemented with 2ng/ml recombinant human BDNF, 2ng/ml recombinant human GDNF, 2ng/ml recombinant human CNTF (PeproTech), 1.5µM RA, and 200nM SAG, and 10uM Y-26732 ROCK Inhibitor (RI, Tocris). On day 20, medium was modified by reducing RI to 2μM. On day 22, RA and SAG was withdrawn and 2uM DAPT (Tocris) was added to the medium. For imaging, cells were re-plated sparsely onto PDL/PLO/Laminin-coated 8-well glass chamber slides (Millipore) in the same medium on day 24. At 26 days, DAPT was withdrawn from the medium**.**

Mammalian Cell Immunofluorescence

HeLa and U2OS cells were passaged and plated onto glass coverslips in 12-well plates and grown for 24 hours. For AdoMet treatment, 4mM AdoMet was added to wells for 3 hours prior to the application of stress or Nocodazole (Sigma Aldrich). For AdOx experiments, cells were grown in the presence of 20μM prior to addition of AdoMet. To induce stress granule formation, sodium arsenite (Sigma Aldrich) was added to a final concentration of 500μM and incubated for 1 hour. For MG132 (Sigma Aldrich) and RocA (Sigma Aldrich) experiments, cells were incubated with compounds for 2 hours in a final concentration of 100μM and 2μM, respectively. Cells were then washed with PBS and fixed in 4% paraformaldehyde (Sigma Aldrich) for 20 minutes. Following removal of fixative, cell were washed with PBS and then permeabilized in 0.5% Triton X-100/PBS for 15 minutes. After permeabilization, cells were washed with PBS and then incubated with blocking solution (4% BSA/PBS) for 30 minutes. Primary antibodies (1:100 mouse anti-DDX3; Santa Cruz Biotech, 1:1000 rabbit anti-G3BP1; Sigma Aldrich) were diluted in blocking solution and added to cells overnight at 4°C. Following PBS washes, secondary antibodies (1:200 donkey anti-rabbit 568; Invitrogen, 1:200 goat anti-mouse 488; Invitrogen) were incubated for 2 hrs in the dark. Cells were washed with PBS and DAPI was added before mounting coverslips with Vectashield (Vector Laboratories).

On Day 28 of culturing, iPSC-derived motor neurons were pretreated with 4mM AdoMet for 3 hours prior to the addition of 250μM sodium arsenite for 1 hour or 5μg/ml puromycin for

24 hours. Following stress, cells were fixed with 4% paraformaldehyde for 45mins at room temperature. After three washes with PBS, the cells were simultaneously blocked and permeabilized with 5% goat serum, 0.1% Triton X-100, 1x PBS for 1hr at room temperature. Cells were rinsed with once with PBS and incubated with primary antibody (1:500 mouse anti-TARBP; Abnova, 1:1000 rabbit anti-G3BP1; Sigma Aldrich) diluted in 0.01% Triton X-100, 5% goat serum, 1x PBS for overnight at 4°C. After five washes with 0.01% Triton-X100, 1x PBS, secondary antibody (1:1000 goat anti-mouse AlexaFluor 488, goat anti-rabbit AlexaFluor 555; Invitrogen) diluted in 0.01% Triton X-100, 5% goat serum, 1x PBS was added for 1hr at room temperature. Cells were washed ten times in 0.01% Triton-X100, 1x PBS prior to nuclei stain with DAPI (1:5000 v/v in PBS) for 15 mins at RT. After one wash with 1x PBS, cells were preserved in 50% v/v glycerol in PBS.

Western Blot Analysis

For yeast samples, whole cell extracts were prepared via NaOH extraction as indicated in Kushnirov et al 2000. Briefly, cells were grown in YPD medium at 30°C to either log phase or 1 day time point. Next, 1 OD600 (log phase) or 2.5 OD600 (1 day) was spun down and resuspended in 0.1N NaOH. After incubation at RT for 5 min, cells were spun down and then resuspended in 2x Sample Buffer with protease inhibitors (Sigma Aldrich). Samples were boiled for 5 min at 95°C and incubated on ice for 3 minutes prior to centrifugation once more. Supernatants were stored at -20°C or used immediately.

For HeLa cells, lysates were obtained by first rinsing cells with cold 1X PBS to remove debris and media. Next, RIPA Buffer (50mM Tris-HCl pH7.5, 150mM NaCl, 1% Triton X-100, 1% Sodium Deoxycholate, 0.1% SDS, 2mM EDTA) with protease inhibitors was added and cells were scraped and centrifuged for 10 min at 15,000rpm at 4°C. Protein concentration was then determined by Bradford assay (Bio-Rad Protein Assay Dye Reagent Concentrate, BioRad) and normalized across samples. Next, 4X Sample Buffer was added and samples were boiled for 5 min at 95°C and placed on ice for 3 minutes prior to centrifugation. Samples were stores at -20°C or used immediately.

Samples were resolved on 10% SDS-PAGE gels and subsequently transferred to nitrocellulose membrane using semi-dry conditions. Membranes were then incubated in blocking solution (5% milk in TBST 0.1%) for 1 hour. After TBST 0.1% washes, membranes were incubated in primary antibody overnight at 4°C (1:5000 rabbit anti-GFP; Torrey Pines, 1:2500 mouse anti-mCherry; Novus Biologicals, 1:10000 mouse anti-PGK1; Invitrogen, 1:500 mouse anti-DDX3; Santa Cruz Biotech, 1:10,000 rabbit anti-G3BP; Sigma-Aldrich, 1:500 mouse anti-actin JLA20; Developmental Studies Hybridoma Bank). Primary antibody was removed and washed with TBST 0.1% prior to adding horseradish peroxidase-conjugated secondary antibody (1:10000 donkey anti-rabbit, 1:2500 sheep anti-mouse) in 5% blocking solution for 2 hours at RT. Membranes were then washed with TBST 0.1% and then incubated in Thermo Scientific Pierce ECL Western Blotting Substrate. Chemiluminescence was detected using FluorChem E system (Protein Simple). Quantification of protein levels was carried out using densitometry methods by comparing signals to internal control signal (PGK1 for yeast samples or Actin for HeLa cells).

Microscopy and Image Analysis

All images (with the exception of motor neuron experiments) were acquired on a Zeiss Axiovert 200M fluorescent microscope equipped with a CSU-X1 spinning disk (Yokogawa), an iChromeMLE laser source (Toptica Photonics) and µManager version 1.4 software. For acquisition of yeast, a 2µm Z-stack was taken with slices at 0.25µm intervals using the 40X (or

100X for intensity ratio determination) objective. Mammalian cell images were acquired by taking slices at 0.3µm intervals to obtain a 3µm Z-stack using the 40X objective.

Images for motor neurons were acquired on a Nikon Ti2 microscope equipped with a Nikon Qi2 Camera, Lumencor SpectraX LED light engine, Semrock quad bandpass filter cube with barrier filters, and NIS Elements 5.11 software. Images were taken using a Nikon 40x 0.95 NA objective. For acquisition, five random non-overlapping positions within each well of a 96-well plate were generated. At each position, an autofocusing routin was run to identify the Z-plane with the highest contrast in the 405nm channel and a symmetrical 7µm thick Z-stack centered around this focal plane with 0.9µm steps was captured

For all images, optimal Z-projections were obtained using FIJI along with subsequent image analysis. Colocalization quanitification was determined manually as the percentage of the number of GFP foci overlapped with mCherry foci divided by the total number of GFP foci. To determine intensity ratio analysis, maximum intensities of foci were measured along with the average intensity of the cytoplasm of that cell. Each value was background-corrected by subtracting the average intensity of the image with no cell. Intensity ratios were calculated by dividing the corrected foci intensity by the corrected cytoplasm intensity.

For mammalian cell image analysis, single cells were isolated using the “freehand” selection tool in FIJI. The number and size of foci as well as total stress granule area were then determined using the FIJI 3D Objects Counter plugin. Data was exported to Microsoft Excel and pooled for further analysis.

Quantification and statistical analysis

Student’s t test was used when comparing the averages between two samples. For dot plot and box plot analysis, Welch’s t test for unequal size and variance and unpaired t test was used to determine the significance respectively. Statistical analysis was performed using GraphPad Prism 7 software.

Acknowledgements

We thank the Nikon Imaging Center UC San Diego for imaging assistance. Work from the Wilhelm lab was supported by a grant from the HCIA program of HHMI and the James Wilhelm Memorial Fund. Kyle Begovich is a Howard Hughes Medical Institute Gilliam Fellow. Work from the Yeo lab was supported by grants from NIH (HG004659), TargetALS and the ALS Association.

Chapter 3 is a manuscript submitted for publication. It may appear in Molecular Cell. “Conserved metabolite regulation of stress granule assembly via AdoMet” Begovich, K., Vu, A.Q., Yeo, G.W., Wilhelm, J.E. A.Q. Vu cultured iPSC-dervied motor neuron lines. All other experiments, imaging, data analysis, and writing this version of this manuscript were my responsibility. G.W. Yeo and J.E. Wilhelm helped edit/revise this manuscript. The dissertation author is the primary experimenter and author on this paper.

References

Anders, M., Chelysheva, I., Goebel, I., Trenkner, T., Zhou, J., Mao, Y., Verzini, S., Qian, S.B., and Ignatova, Z. (2018). Dynamic m(6)A methylation facilitates mRNA triaging to stress granules. Life Sci Alliance *1*, e201800113.

Arimoto, K., Fukuda, H., Imajoh-Ohmi, S., Saito, H., and Takekawa, M. (2008). Formation of stress granules inhibits apoptosis by suppressing stress-responsive MAPK pathways. Nat Cell Biol *10*, 1324-1332.

Bahler, J., Wu, J.Q., Longtine, M.S., Shah, N.G., McKenzie, A., 3rd, Steever, A.B., Wach, A., Philippsen, P., and Pringle, J.R. (1998). Heterologous modules for efficient and versatile PCR-based gene targeting in Schizosaccharomyces pombe. Yeast *14*, 943-951.

Banani, S.F., Lee, H.O., Hyman, A.A., and Rosen, M.K. (2017). Biomolecular condensates: organizers of cellular biochemistry. Nat Rev Mol Cell Biol *18*, 285-298.

Bentmann, E., Neumann, M., Tahirovic, S., Rodde, R., Dormann, D., and Haass, C. (2012). Requirements for stress granule recruitment of fused in sarcoma (FUS) and TAR DNA-binding protein of 43 kDa (TDP-43). J Biol Chem *287*, 23079-23094.

Blokhuis, A.M., Groen, E.J., Koppers, M., van den Berg, L.H., and Pasterkamp, R.J. (2013). Protein aggregation in amyotrophic lateral sclerosis. Acta Neuropathol *125*, 777-794.

Chen-Plotkin, A.S., Lee, V.M., and Trojanowski, J.Q. (2010). TAR DNA-binding protein 43 in neurodegenerative disease. Nat Rev Neurol *6*, 211-220.

Eisinger-Mathason, T.S., Andrade, J., Groehler, A.L., Clark, D.E., Muratore-Schroeder, T.L., Pasic, L., Smith, J.A., Shabanowitz, J., Hunt, D.F., Macara, I.G., Lannigan, D.A. (2008). Codependent functions of RSK2 and the apoptosis-promoting factor TIA-1 in stress granule assembly and cell survival. Mol Cell *31*, 722-736.

Erce, M.A., Abeygunawardena, D., Low, J.K., Hart-Smith, G., and Wilkins, M.R. (2013). Interactions affected by arginine methylation in the yeast protein-protein interaction network. Mol Cell Proteomics *12*, 3184-3198.

Farg, M.A., Soo, K.Y., Warraich, S.T., Sundaramoorthy, V., Blair, I.P., and Atkin, J.D. (2013). Ataxin-2 interacts with FUS and intermediate-length polyglutamine expansions enhance FUS-related pathology in amyotrophic lateral sclerosis. Hum Mol Genet *22*, 717-728.

Gore, A., Li, Z., Fung, H.L., Young, J.E., Agarwal, S., Antosiewicz-Bourget, J., Canto, I., Giorgetti, A., Israel, M.A., Kiskinis, E., Belmonte, J.C.I.B., Rossi, D.J., Thomson, J.A., Eggan, K., Daley, G.Q., Goldstein, L.S.B., Zhang, K. (2011). Somatic coding mutations in human induced pluripotent stem cells. Nature *471*, 63-67.

Harding, H.P., Novoa, I., Zhang, Y., Zeng, H., Wek, R., Schapira, M., and Ron, D. (2000). Regulated translation initiation controls stress-induced gene expression in mammalian cells. Mol Cell *6*, 1099-1108.

Hilliker, A., Gao, Z., Jankowsky, E., and Parker, R. (2011). The DEAD-box protein Ded1 modulates translation by the formation and resolution of an eIF4F-mRNA complex. Mol Cell *43*, 962-972.

Hofweber, M., Hutten, S., Bourgeois, B., Spreitzer, E., Niedner-Boblenz, A., Schifferer, M., Ruepp, M.D., Simons, M., Niessing, D., Madl, T., Dormann, D. (2018). Phase Separation of FUS Is Suppressed by Its Nuclear Import Receptor and Arginine Methylation. Cell *173*, 706-719 e713.

Ivanov, P.A., Chudinova, E.M., and Nadezhdina, E.S. (2003). Disruption of microtubules inhibits cytoplasmic ribonucleoprotein stress granule formation. Exp Cell Res *290*, 227-233.

Jain, S., Wheeler, J.R., Walters, R.W., Agrawal, A., Barsic, A., and Parker, R. (2016). ATPase-Modulated Stress Granules Contain a Diverse Proteome and Substructure. Cell *164*, 487-498.

Kapeli, K., Pratt, G.A., Vu, A.Q., Hutt, K.R., Martinez, F.J., Sundararaman, B., Batra, R., Freese, P., Lambert, N.J., Huelga, S.C., Chun, S.J., Liang, T.Y., Chang, J., Donohue, J.P., Shiue, L., Zhang, Y., Zhu, H., Cambi, F., Kasarskis, E., Hoon, S., Ares, M.J., Burge, C.B., Ravits, J., Rigo, F., Yeo, G.W. (2016). Distinct and shared functions of ALS-associated proteins TDP-43, FUS and TAF15 revealed by multisystem analyses. Nat Commun *7*, 12143.

Kato, M., Han, T.W., Xie, S., Shi, K., Du, X., Wu, L.C., Mirzaei, H., Goldsmith, E.J., Longgood, J., Pei, J., Grishin, N.V., Frantz, D.E., Schneider, J.W., Chen, S., Li, L., Sawaya, M.R., Eisenberg, D., Tycko, R., McKnight, S.L. (2012). Cell-free formation of RNA granules: low complexity sequence domains form dynamic fibers within hydrogels. Cell *149*, 753-767.

Kedersha, N., Chen, S., Gilks, N., Li, W., Miller, I.J., Stahl, J., and Anderson, P. (2002). Evidence that ternary complex (eIF2-GTP-tRNA(i)(Met))-deficient preinitiation complexes are core constituents of mammalian stress granules. Mol Biol Cell *13*, 195-210.

Kedersha, N., Ivanov, P., and Anderson, P. (2013). Stress granules and cell signaling: more than just a passing phase? Trends Biochem Sci *38*, 494-506.

Keller, B.A., Volkening, K., Droppelmann, C.A., Ang, L.C., Rademakers, R., and Strong, M.J. (2012). Co-aggregation of RNA binding proteins in ALS spinal motor neurons: evidence of a common pathogenic mechanism. Acta Neuropathol *124*, 733-747.

Khong, A., Matheny, T., Jain, S., Mitchell, S.F., Wheeler, J.R., and Parker, R. (2017). The Stress Granule Transcriptome Reveals Principles of mRNA Accumulation in Stress Granules. Mol Cell *68*, 808-820 e805.

Kim, B., Cooke, H.J., and Rhee, K. (2012). DAZL is essential for stress granule formation implicated in germ cell survival upon heat stress. Development *139*, 568-578.

Kim, H.J., Kim, N.C., Wang, Y.D., Scarborough, E.A., Moore, J., Diaz, Z., MacLea, K.S., Freibaum, B., Li, S., Molliex, A., Kanagaraj, A.P., Carter, R., Boylan, K.B., Wojtas, A.M., Rademakers, R., Pinkus, J.L., Greenberg, S.A., Trojanowski, J.Q., Traynor, B.J., Smith, B.N., Topp, S., Gkazi, A., Miller, J., Shaw, C.E., Kottlors, M., Kirschner, J., Li, Y.R., Ford, A.F., Gilter, A.D., Benatar, M., King, O.D., Kimonis, W.E., Ross, E.D., Weihl, C.C., Shorter, J., Taylor, J.P. (2013). Mutations in prion-like domains in hnRNPA2B1 and hnRNPA1 cause multisystem proteinopathy and ALS. Nature *495*, 467-473.

Kwiatkowski, T.J., Jr., Bosco, D.A., Leclerc, A.L., Tamrazian, E., Vanderburg, C.R., Russ, C., Davis, A., Gilchrist, J., Kasarskis, E.J., Munsat, T., Valdmanuis, P., Rouleau, G.A., Hosler, B.A., Cortelli, P., De Jong, P.J., Yoshinaga, Y., Haines, J.L., Pericak-Vance, M.A., Yan, J., Ticozzi, N., Siddique, T., McKenna-Yasek, D., Sapp, P.C., Horvitz, H.R., Landers, J.E., Brown, R.H. (2009). Mutations in the FUS/TLS gene on chromosome 16 cause familial amyotrophic lateral sclerosis. Science *323*, 1205-1208.

Kwon, S., Zhang, Y., and Matthias, P. (2007). The deacetylase HDAC6 is a novel critical component of stress granules involved in the stress response. Genes Dev *21*, 3381-3394.

Ling, S.C., Polymenidou, M., and Cleveland, D.W. (2013). Converging mechanisms in ALS and FTD: disrupted RNA and protein homeostasis. Neuron *79*, 416-438.

Liu-Yesucevitz, L., Bilgutay, A., Zhang, Y.J., Vanderweyde, T., Citro, A., Mehta, T., Zaarur, N., McKee, A., Bowser, R., Sherman, M., Petrucelli, L., Wolozin, B. (2010). Tar DNA binding protein-43 (TDP-43) associates with stress granules: analysis of cultured cells and pathological brain tissue. PLoS One *5*, e13250.

Low, J.K., Hart-Smith, G., Erce, M.A., and Wilkins, M.R. (2013). Analysis of the proteome of Saccharomyces cerevisiae for methylarginine. J Proteome Res *12*, 3884-3899.

Mackenzie, I.R., Nicholson, A.M., Sarkar, M., Messing, J., Purice, M.D., Pottier, C., Annu, K., Baker, M., Perkerson, R.B., Kurti, A., Matchett, B.J., Mittag, T., Temirov, J., Hsiung, G.-Y.R., Krieger, C., Murray, M.E., Kato, M., Fryer, J.D., Petrucelli, L., Zinman, L., Weintraub, S., Mesulam, M., Keith, J., Zivkovic, S.A., Hirsch-Reinshagen, V., Roos, R.P., Zuchner, S., Graff-Radford, N.R., Petersen, R.C., Caselli, R.J., Wszolek, Z.K., Finger, E., Lippa, C., Lacomis, D., Stewart, H., Dickson, D.W., Kim, H.J., Rogaeva, E., Bigio, E., Boylan, K.B., Taylor, J.P., Rademakers, R. (2017). TIA1 Mutations in Amyotrophic Lateral Sclerosis and Frontotemporal Dementia Promote Phase Separation and Alter Stress Granule Dynamics. Neuron *95*, 808-816 e809.

Markmiller, S., Soltanieh, S., Server, K.L., Mak, R., Jin, W., Fang, M.Y., Luo, E.C., Krach, F., Yang, D., Sen, A., Fulzele, A., Wozniak, J.M., Gonzalez, D.J., Kankel, M.W., Gao, F.-B., Bennett, E.J., Lecuyer, E., Yeo, G.E. (2018). Context-Dependent and Disease-Specific Diversity in Protein Interactions within Stress Granules. Cell *172*, 590-604 e513.

Martinez, F.J., Pratt, G.A., Van Nostrand, E.L., Batra, R., Huelga, S.C., Kapeli, K., Freese, P., Chun, S.J., Ling, K., Gelboin-Burkhart, C., Fijany, L., Wang, H., Nussbacher, J.K., Broski, S.M., Kim, H.J., Lardelli, R., Sundararaman, B., Donohue, J.P., Javaherian, A., Lykke-Andersen, J., Finkbeiner, S., Bennett, F., Ares, M.J., Burge, C.B, Taylor, J.P., Rigo, F., Yeo, G.W. (2016). Protein-RNA Networks Regulated by Normal and ALS-Associated Mutant HNRNPA2B1 in the Nervous System. Neuron *92*, 780-795.

Mitchell, S.F., Jain, S., She, M., and Parker, R. (2013). Global analysis of yeast mRNPs. Nat Struct Mol Biol *20*, 127-133.

Murakami, T., Qamar, S., Lin, J.Q., Schierle, G.S., Rees, E., Miyashita, A., Costa, A.R., Dodd, R.B., Chan, F.T., Michel, C.H., Kronenberg-Versteeg, D., Li, Y., Yang, S.-P., Wakutani, Y., Meadows, W., Ferry, R.R., Dong, L., Tartaglia, G.G., Favrin, G., Lin, W.-L., Dickson, D.W., Zhen, M., Ron, D., Schmitt-Ulms, G., Fraser, P.E., Shneider, N.A., Holt, C., Vendruscolom, M., Kaminski, C.F., George-Hyslop, P. (2015). ALS/FTD Mutation-Induced Phase Transition of FUS Liquid Droplets and Reversible Hydrogels into Irreversible Hydrogels Impairs RNP Granule Function. Neuron *88*, 678-690.

Orru, S., Coni, P., Floris, A., Littera, R., Carcassi, C., Sogos, V., and Brancia, C. (2016). Reduced stress granule formation and cell death in fibroblasts with the A382T mutation of TARDBP gene: evidence for loss of TDP-43 nuclear function. Hum Mol Genet *25*, 4473-4483.

Panas, M.D., Ivanov, P., and Anderson, P. (2016). Mechanistic insights into mammalian stress granule dynamics. J Cell Biol *215*, 313-323.

Patel, A., Lee, H.O., Jawerth, L., Maharana, S., Jahnel, M., Hein, M.Y., Stoynov, S., Mahamid, J., Saha, S., Franzmann, T.M., Pozniakovski, A., Poser, I., Maghelli, N., Royer, L.A., Weigart, M., Meyers, E.W., Grill, S., Drechsel, D., Hyman, A.A., Alberti, S. (2015). A Liquid-to-Solid Phase Transition of the ALS Protein FUS Accelerated by Disease Mutation. Cell *162*, 1066-1077.

Protter, D.S.W., and Parker, R. (2016). Principles and Properties of Stress Granules. Trends Cell Biol *26*, 668-679.

Rollins, M., Huard, S., Morettin, A., Takuski, J., Pham, T.T., Fullerton, M.D., Cote, J., and Baetz, K. (2017). Lysine acetyltransferase NuA4 and acetyl-CoA regulate glucose-deprived stress granule formation in Saccharomyces cerevisiae. PLoS Genet *13*, e1006626.

Ryan, V.H., Dignon, G.L., Zerze, G.H., Chabata, C.V., Silva, R., Conicella, A.E., Amaya, J., Burke, K.A., Mittal, J., and Fawzi, N.L. (2018). Mechanistic View of hnRNPA2 Low-Complexity Domain Structure, Interactions, and Phase Separation Altered by Mutation and Arginine Methylation. Mol Cell *69*, 465-479 e467.

Saad, S., Cereghetti, G., Feng, Y., Picotti, P., Peter, M., and Dechant, R. (2017). Reversible protein aggregation is a protective mechanism to ensure cell cycle restart after stress. Nat Cell Biol *19*, 1202-1213.

Scherrer, T., Mittal, N., Janga, S.C., and Gerber, A.P. (2010). A screen for RNA-binding proteins in yeast indicates dual functions for many enzymes. PLoS One *5*, e15499.

Schroder, P.C., Fernandez-Irigoyen, J., Bigaud, E., Serna, A., Renandez-Alcoceba, R., Lu, S.C., Mato, J.M., Prieto, J., and Corrales, F.J. (2012). Proteomic analysis of human hepatoma cells expressing methionine adenosyltransferase I/III: Characterization of DDX3X as a target of S-adenosylmethionine. J Proteomics *75*, 2855-2868.

Shang, Y., and Huang, E.J. (2016). Mechanisms of FUS mutations in familial amyotrophic lateral sclerosis. Brain Res *1647*, 65-78.

Shen, H., Wang, H., Liu, Q., Liu, H., Teng, M., and Li, X. (2014). Structural insights into RNA recognition properties of glyceraldehyde-3-phosphate dehydrogenase 3 from Saccharomyces cerevisiae. IUBMB Life *66*, 631-638.

Sreedharan, J., Blair, I.P., Tripathi, V.B., Hu, X., Vance, C., Rogelj, B., Ackerley, S., Durnall, J.C., Williams, K.L., Buratti, E.,Baralle, F., de Belleroche, J., Mitchell, J.D., Leigh, P.N., Al-Chalabi, A., Miller, C.C., Nicholson, G., Shaw, C.E. (2008). TDP-43 mutations in familial and sporadic amyotrophic lateral sclerosis. Science *319*, 1668-1672.

Swisher, K.D., and Parker, R. (2010). Localization to, and effects of Pbp1, Pbp4, Lsm12, Dhh1, and Pab1 on stress granules in Saccharomyces cerevisiae. PLoS One *5*, e10006.

Taylor, J.C., and Markham, G.D. (1999). The bifunctional active site of s-adenosylmethionine synthetase. Roles of the active site aspartates. J Biol Chem *274*, 32909-32914.

Taylor, J.C., and Markham, G.D. (2000). The bifunctional active site of S-adenosylmethionine synthetase. Roles of the basic residues. J Biol Chem *275*, 4060-4065.

Tsai, W.C., Gayatri, S., Reineke, L.C., Sbardella, G., Bedford, M.T., and Lloyd, R.E. (2016). Arginine Demethylation of G3BP1 Promotes Stress Granule Assembly. J Biol Chem *291*, 22671-22685.

Tsai, W.C., Reineke, L.C., Jain, A., Jung, S.Y., and Lloyd, R.E. (2017). Histone arginine demethylase JMJD6 is linked to stress granule assembly through demethylation of the stress granule-nucleating protein G3BP1. J Biol Chem *292*, 18886-18896.

Van Treeck, B., Protter, D.S.W., Matheny, T., Khong, A., Link, C.D., and Parker, R. (2018). RNA self-assembly contributes to stress granule formation and defining the stress granule transcriptome. Proc Natl Acad Sci U S A *115*, 2734-2739.

Vance, C., Rogelj, B., Hortobagyi, T., De Vos, K.J., Nishimura, A.L., Sreedharan, J., Hu, X., Smith, B., Ruddy, D., Wright, P., Ganesalingam, J., Williams, K.L., Tripathi, V.,Al-Saraj, S., Al-Chalabi, A., Leigh, P.N., Blair, I.P., Nicholson, G., de Belleroche, J., Gallo, J.M., Miller, C.C., Shaw, C.E. (2009). Mutations in FUS, an RNA processing protein, cause familial amyotrophic lateral sclerosis type 6. Science *323*, 1208-1211.

Wang, N., Lo Presti, L., Zhu, Y.H., Kang, M., Wu, Z., Martin, S.G., and Wu, J.Q. (2014). The novel proteins Rng8 and Rng9 regulate the myosin-V Myo51 during fission yeast cytokinesis. J Cell Biol *205*, 357-375.

Wang, X., Zhao, B.S., Roundtree, I.A., Lu, Z., Han, D., Ma, H., Weng, X., Chen, K., Shi, H., and He, C. (2015). N(6)-methyladenosine Modulates Messenger RNA Translation Efficiency. Cell *161*, 1388-1399.

Wheeler, J.R., Matheny, T., Jain, S., Abrisch, R., and Parker, R. (2016). Distinct stages in stress granule assembly and disassembly. Elife *5*.

Wippich, F., Bodenmiller, B., Trajkovska, M.G., Wanka, S., Aebersold, R., and Pelkmans, L. (2013). Dual specificity kinase DYRK3 couples stress granule condensation/dissolution to mTORC1 signaling. Cell *152*, 791-805.

Yang, X., Shen, Y., Garre, E., Hao, X., Krumlinde, D., Cvijovic, M., Arens, C., Nystrom, T., Liu, B., and Sunnerhagen, P. (2014). Stress granule-defective mutants deregulate stress responsive transcripts. PLoS Genet *10*, e1004763.

Chapter 4

An in vitro assembly system for yeast stress granules identifies role for RNA nucleation and ATP

Abstract

Stress granules (SGs) are phase-separated assemblies of non-translating mRNPs that form in response to environmental stress. SGs arise by a combination of multivalent protein-protein, protein-RNA, and RNA-RNA interactions. However, the role of RNA-RNA interactions in SG assembly remains understudied. Here, we describe a yeast stress granule reconstitution system that faithfully recapitulates SG assembly in response to trigger RNAs. SGs assembled by stem loop RNAs triggers are ATP-sensitive and exhibits the hallmarks of maturation observed for SGs *in vivo* and SG proteins that phase separate *in vitro*. Additionally, the fraction of total mRNA that can be phase separated *in vitro* is sufficient to trigger SG formation. However, phase separation of NFT1 mRNA, a major transcript in this population, can only assemble an incomplete SG arguing that networks of distinct transcripts are required to form a canonical SG. Altogether, our system provides a platform to investigate how RNA-RNA interactions mediate SG formation.

Introduction

The assembly of RNA granules, non-membrane bound organelles comprised of RNA-binding proteins and non-translating mRNAs, is a hallmark of biochemical organization in eukaryotic cells (Anderson and Kedersha, 2006). RNA granules have been implicated mRNA processing, degradation, subcellular localization and translational control (Buchan, 2014). Stress granules (SGs) represent a conserved class of RNA granules that form in response to environmental stresses that inhibit translation initiation (Protter and Parker, 2016). Much of our understanding of the physical chemistry underpinning SG assembly has come from *in vitro* studies of SG components. Proteomic studies from yeast and mammalian cell lines have found that SGs are enriched in RNA-binding proteins that contain intrinsically disordered regions (IDRs) or low complexity sequences (LCSs) (Han et al., 2012; Jain et al., 2016; Markmiller et al., 2018; Youn et al., 2018). These domains have the ability to partition out of solution via liquid-liquid phase separation (LLPS) (Banani et al., 2017) This has suggested a model where alterations in valency and concentration of SG components can drive SG formation via LLPS (Banani et al., 2017). Consistent with this model, SG assembly is sensitive to the levels of SG components with IDR/LCS domains. Overexpression of SG proteins with IDRs promotes SG assembly in the absence of stress, while their depletion disrupts SG formation (Anderson and Kedersha, 2008; Hilliker et al., 2011; Kedersha et al., 2016; Matsuki et al., 2013; Takahara and Maeda, 2012). Additionally, RNA can act as a scaffold for multiple IDR domain RNA binding proteins. This scaffolding effect can drive LLPS via an increase in valency and has been observed for proteins and RNAs for several types of RNA granules, including SGs (Lin et al., 2015; Maharana et al., 2018; Protter et al., 2018). While these approaches have been useful in defining how networks of RNA-protein and protein-protein interactions can drive LLPS of SG components, the promiscuous nature of these *in vitro* systems, their reliance on crowding agents, and the restriction to examining only 1-2 proteins at a time has made it difficult to understand how a SG forms without recruiting components of other RNA granules.

Recently, specific RNA-RNA interactions have been implicated in the assembly of particular RNA granules suggesting an alternate route to triggering LLPS (Jain and Vale, 2017; Langdon et al., 2018). Interestingly, there is substantial overlap between the SG transcriptome and the fraction of mRNAs with a propensity to phase separate in vitro under physiological salt conditions suggesting that RNA-RNA interactions might contribute to SG assembly (Khong et al., 2017; Van Treeck et al., 2018). This set of RNAs are characterized by poor translatability and long coding region/3'UTR length consistent with the idea that they would be capable of forming extended RNA-RNA networks in vivo (Khong et al., 2017). Together these results argue that extended RNA-RNA networks of mRNAs might be capable of triggering SG assembly. Such an idea is attractive since it would also help explain features of the SG proteome. Because translation initiation factors preferentially bind certain RNA sequences (Sen et al., 2015, 2016; Zinshteyn et al., 2017), the enrichment of specific transcripts in SGs would help explain the presence of these factors in SGs and their absence from other RNA granules (Zid and O'Shea, 2014). Additionally, G-quadraplex formation of C9ORF72 repeat RNA (G4C2) can recruit a subset of SG proteins to foci in cells (Fay et al., 2017) suggesting that multiple RNAs might be necessary to form a canonical SG.

The composition of RNA granules also appears to be tuned by passive and active mechanisms. For instance, the ability of different IDR containing proteins to form distinct LLPS droplets is strongly influenced by the presence of non-IDR proteins independent of their effect of crowding (Protter et al., 2018). This suggests that specificity can be tuned in the cytoplasm by the large number of proteins that can weakly interact with IDR domains and suppress LLPS. Thus, systems that only focus on the phase separation properties of 1-2 proteins at a time are unlikely to fully recapitulate the behavior that is observed *in vivo*. Additionally, *in vivo* SG assembly/disassembly is regulated by chaperones and/or helicases suggesting that constant ATP dependent remodeling might play a role in SG assembly (Hilliker et al., 2011; Jain et al., 2016; Mateju et al., 2017; Walters et al., 2015). Together, these results suggest that the establishment of an *in vitro* SG assembly system where the initiating nucleation event (RNA-RNA, protein-protein, or RNA-protein) could be defined and that recapitulates the ATP regulated assembly in a native environment would allow a better understanding of how energy and the type of nucleator contribute to SG formation.

Here, we describe the development of a yeast cytoplasmic extract system that supports SG formation when specific trigger RNAs are added. These *in vitro* assembled SGs (IVSGs) faithfully recapitulate many of the assembly behaviors of *in vivo* SGs. In addition to the recruitment of multiple SG markers, formation of IVSGs is disrupted in extracts made from SG-defective strains arguing that assembly pathways for IVSGs mirror those of *in vivo* SGs. The assembly of IVSGs is also sensitive to the energy status of the extract, consistent with the behavior of *in vivo* SGs. Furthermore, IVSGs display maturation properties reminiscent of *in vitro* phase-separated proteins and older SGs *in vivo*. Using this system, we have identified a two-step process for IVSG assembly with phase separation of RNA occurring first followed by recruitment mRNPs. Interestingly, while a single phase-separated RNA can only assemble a partial IVSG, a population of phase-separated mRNAs is sufficient to trigger IVSG formation. This argues that a network of RNA-RNA interactions between different mRNA species might be necessary to assemble a canonical SG. Together these findings provide framework for understanding how energy and RNA-RNA mediated LLPS events control the assembly of a bona fide SG.

Results

Criteria for assembling SGs in vitro

Previous biochemical studies of SGs have taken two approaches: the analysis of the phase separation properties of individual SG-associated components or the characterization of purified SGs. While proteomic studies of purified SGs have provided insights into the composition of SGs, these SGs are only comprised of the "core" components and lack the dynamic, ATP-dependent behaviors that characterize SGs *in vivo* (Jain et al., 2016). In contrast, analyses of the phase separation properties of the individual protein and/or RNA components of the SG have revealed the role of valency and LCS/IDR domains in driving demixing (Fay et al., 2017; Jain and Vale, 2017; Li et al., 2012; Patel et al., 2015; Van Treeck et al., 2018). However, given that these proteins and RNAs exist as components of multivalent mRNPs that are being continuously remodeled by chaperones and helicases, it has been difficult to define the specific roles of RNAs or proteins in driving SG formation in non-pathological situations. As a result, we have sought to develop an extract system where SG assembly can be triggered by specific RNAs that recapitulate the dynamic, ATP regulated behavior observed *in vivo*.

There have been two primary barriers to developing an *in vitro* SG assembly system: identifying molecules that specifically trigger SG assembly and validating that any assembled structure is a bona fide SG. Since the biochemical function of the SG remains unclear, we have focused on four biochemical criteria for assessing whether any assembled structure is a bona fide SG. First, assembly should be dependent on specific molecular trigger in order to exclude non-specific assembly processes, such as molecular crowding (Lin et al., 2015; Molliex et al., 2015). Second, the structures should have the key biochemical markers of SGs and lack the markers for other phase-separated structures (e.g P bodies) (Buchan et al., 2011). This will exclude the possibility that the assembled structures are merely non-specifically aggregating mRNPs. Third, extracts from mutant cells defective in SG assembly should fail to support SG assembly *in vitro*. This ensures that the *in vivo* SG assembly pathway is the same pathway used to construct SGs in our extract system. Fourth, SGs assembled *in vitro* should recapitulate the dynamic, energy dependent behavior observed *in vivo* (Jain et al., 2016).

Identification of specific RNAs that trigger SG assembly *in vitro*

One of the problems with studying SG assembly *in vivo* is that there are many routes across the phase transition boundary (Van Treeck et al., 2018). The majority of the *in vitro* studies of SG components have focused on the role protein-protein interactions via IDRs/LCSs in driving phase separation (Lin et al., 2015; McGurk et al., 2018; Molliex et al., 2015). RNA-protein interactions have also been shown to drive phase separation by scaffolding effects that increase valency (Lin et al., 2015). However, recent work has argued that RNA can also undergo phase separation directly via RNA-RNA interactions suggesting that this type of interaction might be a major contributor to RNA granule assembly (Jain and Vale, 2017). Unfortunately, given the multivalent, dynamic nature of mRNPs, it is exceedingly difficult to examine how a single type of interaction can trigger SG formation. In order to address this problem, we first sought to identify RNAs that could phase separate in yeast extracts and trigger SG formation *in vitro*. We first leveraged the previous biochemical isolation of yeast SG for proteomic analysis, to generate an 18,000g supernatant lacked pre-existing SGs, yet contained unincorporated and diffuse SG markers/components (Figure 4.1A). We then tested a variety of *in vitro* transcribed Cy5-labeled RNAs for their ability to phase separate and/or recruit the endogenously expressed SG marker, Ded1-GFP, from extracts (Figure 4.1B). Capped, polyadenylated YFP mRNA did not phase separate into foci in our extract. Thus, merely adding exogenous RNA is insufficient to

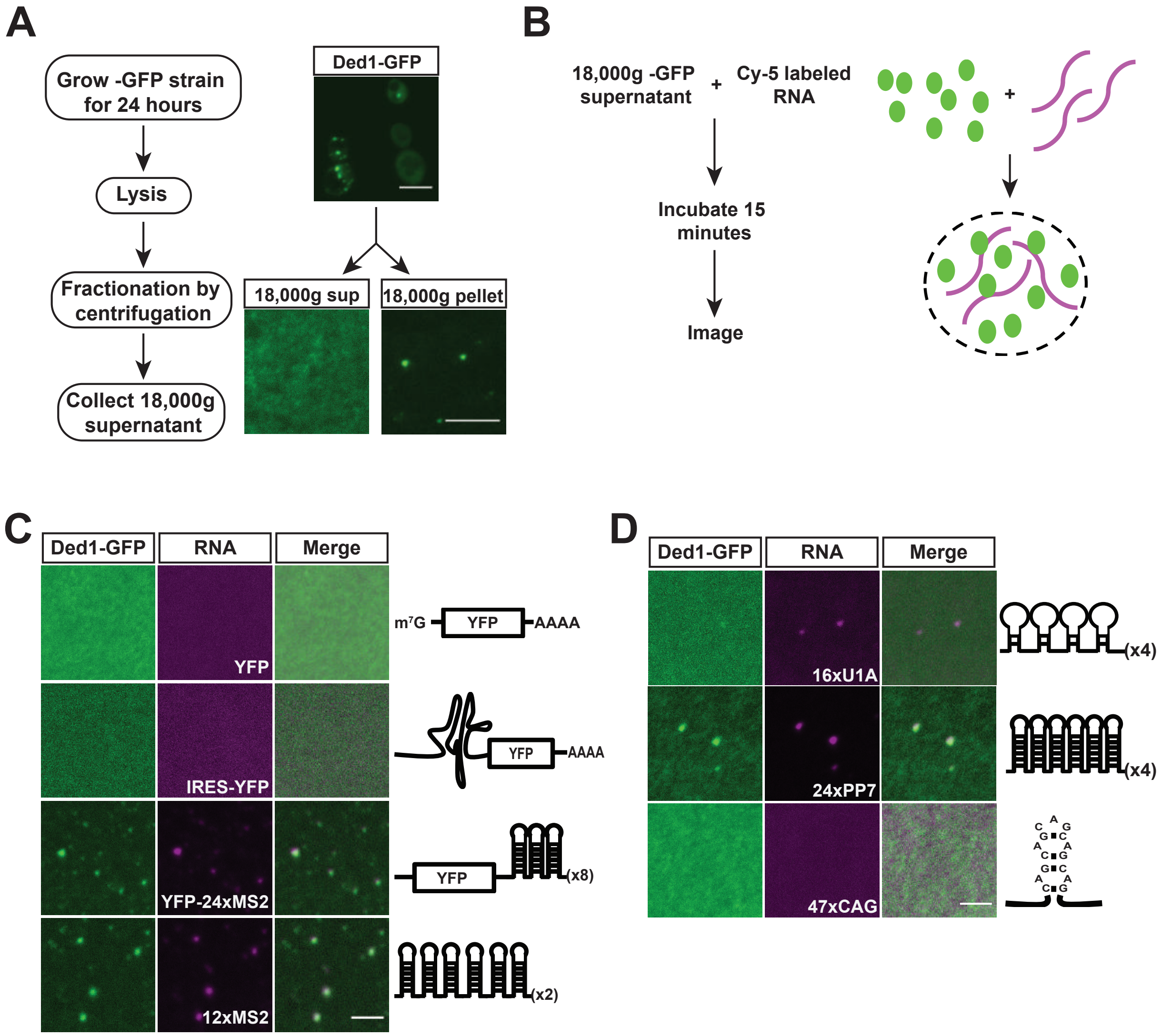

Figure 4.1. Specific stem loop repeat RNAs trigger SG formation in yeast extracts
(A) Schematic depicting growth, lysis, and fractionation of yeast extracts. Scale bar: 5 µm. **(B)** Schematic depicting SG assembly reaction. **(C)** Representative fluorescent images of 18,000g supernatant (80 mg/ml) from a Ded1-GFP strain incubated with various labeled, *in vitro* transcribed RNAs (300 nM). Illustrations of RNAs are shown to the right. Scale bar: 2.5µm. **(D)** Representative fluorescent images of 18,000g supernatant (80 mg/ml) from a Ded1-GFP strain incubated with various labeled, *in vitro* transcribed RNAs (300 nM). Illustrations of RNAs are shown to the right. Scale bar: 2.5 µm.

trigger RNA phase separation and/or SG formation. Similarly, YFP RNA with a 5' internal ribosome entry site (IRES) also failed to phase separate or cause Ded1-GFP to form foci (Figure 4.1C). This suggested that particular sequence features might be necessary to trigger SG formation *in vitro*. Since recent work on RNA phase separation suggested that arrays of interacting sequences might be necessary in order to trigger condensate formation, we next tested whether arrays of stem loops might promote SG formation *in vitro* (Jain and Vale, 2017). Interestingly, insertion of 24xMS2 stem loops into the 3'UTR of our model YFP transcript was sufficient to support the formation of RNA foci that recruited Ded1-GFP (Figure 4.1C). Furthermore, an array of the 12xMS2 stem loops alone was sufficient to recapitulate this result arguing that the array of stem loops was the key sequence/structural feature driving RNA phase separation and Ded1-GFP localization (Figure 4.1C).

In order to test whether the ability to phase separate and/or recruit Ded1-GFP was a feature common to all repetitive sequences, we also examined the ability of 24xPP7 stem loops, 16xU1A stem loops, and 47xCAG repeats to form RNA foci that recruit Ded1-GFP. An array of 24xPP7 stem loops was capable of forming RNA foci that recruited Ded1-GFP (Figure 4.1D). In contrast, an array of 16xU1A stem loops phase separated into RNA foci, but these RNA foci failed to recruit Ded1. Thus, not every phase separated RNA recruits Ded1. Additionally, we found that while 47xCAG repeats have a known propensity to phase separate *in vitro*, the repeat RNA failed to form foci or trigger the formation of Ded1 puncta (Figure 4.1D). Thus, the ability of RNAs to phase separate and recruit Ded1-GFP in yeast extracts is not a general feature of Cy5-labeled RNA, of RNAs containing arrays of stem loops, or of highly structured RNAs, such as IRES.

While these results identified two RNA sequences that are capable of phase separating and recruiting Ded1 in extracts, it was unclear whether these sequences merely bound the SG marker, Ded1, or if they nucleated the assembly of a bona fide SG. In order to distinguish between these two possibilities, we tested the ability of 12xMS2 stem loops to recruit other known SG markers in addition to Ded1. We focused on the ability to recruit SG proteins that act at either the 5’ (eIF4E, eIF4G) or the 3’ (Pab1, Pbp1, Pub1) end of transcripts in order to ensure that we were not merely capturing proteins that were part of the Ded1 interactome. 12xMS2 RNA was able to recruit each SG protein to foci arguing that the assembled structures contain multiple SG markers that act at opposite ends of mRNA (Figure 4.2A). One concern with these studies is that our exogenous RNA could be triggering the nonspecific aggregation of a variety of RNA binding proteins, some of which are SG components. In order to test this possibility, we assayed the ability of the 12xMS2 RNA to recruit the P body specific protein, Dcp2p-GFP, from extracts. While 12xMS2 RNA was able to form foci in these extracts, the foci failed to recruit Dcp2-GFP (Figure 4.2A). Thus, the 12xMS2 RNA triggers the formation of condensates that selectively recruit SG components and exclude P body components.

Extracts made from mutant yeast strains defective in SG formation fail to support SG assembly *in vitro*

While our *in vitro* assembled SGs (IVSGs) recruit SG specific components and exclude components from other types of RNA granules, it was unclear whether the assembly process we observed *in vitro* mirrored the one observed *in vivo*. If our extract system faithfully recapitulated SG assembly, we would expect that mutations that disrupt SG assembly *in vivo* would have similar effects on SGs assembled *in vitro*. To test this prediction, we focused on two mutations that disrupt/alter SG assembly: *ado1Δ* and *ubp3Δ* (Nostramo et al., 2015). In vivo, *ado1Δ* and *ubp3Δ* reduce the ability of SGs to form when assayed with Ded1-GFP (Figure 4.2B). Similarly,

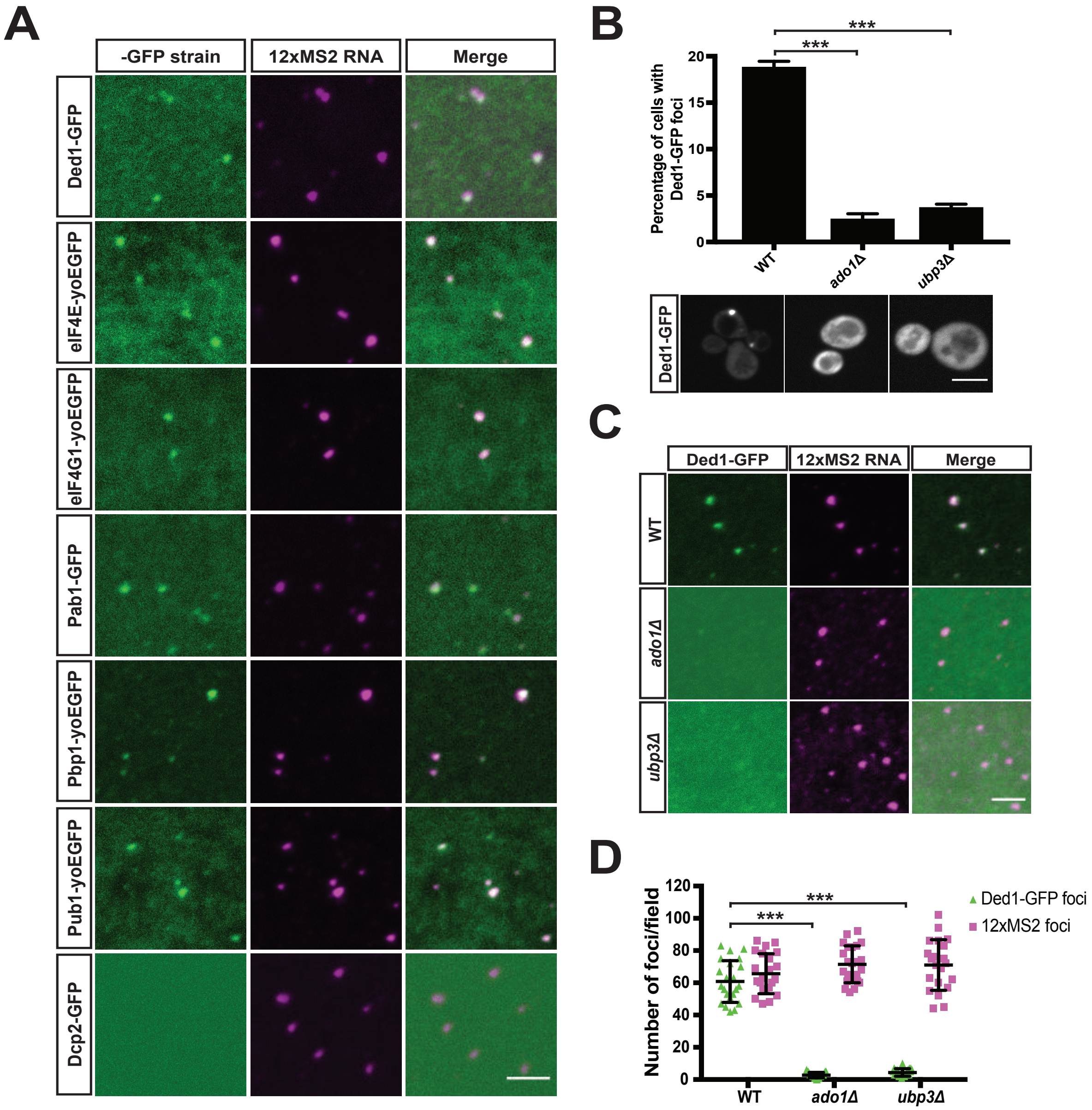

Figure 4.2. 12xMS2 induced SGs resemble composition and assembly pathways as *in vivo* SGs

(A) Representative fluorescent images of 18,000g supernatants (80 mg/ml) from indicated –GFP or –yoEGFP strains incubated with 12xMS2 RNA (300 nM). Scale bar: 2.5µm. **(B)** Quantification and representative fluorescent images of Ded1-GFP foci in WT, *ado1Δ*, and *ubp3Δ* backgrounds. Data is presented as average ± SEM of three independent replicates. Scale bar: 5 µm. **(C)** Representative fluorescent images of 18,000g supernatants (80 mg/ml) from WT, *ado1Δ*, and *ubp3Δ* strains with GFP-tagged Ded1 incubated with 12xMS2 RNA (300 nM). Scale bar: 2.5 µm. **(D)** Quantification of Ded1-GFP foci and 12xMS2 RNA foci in WT, ado1Δ, and ubp3Δ strains. Error bars indicate median and interquartile range. Plotted values are a compilation of three independent experiments. Statistics were performed only on Ded1-GFP foci. Statistical significance was calculated using Student's t test for (B) and (D). ***$p \leq 0.001$.

12xMS2 RNA forms robust foci in extracts from both *ado1Δ* and *ubp3Δ* strains, but these foci lack Ded1-GFP (Figure 4.2C and 4.2D). Thus, our extract system faithfully mirrors the assembly pathway(s) for SGs *in vivo*. Furthermore, the fact that 12xMS2 RNA still forms foci in extracts from both mutant strains argues that both *ado1Δ* and *ubp3Δ* disrupt stress granule assembly at a step downstream from RNA phase separation.

RNA phase separation is a separable step from mRNP recruitment in SG assembly

The fact that we were able to use our extract system to separate the formation of RNA condensates from the recruitment of specific proteins in different mutant backgrounds suggested that our *in vitro* system could be used to define the biochemical steps in SG assembly. Previous studies of SG structure found that purified SGs are comprised of stable “cores” that lose their liquid phase shell of mRNPs upon purification (Jain et al., 2016). This suggested that SGs assemble via an initial seeding event followed by mRNP recruitment. To test this model, we first assayed the ability of 12xMS2 RNA to form foci and recruit Ded1-GFP from extracts that had been treated with micrococcal nuclease (MNase) to eliminate mRNPs. While 12xMS2 RNA still formed foci in MNase-treated extracts, these foci no longer recruited Ded1-GFP and Pab1-GFP (Figure 4.3A and 4.3B). This argues that 12xMS2 RNA does not directly recruit Ded1 or Pab1 to the granule, but rather acts by capturing a subset of mRNPs that contain Ded1 and Pab1. Since 12xMS2 RNA recruits mRNPs, we next tested if IVSGs also contain mRNAs that are enriched in *in vivo* SGs. 12xMS2-induced SGs were able to recruit NFT1 mRNA as well (Figure 4.3C). This argues that IVSGs contain mRNPs and mRNAs known to localize to *in vivo* SGs.

12xMS2 RNA phase separation is not dependent on its ability to interact with mRNPs suggesting that RNA phase separation is biochemically distinct from mRNP capture. Molecular crowding has been shown to promote multivalent interactions that drive phase separation of

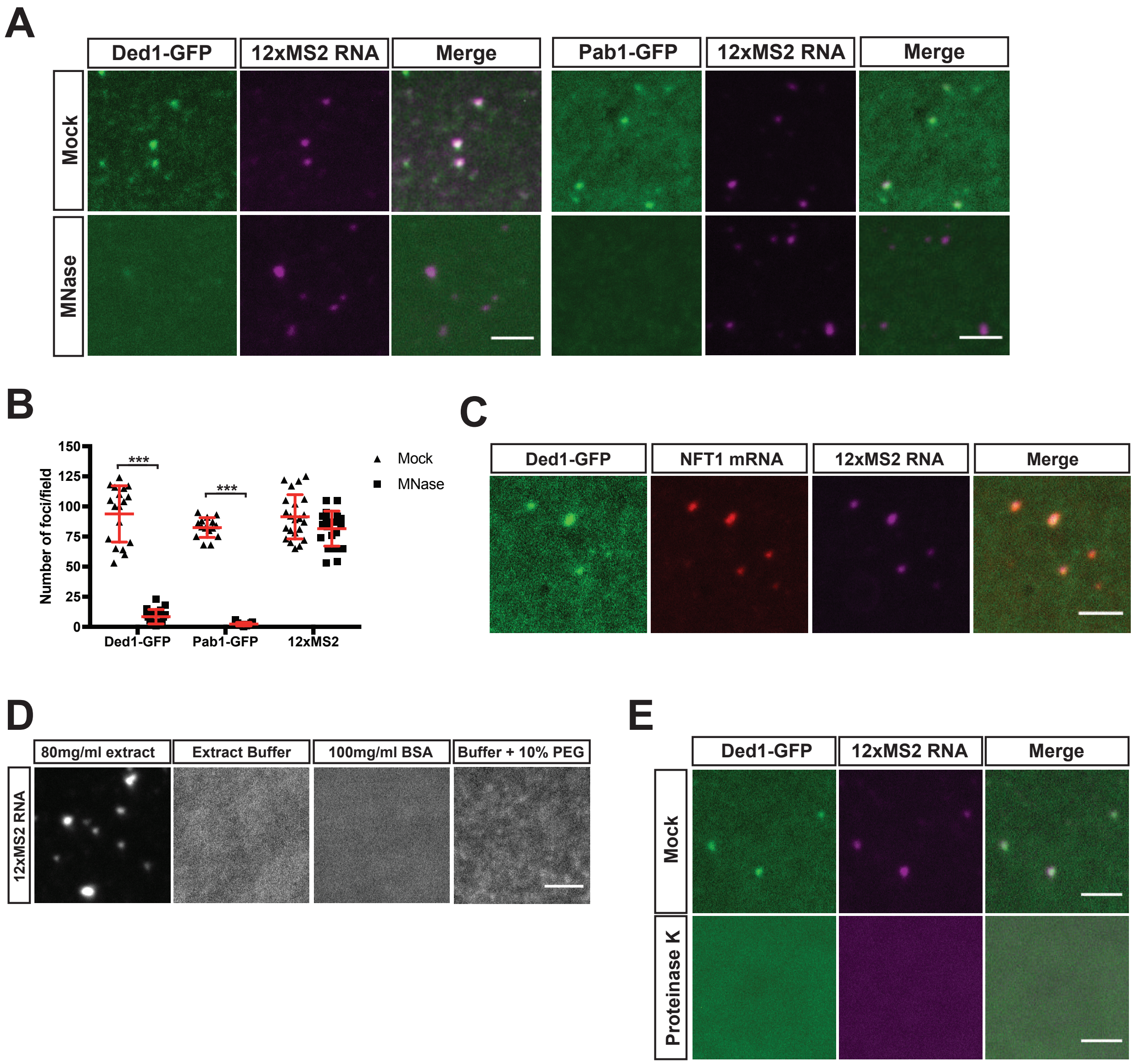

Figure 4.3. The assembly of IVSGs by 12xMS2 RNA can be separated into biochemically distinct steps

(A) Representative fluorescent images of mock- (Mock) or micrococcal nuclease-treated (MNase) 18,000g supernatant (80 mg/ml) from Ded1-GFP or Pab1-GFP strains incubated with 12xMS2 RNA (300 nM). **(B)** Quantification of Ded1, Pab1, and 12xMS2 RNA foci per field in mock- (Mock) and MNase-treated (MNase) extracts. Plotted values are a compilation of three independent experiments. **(C)** Representative fluorescent images of colocalization between NFT1 mRNA (40 nM) and 12xMS2 RNA (300nM) in Ded1-GFP extracts (80 mg/ml). **(D)** Representative fluorescent images of 12xMS2 RNA (300 nM) in crowding (80 mg/ml extract, 100 mg/ml BSA, Buffer + 10% PEG 4000) or non-crowding conditions (Extract Buffer). **(E)** Representative fluorescent images of 18,000g supernatants from a Ded1-GFP (80 mg/ml) strain pretreated with Proteinase K prior to addition of 12xMS2 RNA (300 nM). Scale bar: 2.5 µm. Statistical significance was calculated using Student's t test for (B). ***$p \leq 0.001$.

RNA granules *in vitro*, suggesting that the partitioning of 12xMS2 into foci in our extracts is merely a crowding effect (Lin et al., 2015; Molliex et al., 2015). However, 12xMS2 RNA does not form foci in extract buffer, extract buffer with 100mg/ml BSA, or extract buffer with 10% PEG arguing that assembly is not due to molecular crowding (Figure 4.3D). Interestingly, proteinase K-treated extracts fail to assemble 12xMS2 RNA foci formation (Figure 4.3E). Thus, yeast extracts contain a protein-based activity that allows 12xMS2 RNA to form foci and this initial seeding event is separable from mRNP recruitment.

ATP levels regulate SG nucleation and disassembly in vitro

Many of the stresses that induce SG formation *in vivo*, such as sodium azide or glucose deprivation, cause a drop in intracellular ATP levels (Buchan et al., 2011). However, it has been unclear whether this effect is due to the detergent-like properties of ATP or if it is due to a decrease in the activity of helicases and chaperones that suppress SG formation (Jain et al., 2016; Patel et al., 2017). Since our IVSGs recapitulate the features of *in vivo* SGs, we sought to test these different roles for ATP on IVSG assembly by adding increasing amounts of ATP or AMPPNP to our yeast extracts and assaying the effects on the ability of 12xMS2 RNA to form foci and/or recruit Ded1-GFP. Exogenous ATP and AMPPNP both suppressed 12xMS2 foci formation at high concentration (5-7mM), but had no effect at physiological concentrations (1-2mM) (Figure 4.4A). Consistent with the ability of high concentration of trinucleotides suppressing IVSG nucleation, GTP had similar effects to ATP and AMPPNP (Figure 4.4A).

In contrast, ATP and AMPPNP had different effects on pre-assembled 12xMS2 SGs (Figure 4.4B). Addition of ATP to a final concentration of 5-7mM caused 12xMS2 SGs to disassemble whereas the addition of AMPPNP had no effect on pre-assembled 12xMS2 SGs

Figure 4.4. Effects of ATP on SG assembly, disassembly, and morphology
(A) Schematic of workflow for setting up SG assembly reaction with or without nucleotides is shown on the left. Quantification of the effects of nucleotides on Ded1-GFP and 12xMS2 RNA foci for SG assembly. Samples are normalized to 0 mM nucleotide reactions. Data is presented as average ± SEM of three independent replicates. Representative fluorescent images of Ded1-GFP and 12xMS2 in nucleotide assembly reactions are shown on the right. **(B)** Schematic of workflow for setting up SG disassembly reaction with or without nucleotides is shown on the left. Quantification of the effects of nucleotides on Ded1-GFP and 12xMS2 RNA foci for SG disassembly. Samples are normalized to 0 mM nucleotide reactions. Data is presented as average ± SEM of three independent replicates. Representative fluorescent images of Ded1-GFP and 12xMS2 in nucleotide disassembly reactions are shown on the right. **(C)** Representative fluorescent images of 18,000g supernatants (100 mg/ml) from a Ded1-GFP strain treated with or without apryrase (10 U/ml). **(D)** Representative fluorescent images of 18,000g supernatants (100 mg/ml) from a Ded1-GFP strain pretreated with apyrase (10 U/ml) prior to addition of 12xMS2 RNA (300 nM). **(E)** Quantification of average foci size from mock- and apyrase-treated extracts. Data is presented as average ± SEM of three independent replicates. **(F)** Quantification of the number of structures with a circularity score < 0.75 from mock- and apyrase-treated extracts. Data is presented as average ± SEM of three independent replicates.

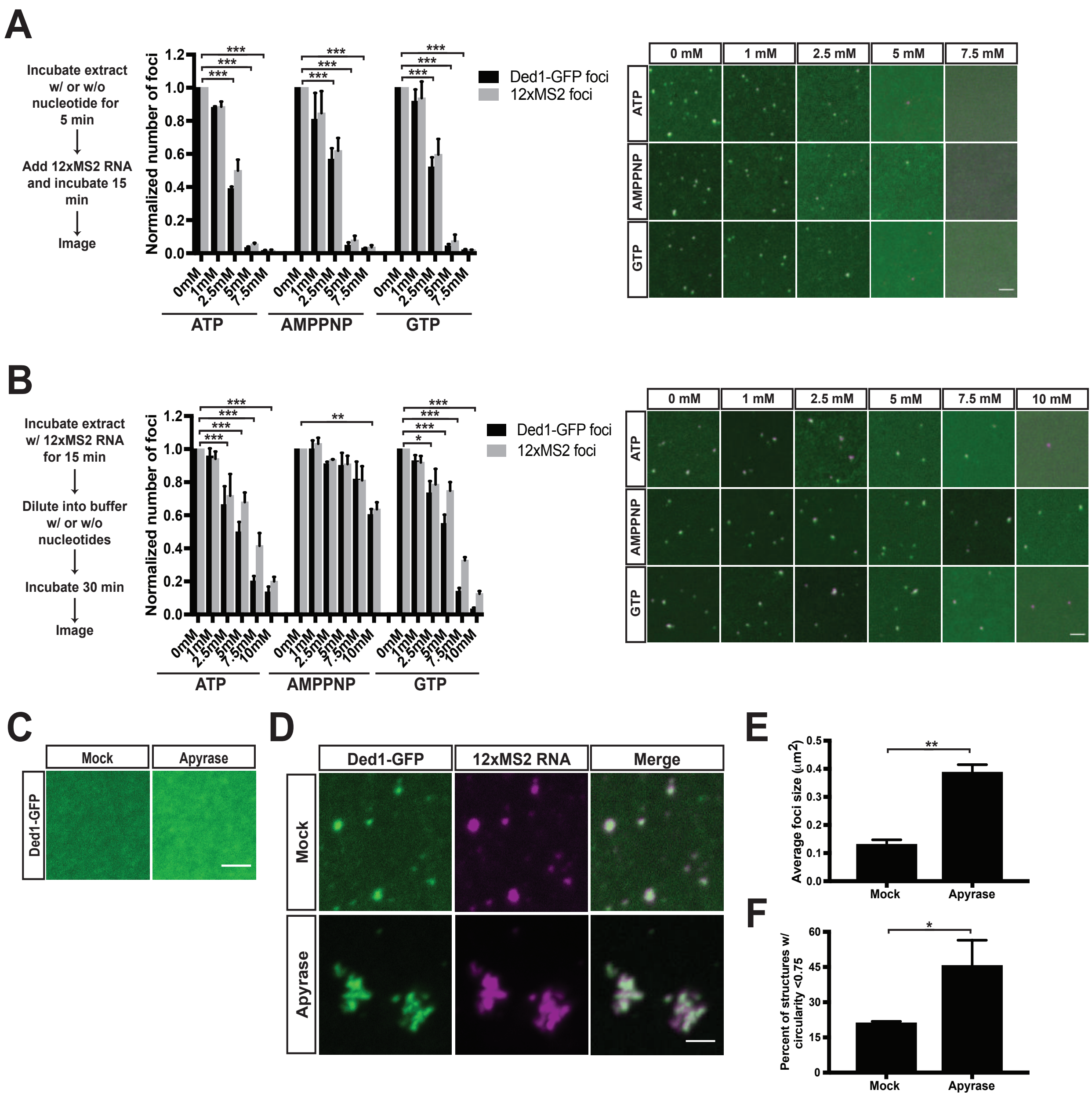
A
Incubate extract w/ or w/o nucleotide for 5 min
Add 12xMS2 RNA and incubate 15 min
Image
Normalized number of foci
1.2
1.0
0.8
0.6
0.4
0.2
0.0
***
0mM
1mM
2.5mM
5mM
7.5mM
ATP
AMPPNP
GTP
■ Ded1-GFP foci
■ 12xMS2 foci
0 mM
1 mM
2.5 mM
5 mM
7.5 mM
ATP
AMPPNP
GTP
B
Incubate extract w/ 12xMS2 RNA for 15 min
Dilute into buffer w/ or w/o nucleotides
Incubate 30 min
Image
Normalized number of foci
***
**
*
0mM
1mM
2.5mM
5mM
7.5mM
10mM
ATP
AMPPNP
GTP
■ Ded1-GFP foci
■ 12xMS2 foci
0 mM
1 mM
2.5 mM
5 mM
7.5 mM
10 mM
ATP
AMPPNP
GTP
C
Mock
Apyrase
Ded1-GFP
D
Ded1-GFP
12xMS2 RNA
Merge
Mock
Apyrase
E
Average foci size (μm^2)
0.5
0.4
0.3
0.2
0.1
0.0
**
Mock
Apyrase
F
Percent of structures w/ circularity <0.75
60
45
30
15
0
*
Mock
Apyrase

(Figure 4.4B). Furthermore, GTP was able to disassemble SG as well (Figure 4.4B). These results suggest that IVSGs can be remodeled via an energy dependent process.

Given this result, we next explored whether the basal level of ATP in the extracts contributed to SG assembly. To test this, we depleted ATP from extracts by treating them with apyrase. Treatment of extracts with apyrase didn't lead to any pre-clustering of Ded1-GFP (Figure 4.4C). However, addition of 12xMS2 to apyrase-treated extracts lead to a dramatic change in the morphology of SGs assembled. While normal IVSGs are largely spherical, the SGs that assembled in the absence of ATP were larger and more fibrous (Figure 4.4D). We found that a 3- and 2.5-fold increase in foci size and structures with circularity score < 0.75 in ATP depleted extracts (Figure 4.4E and 4.4F). This argues that the basal level of ATP in our extract system is low enough to support SG formation, but high enough to support remodeling activities that generate discrete spherical SGs.

IVSGs undergo maturation

One of the hallmarks of SGs *in vivo* is that they become less dynamic in response to prolonged stress. This "maturation" behavior is also observed for SG proteins that are phase-separated (PS) *in vitro*: the proteins initially form a liquid phase that over the course of several hours becomes more gel-like (Lin et al., 2015; Molliex et al., 2015; Patel et al., 2015). Our results with depleting ATP suggested that a similar maturation process might also occur for our IVSGs. By allowing PS proteins to age *in vitro*, recombinant SGs proteins transition from a spherical droplet to a more fibrous, tangle-like structure. We sought to determine if IVSGs matured in a similar fashion as the recombinant proteins. By performing a time course experiment, we observed a decrease in number of foci per field and an increase in the size of the foci (Figure 4.5A-5C). Additionally, more fibrous structures emerged at 45 minutes and became

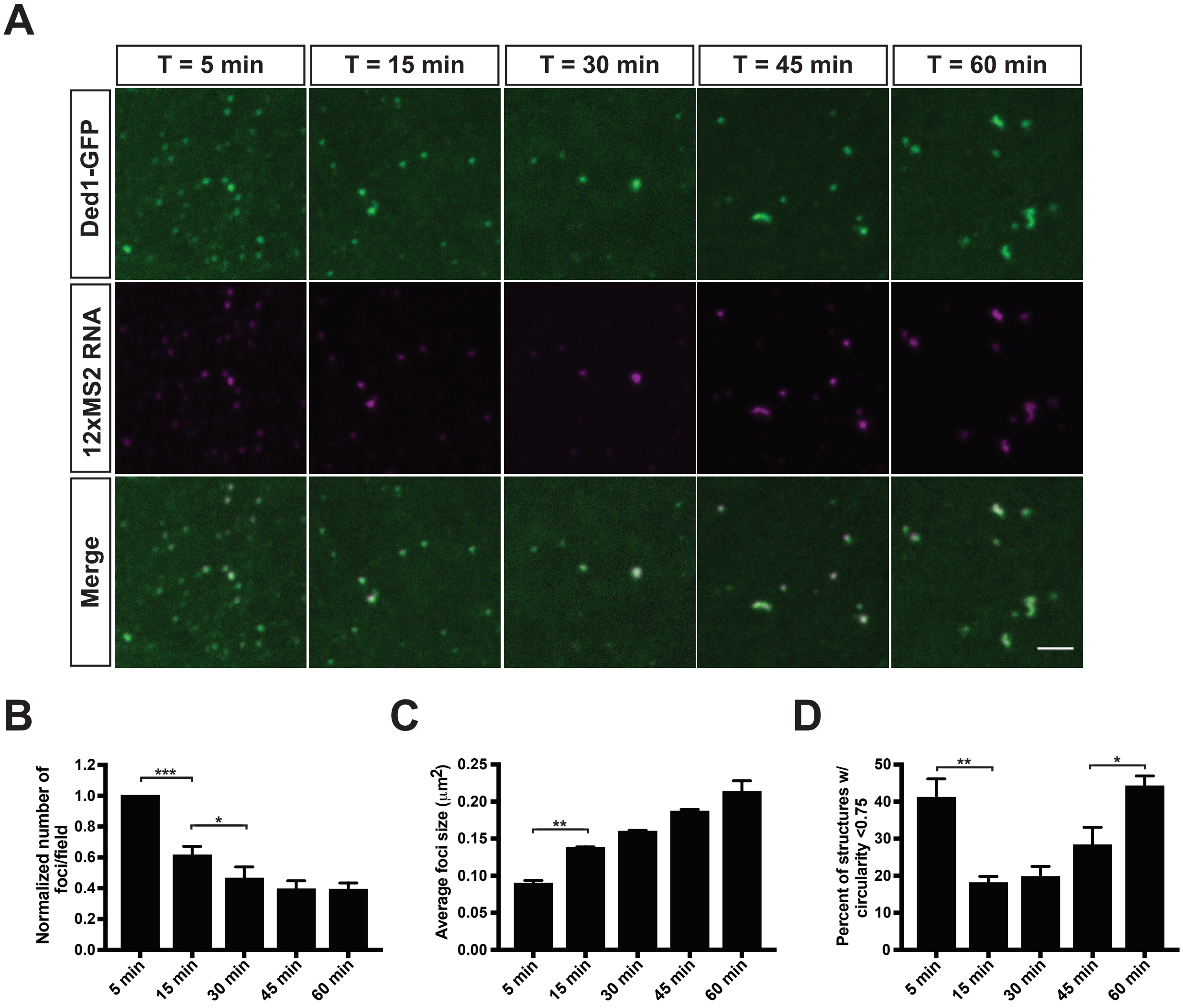

Figure 4.5. IVSGs undergo maturation

(A) Representative fluorescent images of 18,000g (100 mg/ml) supernatant from a Ded1-GFP strain incubated with 12xMS2 RNA (300 nM) at indicated time points. Scale bar: 2.5 μm. **(B)** Quantification of the number of foci per field from indicated time points. Samples are normalized to the 5-minute time point. Data is presented as average ± SEM of three independent replicates. **(C)** Quantification of the average foci size from indicated time points. Data is presented as average ± SEM of three independent replicates. **(D)** Quantification of the number of structures with a circularity score < 0.75 from indicated time points. Data is presented as average ± SEM of three independent replicates. Statistical significance was performed using Student's t test (B, C, D). $^{*}p \leq 0.05$, $^{**}p \leq 0.01$, $^{***}p \leq 0.001$.

more prevalent at 60 minutes (Figure 4.5A and 4.5D). These results suggest that IVSGs mimic similar phase separation properties as those observed alone with purified recombinant proteins.

In addition to changes in structure morphology, a loss in dynamic behavior is another hallmark property of PS structures. Since the size of our IVSGs make it difficult to assess their dynamic behavior via FRAP, we developed an assay to assess the ability of two different labeled RNAs to exchange between SGs. Yeast extracts from a Ded1-GFP strain were incubated with Cy3- or Cy5-labeled 12xMS2 for 0, 5, 15, or 60 minutes and then mixed together and incubated for 5 minutes to allow exchange between SGs prior to imaging. We quantified the exchange/colocalization between Cy3- and Cy5-labeled 12xMS2 RNAs using fold intensity plots and Pearson's correlation coefficient (PCC). While robust colocalization was observed at 0 and 5 minutes, little to no exchange was observed at 15 and 60 minutes (Figure 4.6A and 4.6B). Consequently, the PCC further decreased at 15 and 60 minutes (Figure 4.6C). This result raised two possibilities for how the dynamic properties of these SGs might be changing. First, the RNAs might be irreversibly trapped in the mature IVSGs preventing RNA exchange. Alternatively, mature IVSGs might stop recruiting free RNA, so any free transcript of the opposite label would fail to be captured. In order to distinguish between these two possibilities, Cy3-labeled NFT1 mRNA was added to IVSGs at 15 and 60 minutes and the amount of NFT1 mRNA incorporated into these granules was measured. We found that NFT1 mRNA was recruited to SGs from both 15 and 60 minutes (Figure 4.6D). This argues that the exchange of RNAs between IVSGs decreases over time even though they retain the ability to incorporate additional RNA.

Complimentary stem loop sequences promote 12xMS2 phase separation and Ded1 recruitment

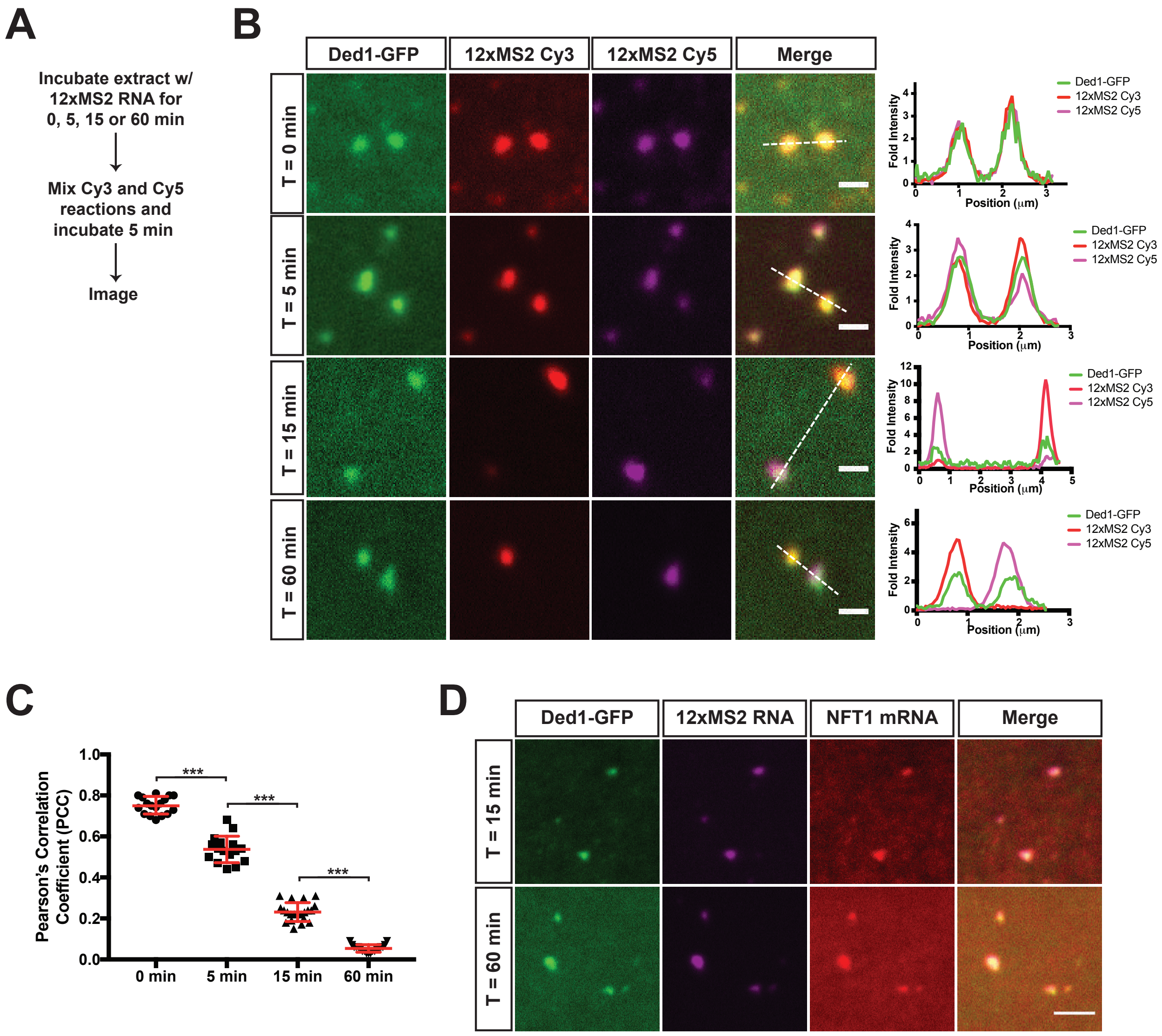

Figure 4.6. RNA exchange within SGs decreases as stress granules mature
(A) Schematic depicting experimental workflow. **(B)** Representative fluorescent images of Ded1-GFP, Cy3- and Cy5-labeled 12xMS2 RNA at indicated time points in the stress granule assembly reaction. Extract and RNA concentration were 80 mg/ml and 300 nM, respectively. Quantification of fold intensities along the dashed lines is shown on the right. Scale bar: 1 μm. **(C)** Quantification of colocalization of Cy3- and Cy5-labeled 12xMS2 RNA at indicated time points using Pearson's correlation coefficient. Error bars indicate median and interquartile range. Plotted values are a compilation of three independent experiments. **(D)** Representative fluorescent images of Cy3-labeled NFT1 mRNA (80 nM) addition to reactions containing 18,000g Ded1-GFP supernatant (80 mg/ml) and Cy5-labeled 12xMS2 RNA (300 nM) at indicated time points. Scale bar: 2.5 μm. Statistical significance was calculated using Student's t test (C). ***$p \leq 0.001$.

The fact that we can separate the formation of RNA condensates from mRNP recruitment in IVSGs raised the question of what features allow 12xMS2 RNA to phase separate in our system. Given that recent work has argued that RNA-RNA interactions of the mRNA transcriptome within SGs can drive SG assembly (Khong et al., 2017; Van Treeck et al., 2018), we examined the possibility that the 12 repeats of the MS2 stem loop were driving phase separation via complimentary sequence interactions between RNA molecules rather than forming an array of intramolecular stem loops (Figure 4.7A). To test this, we used a variant of 12xMS2, 12xMS2 V5, where each stem loop is comprised of a unique sequence but retains the same stem loop structure (Figure 4.7A). If 12xMS2 RNA phase separation is driven by intramolecular stem loops, we would predict that both would be capable of phase separation in the extracts. However, if phase separation were controlled by the ability to form readily exchangeable intermolecular interactions, we would predict that 12xMS2 V5 would not be capable of phase separating. The addition of 12xMS2 V5 RNA to extracts failed to form foci and recruit Ded1-GFP (Figure 4.7B and 4.7C). This suggested that having an array of identical, interchangeable interaction sites might promote phase separation. To test this possibility, we generated an RNA comprised of 12 copies of the first stem loop of the 12xMS2 V5 (12xMS2 V5 loop1) (Figure 4.7A). This RNA was capable of forming foci in yeast extract, but these foci formed less frequently than what we observed for 12xMS2 and the foci that formed lacked Ded1-GFP (Figure 4.7B and 4.7C).

The lack of recruitment of Ded1-GFP to 12xMS2 V5 loop1 RNA foci raised the question of whether phase-separation of RNA alone is sufficient to recruit Ded1. To test this, we phase-separated the MS2 variants prior to addition to yeast extracts. Consistent with the results from MS2 foci formation in extracts, only 12xMS2 and 12xMS2 V5 loop1 RNAs were able to phase separate *in vitro* (Figure 4.7D). Interestingly, both phase-separated RNAs were able to recruit

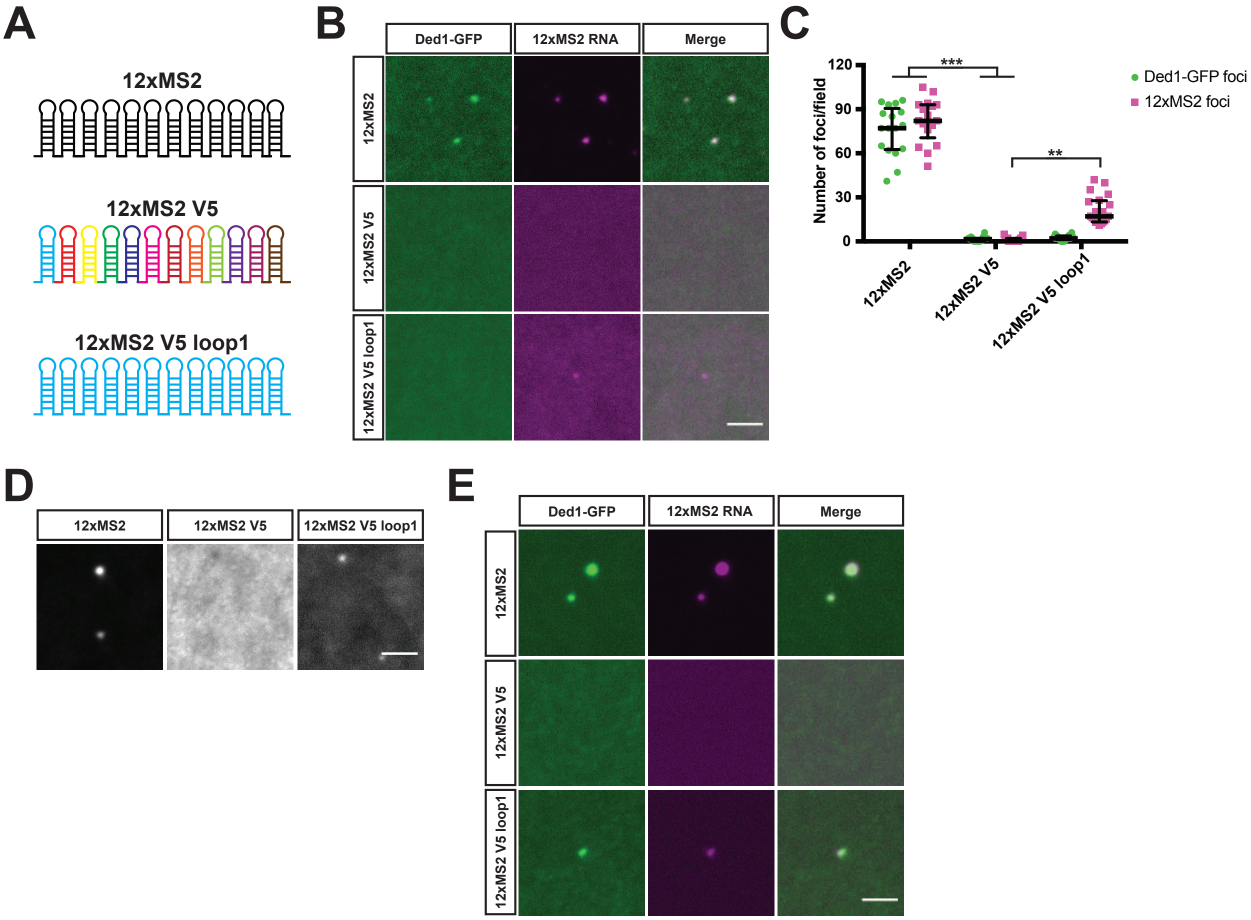

Figure 4.7. Complimentary sequences of MS2 stem loops promote phase separation of RNA and recruitment of Ded1-GFP
(A) Schematic depicting sequence differences of the 12xMS2 variants. **(B)** Representative fluorescent images of 18,000g supernatant (80 mg/ml) from a Ded1-GFP strain incubated with the 12xMS2 RNA (300 nM) variants. **(C)** Quantification of the number of foci per field for Ded1-GFP and 12xMS2 RNA from reactions with 12xMS2 variants. Error bars indicate median and interquartile range. Plotted values are a compilation of three independent experiments. **(D)** Representative fluorescent images of *in vitro* phase-separated 12xMS2 RNA (1 µM) variants. **(E)** Representative fluorescent images of 18,000g supernatant (80 mg/ml) from a Ded1-GFP strain incubated with phase-separated 12xMS2 RNA (100 nM) variants. Scale bar: 2.5 µm. Statistical significance was calculated using Student's t test (B). ***$p \leq 0.001$.

Ded1-GFP (Figure 4.7E). These results argue that arrays of identical inverted repeats can support RNA phase separation while non-identical repeats do not. Our results also suggested that the material state of RNAs could also determine recruitment of SG proteins.

Composition of phase separated RNAs determines SG composition

The fact that phase-separating 12xMS2 RNA prior to adding it to extracts was sufficient to recruit Ded1 raised the question of whether any phase separated RNA could trigger IVSG assembly or is IVSG formation dependent on particular RNAs. To distinguish between these possibilities, we phase separated different RNAs prior to addition to yeast extracts and asked three questions: 1) Does non-phase separated RNA trigger foci formation in extracts? 2) Does phase separated RNA recruit the complete set of SG proteins and exclude non-SG proteins? 3) Do mutants that block SG formation *in vivo* block recruitment to phase-separated RNAs?

First, we tested an 47xCAG repeat RNA which can be phase separated in vitro, but does not form structures comparable to 12xMS2. While 47xCAG failed to form foci when added directly to extract, we observed robust recruitment of Ded1-GFP to 47xCAG RNA foci when the RNA was phase separated prior to addition to the extract (Figure 4.8A and 4.8B). While Ded1 and Pbp1 were strongly recruited the foci, eIF4E, eIF4G1, Pab1, and Pub1 were not recruited (Figure 4.8C). Thus, phase separation of 47xCAG RNA is not sufficient to form a complete SG. Interestingly, the recruitment of Ded1 to 47xCAG RNA foci is dependent on the same pathways that are used by SGs since Ded1 recruitment is impaired in both *ado1Δ* and *ubp3Δ* extracts (median IR = 1.12 and 1.14) as compared to wild type (median IR = 1.46) (Figure 4.8D and 4.8E). Together these results argue that phase separated RNA can recruit SG proteins via canonical assembly pathways, but a single RNA may not be sufficient to build a complete SG.

Figure 4.8. Phase-separated 47xCAG RNA recruits a subset of SG proteins
(A) Representative fluorescent images of 47xCAG RNA (1 μM) under phase separating (PS) or non-phase separating (non-PS) conditions. **(B)** Representative fluorescent images of 18,000g supernatant (80 mg/ml) from a Ded1-GFP strain incubated with phase separated or non-phase separated 47xCAG RNA (100 nM). Quantification of fold intensities along the dashed lines is shown on the right. **(C)** Representative fluorescent images of 18,000g supernatant (80 mg/ml) indicated –GFP or -yoEGFP strains incubated with phase separated 47xCAG RNA (100 nM). Quantification of fold intensities along the dashed lines is shown on the right. **(D)** Representative fluorescent images of 18,000g supernatants (80 mg/ml) from WT, *ado1Δ*, and *ubp3Δ* strains with GFP-tagged Ded1 incubated with PS 47xCAG RNA (100 nM). **(E)** Quantification of the intensity ratios of Ded1-GFP from WT, *ado1Δ*, and *ubp3Δ* extracts. Error bars indicate median and interquartile range. Plotted values are a compilation of three independent experiments. Scale bar: 2.5 μm. Statistical significance was performed using Student's t test (E). ***$p \leq 0.001$.

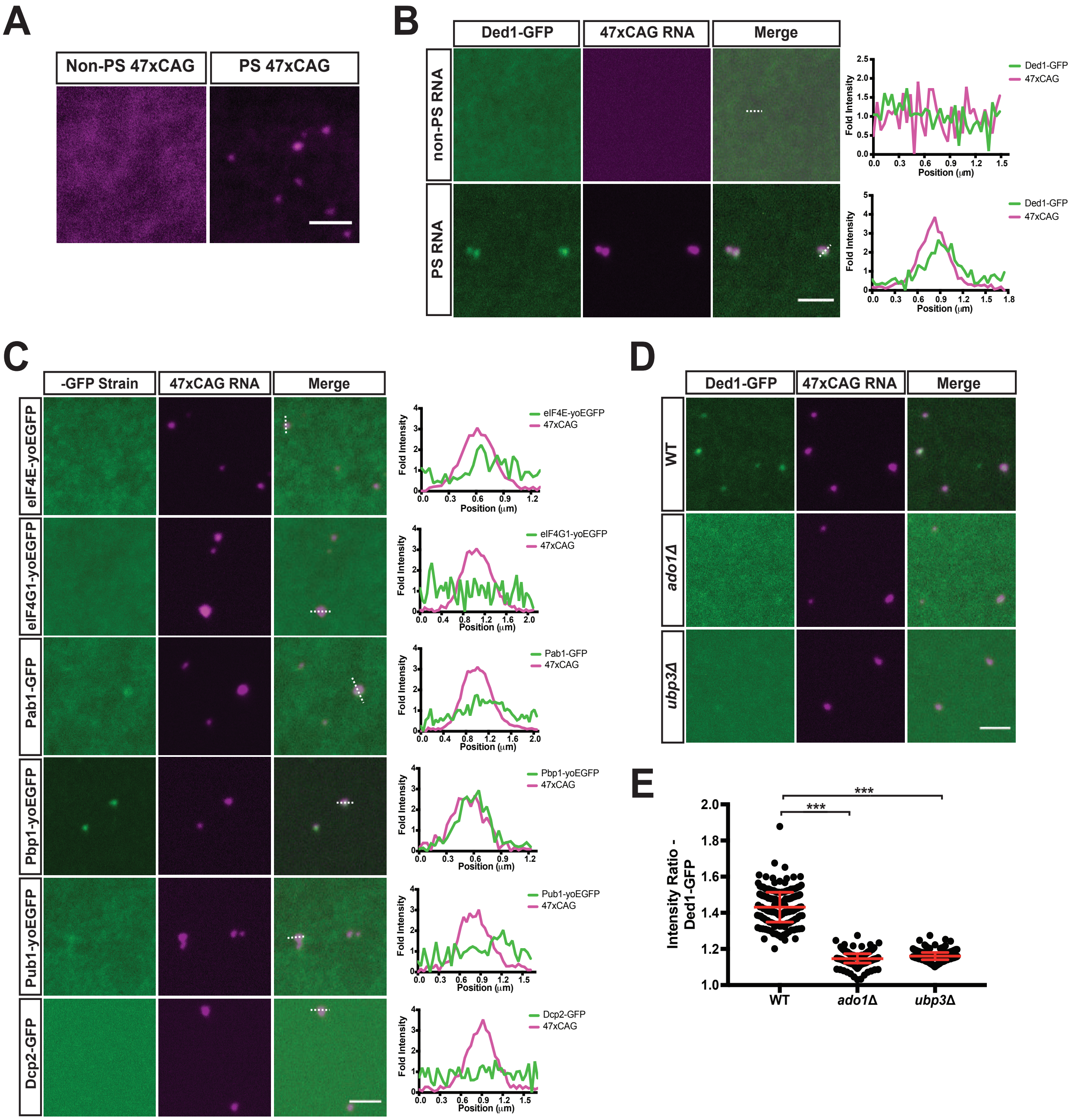
A
Non-PS 47xCAG
PS 47xCAG
B
Ded1-GFP
47xCAG RNA
Merge
non-PS RNA
PS RNA
Fold Intensity
Position (μm)
Ded1-GFP
47xCAG
C
-GFP Strain
47xCAG RNA
Merge
eIF4E-yoEGFP
eIF4G1-yoEGFP
Pab1-GFP
Pbp1-yoEGFP
Pub1-yoEGFP
Dcp2-GFP
Fold Intensity
Position (μm)
47xCAG
D
Ded1-GFP
47xCAG RNA
Merge
WT
ado1Δ
ubp3Δ
E
Intensity Ratio - Ded1-GFP
***
***
2.0
1.8
1.6
1.4
1.2
1.0
WT
ado1Δ
ubp3Δ

In order to test this possibility in a more physiological setting, we leveraged recent work that the fraction of total yeast RNA that can phase separate *in vitro* overlaps to a large degree with the SG transcriptome (Van Treeck et al., 2018). Thus, we would predict that the phase separated fraction of total yeast mRNA would support IVSG assembly, while a single mRNA would not. In order to visualize the RNA, a small amount of NFT1 mRNA was spiked into the phase separation reaction (Figure 4.9A). Phase separated total mRNA recruited Ded1 as well as eIF4E, eIF4G1, Pab1, Pbp1, and Pub1 (Figure 4.9B and 4.9C). Furthermore, these structures did not recruit the P-body protein, Dcp2, arguing that the phase-separated mRNAs were specifically recruiting SG components (Figure 4.9C). Additionally, *ado1Δ* and *ubp3Δ* mutant extracts decreased Ded1-GFP recruitment to the phase separated RNA by ~70% as compared to WT (Figure 4.9D and 4.9E) arguing that the IVSGs formed from phase separated total mRNA recruit proteins via the same pathways that SGs use *in vivo*. Thus, phase-separated total mRNA is sufficient to assemble a SG *in vitro*.

Nest, we explored whether phase separation of a single mRNA known to localize to SGs was sufficient to build a SG. We have found that NFT1mRNA and 47xCAG phase separate *in vitro* under similar conditions making it an ideal test transcript (Figure 4.10A). Untreated NFT1 mRNA was unable to form RNA foci when added directly to yeast extracts (Figure 4.10B). In contrast when NFT1 mRNA was phase separated prior to addition to yeast extracts, NFT1 mRNA foci recruited Ded1, Pab1, Pbp1, and Pub1 while excluding eIF4E and eIF4G1 (Figure 4.10B and 4.10C). Consistent with other phase separated RNAs, NFT1 mRNA failed to recruit Ded1-GFP in both *ado1Δ* and *ubp3Δ* extracts (median IR = 1.13 and 1.14) compared to WT extracts (median IR = 1.45) (Figure 4.10D and 4.10E). Thus, phase separation of NFT1 mRNA

Figure 4.9. Phase separation of total yeast RNA is capable of building a SG
(A) Schematic of NFT1 mRNA in phase separated total yeast RNA. Representative fluorescent images of total yeast RNA (500 ng/µl) spiked with labeled NFT1 mRNA (80 nM) under phase separating (PS) or non-phase separating (non-PS) conditions. **(B)** Representative fluorescent images of 18,000g supernatant (80 mg/ml) from a Ded1-GFP strain incubated with phase separated or non-phase separated total yeast RNA (50 ng/µl) spiked with NFT1mRNA (8 nM). Quantification of fold intensities along the dashed lines is shown on the right. **(C)** Representative fluorescent images of 18,000g (80 mg/ml) supernatant indicated –GFP or -yoEGFP strains incubated with phase separated total yeast RNA (50 ng/µl) spiked with NFT1 mRNA (8 nM). Quantification of fold intensities along the dashed lines is shown on the right. **(D)** Representative fluorescent images of 18,000g supernatants (80 mg/ml) from WT, *ado1Δ*, and *ubp3Δ* strains with GFP-tagged Ded1 incubated with PS total yeast RNA (50 ng/µl) spiked with NFT1 mRNA (8 nM). **(E)** Quantification of the intensity ratios of Ded1-GFP from WT, *ado1Δ*, and *ubp3Δ* extracts. Error bars indicate median and interquartile range. Plotted values are a compilation of three independent experiments.Scale bar: 2.5 µm. Statistical significance was performed using Student's t test (E). $^{***}p \leq 0.001$.

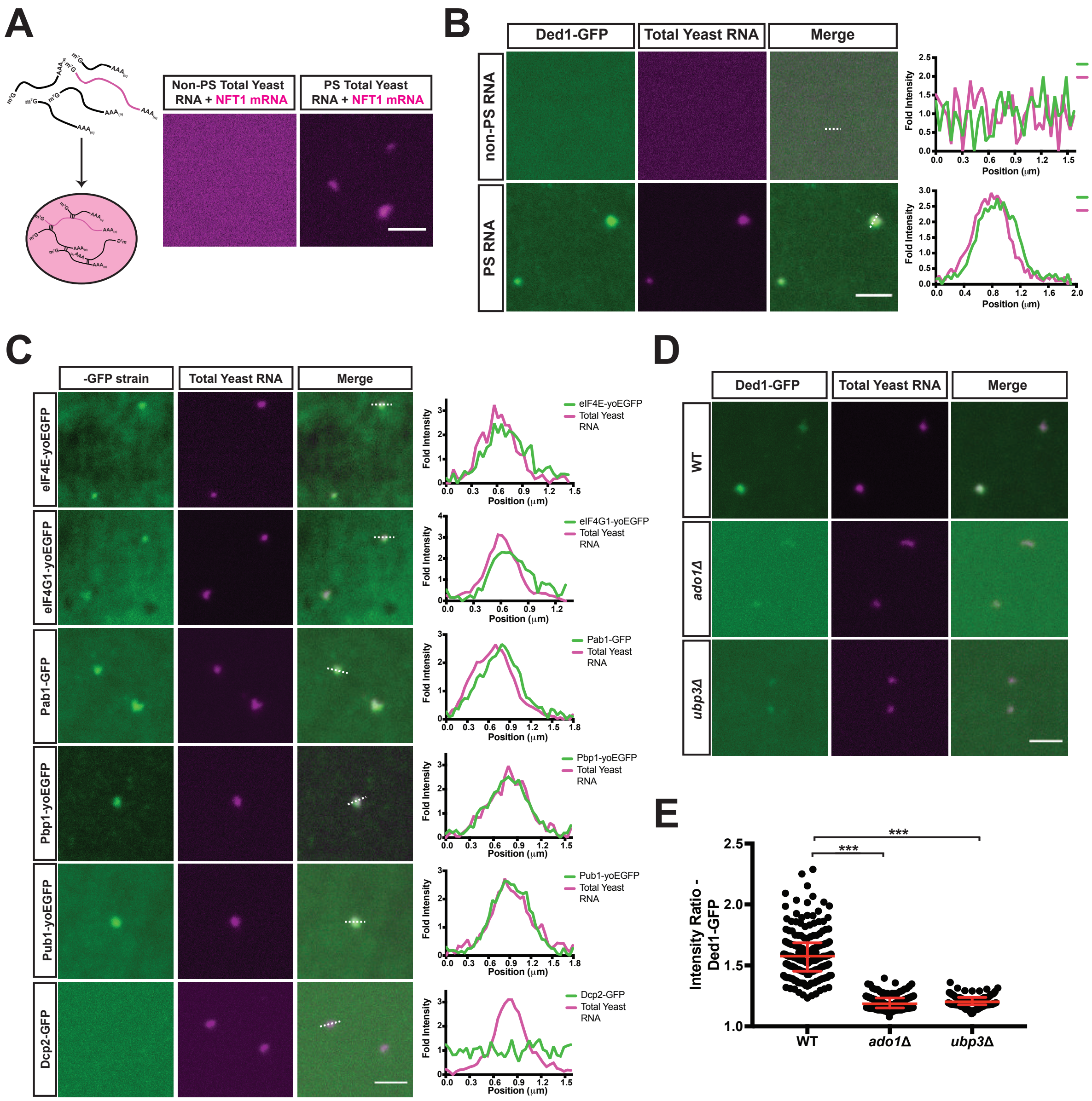

A
Non-PS Total Yeast RNA + NFT1 mRNA
PS Total Yeast RNA + NFT1 mRNA
B
Ded1-GFP
Total Yeast RNA
Merge
non-PS RNA
PS RNA
Fold Intensity
Position (μm)
Ded1-GFP
Total Yeast RNA
C
-GFP strain
Total Yeast RNA
Merge
eIF4E-yoEGFP
eIF4G1-yoEGFP
Pab1-GFP
Pbp1-yoEGFP
Pub1-yoEGFP
Dcp2-GFP
Fold Intensity
Position (μm)
Total Yeast RNA
D
Ded1-GFP
Total Yeast RNA
Merge
WT
ado1Δ
ubp3Δ
E
Intensity Ratio - Ded1-GFP
***
***
WT
ado1Δ
ubp3Δ

Figure 4.10. Phase separation of NFT1 mRNA recruits only a subset of SG proteins
(A) Representative fluorescent images of NFT1 mRNA (500 nM) under phase separating (PS) or non-phase separating (non-PS) conditions. **(B)** Representative fluorescent images of 18,000g supernatant (80 mg/ml) from a Ded1-GFP strain incubated with phase separated or non-phase separated NFT1 mRNA (50 nM). Quantification of fold intensities along the dashed lines is shown on the right. **(C)** Representative fluorescent images of 18,000g supernatant (80 mg/ml) indicated –GFP or -yoEGFP strains incubated with phase separated NFT1 mRNA (50 nM). Quantification of fold intensities along the dashed lines is shown on the right. **(D)** Representative fluorescent images of 18,000g supernatants (80 mg/ml) from WT, *ado1Δ*, and *ubp3Δ* strains with GFP-tagged Ded1 incubated with PS NFT1 mRNA (50 nM). **(E)** Quantification of the intensity ratios of Ded1-GFP from WT, *ado1*Δ, and *ubp3Δ* extracts. Error bars indicate median and interquartile range. Plotted values are a compilation of three independent experiments.
Scale bar: 2.5 μm. Statistical significance was calculated using Student's t test (B). $^{***}p \leq 0.001$.

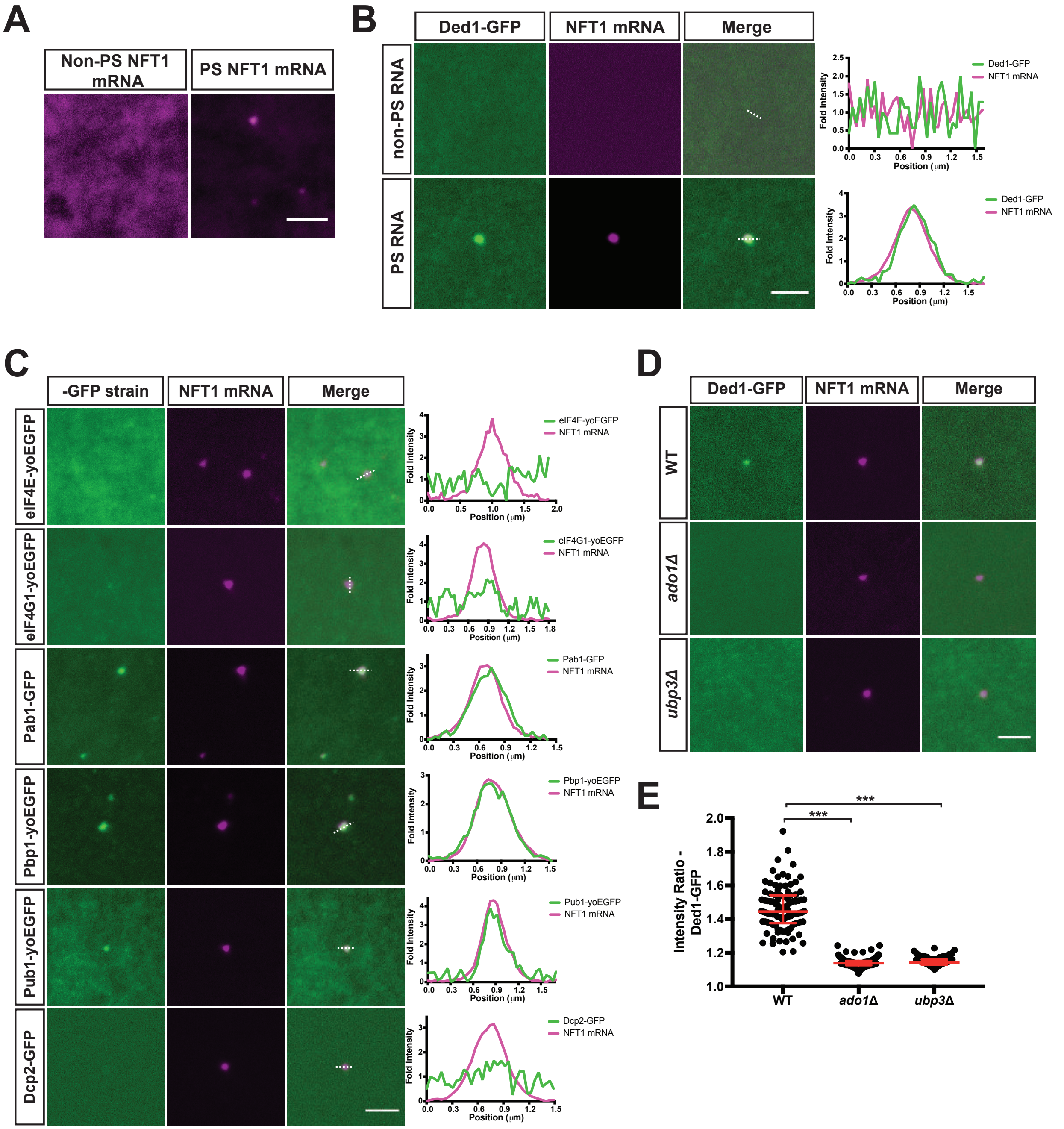
A
Non-PS NFT1 mRNA
PS NFT1 mRNA
B
Ded1-GFP
NFT1 mRNA
Merge
non-PS RNA
PS RNA
Fold Intensity
Position (μm)
Ded1-GFP
NFT1 mRNA
C
-GFP strain
NFT1 mRNA
Merge
eIF4E-yoEGFP
eIF4G1-yoEGFP
Pab1-GFP
Pbp1-yoEGFP
Pub1-yoEGFP
Dcp2-GFP
Fold Intensity
Position (μm)
D
Ded1-GFP
NFT1 mRNA
Merge
WT
ado1Δ
ubp3Δ
E
Intensity Ratio - Ded1-GFP
***
***
WT
ado1Δ
ubp3Δ
1.0
1.2
1.4
1.6
1.8
2.0

is not sufficient to assemble a complete IVSG. These results argue that the assembly of a complete SG is likely dependent on the phase separation of multiple distinct mRNAs.

Discussion

SGs play an integral role in modulating gene expression programs and signaling outputs in response to environmental stress (Mahboubi and Stochaj, 2017). Most of our understanding of how SGs assemble has been driven by studies of the mechanisms underpinning SG protein phase separation *in vitro* and *in vivo* (Boeynaems et al., 2018). In contrast, the role of RNA-RNA interactions in driving SG assembly is poorly understood (Fay et al., 2017; Khong et al., 2017; Van Treeck et al., 2018). To address this, we developed an *in vitro* reconstitution system where SGs form in response to addition of exogenous RNA. While most studies have focused on understanding the phase separation properties of one or two recombinant SG proteins, utilization of yeast extracts provides a physiological environment to address the role of RNA-RNA interactions in SG assembly. Our IVSGs mimic assembly patterns of *in vivo* assembly of SGs and recapitulate similar properties to phase-separated recombinant proteins. This system identified a two-step process for SG assembly where RNAs phase separate first followed by recruitment of mRNPs. With our IVSGs, we find that triphosphate nucleotides can prevent SG formation while triphosphate nucleotide hydrolysis is required for stress granule disassembly. Additionally, the composition of phase-separated RNA plays a critical role in determining the proteome of SGs.

ATP plays a crucial role in SG assembly and remodeling

Since ATP levels drop in response to most of the of environmental stressors that trigger SG formation (Buchan et al., 2011), there has been a great deal of interest in the role of ATP in modulating SG assembly. The majority of this focus has been on identifying ATP–dependent helicases and chaperones that play a role in SG remodeling (Hilliker et al., 2011; Jain et al., 2016; Mateju et al., 2017; Walters et al., 2015). However, more recently, *in vitro* work has shown that ATP can act as a biological hydrotrope to prevent proteins from phase separating suggesting that high levels of ATP can suppress SG formation *in vivo* independent of any ATPases (Patel et al., 2017). Our *in vitro* system has allowed us to assess the relative contributions of these two effects. Pre-incubation of extracts with increasing levels of ATP, suppressed SG formation (Figure 4.4). Furthermore, AMPPNP had a similar effect suggesting that the hydrotrope effects of ATP might suppress SG formation *in vivo*. In contrast, while high levels of ATP were able to disassemble IVSGs, AMPPNP could not (Figure 4.4). Thus, the hydrotrope effect of ATP appears to be limited to suppressing SG formation, while nucleotide turnover is required for disassembly. Consistent with this, disassembly of a different type of RNA granule, the *C.elegans* P-granule, requires the ATPase activity of Ddx4, when the granules are extruded from the germline (Putnam et al., 2018). Our results suggest that ATP's roles as a hydrotrope and energy source may act at distinct steps of SG dynamics.

In addition to determining the properties of ATP that regulate SG assembly and disassembly, our system provides a useful bridge from studies of the phase separation of recombinant SG proteins to SG formation *in vivo*. Our time course experiments show that IVSGs increase in size and become less spherical/more fibrillar over the course of the experiment (Figure 4.5). This "maturation" is similar to the behavior of in vitro phase separated SG proteins transition over time from a fluid state into amyloid-like fibers (Lin et al., 2015; Molliex et al., 2015; Patel et al., 2015). Furthermore, the fact that IVSGs transition to a fibrillar state more quickly in ATP-depleted extracts suggests that this process is opposed by ATP-utilizing enzymes (Figure 4.4). Our IVSGs also continue to capture exogenous RNAs even as they mature and stop exchanging transcripts between SGs (Figure 4.6). This mimics the behavior of persistent SGs *in vivo* that are thought to cause disease by continually sequestering mRNAs/proteins. Together these observations argue that our system will be useful for testing the relative contributions of helicases and chaperones in modulating SG dynamics as well as defining how SGs transition to a pathological state.

Composition of phase separated RNA regulates SG assembly

While the majority of the work on SG formation has focused on the role of protein-protein and RNA-protein interactions in driving SG assembly, recent work on the ability of RNA repeats to phase separate *in vitro* and *in vivo* has drawn new attention to the role of RNA-RNA interactions in triggering SG formation (Fay et al., 2017; Khong et al., 2017; Van Treeck et al., 2018). In particular, the substantial overlap between the SG transcriptome and the subset of mRNAs that can phase separate from total yeast total RNA *in vitro* has suggested that RNA-RNA interactions might be sufficient to explain the composition of SGs. However, phase separated yeast total RNA recruits recombinant IDR proteins specific to either the SG or the P body raising the question of what establishes the specificity of the SG proteome (Van Treeck et al., 2018). In contrast to these studies with recombinant IDR proteins, we have found that the phase separated fraction of total yeast mRNA is sufficient to trigger the assembly of IVSGs in extracts (Figure 4.9). Furthermore, these IVSGs lack the P body marker, Dcp2, and are sensitive to mutations that block SG assembly *in vivo* arguing that they are bona fide SGs. This result allowed us to address a long standing question: will any phase separated RNA trigger SG formation or does that composition of the phase-separated transcripts determine the proteome of the RNA granule. Our results with 47xCAG RNA and NFT1 mRNA argue that the transcriptome is a major driver of the protein composition of the RNA granule. Phase-separated 47xCAG RNA or NFT1 mRNA, an SG transcript, only recruit a subset of SG proteins (Figure 4.8 and 4.10). This incomplete recruitment is in spite of the fact that the proteins recruited, Ded1 and Pbp1, are both known to trigger SG formation *in vivo* when they are over-expressed (Hilliker et al., 2011; Swisher and Parker, 2010) . Thus, merely capturing and concentrating the SG nucleators, Ded1 and Pbp1, on a phase separated RNA is insufficient to build a SG. This argues that the RNA components of SGs play a key role in SG formation and are not merely acting as a scaffold for IDR containing proteins that capture mRNPs.

The idea that RNA phase separation is a specific step in SG assembly is also supported by our work with IVSGs. *ado1Δ* and *ubp3Δ* strains are both defective in SG assembly *in vivo*, however, it was unclear if these strains were defective in SG nucleation or protein/mRNP recruitment. Our analysis with IVSGs formed using 12xMS2 RNA argue that these mutants have a specific defect in recruiting SG proteins, such as Ded1, to phase separated RNA (Figure 4.2). This conclusion is supported by the fact that we observe the same Ded1 recruitment defect in *ado1Δ* and *ubp3Δ* strains even using *in vitro* phase separated trigger RNAs, such as 47xCAG, NFT1 mRNA, and total yeast mRNA (Figure 4.8, 4.9, and 4.10). Thus, *ado1Δ* and *ubp3Δ* appear to be the first examples of mutations that specifically block the recruitment of Ded1 to phase separated RNA. While it remains unclear whether *ado1Δ* and *ubp3Δ* directly affect Ded1 recruitment or act via other SG proteins, the ability to distinguish RNA phase separation from protein recruitment presents a new tool for defining the role of known SG regulators in the SG assembly pathway.

The current "four-phase" model for the formation of RNA granules, such as SGs, argues that assembly is driven by the sum of the protein-protein, protein-RNA, and RNA-RNA interactions of the mRNPs (Treeck and Parker, 2018). However, to date, each of these interactions has largely been studied in isolation making it difficult to determine how each of these interactions act in concert to drive the assembly of a specific RNA granule. Our yeast extract system has provided a new route into dissecting how RNA-RNA interactions can drive assembly of SGs. This work also lays the foundation for exploring protein-protein and RNA-protein dependent paths across the phase boundary to define how distinct stresses define the pathway used to drive SG assembly.

Materials and Methods

Yeast growth conditions

All yeast experiments were carried out in *Saccharomyces cerevisiae* budding yeast in the BY4741 background. All yeast strains were grown at 30°C in YPD medium (1% yeast extract, 2% peptone, 2% dextrose).

Yeast strain construction

S. cerevisae strains are listed in Table 4.1. All yeast strains were derived from a parent strain with the genotype MATa his3Δ1 leu2Δ0 met15Δ0 ura3Δ0 (BY4741). Generation of endogenous GFP-tagged strains and gene disruption was created using standard PCR-mediated techniques.

Plasmid construction

Plasmids used in this study are listed in Table 4.2. Construction of the pSP64-NFT1 plasmid was performed by amplifying the coding sequence of the *NFT1* gene from genomic DNA and cloned into the pSP64 plasmid using restriction enzyme cloning. Generation of the 12xMS2V5 loop1 template was performed by GenScript and replaced the 12xMS2 sequence in pSL-12xMS2 plasmid to create the pSL-12xMS2V5loop1 construct.

Extract preparation

An overnight starter culture was diluted to OD_{600} 0.2 into fresh YPD medium and then grown for 24 hours at 30°C. 500 ODs were spun down for 2 min at 5000g and washed in sterile H_2O and spun once more. After removing the water wash, pellets were resuspended in 1µl/1 OD_{600} of extract buffer (50mM Tris HCl pH 7.5, 150mM Potassium Acetate, 2mM Magnesium Acetate, 5mM Beta Mercaptoethanol, 1X Protease Cocktail

Table 4.1. List of yeast strains used in this study

Name	**Genetic background**	**Reference**
BY4741	*MATa his3Δ1 leu2Δ0 met15Δ0 ura3Δ0*	Dharmacon
Dcp2-GFP	BY4741, Dcp2-GFP::HphNT1	This study
Ded1-GFP	BY4741, Ded1-GFP::HphNT1	This study
ado1Δ; Ded1-GFP	BY4741, Ded1-GFP::HphNT1, *ado1Δ*::NatMx6	This study
ubp3Δ; Ded1-GFP	BY4741, Ded1-GFP::HphNT1, *ubp3Δ*::KanMx6	This study
eIF4G1-yoEGFP	BY4741, eIF4G1-yoEGFP::KanMx6	This study
eIF4E(Cdc33)-yoEGFP	BY4741, eIF4E(Cdc33)-yoEGFP::KanMx6	This study
Pab1-GFP	BY4741, Ded1-GFP::HphNT1	This study
Pbp1-yoEGFP	BY4741, Pbp1-yoEGFP::KanMx6	This study
Pub1-yoEGFP	BY4741, Pub1-yoEGFP::KanMx6	This study

Table 4.2. List of plasmids used in this study

Plasmid Number	Description
pJW612	pFA6a-GFP-HphNT1
pJW750	pFA6a-yoEGFP-KanMx6
pJW523	pFA6a-NatMx6
pJW121	pFA6a-KanMx6
pJW741	pSP64
pJW747	pSP64-NFT1
pJW757	pSP64-mYFP
pJW728	pCFE1-IRES-mYFP
pJW758	pBlueScript-mYFP-24xMS2
pJW688	pSL-12xMS2
pJW694	pSL-12xMS2 V5
pJW729	pSL-12xMS2 V5 loop1
pJW759	pBlueScript-24xPP7
pJW746	pPS2037-16xU1A
pJW691	pBlueScript-47xCAG

Inhibitor). Cells were spun down at 5000g for 5 minutes and resuspended again in 1µl/1 OD_{600} of extract buffer. Resuspensions were dropped into liquid nitrogen and lysed using a mortar and pestle. Following lysis, extract powder was thawed on ice and then spun down twice at 5000g for 5 minutes at 4°C. The 5000g supernatant was spun for 10 minutes at 18000g at 4°C. The 18000g supernatant (avoiding the pellet and lipid layer) was collected and saved on ice until ready for reactions. A Nanodrop Spectrophotometer was used to determine the protein concentration of extracts. 18000g supernatants were used the same day and never frozen.

For micrococcal nuclease treatments, 18000g supernatants were diluted to 80mg/ml in extract buffer with 5mM $CaCl_2$ and ~50 units of micrococcal nuclease. Reactions were placed at 37°C for 10 minutes and then stopped by adding 20mM EGTA. Reactions were placed on ice until ready to use for reactions. Mock reactions were prepared as a control and lacked only micrococcal nuclease. For Proteinase K, 2mg/ml was added to 18000g supernatants diluted in extract buffer. Reactions were set at room temperature for 15 minutes and then placed on ice until ready for use.

***In vitro* transcription**

Templates for mRNA transcription were generated by performing PCR using KOD Polymerase on pSP64 plasmids. For 12xMS2 variants and 47xCAG, templates for transcription were generated by performing PCR on those plasmids using Advantage GC 2 Polymerase. Primers for 12xMS2 variants contained T7 promoter and T7 termination sequences. Following PCR, products were run on a 1% agarose-TAE gel and gel isolated. Transcription was performed using mMessage Machine SP6 or Megascript T7 kits according to manufacturer’s protocol. Reactions were spiked with either Cy3- or Cy5-conjugated UTP (Enzo Lifesciences). RNAs were run on a denaturing gel to determine purity of products. RNAs were aliquoted, flash frozen in liquid nitrogen, and stored at -20°C for no longer than 1 month.

Stress granule assembly reaction

18000g supernatant was diluted to 80 mg/ml in extract buffer and incubated with *in vitro* transcribed RNA or mRNA. All reaction volumes totaled to 20µl. Reactions were incubated at room temperature for 15 minutes. 11µl of the reaction was placed between a microscope slide and coverslip. Particles were allowed to settle onto the coverslip for 5 minutes prior to imaging.

For assembly/nucleotide experiments, 18000g supernatant were diluted to 80 mg/ml in extract buffer with various amounts of ATP, AMPPNP, or GTP for 5 minutes prior to addition of 12xMS2 RNA. For disassembly/nucleotide experiments, 150 mg/ml 18000g supernatants were incubated with 12xMS2 RNA for 15 minutes and then diluted to 75 mg/ml in extract buffer with or without various amounts of ATP, AMPPNP, or GTP. These reactions were incubated for 30 minutes at room temperature prior to imaging.

Yeast Total RNA isolation

BY4741 strain was grown for 24 hours prior to RNA isolation. RNA was extracted using acid phenol-chloroform protocol. Total RNA was obtained by harvesting 40 OD600 units of cells and resuspending pellets in RNA lysis buffer (10mM EDTA, 50mM NaOAc pH 5.5). Next, SDS was added to a final volume of 1%. Samples were then subjected to a series of hot acid phenol/chloroform, acid phenol/chloroform, and chloroform extractions followed by precipitation. RNA was aliquoted, flash frozen and stored at -20°C for no longer than 1 month.

RNA phase separation

For phase separation reactions of 12xMS2 RNA, 47xCAG RNA, and NFT1mRNA, RNAs were diluted into 10mM Tris-HCl pH 8.0, 10mM Potassium Acetate, and 10mM

Magnesium Acetate. Reactions were denatured at 95°C for 3 minutes and cooled down to 23°C at 1-4°C/minute in a thermocycler. For non-phase separation conditions, RNA concentration was kept the same while excluding magnesium acetate from the reaction. RNA was then imaged immediately or 2µl of the RNA reaction was added to 18µl of 18000g supernatant and incubated for 15 minutes prior to imaging.

Yeast total RNA phase separation was performed as previously described. Total RNA and NFT1 mRNA was denatured at 95°C for 3 minutes and placed on ice immediately for 3 minutes. Total RNA and NFT1 mRNA was added to a mixture of 165mM NaCl, 1mM $MgCl_2$, and 7.5% PEG-4000 to a final concentration of 500ng/µl and xxx. For non-phase separating condition, RNA concentration was kept the same while excluding $MgCl_2$. Reactions were incubated at room temperature for 5 minutes. RNA was then imaged immediately or 2µl of the RNA reaction was added to 18µl of 18000g supernatant and incubated for 15 minutes prior to imaging.

Microscopy and Image Analysis

All images were acquired on a Zeiss Axiovert 200M fluorescent microscope equipped with a CSU-X1 spinning disk (Yokogawa), an iChromeMLE laser source (Toptica Photonics) and µManager version 1.4 software. For all images, a 2µm Z-stack was taken with slices at 0.25µm intervals using the 100X objective. Optimal Z-projections were obtained using FIJI along with subsequent image analysis.

To determine the number and size of foci per imaging field, the 3D Objects Counter Plugin was used. For nucleotide assembly, disassembly and maturation, the number of foci per imaging field for 5-7 images was determined and the average of each condition was calculated. The average of the conditions with nucleotides was normalized to the average of the nonnucleotide control. For maturation experiment, the average of 15, 30, 45 and 60 minutes were normalized to the average of the 5-minute time point. Circularity of structures was determined using the Analyze Particles Plugin. Intensity ratios were calculated by the ratio of the maximum fluorescent intensity of the foci to the mean fluorescent intensity of the area with no foci.

To calculate the fold intensities, a line was drawn over the image to first measure the mean and minimum fluorescent intensity of the lines for each channel. The maximum fluorescent intensity measurements of each channel along the line were generated using the Plot Profile Plugin. Fold intensity was determined by calculating the ratio of maximum fluorescent intensity at each position along the line minus the minimum fluorescent intensity to the mean fluorescent intensity minus the minimum fluorescent intensity.

Acknowledgements

We would like to thank Ankur Jain for assistance and planning of the RNA phase separation experiments.

Chapter 4 is a manuscript submitted for publication. It may appear in Cell. Begovich, K., Wilhelm, J.E. “Reconstitution of stress granules reveals properties of remodeling, maturation and RNA composition.” All experiments, imaging, data analysis and writing were my responsibility. J.E. Wilhelm helped edit/revise this manuscript. The dissertation author is the primary experimenter and author on this paper.

References

Anderson, P., and Kedersha, N. (2006). RNA granules. J. Cell Biol. *172*, 803–808.

Anderson, P., Kedersha, N., and Ivanov, P. (2015). Stress granules, P-bodies and cancer. Biochim. Biophys. Acta BBA - Gene Regul. Mech. *1849*, 861–870.

Boeynaems, S., Alberti, S., Fawzi, N.L., Mittag, T., Polymenidou, M., Rousseau, F. Schymkowitz, J., Shorter, J., Wolozin, B., Van Den Bosch, L., Tompa, P., Fuxreiter, M. (2018). Protein Phase Separation: A New Phase in Cell Biology. Trends Cell Biol. *28*, 420–435.

Buchan, J.R. (2014). mRNP granules. RNA Biol. *11*, 1019–1030.

Buchan, J.R., Yoon, J.-H., and Parker, R. (2011). Stress-specific composition, assembly and kinetics of stress granules in Saccharomyces cerevisiae. J. Cell Sci. *124*, 228–239.

Fan, A.C., and Leung, A.K.L. (2016). RNA Granules and Diseases — A Case Study of Stress Granules in ALS and FTLD. Adv. Exp. Med. Biol. *907*, 263–296.

Fay, M.M., Anderson, P.J., and Ivanov, P. (2017). ALS/FTD-associated C9ORF72 repeat RNA promotes phase transitions in vitro and in cells. Cell Rep. *21*, 3573–3584.

Han, T.W., Kato, M., Xie, S., Wu, L.C., Mirzaei, H., Pei, J., Chen, M., Xie, Y., Allen, J., Xiao, G., McKnight, S.L. (2012). Cell-free Formation of RNA Granules: Bound RNAs Identify Features and Components of Cellular Assemblies. Cell *149*, 768–779.

Hilliker, A., Gao, Z., Jankowsky, E., and Parker, R. (2011). The DEAD-Box Protein Ded1 Modulates Translation by the Formation and Resolution of an eIF4F-mRNA Complex. Mol. Cell *43*, 962–972.

Jain, A., and Vale, R.D. (2017). RNA Phase Transitions in Repeat Expansion Disorders. Nature *546*, 243–247.

Jain, S., Wheeler, J.R., Walters, R.W., Agrawal, A., Barsic, A., and Parker, R. (2016). ATPase-Modulated Stress Granules Contain a Diverse Proteome and Substructure. Cell *164*, 487–498.

Kedersha, N., Panas, M.D., Achorn, C.A., Lyons, S., Tisdale, S., Hickman, T., Thomas, M., Lieberman, J., McInerney, G.M., Ivanov, P., and Anderson, P. (2016). G3BP–Caprin1–USP10 complexes mediate stress granule condensation and associate with 40S subunits. J Cell Biol *212*, 845–860.

Khong, A., Matheny, T., Jain, S., Mitchell, S.F., Wheeler, J.R., and Parker, R. (2017). The Stress Granule Transcriptome Reveals Principles of mRNA Accumulation in Stress Granules. Mol. Cell *68*, 808-820.e5.

Li, P., Banjade, S., Cheng, H.-C., Kim, S., Chen, B., Guo, L., Llaguno, M., Hollingsworth, J.V., King, D.S., Banani, S.F., Russo, P.S., Jiang, Q.-X., Nixon, T., and Rosen, M.K (2012). Phase Transitions in the Assembly of Multi-Valent Signaling Proteins. Nature *483*, 336–340.

Lin, Y., Protter, D.S.W., Rosen, M.K., and Parker, R. (2015). Formation and Maturation of Phase-Separated Liquid Droplets by RNA-Binding Proteins. Mol. Cell *60*, 208–219.

Mahboubi, H., and Stochaj, U. (2017). Cytoplasmic stress granules: Dynamic modulators of cell signaling and disease. Biochim. Biophys. Acta BBA - Mol. Basis Dis. *1863*, 884–895

Markmiller, S., Soltanieh, S., Server, K.L., Mak, R., Jin, W., Fang, M.Y., Luo, E.C., Krach, F., Yang, D., Sen, A., Fulzele, A., Wozniak, J.M., Gonzalez, D.J., Kankel, M.W., Gao, F.-B., Bennett, E.J., Lecuyer, E., Yeo, G.E. (2018). Context-Dependent and Disease-Specific Diversity in Protein Interactions within Stress Granules. Cell *172*, 590-604.e13.

Mateju, D., Franzmann, T.M., Patel, A., Kopach, A., Boczek, E.E., Maharana, S., Lee, H.O., Carra, S., Hyman, A.A., and Alberti, S. (2017). An aberrant phase transition of stress granules triggered by misfolded protein and prevented by chaperone function. EMBO J. *36*, 1669–1687.

Matsuki, H., Takahashi, M., Higuchi, M., Makokha, G.N., Oie, M., and Fujii, M. (2013). Both G3BP1 and G3BP2 contribute to stress granule formation. Genes Cells *18*, 135–146.

McGurk, L., Gomes, E., Guo, L., Mojsilovic-Petrovic, J., Tran, V., Kalb, R.G., Shorter, J., and Bonini, N.M. (2018). Poly(ADP-Ribose) Prevents Pathological Phase Separation of TDP-43 by Promoting Liquid Demixing and Stress Granule Localization. Mol. Cell *71*, 703-717.e9.

Molliex, A., Temirov, J., Lee, J., Coughlin, M., Kanagaraj, A.P., Kim, H.J., Mittag, T., and Taylor, J.P. (2015). Phase Separation by Low Complexity Domains Promotes Stress Granule Assembly and Drives Pathological Fibrillization. Cell *163*, 123–133.

Nostramo, R., Varia, S.N., Zhang, B., Emerson, M.M., and Herman, P.K. (2015). The Catalytic Activity of the Ubp3 Deubiquitinating Protease Is Required for Efficient Stress Granule Assembly in Saccharomyces cerevisiae. Mol. Cell. Biol. *36*, 173–183.

Patel, A., Lee, H.O., Jawerth, L., Maharana, S., Jahnel, M., Hein, M.Y., Stoynov, S., Mahamid, J., Saha, S., Franzmann, T.M., Pozniakovski, A., Poser, I., Maghelli, N., Royer, L.A., Weigart, M., Meyers, E.W., Grill, S., Drechsel, D., Hyman, A.A., and Alberti, S. (2015). A Liquid-to-Solid Phase Transition of the ALS Protein FUS Accelerated by Disease Mutation. Cell *162*, 1066–1077.

Patel, A., Malinovska, L., Saha, S., Wang, J., Alberti, S., Krishnan, Y., and Hyman, A.A. (2017). ATP as a biological hydrotrope. Science *356*, 753–756.

Protter, D.S.W., and Parker, R. (2016). Principles and Properties of Stress granules. Trends Cell Biol. *26*, 668–679.

Protter, D.S.W., Rao, B.S., Treeck, B.V., Lin, Y., Mizoue, L., Rosen, M.K., and Parker, R. (2018). Intrinsically Disordered Regions Can Contribute Promiscuous Interactions to RNP Granule Assembly. Cell Rep. *22*, 1401–1412.

Putnam, A., Cassani, M., Smith, J., and Seydoux, G. (2018). Analysis of P granules. BioRxiv.

Sen, N.D., Zhou, F., Harris, M.S., Ingolia, N.T., and Hinnebusch, A.G. (2016). eIF4B stimulates translation of long mRNAs with structured 5′ UTRs and low closed-loop potential but weak dependence on eIF4G. Proc. Natl. Acad. Sci. *113*, 10464–10472.

Swisher, K.D., and Parker, R. (2010). Localization to, and Effects of Pbp1, Pbp4, Lsm12, Dhh1, and Pab1 on Stress Granules in Saccharomyces cerevisiae. PLOS ONE *5*, e10006.

Takahara, T., and Maeda, T. (2012). Transient Sequestration of TORC1 into Stress Granules during Heat Stress. Mol. Cell *47*, 242–252.

Treeck, B.V., and Parker, R. (2018). Emerging Roles for Intermolecular RNA-RNA Interactions in RNP Assemblies. Cell *174*, 791–802.

Van Treeck, B., Protter, D.S.W., Matheny, T., Khong, A., Link, C.D., and Parker, R. (2018). RNA self-assembly contributes to stress granule formation and defining the stress granule transcriptome. Proc. Natl. Acad. Sci. U. S. A. *115*, 2734–2739.

Walters, R.W., Muhlrad, D., Garcia, J., and Parker, R. (2015). Differential effects of Ydj1 and Sis1 on Hsp70-mediated clearance of stress granules in Saccharomyces cerevisiae. RNA *21*, 1660–1671.

Wippich, F., Bodenmiller, B., Trajkovska, M.G., Wanka, S., Aebersold, R., and Pelkmans, L. (2013). Dual Specificity Kinase DYRK3 Couples Stress Granule Condensation/Dissolution to mTORC1 Signaling. Cell *152*, 791–805.

Wheeler, J.R., Matheny, T., Jain, S., Abrisch, R., and Parker, R. Distinct stages in stress granule assembly and disassembly. ELife *5*.

Yang, X., Shen, Y., Garre, E., Hao, X., Krumlinde, D., Cvijović, M., Arens, C., Nyström, T., Liu, B., and Sunnerhagen, P. (2014). Stress Granule-Defective Mutants Deregulate Stress Responsive Transcripts. PLOS Genet. *10*, e1004763.

Youn, J.-Y., Dunham, W.H., Hong, S.J., Knight, J.D.R., Bashkurov, M., Chen, G.I., Bagci, H., Rathod, B., MacLeod, G., Eng, S.W.M., Angers, S., Morris, Q., Fabian, M., Cote, J.-F., and Gingras, A.-C. (2018). High-Density Proximity Mapping Reveals the Subcellular Organization of mRNA-Associated Granules and Bodies. Mol. Cell *69*, 517-532.e11.

Zid, B.M., and O'Shea, E.K. (2014). Promoter sequences direct cytoplasmic localization and translation of mRNAs during starvation in yeast. Nature *514*, 117–121.

Zinshteyn, B., Rojas-Duran, M.F., and Gilbert, W.V. (2017). Translation initiation factor eIF4G1 preferentially binds yeast transcript leaders containing conserved oligo-uridine motifs. RNA *23*, 1365–1375.

Chapter 5

Summary and Future Directions

Summary

While compartmentalization of biochemical processes into membrane-bound organelles is well known, the molecular mechanisms of cytoplasmic spatial organization remain poorly understood. Advances in microscopy techniques have revealed a plethora of cytoplasmic proteins and RNAs coalescing into biomolecular condensates (Banani et al., 2017; Shin and Brangwynne, 2017). My thesis work has focused on two different aspects of spatial organization within the cytoplasm: 1) identification of rules and regulations for metabolic enzyme assembly within individual pathways and the metabolic network and 2) identification of novel mechanisms that regulate stress granule (SG) assembly.

The first part of this thesis focused on determing any underlying patterns of metabolic enzyme assembly into intracellular condensates. While many targeted visual screens and proteomic approaches have highlighted the ability of metabolic enzymes to form supramolecular structures, it remained unclear what rules might predict or dictate their assembly (An et al., 2008; Narayanaswamy et al., 2009; Noree et al., 2010). In Chapter 2, I screened 440 metabolic enzymes from the yeast GFP collection at different stages of yeast growth and found that 60 enzymes assembled into filament or foci structures. This data set revealed that most metabolic enzymes that formed structures were enriched at branch points in the metabolic network suggesting that assembly plays a key regulatory role in mediating flux through their respective and connecting pathways. Consistent with this, my analysis of the first two enzymes in *de novo* purine biosynthesis pathway (Prs5 and Ade4) illustrated that assembly is highly coordinated and based on hierarchical position in the pathway. Additionally, my work revealed that not all metabolic enzymes are independent structures as a select subset of enzymes can associate with other membrane-less organelles like SGs. Thus, recruitment of an enzyme to another structure acts as another mechanism to regulate enzyme activity. Lastly, this work illustrates the conservation of PRPP synthetase polymerization across other higher order eukaryotes, revealing it as the second known metabolic filament that is conserved from yeast to humans.

The last two parts of this thesis is focused on identifying and testing new mechanisms that regulate SG assembly. Despite the fact that many of the known triggers for SG formation in yeast are nutrient or metabolic stresses, only two metabolic enzymes were found in SGs via proteomic studies (Jain et al., 2016; Mitchell et al., 2013). In Chapter 3, I identified 17 metabolic enzymes that robustly localized to SGs when grown to diauxic shift and stationary phase. Not only was their recruitment stress-specific, but I also found that AdoMet, which is the product of a SG-localized enzyme Sam1, regulates the formation of SGs. I observed a two-phase regulation of SG assembly and composition mediated by AdoMet in yeast. First, during diauxic shift, mutations in Sam1 that decreased AdoMet levels increased SG assembly, while mutations that increased AdoMet levels at this time point blocked the accumulation of 5'UTR associated proteins (Ded1, eIF4E, and eIF4G1) to SGs. Second, supplementation of AdoMet suppressed SG formation in response to azide or glucose starvation. Furthermore, I found that AdoMet-mediated regulation of SGs is conserved in human cell lines. In HeLa and U2OS cell lines, AdoMet blocked the fusion step in SG assembly suggesting that AdoMet might affect the recruitment of specific proteins required for fusion in proliferating cells. Similar to yeast SGs, AdoMet suppressed the formation of arsenite- and puromycin-induced SGs in motor neurons derived from amyotrophic lateral sclerosis (ALS) patients. Given the connection between SGs and ALS (Fernandes et al., 2018; Li et al., 2013), this work argues that AdoMet, or its targets, could be used as a potential therapeutic for ALS.

Despite reports suggesting a role for RNA-RNA interactions in regulating SG assembly, very few reports have supported this notion (Fay et al., 2017; Van Treeck et al., 2018). In Chapter 4, I developed a SG reconstitution system by coupling yeast cytoplasmic extracts with *in vitro*, transcribed, repeat containing RNA. Using a 12xMS2 stem loop RNA, I built SGs that contained SG-specific proteins and were sensitive to mutations that disrupted SG assembly *in vivo*. My work identified a pivotal role for ATP in regulating assembly and disassembly of SGs. While ATP hydrolysis was not required for SG assembly, it was necessary for SGs to disassemble. Furthermore, my work revealed that extracts depleted of ATP promote the formation of fibrous structures upon addition of 12xMS2 RNA. These structures were also observed when the reaction was taken out to longer time points suggesting that ATP levels are being reduced as the reaction proceeds. Consistent with this, *in vitro* assembled SGs became less dynamic over time and lost the ability to exchange RNAs with each other. My reconstitution system also allowed me to determine if the material state or composition of RNA is sufficient to build a SG. The recruitment of all SG markers to phase-separated, total yeast RNA, and not to phase-separated single RNAs (47xCAG or NFT1 mRNA), suggested that composition is important for assembling a canonical SG. Together, my work allowed me to validate and understand how RNA-RNA interactions mediate SG assembly.

Future Directions

Conservation of PRPP synthetase polymerization in human fibroblasts highlights the possibility of other metabolic enzymes assembling in human cell lines. However, we found no PRPP synthetase filaments in widely used human cells lines like HeLa cells. Due to their upregulated metabolic activity, identifying metabolic enzymes whose assembly state is driven by enzyme inactivity might not be possible in these cell lines. Thus, future work on conservation of enzyme condensation would require the use of other primary cell lines like fibroblasts, hepatocytes, and/or neurons. Utilization of various, non-immortalized cell lines would be important since gene expression profiles of metabolic enzymes can vary in different cell types. For example, in immortalized Huh7 cells, Mat2A, the human ortholog of yeast Sam1/2, is highly expressed where as the paralog, Mat1A, is not observed (Cai et al., 1998). However, in isolated primary hepatocytes, both versions are expressed (Cai et al., 1996). Thus, using the correct cell line will be important for identifying conservation of metabolic enzyme assembly.

PRPP synthetase filaments were detected with a custom, affinity purified antibody since we did not see filaments using other commercially available antibodies. The variability between antibodies could lead to problems for identifying conservation in other cell lines. To navigate this, transfection of epitope-tagged fusion constructs will be used to first identify enzyme assembly. Antibodies from those candidates capable of assembly will then be raised to validate our findings from the transfections to rule out any artifacts due to overexpression or tagging. Lastly, these candidate metabolic enzymes will be counterstained against other biomolecular condensates, such as purinosomes and SGs, to determine if they are independent structures (An et al., 2008; Protter and Parker, 2016). In addition to expanding the repertoire of metabolic enzyme assembly in human cells, these efforts could begin to provide a link to understand how atypical phenotypes emerge in various metabolic diseases.

While my work provides new insights into the connections between metabolism and SG assembly, the mechanisms that contribute to their interactions remain to be addressed. With protein methylation not playing a role in AdoMet-mediated SG phenotypes, the targets of AdoMet that regulate SG assembly remain unknown. However, fluctuations in metabolite concentration are known to alter signaling cascades (Carling, 2017; González and Hall, 2017). One approach to determine if AdoMet is acting through a signaling pathway would be to disrupt kinase function using gene deletion or pharmacological inhibitors and assay for rescue of AdoMet-mediated SG suppression in yeast. If any kinases scored as a positive hit, characterization of their downstream targets would be investigated for their role in AdoMet-mediated suppression of SGs. Any candidate hits would then be followed up in mammalian cells to identify conservation of mechanism.

Mammalian SGs assembly follows a step-wise process that begins with initial nucleation of small foci that then coalesce and fuse together to form bigger granules (Kedersha et al., 2005; Zhang et al., 2011). While knockdown of specific SG proteins prevents the initial nucleation step (Matsuki et al., 2013; Ohshima et al., 2015; Shih et al., 2012), it remains unknown which SG components control fusion. AdoMet's effect on preventing fusion of SGs provides a unique experimental set up to identify such components. Proximity labeling followed by mass spectrometry in AdoMet-treated vs AdoMet-untreated cells could help distinguish proteins required for fusion. Additionally, AdoMet is just one metabolite that has been tested for its effects on SG assembly. Given that AdoMet is the product of a metabolic enzyme associated with SGs, the results from my screen provide a roadmap to identify other metabolites that could regulate SG assembly.

While proteins found in SGs have been observed in harmful protein deposits in models of degenerative diseases like ALS and FTD, the connection between SGs and these aggregates is largely unknown. One disconnect is that most reports use triggers that allow for rapid assembly of SGs whereas toxic protein deposits occur over a much longer time scale (Jain et al., 2016; Markmiller et al., 2018). Recent work has highlighted that chronic starvation in mammalian cells assemble SGs that resemble disease-associated deposits and promote cell death (Reineke et al., 2018). This represents the first example of a chronic stress inducing SGs in proliferative cells and could resemble nutrient starvation-induced SGs in yeast. Given that metabolic enzymes don't accumulate in acute-stress induced SGs in yeast and mammalian cells, chronic starvation in mammalian cells presents a promising condition to identify conservation of metabolic enzyme recruitment to SGs. To accomplish this, HeLa and U2OS cell lines would be immunostained for SG markers and metabolic enzymes identified in Chapter 3 under chronic starvation conditions. Furthermore, AdoMet or any new metabolite identified above would be examined for their ability to suppress chronic starvation-induced SGs. This work would provide evidence for utilization of intermediate metabolites as potential therapeutics for these diseases.

Using a yeast extract reconstitution system, I identified that repeat containing RNAs nucleate SGs and that ATP regulates morphology and dynamics of SGs. While these experiments focused on ATP and its analogs, this system can be expanded to conduct a small molecule screen for compounds that target specific proteins or RNAs for their effects on assembly and disassembly. These experiments would provide further insights in the assembly pathway(s) of SGs. Additionally, the identification that phase-separation of 12xMS2 RNA requires a protein component from yeast extracts coupled with the requirement of mRNPs for recruitment of SG proteins suggests an stepwise process for formation of SGs. By pulling down 12xMS2 RNA from mock and MNase-treated extracts and performing mass spectrometry, one will be able to understand which proteins are needed for each step in this process. Candidates identified only in MNase-treated extracts would be assayed for their role to promote 12xMS2 RNA clustering and mRNP recruitment in mutant extracts. Furthermore, SG formation would be assayed in cells to couple the results from extract experiments with *in vivo* data. This would provide a previously unknown "protein interaction roadmap" to SG formation.

My reconstitution system allows for manipulation of various RNA features that couldn't be tested in cells. For example, mRNAs with poor codon optimality are enriched in both yeast and mammalian SGs when compared to SG-depleted mRNAs (Khong et al., 2017). The sequence of an SG-depleted mRNA could be mutated to contain poor codon optimality and assayed for its ability to form RNA foci and build a SG. Features like 5'UTR, transcript, and polyA tail length of mRNAs could also be examined as well.

While my work has focused mainly on how RNA phase separation contributes to SG assembly, the yeast cytoplasmic extracts could be utilized to ask questions about protein phase separation in a physiologically relevant environment. It's unclear if phase separation of any protein is sufficient to nucleate and recruit SG proteins. To test this, phase separation of a known SG protein (i.e. Ded1) would be added to extracts to determine its potential to recruit other endogenous SG proteins. Conversely, the same experimental setup would be performed with the phase separation of a protein not found in SGs (i.e. Pgk1) to establish if material state or protein specificity is important for SG assembly. These experiments would further validate yeast extracts as a system to study SGs and contribute to the idea of the "four-phase" model of SG formation.

References

An, S., Kumar, R., Sheets, E.D., and Benkovic, S.J. (2008). Reversible Compartmentalization of de Novo Purine Biosynthetic Complexes in Living Cells. Science *320*, 103–106.

Banani, S.F., Lee, H.O., Hyman, A.A., and Rosen, M.K. (2017). Biomolecular condensates: organizers of cellular biochemistry. Nat. Rev. Mol. Cell Biol. *18*, 285–298.

Cai, J., Sun, W., Hwang, J., Stain, S.C., and Lu, S.C. (1996). Changes in S-adenosylmethionine synthetase in human liver cancer: Molecular characterization and significance. Hepatology *24*, 1090–1097.

Cai, J., Mao, Z., Hwang, J.-J., and Lu, S.C. (1998). Differential Expression of Methionine Adenosyltransferase Genes Influences the Rate of Growth of Human Hepatocellular Carcinoma Cells. Cancer Res. *58*, 1444–1450.

Carling, D. (2017). AMPK signalling in health and disease. Curr. Opin. Cell Biol. *45*, 31–37.

Fay, M.M., Anderson, P.J., and Ivanov, P. (2017). ALS/FTD-associated C9ORF72 repeat RNA promotes phase transitions in vitro and in cells. Cell Rep. *21*, 3573–3584.

Fernandes, N., Eshleman, N., and Buchan, J.R. (2018). Stress Granules and ALS: A Case of Causation or Correlation? In RNA Metabolism in Neurodegenerative Diseases, R. Sattler, and C.J. Donnelly, eds. (Cham: Springer International Publishing), pp.173–212.

González, A., and Hall, M.N. (2017). Nutrient sensing and TOR signaling in yeast and mammals. EMBO J. *36*, 397–408.

Jain, S., Wheeler, J.R., Walters, R.W., Agrawal, A., Barsic, A., and Parker, R. (2016). ATPase-Modulated Stress Granules Contain a Diverse Proteome and Substructure. Cell *164*, 487–498.

Kedersha, N., Stoecklin, G., Ayodele, M., Yacono, P., Lykke-Andersen, J., Fritzler, M.J., Scheuner, D., Kaufman, R.J., Golan, D.E., and Anderson, P. (2005). Stress granules and processing bodies are dynamically linked sites of mRNP remodeling. J. Cell Biol. *169*, 871–884.

Khong, A., Matheny, T., Jain, S., Mitchell, S.F., Wheeler, J.R., and Parker, R. (2017). The Stress Granule Transcriptome Reveals Principles of mRNA Accumulation in Stress Granules. Mol. Cell *68*, 808-820.e5.

Li, Y.R., King, O.D., Shorter, J., and Gitler, A.D. (2013). Stress granules as crucibles of ALS pathogenesis. J. Cell Biol. *201*, 361–372.

Markmiller, S., Soltanieh, S., Server, K.L., Mak, R., Jin, W., Fang, M.Y., Luo, E.C., Krach, F., Yang, D., Sen, A., Fulzele, A., Wozniak, J.M., Gonzalez, D.J., Kankel, M.W., Gao, F.-B., Bennett, E.J., Lecuyer, E., Yeo, G.E. (2018). Context-Dependent and Disease-Specific Diversity in Protein Interactions within Stress Granules. Cell *172*, 590-604.e13.

Matsuki, H., Takahashi, M., Higuchi, M., Makokha, G.N., Oie, M., and Fujii, M. (2013). Both G3BP1 and G3BP2 contribute to stress granule formation. Genes Cells *18*, 135–146.

Mitchell, S.F., Jain, S., She, M., and Parker, R. (2013). Global Analysis of Yeast mRNPs. Nat. Struct. Mol. Biol. *20*, 127–133.

Narayanaswamy, R., Levy, M., Tsechansky, M., Stovall, G.M., O'Connell, J.D., Mirrielees, J., Ellington, A.D., and Marcotte, E.M. (2009). Widespread reorganization of metabolic enzymes into reversible assemblies upon nutrient starvation. Proc. Natl. Acad. Sci. *106*, 10147–10152.

Noree, C., Sato, B.K., Broyer, R.M., and Wilhelm, J.E. (2010). Identification of novel filament-forming proteins in Saccharomyces cerevisiae and Drosophila melanogaster. J. Cell Biol. *190*, 541–551.

Ohshima, D., Arimoto-Matsuzaki, K., Tomida, T., Takekawa, M., and Ichikawa, K. (2015). Spatio-temporal Dynamics and Mechanisms of Stress Granule Assembly. PLOS Comput. Biol. *11*, e1004326.

Protter, D.S.W., and Parker, R. (2016). Principles and Properties of Stress granules. Trends Cell Biol. *26*, 668–679.

Reineke, L.C., Cheema, S.A., Dubrulle, J., and Neilson, J.R. (2018). Chronic starvation induces noncanonical pro-death stress granules. J Cell Sci *131*, jcs220244.

Shih, J.-W., Wang, W.-T., Tsai, T.-Y., Kuo, C.-Y., Li, H.-K., and Wu Lee, Y.-H. (2012). Critical roles of RNA helicase DDX3 and its interactions with eIF4E/PABP1 in stress granule assembly and stress response. Biochem. J. *441*, 119–129.

Shin, Y., and Brangwynne, C.P. (2017). Liquid phase condensation in cell physiology and disease. Science *357*, eaaf4382.

Van Treeck, B., Protter, D.S.W., Matheny, T., Khong, A., Link, C.D., and Parker, R. (2018). RNA self-assembly contributes to stress granule formation and defining the stress granule transcriptome. Proc. Natl. Acad. Sci. U. S. A. *115*, 2734–2739.

Zhang, J., Okabe, K., Tani, T., and Funatsu, T. (2011). Dynamic association–dissociation and harboring of endogenous mRNAs in stress granules. J Cell Sci *124*, 4087–4095.

Appendix A

PRPS polymerization is required for proper lens fiber organization in zebrafish

Abstract

Phosphoribsoyl pyrphosphate synthetase (PRPS) catalyzes the first step in purine nucleotide synthesis. Mutations in PRPS have been implicated in a variety of diseases such as cancer or sensory neuropathies. Previously, we identified polymerization of PRPS in yeast, *Drosophila* oocyte, rat neurons, and human fibroblasts. However, the extent to which PRPS filament formation affects development remains unknown. In this report, we leveraged zebrafish as our model organism and created loss of function mutations in PRPS paralogs, *prps1a* and *prps1b*, to understand how PRPS filaments affect vertebrate development. First, PRPS filaments assemble in the retina at 5dpf. Second, we found that loss of *prps1a* alone was sufficient to generate severe small eye phenotype in zebrafish embryos. Additionally, truncation of *prps1a* robustly prevented PRPS filament formation and resulted in lens fiber disorganization in these mutants. Given that some mutations in PRPS result in optic atrophy, we identified a potential connection between PRPS polymerization and eye development in zebrafish.

Introduction

Proper coordination and compartmentalization of metabolic reactions is essential for maintaining cellular homeostasis. The localization of metabolic enzymes to membrane-bound organelles represents the most characterized mechanism for spatial organization in eukaryotic cells. However, over the past decade, its been shown that metabolic enzymes are capable of assembling into higher order structures (i.e. filaments or foci) in the cytoplasm (An et al., 2008; Narayanaswamy et al., 2009; Noree et al., 2010; Shen et al., 2016). Much work has focused on the connection between assembly and regulation of enzymatic activity. For instance, yeast CTP synthetase forms an inactive polymer in response to end product inhibition by CTP whereas enzymatic activity promotes polymerization of mammalian Acetyl-CoA carboxylase and phosphofructokinase (Hunkeler et al., 2018; Noree et al., 2014; Webb et al., 2017). Thus, formation of higher order structures can act as a mechanism to regulate flux through a particular metabolic pathway.

While many self-assembling enzymes were identified in yeast, other reports have revealed conservation of polymerization in other organisms. CTP synthetase filaments represent the best-characterized example of this conservation as polymerization has been observed in prokaryotes and higher order eukaryotes (Carcamo et al., 2011; Ingerson-Mahar et al., 2010; Liu, 2010; Noree et al., 2014). Recently, we found that phosphoribosyl pyrophosphate (PRPP) synthetase (PRPS), which catalyzes the conversion of ribose-5-phosphate to PRPP, forms filaments in yeast, *Drosophila* oocytes, rat hippocampal neurons, and human fibroblasts (Noree et al., submitted). Despite the identification of metabolic enzyme filaments in different cell types, it remains unknown if a relationship between the assembly of these polymers and other aspects of cell physiology and organ development exists.

The unusual disease phenotypes associated with loss-of-function (LoF) and gain-of-function mutations in PRPS provides a framework to potentially connect PRPS polymerization with defects in tissue development and function. Mutations that result in PRPP synthetase overexpression result in gout due to the overproduction of purines (Becker et al., 1982; Zoref et al., 1975). Secondly, loss-of-function mutations in PRPP synthetase cause sensorineural deafness, optic atrophy, ataxia, and, in severe cases, intellectual disability (Arts et al., 1993; Kim et al., 2007; Zoref et al., 1975). Lastly, mutations that disrupt feedback inhibition of PRPP synthetase result in phenotypes observed in both LoF and overexpression mutants (Ahmed et al., 1999; Becker et al., 1980, 1988a, 1988b; Zoref et al., 1975). The fact that similar defects are produced despite the different modes of enzyme misregulation suggests that PRPS polymerization may account for these phenotypes.

Despite the connection between PRPS and disease, only one animal model has been created in an effort to understand how altered PRPS function could cause the associated disease phenotypes (Pei et al., 2016). Creation of LoF alleles in the two zebrafish paralogs (*prps1a* and *prps1b*) of PRPS yielded embryos with smaller eyes and reduced hair cell number. These defects are consistent with the optic atrophy and hearing impairment observed in human patients. Additionally, the severity of these phenotypes increased as copies of mutant alleles increased with the most severe in *prps1a*$^{-/-}$;*prps1b*$^{-/-}$ mutants. These developmental perturbations are believed to be an effect of delays in cell cycle progression as a result of reduced nucleotide synthesis. While this study established a connection between PRPS activity and tissue development, the relationship between of PRPS filaments and the development of either of these organs remains unknown.

In this report, we examine the relationship between PRPS polymerization and retina morphogenesis in zebrafish. We find robust cytoplasmic filament formation of PRPS in the region adjacent to the retinal pigment epithelium, (choroid and sclera) of the retina at 5 days post-fertilization (dpf). To address the relationship between PRPS filaments and eye development, we generated LoF alleles in both *prps1a*and *prps1b*. Loss of *prps1a* alone was sufficient to generate a severe small eye phenotype, whereas mutations in *prps1b* failed to exhibit any developmental abnormalities. While both *prps1a*mutants resulted in smaller eyes, only the frameshift mutation predicted to truncate the Prps1a protein sequence failed to assembly PRPS filaments. Serendipitously, we find that loss of PRPS filaments results in a disrupted lens fiber network. Taken together, these results highlight the first connection between PRPS filaments and lens fiber defects in zebrafish.

Results

PRPS filaments assemble in the layer surrounding the RPE

Since previous work has highlighted that PRPS activity is important for proper eye development in zebrafish (Pei et al., 2016), we examined if PRPS assembled into filaments in the retina. Given that the PRPS polymerization was identified using an antibody raised against the human ortholog of PRPS (hPRPS1), we first performed BLAST analysis to compare hPRPS1 to both zebrafish paralogs, Prps1a and Prps1b. This analysis revealed that Prps1a and Prps1b had a ~92% and ~93% identity with hPRPS1 (Figure A.1A), suggesting that our antibody would recognize zebrafish PRPS. Next, we performed whole-mount immunofluorescence on 2 and 5 dpf embryos to identify polymerization of PRPS in the eye. At 2 dpf, PRPS staining in the eye appeared diffuse in the cytoplasm in the outer layer of the eye (Figure A.1B). However, at 5 dpf, we observed robust filament formation of PRPS (Figure A.1B).

Given that *prps1a* and *prps1a;prps1b* mutants resulted in a decrease in eye pigmentation (Pei et al., 2016), we tested if PRPS filaments localized to the retinal pigment epithelium (RPE) layer. However, PRPS filaments were not found in the RPE, but instead appeared to localize to the surrounding layer (Figure A.2A). This layer is compromised of the choroid followed by the sclera. Due to a lack of available markers for either layer, it's unclear in which layer PRPS filaments reside. Additionally, we find that PRPS filaments are not localized to the nucleus as in other examined eukaryotes (Figure A.2A and A.2B) (Noree et al., submitted). While its subcellular localization may not be conserved, the identification of PRPS filaments in the zebrafish eye provides a platform to examine the relationship between the polymer and eye development.

A

```
Human Prps1      MPNIKIFSGSSHQDLSQKIADRLGLELGKVVTKKFSNQETCVEIGESVRGEDVYIVQSGC 60
Zebrafish Prps1a MPNIKIFSGSSHPDLSQKIADRLGLELGKVVTKKFSNQETCVEIGESVRGEDVYIVQSGC 60
Zebrafish Prps1b MPNIKIFSGSSHQDLSQKIADRLGLELGKVVTKKFSNQETCVEIGESVRGEDVYIVQSGC 60
                 ************ ***********************************************

Human Prps1      GEINDNLMELLIMINACKIASASRVTAVIPCFPYARQDKKDK--SRAPISAKLVANMLSV 118
Zebrafish Prps1a GEINDNLMELLIMINACKIASASRVTAVIPCFPYARQDKKDKVGSRAPISAKLVANMLSV 120
Zebrafish Prps1b GEINDNLMELLIMINACKIASATRVTAVIPCFPYARQDKKDK--SRAPISAKLVANMLSV 118
                 **********************:*******************  ****************

Human Prps1      AGADHIITMDLHASQIQGFFDIPVDNLYAEPAVLKWIRENISEWRNCTIVSPDAGGAKRV 178
Zebrafish Prps1a AGADHIITMDLHASQIQGFFDIPVDNLYAEPAVLKWIKENINEWKNCTIVSPDAGGAKRV 180
Zebrafish Prps1b SGADHIITMDLHASQIQGFFDIPVDNLYAEPAVLKWIKENIPEWKNCTIVSPDAGGAKRV 178
                 :************************************:*** **:***************

Human Prps1      TSIADRLNVDFALIHKERKKANEVDRMVLVGDVKDRVAILVDDMADTCGTICHAADKLLS 238
Zebrafish Prps1a TSIADRLNVDFALIHKERKKANEVDRMVLVGDVKDRVAILVDDMADTCGTVCHAADKLVS 240
Zebrafish Prps1b TSIADRLNVDFALIHKERKKANEVDRMVLVGDVKDRVAILVDDMADTCGTVCHAADKLIS 238
                 **************************************************:*******:*

Human Prps1      AGATRVYAILTHGIFSGPAISRINNACFEAVVVTNTIPQEDKMKHCSKIQVIDISMILAE 298
Zebrafish Prps1a AGAIKVYAILTHGIFSGPAISRINNANFEAVVVTNTIPQEDKIKHCSKIQVIDISMILAE 300
Zebrafish Prps1b AGATKVYAILTHGIFSGPAISRINNACFEAVVVTNTIPQEEKMKHCPKIQVIDISMILAE 298
                 *** :********************* *************:*:*** *************

Human Prps1      AIRRTHNGESVSYLFSHVPL 318
Zebrafish Prps1a AIRRTHNGESVSYLFSHVPL 320
Zebrafish Prps1b AIRRTHNGESVSYLFSHVPL 318
                 ********************
```

B

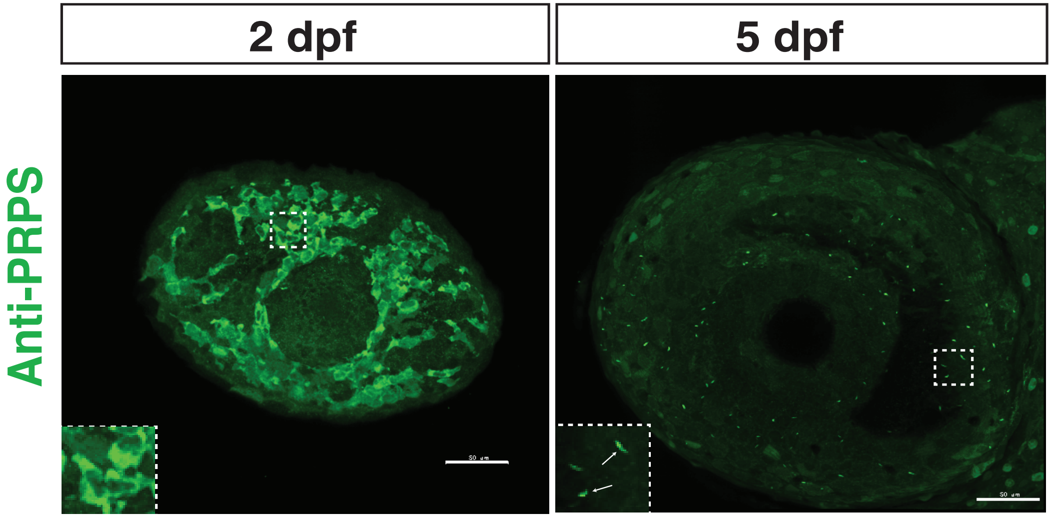

Figure A.1. PRPS forms filaments in the retina at 5 dpf
(A) Protein sequence alignment (UniProt) of human PRPP Synthetase (P60891) to zebrafish PRPP Synthetase paralogs Prps1a (Q4KME9) and Prps1b (Q08CA5). Human PRPS1 has ~96% identity to both zebrafish paralogs. **(B)** Antibody raised against human PRPS1 recognizes filaments at 5 dpf in the zebrafish eye. Representative confocal images of 2 dpf and 5 dpf embryos stained for PRPS. Scale bar: 50 µm. (n = 10 emrbyos for each time point)

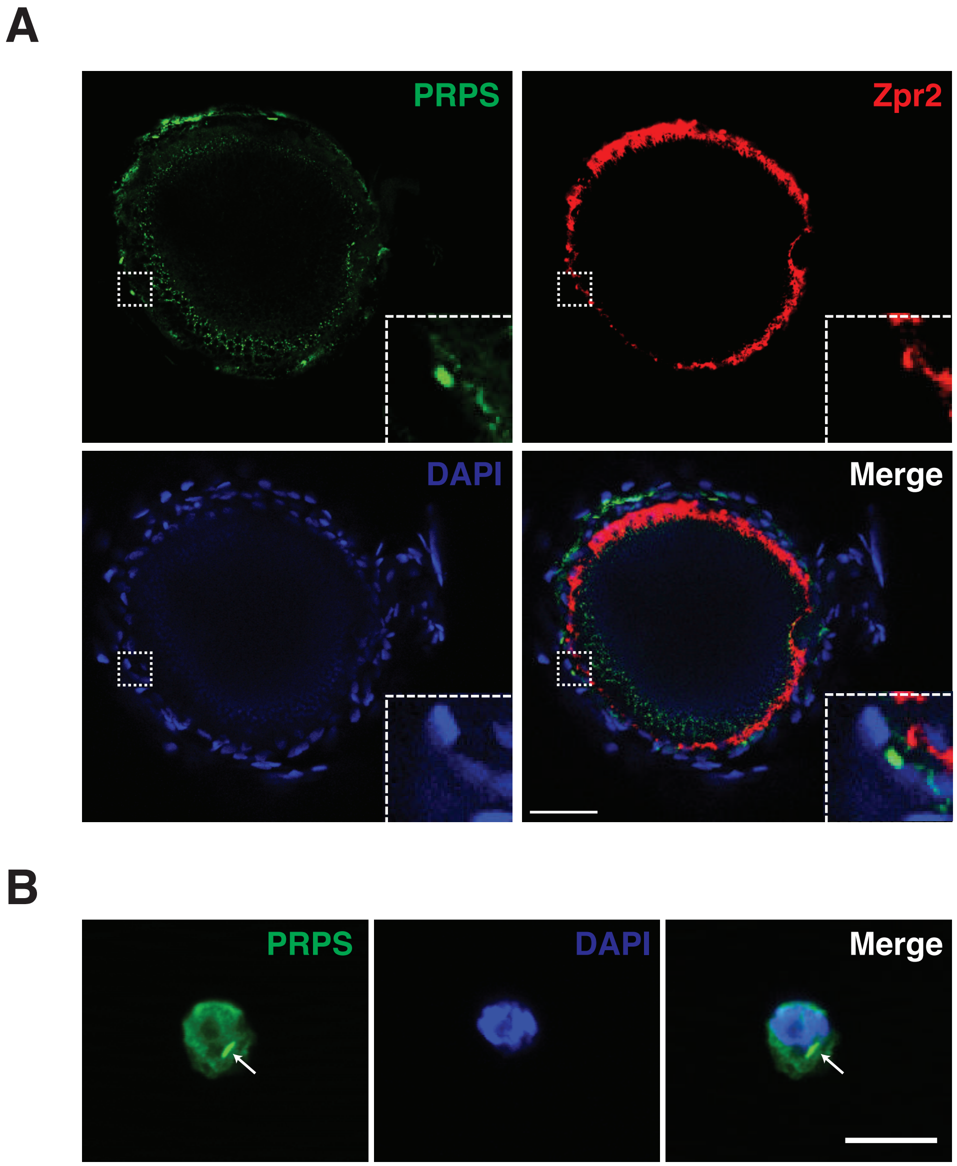

Figure A.2. PRPS cytoplasmic filaments assemble in sclera/choroid.
(A) Representative confocal images of 5 dpf embryos stained for PRPS, Zpr2 (RPE marker), and DAPI depicting PRPS filament formation in the cytoplasm and adjacent to the RPE layer. Scale bar: 40 µm. (n = 6 embryos) **(B)** Representative confocal images of a single cell dissected from retinal tissue stained for PRPS and DAPI depicting cytoplasmic localization of PRPS filaments. Arrows indicate PRPS filament. Scale bar: 10 µm. (n = 3 embryos)

LoF of *prps1a* alone is sufficient to decrease eye size

In order to assess the role of PRPS filaments and the eye development, we utilized CRISPR-Cas9 genome editing techniques to generate LoF mutants in both *prps1a* and *prps1b*. Two different guide RNAs (gRNAs) were used to target either exon 1 or exon 5 of the *prps1a* genomic locus, in addition to one gRNA that targets exon 2 in *prps1b* (Figure A.3A). For *prps1a*, we identified two alleles that resulted in different changes in the predicted protein sequence. The *prps1a*^{sd59} mutation caused a 1 bp deletion in exon 1 that introduced a frameshift and resulted in an early termination codon, while the *prps1a*^{sd60} allele had a 21 bp in-frame deletion in exon 5 leading to a 7 amino acid deletion (Figure A.3B and A.3C). For *prps1b*, the *prps1b*^{sd61} mutation introduced a 23 bp insertion that caused a frameshift and resulted in an early stop codon (Figure A.3B and A.3C).

Consistent with other *prps1a* and *prps1b* mutants (Pei et al., 2016), heterozygotes for our *prps1a* and *prps1b* mutations showed no distinguishable phenotypes (data not shown). However, homozygotes for either *prps1a* mutation resulted in reduced retina size at both 2 and 5dpf (Figure A.4A and A.4B). Additionally, both *prps1a* mutants had defects in inflation of the brain ventricle and swim bladder defects at 5 dpf, while *prps1*^{sd59} embryos showed a smaller yolk sac at 5 dpf. Homozygotes for the *prps1b* mutation showed no morphological changes at either time point (Figure A.4A and A.4B). Interestingly, we find no additional or more severe phenotypes in the *prps1a*^{sd59}*;prps1b*^{sd61} double homozygote. These results suggest that loss of *prps1a* function alone is sufficient to generate developmental defects. Given the similarities of eye phenotypes observed here and in previous work (Pei et al., 2016) along with the localization of PRPS filaments in the eye, we will focus on building a connection between PRPS assembly and retinal development.

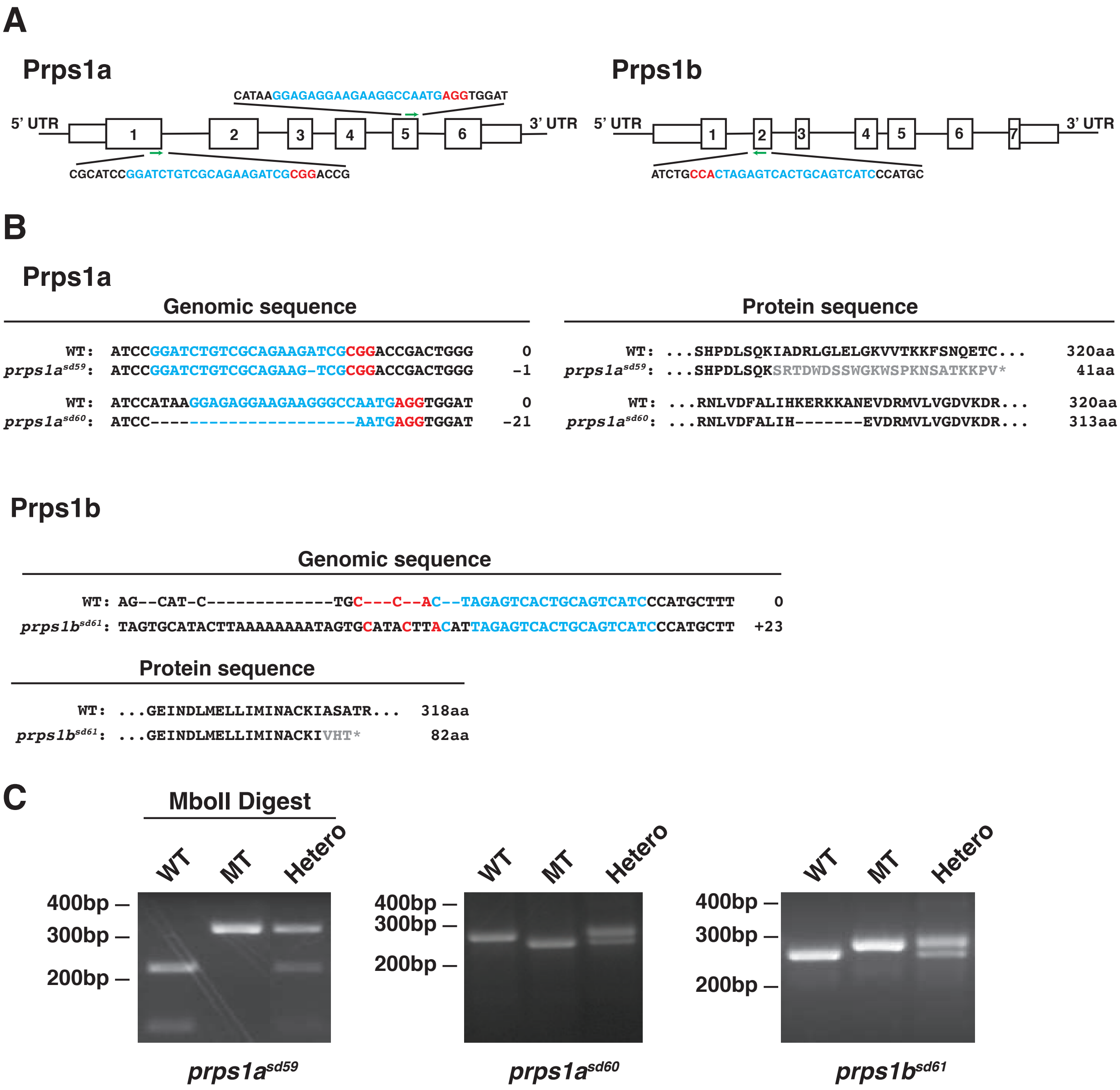

Figure A.3. Generation and genotyping of *prps1a* and *prps1b* mutations.
(A) Schematic of gRNAs targeting genomic loci of *prps1a* and *prpsb1*. Green arrows indicate where gRNAs target. Blue text depicts the sequence upstream of the PAM recognition sequence (red). **(B)** Schematic of changes in genomic (left) and predicted protein sequence (right) for *prps1a* and *prps1b*. Premature stop codons are shown as asterisks (*). Depicted protein sequences for prps1a display amino acids 11 – 41 (*prps1a*^{sd59}) and 186 – 216 (*prps1a*^{sd60}). Depicted protein sequence for prps1b display amino acids 61 – 84. **(C)** Representative agarose gel images of genotyping of *prps1a* and *prps1b* mutants. *prps1a*^{sd60} and *prps1b*^{sd61} mutants can be identified by changes in PCR product size. *prsp1a*^{sd59} mutants lose MboII restriction site in PCR product. MT indicates homozygous mutants

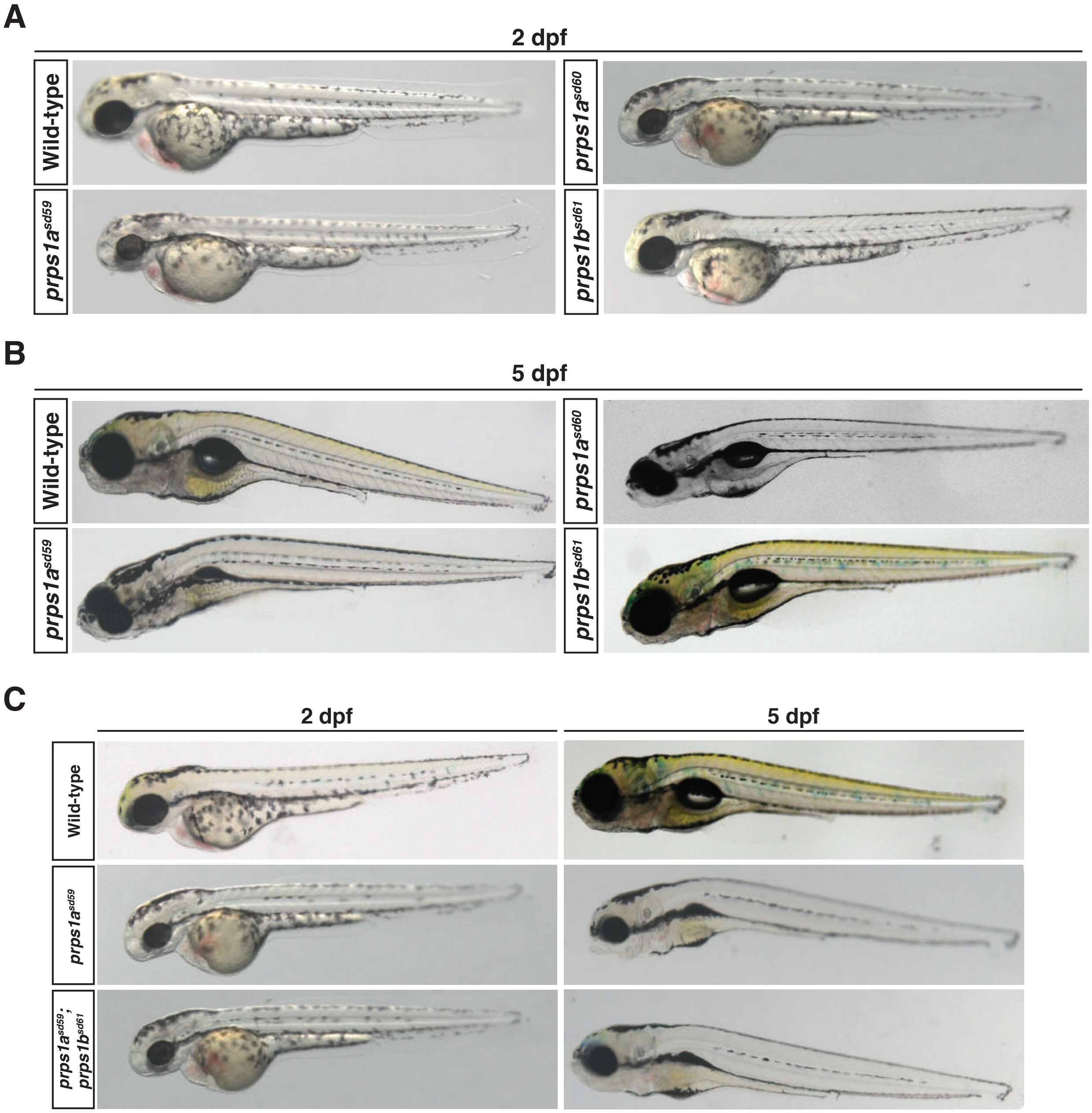

Figure A.4. Loss of *prps1a*, not prps1b, generates eye, pigmentation, brain ventricle and swim bladder phenotypes

(A) Representative bright-field images of wild-type, *prps1a*, and *prps1b* mutant embryos at 2 dpf. Reduced eye size and pigmentation are observed in both *prps1a* mutants, but not in *prps1b* mutants. (n = 16 embryos for each genotype) **(B)** Representative bright-field images of wild-type, *prps1a*, and *prps1b* mutant embryos at 5 dpf. Reduced eye size, yolk sac, swim bladder and brain ventricle defect are observed in both *prps1a* mutants, but not *prps1b*^{sd61} mutants. (n = 16 embryos for each genotype) **(C)** Representative bright-field images of wild-type, *prps1a*^{sd59}, and *prps1a*^{sd60}*; prps1b*^{sd61} mutant embryos at 2 dpf and 5 dpf. No additional phenotypes are observed in the double mutant compared to *prps1a*^{sd59} alone. (n = 12 embryos for each genotype and time point)

Truncation of *prps1a* blocks PRPS polymerization

Next, we sought to determine if either *prps1a* LoF allele disrupted PRPS filament formation in the eye. We raised WT and homozygous *prps1a* and *prps1b* mutant zebrafish to 5 dpf and performed whole-mount immunofluorescence to examine PRPS polymerization. PRPS staining revealed no filament formation in *prps1a*^{sd59} mutants whereas filaments were still observed in *prps1a*^{sd60} or *prps1b*^{sd61} mutants (Figure A.5). These data argue two points about PRPS polymerization in zebrafish. First, only *prps1a* is required for filament formation as filaments are still observed in truncated *prps1b* mutants. Second, while it's likely that both *prps1a* alleles decrease enzymatic activity as evident by the reduction of eye size, only a severe truncation in the *prps1a* protein was able to disrupt PRPS polymerization.

***Prps1a*^{sd59} mutants exhibit disrupted lens fiber organization**

As a part of our whole-mount immunofluorescence experiments, we used rhodamine phalloidin as a counterstain to test permeability in our protocol. Serendipitously, we observed a defect in lens fiber organization in the eyes of *prps1a*$^{A1-/-}$ mutants. In wild-type embryos, phalloidin staining robustly reveals a well-ordered and structured array of actin cables in the lens fibers at the center of the eye (Figure A.6A). However, in *prps1a*^{sd59} embryos, we found that this actin array in lens fibers is disrupted. Compared to lattice-like structure in wild-type embryos, *prps1a*^{sd59} mutants lacked regularly spaced radial and coaxial spokes (Figure A.6A). Additionally, an accumulation of actin is present at the center of the eye in *prps1a*^{sd59} embryos. The lens fiber disruption was specific to *prps1a*^{sd59} mutants as the phalloidin staining in *prps1a*^{sd60} and *prps1b*^{sd61} fish displayed an identical pattern from wild-type embryos (Figure A.6A). Since both of our *prps1a* mutations resulted in smaller eyes, it's possible that this additional defect in *prps1a*^{sd59} embryos is due to a lack of PRPS filaments. To test this, we examined the lens fiber organization at 2 dpf, when no PRPS filaments are evident (Figure

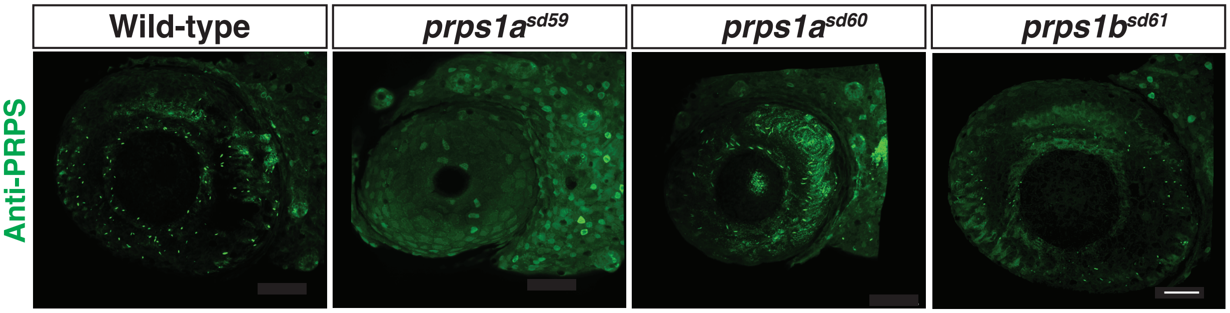

Figure A.5. Truncation of prps1a prevents PRPS filament formation.
Representative confocal images of 5 dpf embryos from wild-type, *prps1a*, and *prps1b* mutant backgrounds stained for PRPS. Only *prps1a*^{sd59} mutants failed to form PRPS filaments in the eye. Scale bar: 40 µm. (n = 12 embryos for wild-type, n = 8 for *prps1a*^{sd59} and *prps1a*^{sd60}, n = 7 for *prps1b*^{sd61})

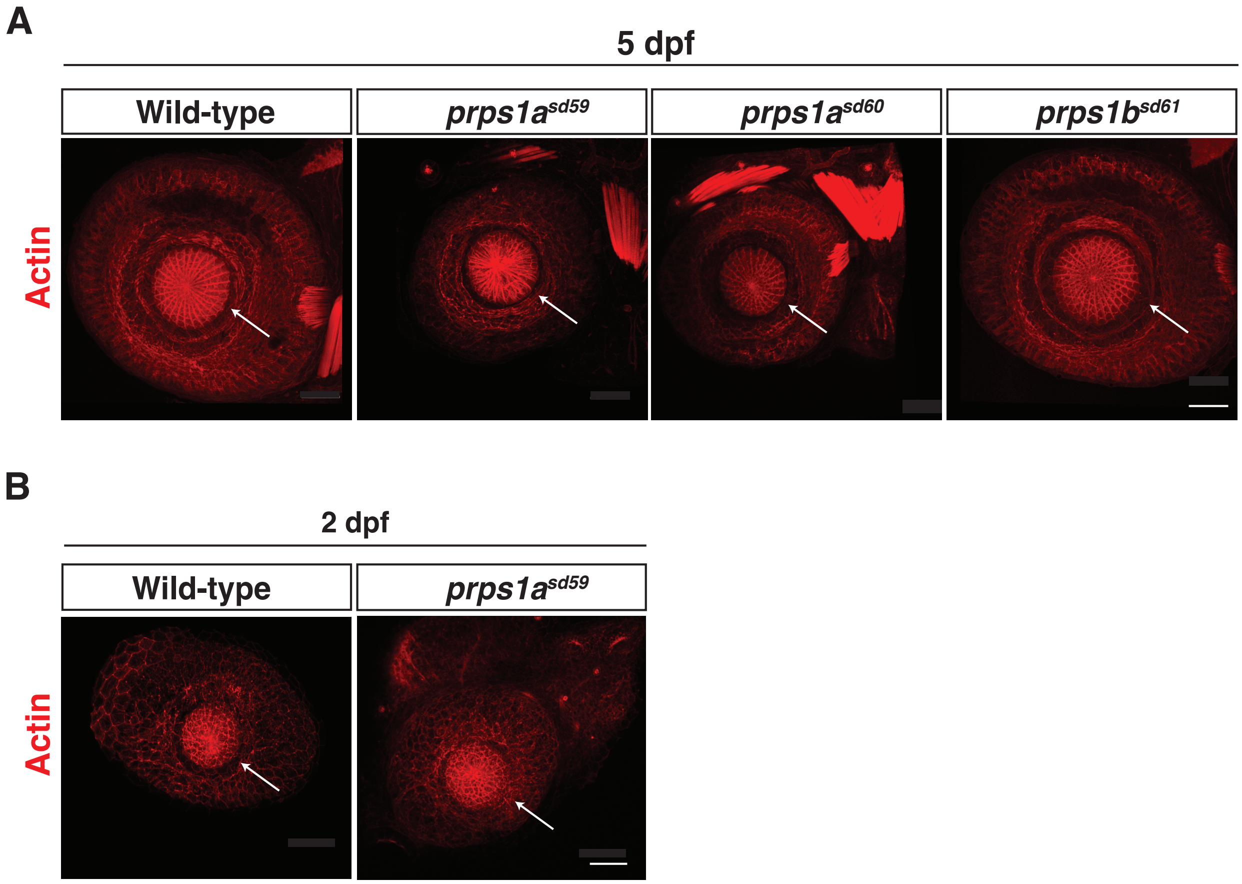

Figure A.6. Loss of PRPS filaments results in lens fiber disorganization.
(A) Representative confocal images of 5 dpf embryos from wild-type, *prps1a*, and *prps1b* mutant backgrounds stained with rhodamine phalloidin. Only *prps1a*^{sd59} mutants had disorganized lens fibers in the eye. Arrows indicate lens fiber core. Scale bar: 40 µm. (n = 12 embryos for wild-type, n = 8 for *prps1a*^{sd59} and *prps1a*^{sd60}, n = 7 for *prps1b*^{sd61}) **(B)** Representative confocal images of 2 dpf embryos from wild-type, *prps1a*, and *prps1b* mutant backgrounds stained with rhodamine phalloidin. No defects are observed in *prps1a*^{sd59} mutants at 2 dpf. Arrows indicate lens fiber core. Scale bar: 40 µm. (n = 6 embryos for each genotype)

A.1B). This would allow us to determine if lens fiber disorganization occurs at an earlier time point in development of *prps1a*^{sd59} embryos or if lens fiber disruption correlates with PRPS polymerization. In wild-type embryos at 2 dpf, the lens fibers displayed a honeycomb-like actin array (Figure A.6B). Unlike at 5dpf, we observed similar lens fiber organization in *prps1a*^{sd59} embryos at 2 dpf (Figure A.6B). Together, these results suggest a potential connection between PRPS filaments and lens fiber organization.

Cell polarity and retinal lamination is not affected in *prps1a*^{sd59} mutants

With the defect in actin organization in the lens fibers, we sought to determine if other cytoskeletal defects that also result in small eyes were present in *prps1a*^{sd59} embryos. For instance, mutants like *ncad*, *heart and soul (has)*, and *mosaic eyes (moe)* exhibited small eyes as a result of defects in cell polarity and retinal lamination (Horne-Badovinac et al., 2001; Jensen and Westerfield, 2004; Masai et al., 2003). To test if cell polarity was disrupted in *prps1a*^{sd59} mutants, we performed immunohistochemistry on cryosections of eyes from 5 dpf embryos and examined the localization of cell polarity marker ZO-1, which encodes for a tight-junction protein. At 5 dpf, ZO-1 is localized to the apical membrane of the photoreceptor cell layer (PCL) (Krock and Perkins, 2014) (Figure A.7A). Interestingly, we found no change in ZO-1 localization in *prps1a*^{sd59} mutants suggesting that cell polarity is not affected (Figure A.7A). Next, we performed phalloidin staining to determine if any defects in retinal patterning were observed in *prps1a*^{sd59} embryos at 5 dpf. Consistent with no change in cell polarity, *prps1a*^{sd59} embryos displayed a similar retinal layer organization as wild-type embryos despite the smaller eye size (Figure A.7B). Thus, the lens fiber defects observed in *prps1a*^{sd59} embryos are not accompanied by abnormalities in cell polarity and retinal lamination.

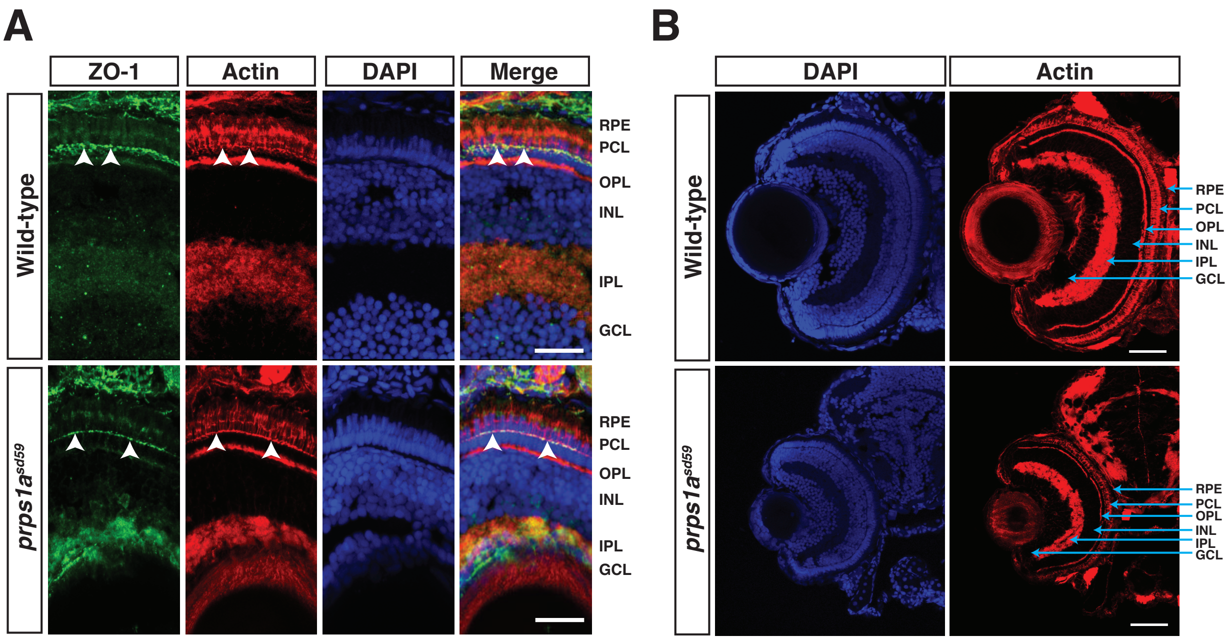

Figure A.7. Cell polarity and retina lamination is unaffected in *prps1a*^{sd59} mutants. **(A)** Representative confocal images of transverse cryosections from wild-type and *prps1a*^{sd59} mutant embryos at 5 dpf stained for ZO-1, actin, and DAPI. No change in ZO-1 localization is observed in *prps1a*^{sd59} mutants compared to wild-type fish. Arrowheads indicate ZO-1 localization to the apical membrane of the photoreceptor cell layer (PCL). Scale bar: 20 µm. (n = 6 embryos for each genotype) **(B)** Representative confocal images of transverse cryosections from wild-type and *prps1a*^{sd59} mutant embryos at 5 dpf stained for actin and DAPI. Retina patterning is unaffected in *prps1a*^{sd59} mutants. Scale bar: 20 µm. GCL, ganglion cell layer. IPL, inner plexiform layer. INL, inner nuclear layer. OPL, outer plexiform layer. PCL, photoreceptor cell layer. RPE, retina pigment epithelium. (n = 6 embryos for each genotype)

Discussion

PRPS is involved in the rate-limiting step in purine nucleotide synthesis. Previously, we found that PRPS assembles in filaments in eukaryotes ranging from yeast, fruit flies and humans (Noree et al submitted). In this study, we identified polymerization of PRPS in the zebrafish embryonic retina at 5 dpf. Not only did loss-of-function mutation in *prps1a* result in small eyes, but also the truncation of *prps1a* prevented PRPS filament assembly. Serendipitously, we found that loss of PRPS filaments resulted in disorganized lens fibers in the retina. These results suggest the first connection between PRPS filament assembly and lens fiber organization.

Our finding that loss of *prps1a* activity resulted in small eye phenotypes is consistent with another PRPS zebrafish model (Pei et al., 2016). However, we observed some discrepancies between our two studies. Pei et al found increased severity of developmental defects with either maternal-zygotic homozygotes of *prps1a* or *prps1a*$^{-/-}$;*prps1b*$^{-/-}$ double mutants. Conversely we found that zygotic homozygotes of *prps1a* alone was sufficient to match the early onset of reduced eye size seen in their *prps1a*$^{-/-}$;*prps1b*$^{-/-}$ double mutants. This discrepancy could be due to the relative strength of the LoF alleles used between studies. *prps1a* mutants from Pei et al were generated using retroviral insertion in the first intron, resulting in destabilized mRNA levels. However, our CRISPR-Cas9-generated *prps1a* mutants are predicted to result in significant changes in the protein sequence, potentially resulting in significantly diminished Prps1a activity. Consistent with the increased potency of our alleles, we found that *prps1a* homozygotes exhibited defects in the inflation of the brain ventricle and swim bladder. It’s also possible that our *prps1a* mutations exert a dominant effect on *prps1b* function. While it's unclear if Prps1a and Prps1b physically interact with each other, interactions between paralogous proteins has been observed in yeast PRPS and is a common hallmark of duplicated metabolic enzymes (Hernando et al., 1998). Additionally, our observations that loss of *prps1b* activity had no morphological abnormalities suggested that prps1a activity is the main contributor in zebrafish development. Genetic compensation for the loss of *prps1b* via *prps1a* could also explain for the lack of phenotypes observed in *prps1b* mutants.

Given that mutations in downstream purine biosynthetic enzymes *gart* and *paics* possessed defects in eye pigmentation (Ng et al., 2009) similar to our *prps1a* mutants, we wondered if PRPS filaments were localized to the RPE. Instead, our staining revealed that PRPS filaments assembled in the choroid/sclera layer adjacent to the RPE. Both the choroid and sclera are compromised of melanocytes, fibroblasts, and immunocompetent cells to assist and offer protection to the interior retinal layers (Metlapally and Wildsoet, 2015; Zhang and Wildsoet, 2015). Since these cell types are very metabolically active, its possible that PRPS's role is to provide PRPP and/or purine nucleotides to support the other layers of the retina. This also raises the question of whether PRPS filaments are active or inactive in zebrafish. While assembly of PRPS in yeast correlates with decrease activity (Noree et al, submitted), the enzymatic state of a filament alters from organism to organism (Lynch et al., 2017; Noree et al., 2014). Having an active PRPS filament at 5 dpf would make sense as this coincides with the shrinkage of the yolk and subsequently, depletion of metabolites supplied from that source. Since the retina continues to grow in zebrafish, assembly of active PRPS filaments would be beneficial around this time point.

In addition to preventing PRPS assembly, *prps1a*^{sd59} mutants also exhibited a disrupted lens fiber array in the retina. We demonstrate that this effect was not simply due to a loss of Prps1a activity as *prps1a*^{sd60} mutants, who also displayed small eyes, retained a lens fiber pattern similar to wild-type embryos. This suggested that PRPS filaments play a role in maintaining lens fiber organization. However, it remains unclear how lens fiber organization is disrupted in *prps1a*^{sd59} mutants. Previous studies have shown mutations in genes involved in endocytic trafficking and ubiquitin proteasome system are involved in the lens fiber differentiation and morphogenesis and display early lens fiber phenotypes (Imai et al., 2010; Mochizuki et al., 2018). However, we demonstrate that lens fibers remain intact at these early time points in *prps1a*^{sd59} mutants. Additionally, early lens fiber defects observed in *fn1* and *itga5* mutants result in the formation of cataracts (Hayes et al., 2012). Since we found no cataracts in *prps1a*^{sd59} embryos, these data suggests that lens fiber disruption could be due to defects in maintenance of lens fibers rather than development of the lens. Furthermore, our immunostaining protocol provides a quick and robust method for observing lens fiber organization.

One question that remains unclear is how PRPS filament formation in the choroid/sclera affects lens fiber organization in a cell non-autonomous manner. It's unknown what kind of crosstalk exists between these tissues. Given the proximity of the choroid with other layers of the retina like the RPE or PCL, it's unclear if defects in the choroid can regulate other aspects (i.e. cell polarity) in proximal tissues. However, we found no evidence of this in the case of cell polarity, as ZO-1 localization was unaffected in *prps1a*^{sd59} mutants. The intact PCL polarity in *prps1a*^{sd59} embryos suggested that the cell polarity of other tissues is intact highlighting the specificity of this phenotype to the lens fibers.

Despite this cell non-autonomous effect of *prps1a*^{sd59} mutants, our observation of lens fiber disorganization in filament-deficient mutants suggests an additional role for PRPS assembly in eye development. This secondary role of PRPS polymerization could provide a framework to connect PRPS polymerization with PRPS-associated disease phenotypes. For example, optic atrophy is a common phenotypes observed in many cases of PRPS-linked diseases (de Brouwer et al., 2010; Park et al., 2013). Missense variants of human PRPS1 have also been identified to cause retinal degeneration (Fiorentino et al., 2018). However, it's unclear what the functional significance of the lens fiber disorganization in *prps1a*^{sd59} mutants and if this phenotype contributes to PRPS-associated disease defects like optic atrophy and retinal degeneration. Some potential causes for this discrepancy could be due to differences in alleles (protein truncation vs point mutation) or species-specific effects. Regardless, establishing a connection between the secondary role of PRPS assembly and disease-specific phenotypes might be better suited in other tissues. Since the deafness and ataxia can arise from LoF or feedback inhibition mutations in hPRPS1, the identification of PRPS assembly in the hair cells and neurons of zebrafish could provide a potential pathway for linking PRPS filament formation with other PRPS-related phenotypes.

Materials and Methods

Zebrafish maintenance

Zebrafish (*Danio rerio*) were raised and maintained on a 14 h light/10 h dark cycle using standard protocols. The embryos used for these studies were obtained by natural spawning and raised at approximately 28°C with their developmental stage determined in days post-fertilization. All experiments followed Institutional Animal Care and Use Committee-approved protocols.

Generation of PRPS mutants and genotyping

Identification of target sites and generation of gRNAs were conducted according to a previously established protocol (Gagnon et al., 2014). In brief, an online webtool, CHOPCHOP, was used to identify target sites for CRISPR/Cas9-mediated mutagenesis. DNA templates for gRNAs were created using a cloning-independent protocol with oligonucleotides from IDT Technologies. gRNAs (*prps1a* exon 1: CGCATCCGGATCTGTCGCAGAAGATCGCGGACCG, *prps1a* exon 5: CATAAGGAGAGGAAGAAGGCCAATGAGGTGGAT, *prps1b* exon 2: ATCTGCCACTAGAGTCACTGCAGTCATCCCATGC) were transcribed using the MEGAshortscript T7 transcription kit and cleaned up according to the manufacturer's protocol. gRNAs were stored at -20°C until ready for use.

gRNAs were incubated with EnGen Spy Cas9 NLS protein (New England BioLabs) for 5 minutes at room temperature and placed on ice until ready for injection. All injections were performed in the wild-type strain AB. Injected embryos were raised to adulthood to generate potential founder fish (F_0). To determine somatic indel frequency associated with each gRNA, a small population of injected embryos was sacrificed to obtain genomic DNA (Meeker et al., 2007). The genomic locus flanking the target loci was amplified via PCR using KOD Hot Start Polymerase. PCR products were purified and sent for sequencing (Eton Sequencing) to identify secondary peaks in the resulting chromatogram.

Next, F_0 fish were outcrossed to create the F_1 generation and germline transmission was determined in the same fashion as mentioned above. Adult F_1 progeny were fin clipped to obtain genomic DNA. Fish were genotyped by performing TA cloning and sequencing to ensure clean sequencing reads. Heterozygous mutant fish were kept for further breeding. For *prps1a*^{sd59} mutants, the primer pair 5'-CTGTACGCCACCCCGACACTATAGG-3' and 5'-GAGTCCGCTGCCTGTGAGACTCG-3' amplified a 329 bp PCR product flanking the targeted gRNA site. While digestion with MboII creates 230 and 99 bp fragments in wild-type alleles, the *prps1a*^{sd59} allele has lost the MboII restriction site and remains uncut. In *prps1a*^{sd60} mutants, the PCR product using the primer pair 5'-GTGCAGAGAAGTCTAAATGCATCT-3' and 5'-CTGCATATCATGCATGTCCTCAC-3' created a 258 bp band compared to the 279 bp size product in wild-type fish. In *prps1b*^{sd61} mutants, the PCR product using the primer pair 5'-TCCTGCAGTGTGGAGATTGG-3' and 5'-TGGCTATAGACATTACCAGCACA-3' created a 285 bp band compared to the 262 bp size product in wild-type fish. The change in PCR product size for prps1a and prps1b alleles could be visualized on a 3% TAE-agarose gel. Representative gels genotyping for each allele is shown in Figure 3C. Since *prps1b*^{sd61} mutants exhibited no morphological phenotypes, embryos were imaged prior to collecting genomic DNA for genotyping.

Whole-mount immunofluorescence

Embryos were grown to indicated time points and fixed in 4% paraformaldehyde (PFA) in PBS at 4°C overnight. PFA was removed and embryos were washed 5 times in PBS for 5 minutes at room temperature. Embryos were then permeablized in PBS-Triton 2% for 1.5 hours. After 5 PBS-0.5% Triton washes, embryos were blocked in 2% BSA in PBS-0.5% Triton for 1 hour. Rabbit anti-hPRPS1 polyclonal antiserum was diluted 1:1000 in blocking solution and embryos were incubated O/N at 4°C. Following 5 PBS-0.5% Triton washes, embryos were incubated with 1:200 goat anti-rabbit Alexa Fluor 488 and 1:200 rhodamine phalloidin for 2 hours at room temp in the dark. After washing to remove unbound secondary antibodies and phalloidin, embryos were stored in SlowFade Gold Antifade with DAPI prior to imaging at 4°C. Upon imaging, 50% glycerol was added to embryos before they were mounted for imaging..

Dissection of retinas and immunostaining

Retina dissection and trypsinization followed a previously established protocol (Zou et al., 2008). In brief, retinas from embryos at 5 dpf were manually dissected and placed in DMEM media. Next, retinas were trypsinized in TrypLE Express for 30 minutes at room temperature. FBS was added to 10% to inhibit trypsin activity. Intact retinas were discarded and disassociated cells were pelleted by spinning down for 2 minutes at 3000 rpm. Supernatant was removed and pellets were resuspended in 1xPBS and added to poly-l-lysine coated dishes for 1 hour at room temperature. Adhered cells were then fixed in 4% PFA for 30 min at room temperature. Following 3 PBS washes, cells were permeabilized for 15 minutes in PBS- 0.5% Triton and subsequently blocked in 2% BSA in PBS for 30 minutes. 1:1000 rabbit anti-hPRPS1 was added to blocking solution and incubated at 4°C O/N. Following 3 PBS washes, cells were incubated in 1:200 goat anti-rabbit Alexa Fluor 488 for 2 hours in the dark. After removing unbound secondary antibody, SlowFade Gold Antifade with DAPI was added and cells were imaged immediately.

Histology

Embryos were grown to indicated time points in E3/PTU and fixed in 4% PFA in PBS at 4°C overnight. Following 3 PBS washes, embryos were dropped in 35% sucrose until embryos sunk to the bottom. 35% sucrose/PBS solution was removed by washing once with OCT freezing medium. Cryomolds were prepared by lining up embryos in OCT freezing medium and freezing on dry ice. Cryomolds were stored at -80°C until ready for use. Sections were cut at 12μm thickness and transferred onto a microscope slide. Areas of interest were outlined with a hydrophobic PAP pen prior to rehydrating slides in PBS-0.1% Tween-20 for 5 minutes. Sections were blocked in 2% BSA in PBS-0.1% Tween-20 for 1 hour at room temp followed by addition of primary antibodies in blocking solution (1:200 mouse anti-Zpr2 and 1:200 rabbit anti ZO-1) O/N at 4°C. Following 3 PBS-0.1% Tween washes, sections were incubated in secondary solution (1:200 goat anti-rabbit Alexa Fluor 488, 1:200 sheep anti-mouse Alexa Fluor 546, or 1:200 Rhodamine Phalloidin) for 2 hours at room temperature in the dark. After 3 PBS-0.1% Tween washes, slides were dried and SlowFade Gold Antifade with DAPI was added before sealing with a coverslip and nail polish. Slides were stored at 4°C until ready for imaging.

Imaging

Images were captured using a Zeiss Axioimager and Axiocam and were processed using Zeiss Axiovision and Adobe Creative Suite software. Confocal imaging was performed with a Leica SP5 confocal laser-scanning microscope and analyzed using Imaris software (Bitplane).

Replicates

All assessments of phenotypes and immunofluorescence were replicated in at least two experiments with comparable results from independent crosses. For each experiment, the n is reported in the associated figure legend.

Acknowledgements

Appendix A is a manuscript in preparation and will be submitted for publication. Begovich, K., Yelon, D., J.E. Wilhelm. “PRPS polymerization is required for proper lens fiber organization in zebrafish.” All experiments, imaging, data analysis and writing were my responsibility. D. Yelon and J.E. Wilhelm helped edit/revise this manuscript. The dissertation author is the primary experimenter and author on this paper.

References

Ahmed, M., Taylor, W., Smith, P.R., and Becker, M.A. (1999). Accelerated Transcription of PRPS1 in X-linked Overactivity of Normal Human Phosphoribosylpyrophosphate Synthetase. J. Biol. Chem. *274*, 7482–7488.

An, S., Kumar, R., Sheets, E.D., and Benkovic, S.J. (2008). Reversible Compartmentalization of de Novo Purine Biosynthetic Complexes in Living Cells. Science *320*, 103–106.

Arts, W.F.M., Loonen, M.C.B., Sengers, R.C.A., and Slooff, J.L. (1993). X-linked ataxia, weakness, deafness, and loss of vision in early childhood with a fatal course. Ann. Neurol. *33*, 535–539.

Becker, M.A., Raivio, K.O., Bakay, B., Adams, W.B., and Nyhan, W.L. (1980). Variant human phosphoribosylpyrophosphate synthetase altered in regulatory and catalytic functions. J. Clin. Invest. *65*, 109–120.

Becker, M.A., Losman, M.J., Itkin, P., and Simkin, P.A. (1982). Gout with superactive phosphoribosylpyrophosphate synthetase due to increased enzyme catalytic rate. J. Lab. Clin. Med. *99*, 495–511.

Becker, M.A., Puig, J.G., Mateos, F.A., Jimenez, M.L., Kim, M., and Simmonds, H.A. (1988a). Inherited superactivity of phosphoribosylpyrophosphate synthetase: Association of uric acid overproduction and sensorineural deafness. Am. J. Med. *85*, 383–390.

Becker, M.A., Puig, J.G., Mateos, F.A., Jimenez, M.L., Kim, M., and Simmonds, H.A. (1988b). Inherited superactivity of phosphoribosylpyrophosphate synthetase: Association of uric acid overproduction and sensorineural deafness. Am. J. Med. *85*, 383–390.

de Brouwer, A.P.M., van Bokhoven, H., Nabuurs, S.B., Arts, W.F., Christodoulou, J., and Duley, J. (2010). PRPS1 Mutations: Four Distinct Syndromes and Potential Treatment. Am. J. Hum. Genet. *86*, 506–518.

Carcamo, W.C., Satoh, M., Kasahara, H., Terada, N., Hamazaki, T., Chan, J.Y.F., Yao, B., Tamayo, S., Covini, G., Mühlen, C.A. von, and Chan, E.K.L. (2011). Induction of Cytoplasmic Rods and Rings Structures by Inhibition of the CTP and GTP Synthetic Pathway in Mammalian Cells. PLOS ONE *6*, e29690.

Fiorentino, A., Fujinami, K., Arno, G., Robson, A.G., Pontikos, N., Armengol, M.A., Plagnol, V., Hayashi, T., Iwata, T., Parker, M., Fowler, T., Rendon, A., Gardner, J.C., Henderson, R.H., Cheetham, M.E., Webster, A.R., Michaelides, M., and Hardcastle, A.J. (2018). Missense variants in the X-linked gene PRPS1 cause retinal degeneration in females. Hum. Mutat. *39*, 80–91.

Gagnon, J.A., Valen, E., Thyme, S.B., Huang, P., Ahkmetova, L., Pauli, A., Montague, T.G., Zimmerman, S., Richter, C., and Schier, A.F. (2014). Efficient Mutagenesis by Cas9

Protein-Mediated Oligonucleotide Insertion and Large-Scale Assessment of Single-Guide RNAs. PLOS ONE *9*, e98186.

Hayes, J.M., Hartsock, A., Clark, B.S., Napier, H.R.L., Link, B.A., and Gross, J.M. (2012). Integrin α5/fibronectin1 and focal adhesion kinase are required for lens fiber morphogenesis in zebrafish. Mol. Biol. Cell *23*, 4725–4738.

Hernando, Y., Parr, A., and Schweizer, M. (1998). PRS5, the Fifth Member of the Phosphoribosyl Pyrophosphate Synthetase Gene Family in Saccharomyces cerevisiae, Is Essential for Cell Viability in the Absence of either PRS1 or PRS3.*180*, 4.

Horne-Badovinac, S., Lin, D., Waldron, S., Schwarz, M., Mbamalu, G., Pawson, T., Jan, Y.-N., Stainier, D.Y.R., and Abdelilah-Seyfried, S. (2001). Positional cloning of heart and soul reveals multiple roles for PKCλ in zebrafish organogenesis. Curr. Biol. *11*, 1492–1502.

Hunkeler, M., Hagmann, A., Stuttfeld, E., Chami, M., Guri, Y., Stahlberg, H., and Maier, T. (2018). Structural basis for regulation of human acetyl-CoA carboxylase. Nature *558*, 470–474.

Imai, F., Yoshizawa, A., Fujimori-Tonou, N., Kawakami, K., and Masai, I. (2010). The ubiquitin proteasome system is required for cell proliferation of the lens epithelium and for differentiation of lens fiber cells in zebrafish. Development *137*, 3257–3268.

Ingerson-Mahar, M., Briegel, A., Werner, J.N., Jensen, G.J., and Gitai, Z. (2010). The metabolic enzyme CTP synthase forms cytoskeletal filaments. Nat. Cell Biol. *12*, 739–746.

Jensen, A.M., and Westerfield, M. (2004). Zebrafish Mosaic Eyes Is a Novel FERM Protein Required for Retinal Lamination and Retinal Pigmented Epithelial Tight Junction Formation. Curr. Biol. *14*, 711–717.

Kim, H.-J., Sohn, K.-M., Shy, M.E., Krajewski, K.M., Hwang, M., Park, J.-H., Jang, S.-Y., Won, H.-H., Choi, B.-O., Hong, S.H., Kim, B.J., Suh, Y.L., Ki, C.S., Lee, S.Y., Kim, S.H., and Kim, J.W. (2007). Mutations in PRPS1, Which Encodes the Phosphoribosyl Pyrophosphate Synthetase Enzyme Critical for Nucleotide Biosynthesis, Cause Hereditary Peripheral Neuropathy with Hearing Loss and Optic Neuropathy (CMTX5). Am. J. Hum. Genet. *81*, 552–558.

Krock, B.L., and Perkins, B.D. (2014). The Par-PrkC Polarity Complex Is Required for Cilia Growth in Zebrafish Photoreceptors. PLOS ONE *9*, e104661.

Liu, J.-L. (2010). Intracellular compartmentation of CTP synthase in Drosophila. J. Genet. Genomics *37*, 281–296.

Lynch, E.M., Hicks, D.R., Shepherd, M., Endrizzi, J.A., Maker, A., Hansen, J.M., Barry, R.M., Gitai, Z., Baldwin, E.P., and Kollman, J.M. (2017). Human CTP synthase filament structure reveals the active enzyme conformation. Nat. Struct. Mol. Biol. *24*, 507–514.

Masai, I., Lele, Z., Yamaguchi, M., Komori, A., Nakata, A., Nishiwaki, Y., Wada, H., Tanaka, H., Nojima, Y., Hammerschmidt, M., et al. (2003). N-cadherin mediates retinal lamination, maintenance of forebrain compartments and patterning of retinal neurites. Development *130*, 2479–2494.

Meeker, N.D., Hutchinson, S.A., Ho, L., and Trede, N.S. (2007). Method for isolation of PCR-ready genomic DNA from zebrafish tissues. BioTechniques *43*, 610–614.

Metlapally, R., and Wildsoet, C.F. (2015). Scleral Mechanisms Underlying Ocular Growth and Myopia. Prog. Mol. Biol. Transl. Sci. *134*, 241–248.

Mochizuki, T., Kojima, Y., Nishiwaki, Y., Harakuni, T., and Masai, I. (2018). Endocytic trafficking factor VPS45 is essential for spatial regulation of lens fiber differentiation in zebrafish. Development *145*, dev170282.

Narayanaswamy, R., Levy, M., Tsechansky, M., Stovall, G.M., O'Connell, J.D., Mirrielees, J., Ellington, A.D., and Marcotte, E.M. (2009). Widespread reorganization of metabolic enzymes into reversible assemblies upon nutrient starvation. Proc. Natl. Acad. Sci. *106*, 10147–10152.

Ng, A., Uribe, R.A., Yieh, L., Nuckels, R., and Gross, J.M. (2009). Zebrafish mutations in gart and paics identify crucial roles for de novo purine synthesis in vertebrate pigmentation and ocular development. Dev. Camb. Engl. *136*, 2601–2611.

Noree, C., Sato, B.K., Broyer, R.M., and Wilhelm, J.E. (2010). Identification of novel filament-forming proteins in Saccharomyces cerevisiae and Drosophila melanogaster. J. Cell Biol. *190*, 541–551.

Noree, C., Monfort, E., Shiau, A.K., and Wilhelm, J.E. (2014). Common regulatory control of CTP synthase enzyme activity and filament formation. Mol. Biol. Cell *25*, 2282–2290.

Park, J., Hyun, Y.S., Kim, Y.J., Nam, S.H., Kim, S.-H., Hong, Y.B., Park, J.-M., Chung, K.W., and Choi, B.-O. (2013). Exome Sequencing Reveals a Novel PRPS1 Mutation in a Family with CMTX5 without Optic Atrophy. J. Clin. Neurol. Seoul Korea *9*, 283–288.

Pei, W., Xu, L., Varshney, G.K., Carrington, B., Bishop, K., Jones, M., Huang, S.C., Idol, J., Pretorius, P.R., Beirl, A., Schimmenti, L.A., Kindt, K.S., Sood, R., and Burgess, S.M. (2016). Additive reductions in zebrafish PRPS1 activity result in a spectrum of deficiencies modeling several human PRPS1-associated diseases. Sci. Rep. *6*.

Shen, Q.-J., Kassim, H., Huang, Y., Li, H., Zhang, J., Li, G., Wang, P.-Y., Yan, J., Ye, F., and Liu, J.-L. (2016). Filamentation of Metabolic Enzymes in Saccharomyces cerevisiae. J. Genet. Genomics *43*, 393–404.

Webb, B.A., Dosey, A.M., Wittmann, T., Kollman, J.M., and Barber, D.L. (2017). The glycolytic enzyme phosphofructokinase-1 assembles into filaments. J. Cell Biol. *216*, 2305–2313.

Zhang, Y., and Wildsoet, C.F. (2015). RPE and Choroid Mechanisms Underlying Ocular Growth and Myopia. Prog. Mol. Biol. Transl. Sci. *134*, 221–240.

Zoref, E., De Vries, A., and Sperling, O. (1975). Mutant feedback-resistant phosphoribosylpyrophosphate synthetase associated with purine overproduction and gout. Phosphoribosylpyrophosphate and purine metabolism in cultured fibroblasts. J. Clin. Invest. *56*, 1093–1099.

Zou, J., Lathrop, K.L., Sun, M., and Wei, X. (2008). Intact Retinal Pigment Epithelium Maintained by Nok Is Essential for Retinal Epithelial Polarity and Cellular Patterning in Zebrafish. J. Neurosci. *28*, 13684–13695.

Appendix B

AdoMet binding regulates stress granule-independent assembly and stress granule recruitment of Cys4

Introduction

Cells under stress must adjust their biochemical processes in order to promote cellular fitness and survival. Often times, many cellular functions, such as translation, must be down regulated to meet the energetic demands of the cell. To accomplish this, non-essential mRNPs are sequestered away from translating polysomes into cytosolic assemblies known as stress granules (SGs) (Protter and Parker, 2016). Despite the fact that many SGs form under numberous metabolic and nutrient stresses, metabolic enzymes remained an unrepresented class of proteins present in SGs. To address this, we conducted a targeted visual screen and identified 17 metabolic enzymes that localized to chronic nutrient stress-induced SGs. The results from our screen revealed two distinct patterns of metabolic enzyme localization to SGs. While exclusive colocalization with SGs was observed for some enzymes, a subset of enzymes could form foci independent of SGs in addition to their recruitment to SGs. The mechanisms that allow for this two-pattern localization remain unknown. To investigate this, we chose *CYS4*, which encodes for cystathionine beta-synthase, as our follow up candidate to understand the mechanisms that allow for SG-independent assembly and SG localization. In addition to its unique foci formation pattern, the enzymology of cystathionine beta-synthases (CBSs) is well established and mutations that disrupt the human ortholog, CBS, result in homocysteinuria (Koutmos et al., 2010; Majtan et al., 2014; Zhu et al., 2018).

Cys4 catalyzes the condensation of homocysteine and serine into cystathionine (Figure B.1A), which can then be converted into cysteine. CBS enzymatic activity of the human ortholog is activated upon the binding of AdoMet to the CBS domains in regulatory C-terminus. This action alleviates the autoinhibition of the regulatory C-terminus on its catalytic domain (Janošík et al., 2001; McCorvie et al., 2014). Consistent with this, truncation of the regulatory domain in yeast and human CBSs promotes the formation of enzymatically active dimer compared to their native tetrameric state (Majtan et al., 2014). While AdoMet regulation is clear in humans, the role of AdoMet binding in yeast Cys4 is unknown. Incubation of AdoMet with recombinant purified Cys4 did not increase enzyme activity, suggesting that AdoMet may serve another purpose for Cys4 in yeast (Majtan et al., 2014). Here, we use genetic approaches to reveal that AdoMet binding regulates SG-independent foci and SG localization of Cys4.

Results

Cys4 recruitment to SGs increases with prolonged nutrient stress

Previously, we identified metabolic enzymes as bonafide components of yeast SGs induced by growth diauxic phase and stationary phase. One of those enzymes, Cys4, assembled into SG-independent foci in addition to its localization to SGs, as indicated by SG marker Ded1 (Figure B.1B). Consistent with Cys4 forming SG-independent foci, we observed that Cys4 assembly was present during logarithmic growth and exhibited different assembly kinetics than Ded1 during the yeast growth cycle (Figure B.1C). Interestingly, Cys4 had a ~3 fold increase in stress granule localization upon growth to stationary phase when compared to diauxic shift (Figure B.1D). These results suggest that recruitment of Cys4 into SGs could be regulated by the severity of nutrient deprivation.

Recruitment of Cys4 to SGs is stress specific

Cys4's localization to SGs during growth to diauxic shift and stationary phase raised the question if Cys4 was recruited to SGs under other known conditions. To test

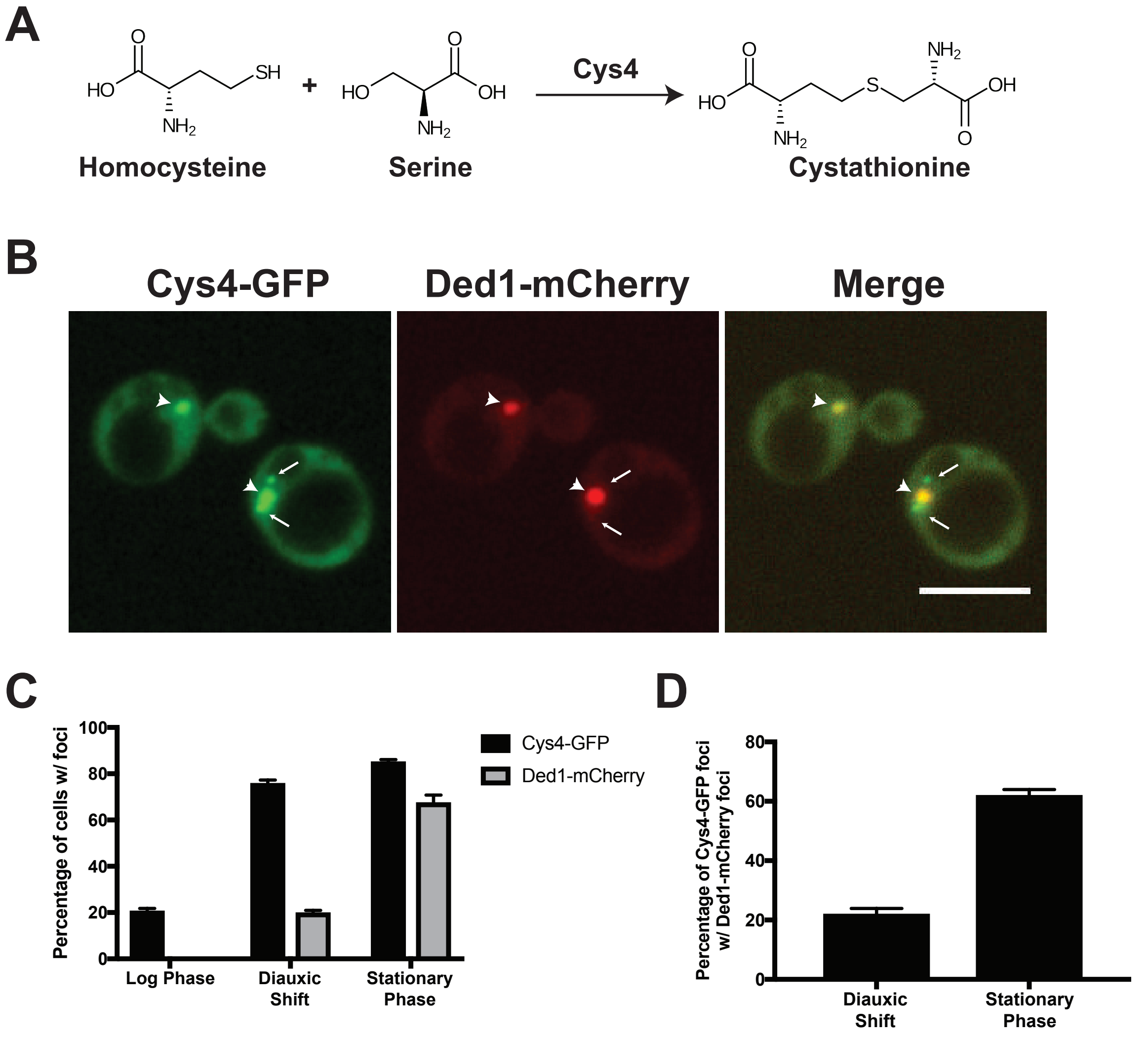

Figure B.1. Cys4 recruitment to SGs increases with prolonged nutrient stress
(A) Schematic depicting the enzymatic reaction of Cys4. **(B)** Representative fluorescent images of endogenously tagged Cys4-GFP and Ded1-mCherry at diauxic shift. Arrowheads indicate colocalization. Arrows indicate Cys4-GFP foci independent of SGs. Scale bar: 5 µm. **(C)** Quantification of the number of cells with Cys4-GFP and Ded1-mCherry foci at indicated time points in growth. Data is presented as the average of three independent experiments. Error bars indicate SEM. **(D)** Quantification of Cys4-GFP colocalization with Ded1-mCherry at indicated time points in growth. Data is presented as the average of three independent experiments. Error bars indicate SEM.

this, we exposed logarithmic growing cells to conditions known to assemble SGs (Buchan et al., 2011). While Ded1-mCherry assembly was robust, we found no localization of Cys4-GFP with Ded1-mCherry foci under glucose/methionine deprivation, azide treatment, or ethanol shock (Figure B.2A-B). Neither of these stresses triggered an increase in Cys4-GFP foci as well (Figure B.2).

In addition to acute stresses, overexpression of SG nucleating proteins Ded1 and Pbp1 have been shown to promote SG formation in the absence of an environmental stress (Takahara and Maeda, 2012). To determine if SG protein overexpression could increase Cys4 foci formation, we transformed Cys4-GFP cells with plasmids overexpressing Ded1 and Pbp1. We found no increase in Cys4-GFP assembly in overexpression strains compared to control strains (Figure B.2C-D). Additionally, we determined that overexpression of Cys4 is not sufficient to increase Cys4-GFP foci (Figure B.2C-D). Together, these results argue that Cys4 recruitment to SGs is stress specific and that protein levels do not dictate Cys4 foci formation.

AdoMet binding in CBS2 domain regulates Cys4 assembly

The stress specific localization of Cys4 to SGs suggests that its localization could be coupled with its function rather than a generalized response to stress. To determine this, we performed structure-function analysis on Cys4 to identify what domains were required for Cys4 assembly at log phase and diauxic shift (Figure B.3A). All variants were GFP tagged and expressed at the endogenous *CYS4* locus. Expression of solely the regulatory domain (cys4ΔN) prevented Cys4 assembly at both time points where as truncation of the regulatory domain (cys4ΔC) exhibited little foci formation at diauxic

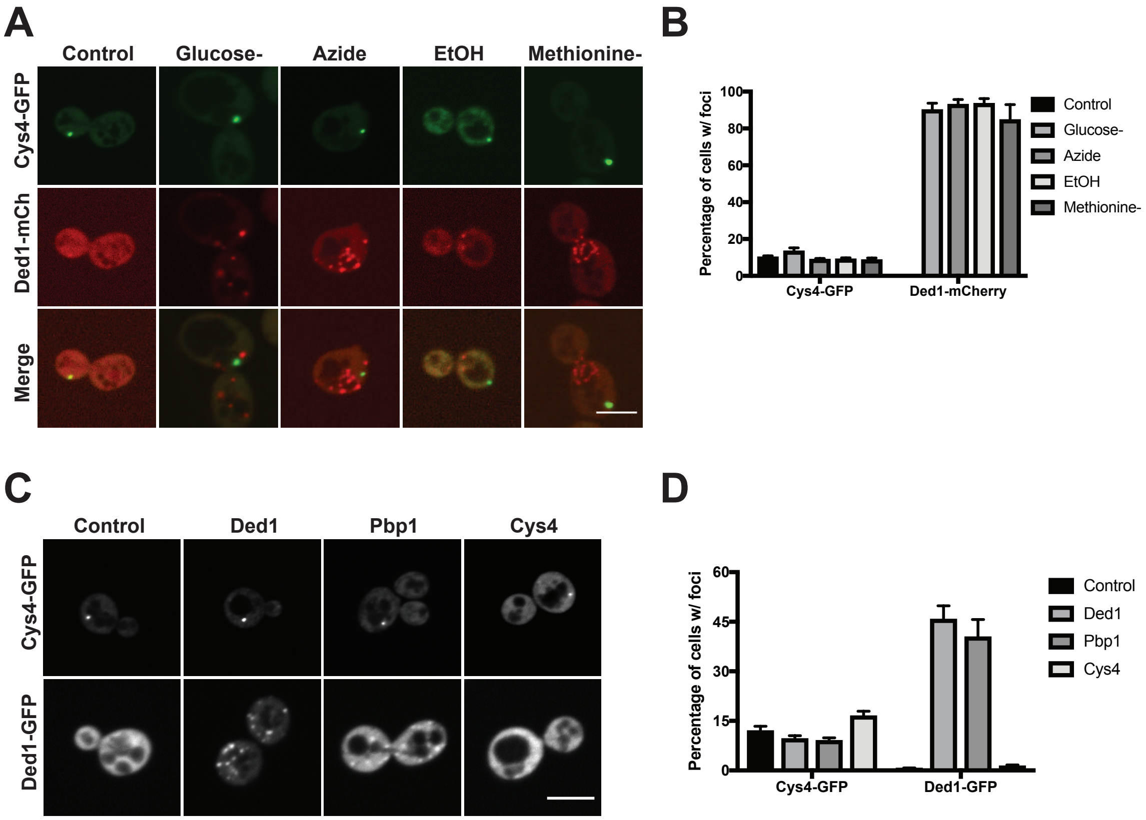

Figure B.2. Recruitment of Cys4 to SGs is stress specific
(A) Representative fluorescent images of endogenously tagged Cys4-GFP and Ded1-mCherry upon exposure to various acute stresses. Scale bar: 5 µm. **(B)** Quantification of Cys4-GFP and Ded1-mCherry foci from Figure B.2A. Data is presented as the average of three independent experiments. Error bars indicate SEM. **(C)** Representative fluorescent images of endogenously tagged Cys4-GFP and Ded1-GFP in log phase overexpressing empty plasmid (control), stress granule proteins (Ded1, Pbp1) or Cys4. Scale bar: 5 µm.
(D) Quantification of Cys4-GFP and Ded1-GFP foci from Figure B.2C. Data is presented as the average of three independent experiments. Error bars indicate SEM.

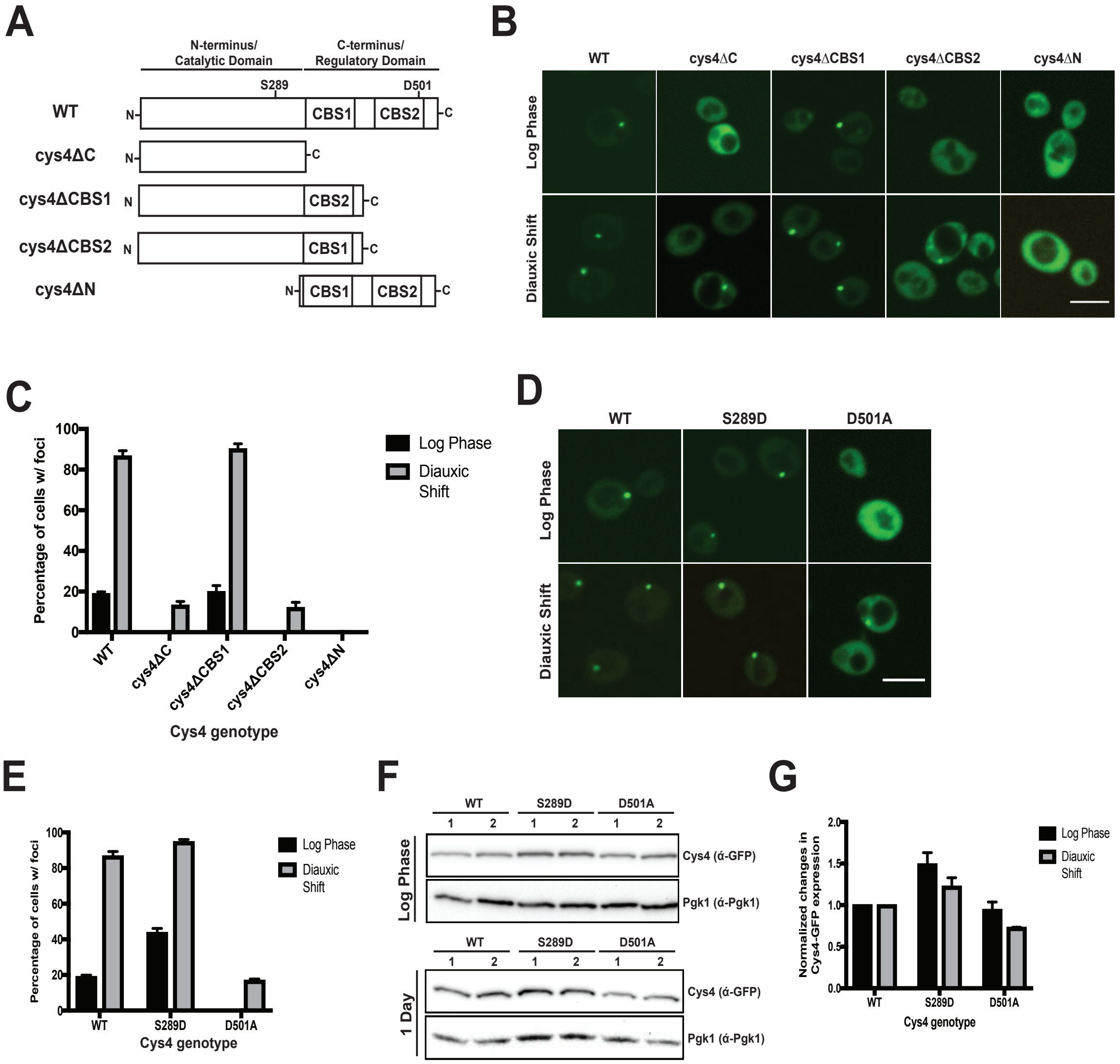

Figure B.3. AdoMet binding in CBS2 domain of Cys4 regulates foci formation
(A) Schematic depicting various mutant constructs of Cys4. **(B)** Representative fluorescent images of endogenously tagged WT and mutant Cys4-GFP at log phase and diauxic shift. Scale bar: 5 µm. **(C)** Quantification of Cys4-GFP foci from Figure B.3C. Data is presented as the average of three independent experiments. Error bars indicate SEM. **(D)** Representative fluorescent images of endogenously tagged WT and mutant Cys4-GFP at log phase and diauxic shift. Scale bar: 5 µm. **(E)** Quantification of Cys4-GFP foci from Figure B.3D. Data is presented as the average of three independent experiments. Error bars indicate SEM. **(F)** Western blot analysis from strains used in Figure B.3E at log phase and diauxic shift. **(G)** Quantification of Cys4 protein levels foci from Figure B.3F. Data is presented as the average of three independent experiments. Error bars indicate SEM.

shift (Figure B3.A-C). This argues that the regulatory domain is necessary, but not sufficient, for Cys4 foci formation. Since Cys4 contains two CBS domains in the regulatory domain, we next created single CBS deletions and assayed for their role in Cys4 assembly. Truncation of the CBS2 domain (cys4ΔCBS2) mimicked the phenotype of the cys4ΔC mutants while cys4ΔCBS1 mutants displayed the same assembly patterns as WT Cys4. This suggests that some aspect of CBS2 domain in Cys4 is required for Cys4 assembly.

Defects in Cys4 assembly in the cys4ΔCBS2 mutant raised the possibility that enzymatic activity or AdoMet binding regulates foci formation. Deletion of the regulatory domain promotes the formation of dimers with increased enzymatic activity, while the D501 residue aligns with the AdoMet binding site of human CBS (Majtan et al., 2014). To distinguish between these two possibilities, we created enzymatically inactive (S289D) and AdoMet binding defect (D501A) mutations in Cys4 and assayed for foci formation at log phase and diauxic shift (Quazi and Aitken, 2009). The D501A mutant failed to assemble in log phase and had greatly reduced foci at diauxic shift similar to cys4ΔC and cys4ΔCBS2 mutants (Figure B3.D-E). Enzyme activity is not required for Cys4 assembly, as the S289D mutant displayed the same foci formation as WT at diauxic shift (Figure B.3D-E). However, we did observe that the Cys4 S289D strain had a two-fold increase in foci during log phase. The effects of both mutants on Cys4 assembly were not due to dramatic changes in protein levels of Cys4 at either time point (Figure B.3F-G). This argues that AdoMet binding plays a significant role in Cys4 foci formation.

AdoMet binding is crucial for SG-independent Cys4 assembly

The decrease in Cys4 foci formation in D501A mutants raised the question if this mutation affected stress granule recruitment or if it was specific to SG-independent foci. We endogenously tagged Ded1 with mCherry in WT and mutant Cys4-GFP strains and assayed for Cys4 localization to stress granules at diauxic shift (Figure B.4A). We found that Cys4 foci in D501A mutants exclusively localized to SGs whereas inactive mutants (S289D) did not affect Cys4 recruitment to SGs (Figure B.4B). Additionally, neither Cys4 mutation disrupted SG assembly (Figure B.4C). In conjunction with results from Figure B.3, this data argues that AdoMet binding regulates SG-independent Cys4 assembly and loss of AdoMet binding drives Cys4 into SGs.

Lower AdoMet levels increase Cys4 recruitment to SGs

The fact that AdoMet binding regulates Cys4 assembly and recruitment to SGs prompted us to investigate whether intracellular AdoMet levels affects Cys4 assembly and recruitment. To test this, we utilized mutants with decreased enzymatic activity in the AdoMet synthetase, *SAM1*, and created dual fluorescent-tagged strains with Sam1-mCherry variants. We have previously shown that Sam1 is a robust diauxic phase SG marker and mutations that disrupt Sam1 enzymatic activity dramatically increase SG assembly at this time point.

We first examined the effects of decreased AdoMet levels affecting SG-independent Cys4 foci in logarithmically growing WT and K252M *SAM1* strains. The *SAM1 K252M* mutation displayed a 2-fold decrease in Cys4 assembly compared to the WT strain, supporting with the idea that AdoMet binding regulates SG-independent Cys4

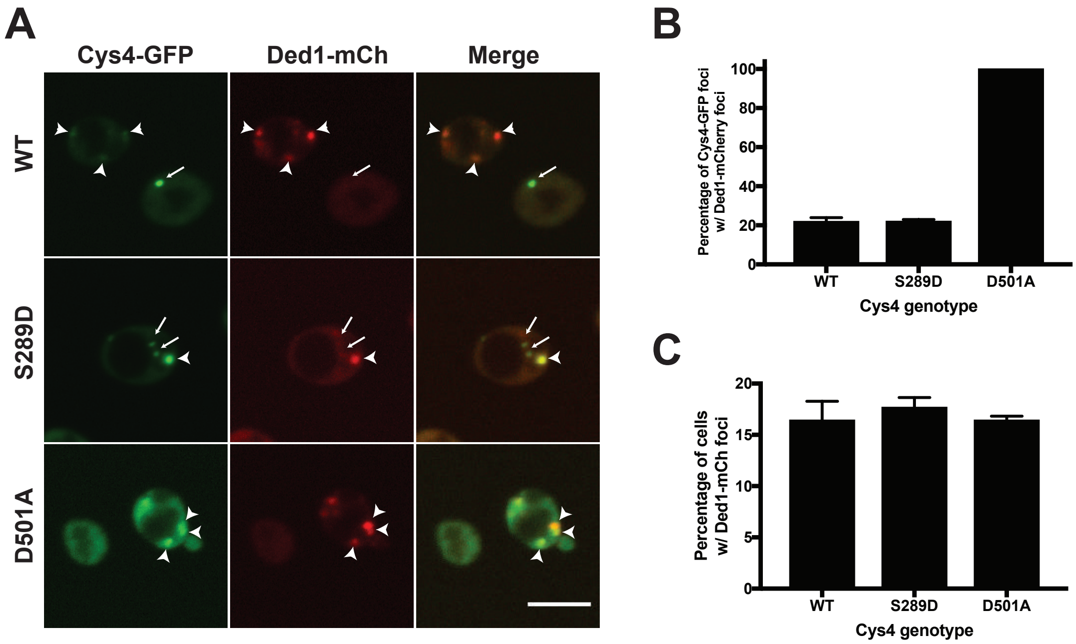

Figure B.4. AdoMet binding is crucial for SG-independent Cys4 foci
(A) Representative fluorescent images of endogenously tagged WT and mutant Cys4-GFP with Ded1-mCherry at diauxic shift. Arrowheads indicate colocalization. Arrows indicate Cys4-GFP foci independent of SGs. Scale bar: 5 µm. **(B)** Quantification of Cys4-GFP recruitment to Ded1-mCherry foci in WT and mutant strains. Data is presented as the average of three independent experiments. Error bars indicate SEM. **(C)** Quantification of Ded1-mCherry foci from Figure B.4A. Data is presented as the average of three independent experiments. Error bars indicate SEM.

assembly (Figure B.5A-B). Additionally, the *SAM1* K252M strain didnt induce Sam1-mCherry foci formation during log phase (Figure B.5A-B). We next examined Cys4 protein levels to determine if disruption in Cys4 assembly was due to decreased Cys4 expression. However, Cys4 protein levels were 2-fold higher in the *SAM1* K252M background suggesting that protein levels did not influence Cys4 assembly (Figure B.5C).

With *SAM1* K252M mutants disrupting SG-independent Cys4 foci, we next tested how decreased AdoMet levels affect Cys4 recruitment to SGs. While the percentage of cells with Cys4 foci was unaffected at diauxic shift, Cys4 foci were found almost exclusively in SGs in the *SAM1* K252M background (Figure B.5D-F). By manipulating AdoMet levels, this data supports the conclusion that AdoMet regulates SG-independent Cys4 assembly and localization to SGs.

Cystathionine accumulation increases SG formation but doesn’t increase Cys4 recruitment

The increased recruitment of Cys4 to SGs in *SAM1* mutant strains raised the question if this was simply due to increased SG formation or decreased in AdoMet levels/binding. To test this, we created pathway disruptions in the methionine and cysteine biosynthetic pathways (Figure B.6A) to identify other mutants that would increase SG assembly at diauxic shift. We identified that deletion of *CYS3*, which encodes for cystathioine gamma-lyase, increased SG formation (Figure B.6B). Since *cys4Δ* had no effect on SG formation, cystathionine accumulation is likely the cause for increased SG assembly in *cys3Δ* strains. Next, we examined Cys4 recruitment to SGs in *cys3Δ* background and found no increase in the localization of Cys4 foci (Figure B.6C-

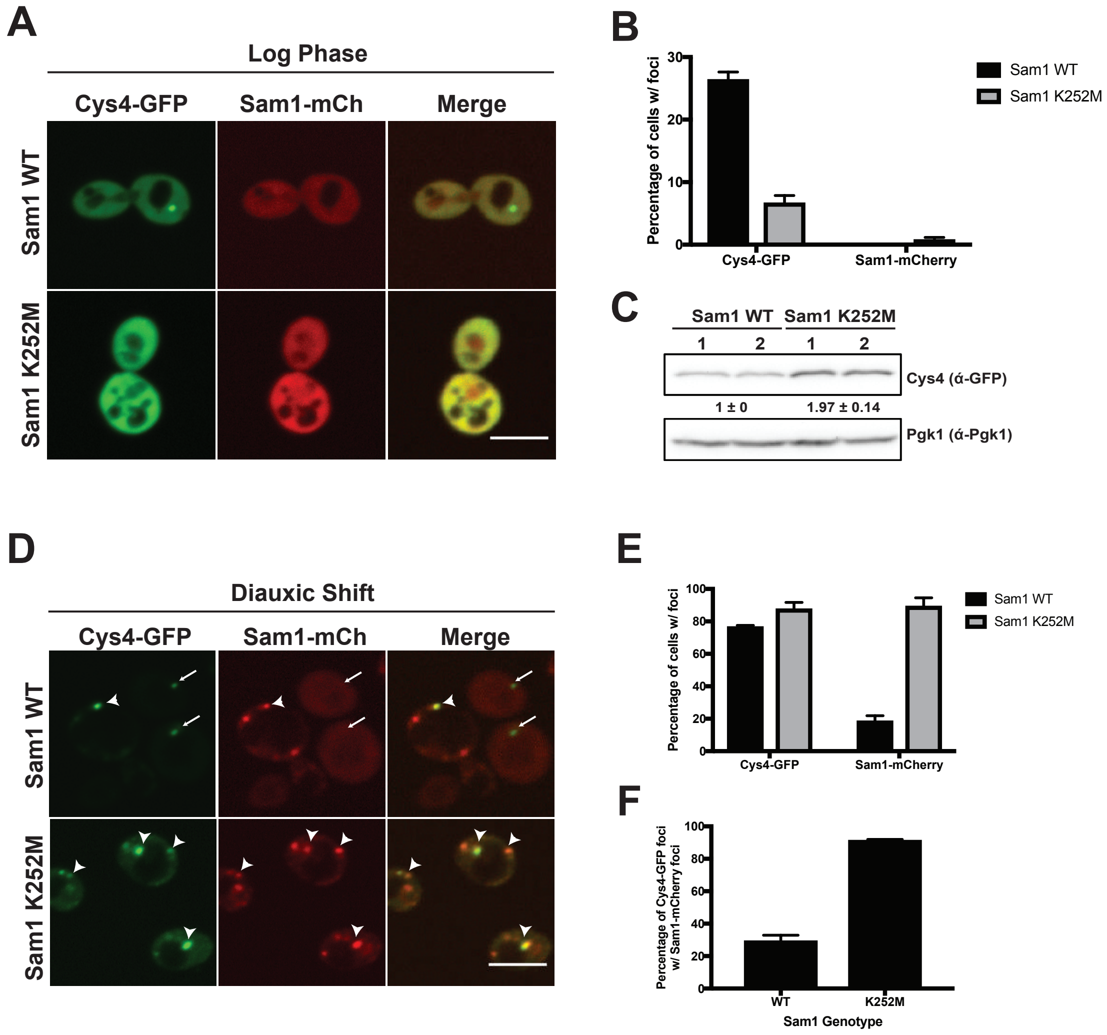

Figure B.5. Decreases in AdoMet levels promotes Cys4 recruitment to SGs
(A) Representative fluorescent images of endogenously tagged Cys4-GFP with WT and K252M mutant Sam1-mCherry at log phase. Scale bar: 5 µm. **(B)** Quantification of Cys4-GFP and Sam1-mCherry foci in WT and *SAM1 K252M* backgrounds from Figure B.5A. Data is presented as the average of three independent experiments. Error bars indicate SEM. **(C)** Western blot analysis from strains used in Figure B.5A. Normalized quantification of Cys4 protein levels is shown below the GFP blot. Data is presented as the average ± SEM of three independent experiments. **(D)** Representative fluorescent images of endogenously tagged Cys4-GFP with WT and K252M mutant Sam1-mCherry at diauxic shift. Arrowheads indicate colocalization. Arrows indicate Cys4-GFP foci independent of SGs. Scale bar: 5 µm. **(E)** Quantification of Cys4-GFP and Sam1-mCherry foci in WT and *SAM1 K252M* backgrounds from Figure B.5D. Data is presented as the average of three independent experiments. Error bars indicate SEM. **(F)** Quantification of Cys4-GFP recruitment to Sam1-mCherry foci in WT and mutant strains. Data is presented as the average of three independent experiments. Error bars indicate SEM.

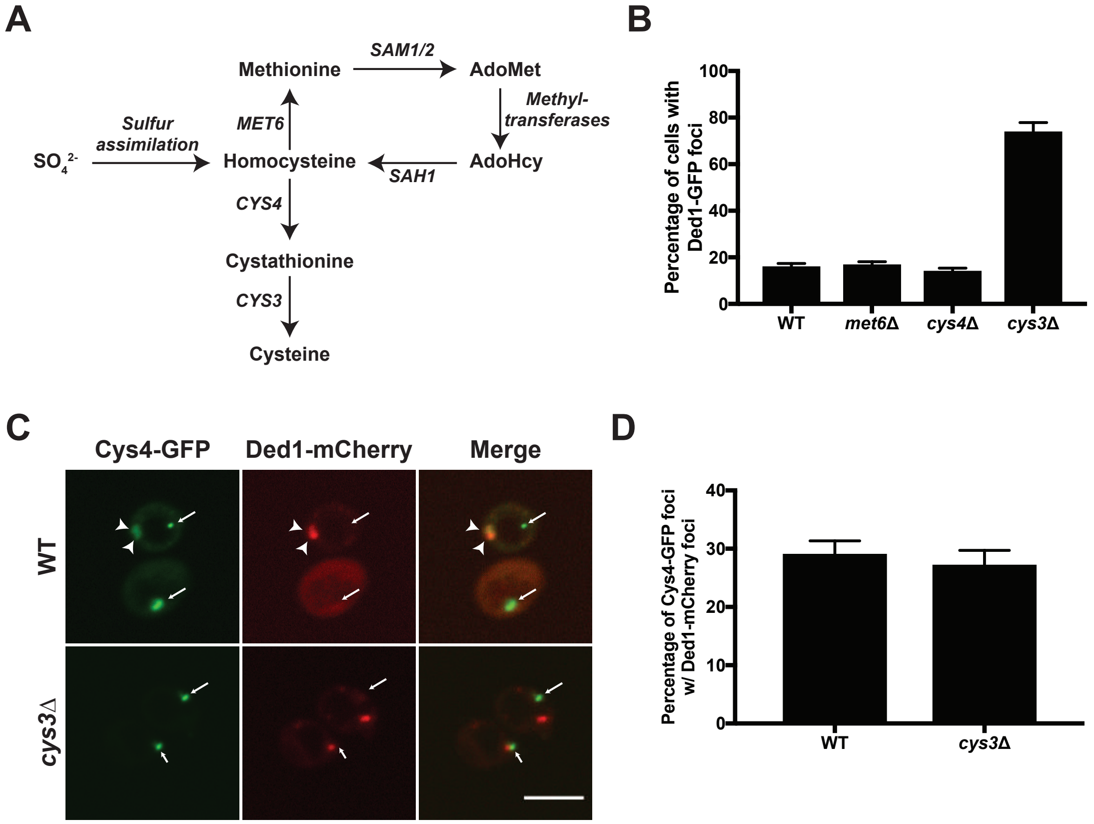

Figure B.6. Cystathionine accumulation increases SG formation but doesn't increase Cys4 recruitment

(A) Schematic depicting the methionine and cysteine biosynthetic pathways in yeast. **(B)** Quantification of Ded1-GFP foci formation in WT, *met6Δ, cys4Δ,* and *cys3Δ* backgrounds at diauxic shift. Data is presented as the average of three independent experiments. Error bars indicate SEM. **(C)** Representative fluorescent images of endogenously tagged Cys4-GFP and Ded1-mCherry in WT and *cys3Δ* strains. Arrowheads indicate colocalization. Arrows indicate Cys4-GFP foci independent of SGs. Scale bar: 5 µm. **(D)** Quantification of Cys4-GFP recruitment to Ded1-mCherry foci in WT and *cys3Δ* strains. Data is presented as the average of three independent experiments. Error bars indicate SEM.

D). Consistent with the acute stress data (Figure B.2), these results emphasize the stress specific nature of Cys4 recruitment to SGs.

The D501A mutant alters morphology of phase-separated Cys4

In yeast, SGs and metabolic enzymes have been proposed to assemble via phase separation. Recent reports have highlighted the ability of yeast SG proteins to phase separate *in vitro*. While reconstitution of metabolic filaments has been observed, *in vitro* assembly of a metabolic enzyme that forms foci has yet to be identified. We found that incubating recombinant 6xHis-SNAP::Cys4 protein with poly-L-lysine was sufficient to form phase-separated droplets (Figure B.7). Phase separation of Cys4 raised the question if this structure we observed was reminiscent of SG-independent or SG-associated Cys4 foci. To test this, we purified the D501A mutant and incubated the protein with poly-L-lysine. If Cys4 droplets mimicked SG-independent Cys4 foci, we predicted that no droplets would be seen with the D501A mutant protein. However, the presence of the phase-separated structures in the D501A mutant indicated that these resembled SG-associated Cys4 foci (Figure B.7). Surprisingly, we observed a change in the morphology of Cys4 structures in the D501A mutant. Unlike the spherical droplets seen with WT protein, Cys4 D501A mutants had much more fibrous-like structures (Figure B.7). Together, this represents the first example of *in vitro* assembly of metabolic enzyme foci and suggests how potential changes in the phase separation properties of Cys4 contribute to its recruitment to SGs.

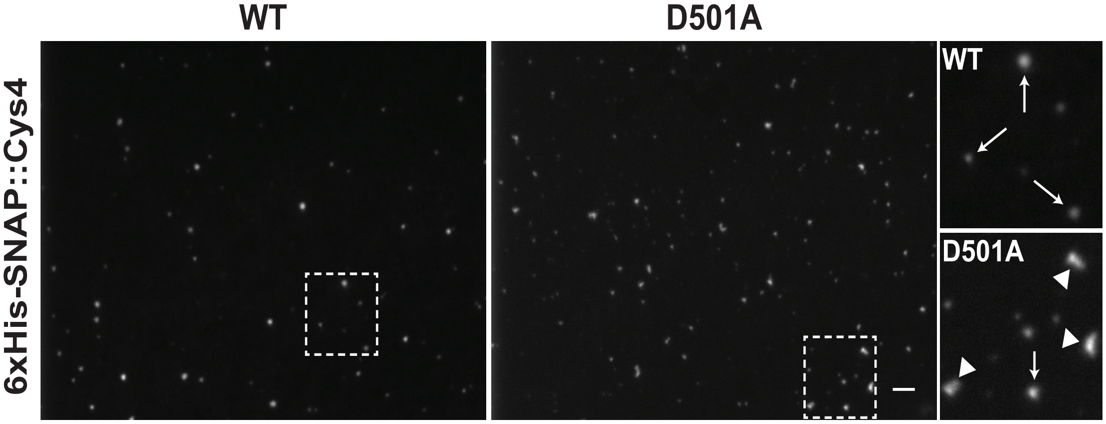

Figure B.7. The D501A mutant alters the morphology of phase-separated Cys4
Representative fluorescent images of 500nM recombinant purified WT and D501A 6xHis-SNAP::Cys4 protein labeled with SNAP Surface 647 incubated with 1µg/µl poly-L-lysine. Arrows indicate circular structures, arrowheads indicate less circular structures. Scale bar: 10 µm

Materials and Methods

Yeast medium and growth conditions

All yeast strains were grown at 30°C unless otherwise indicated in either YPD medium (1% yeast extract, 2% peptone, 2% dextrose) or synthetic defined medium (0.17% yeast nitrogen base without ammonium sulfate or amino acids, 0.5% ammonium sulfate, amino acids, 2% glucose).

Plasmid construction

Plasmids used in this study are listed in Table B.1. All plasmids were constructed with standard molecular biology techniques. The *CYS4* and *SAM1* locus were first amplified by PCR (KOD Hot Start Polymerase) from genomic DNA from wild-type BY4741 cells. These cassettes were then subcloned into pFA6a-GFP-KanMx6 plasmid (for *CYS4*) or pFA6a-mCherry-HphMx6 (for *SAM1*) and subsequently used as a template for generating point mutations via PCR-based site directed mutagenesis. Resulting plasmids were verified by sequencing. Overexpression plasmids were obtained by amplifying the coding sequence of DED1, PBP1, and CYS4 by PCR and then subcloned into empty p416GPD plasmids using restriction enzyme cloning.

Yeast strain construction

S. cerevisae strains are listed in Table B.2. All yeast strains were derived from a parent strain with the genotype *MATa his3Δ1 leu2Δ0 met15Δ0 ura3Δ0* (BY4741). Generation of endogenous GFP-tagged strains and gene disruption was created using standard PCR-mediated techniques. Cys4-GFP and Sam1-GFP variants were introduced into their respective endogenous loci by PCR amplifying cassettes that contained the coding sequence of Cys4-GFP or Sam1-GFP, a kanamycin or hygromycin resistance

Table B.1. List of plasmids used in Appendix B

Plasmid Number	Description
pJW12	pFA6a-GFP-KanMx6
pJW612	pFA6a-GFP-HphNT1
pJW611	pFA6a-mCherry-HphNt1
pJW523	pFA6a-NatMx6
pJW606	pFA6a-Cys4::GFP-KanMx6
pJW648	pFA6a-Cys4ΔCBS1::GFP-KanMx6
pJW613	pFA6a-Cys4ΔN::GFP-KanMx6
pJW607	pFA6a-Cys4(S289D)::GFP-KanMx6
pJW647	pFA6a-Cys4(D501A)::GFP-KanMx6
pJW761	pFA6a-Sam1::mCherry-HphNT1
pJW762	pFA6a-Sam1(K252M)::mCherry-HphNT1
pJW641	p416GPD
pJW633	p416GPD-Ded1
pJW634	p416GPD-Pbp1
pJW763	p416GPD-Cys4
pJW627	pProExHtC-SNAP-CYS4 WT
pJW628	pProExHtC-SNAP-CYS4 D501A

Table B.2. List of yeast strains used in Appendix B

Name	**Genetic background**
BY4741	*MATa his3Δ1 leu2Δ0 met15Δ0 ura3Δ0*
Cys4-GFP	BY4741, CYS4-GFP::KanMx6
Cys4-GFP, Ded1-mCherry	BY4741, CYS4-GFP::KanMX6, DED1-mCherry::HphNT1
Cys4ΔC-GFP	BY4741, CYS4 (1-353aa)-GFP::KanMx6
Cys4ΔCBS1-GFP	BY4741, CYS4 (1-371,433-507aa)-GFP::KanMx6
Cys4ΔCBS2-GFP	BY4741, CYS4 (1-462aa)-GFP::KanMx6
Cys4ΔN-GFP	BY4741, CYS4 (354-507aa)-GFP::KanMx6
Cys4 (S289D)-GFP	BY4741, CYS4 (S289D)-GFP::KanMx6
Cys4 (S289D)-GFP; Ded1-mCherry	BY4741, CYS4 (S289D)-GFP::KanMx6; DED1-mCherry::HphNT1
Cys4 (D501A)-GFP	BY4741, CYS4 (D501A)-GFP::KanMx6
Cys4 (D501A)-GFP; Ded1-mCherry	BY4741, CYS4 (D501A)-GFP::KanMx6; DED1-mCherry::HphNT1
Cys4-GFP; Sam1(WT)-mCherry	BY4741, CYS4-GFP::KanMx6; SAM1-mCherry::HphNT1
Cys4-GFP; Sam1(K252M)-mCherry	BY4741, CYS4-GFP::KanMx6; SAM1-mCherry::HphNT1
Ded1-GFP	BY4741, DED1-GFP::HphNT1
met6Δ; Ded1-GFP	BY4741, DED1-GFP::HphNT1, *met6Δ::NatMx6*
cys3Δ; Ded1-GFP	BY4741, DED1-GFP::HphNT1, *cys3Δ::NatMx6*
cys4Δ; Ded1-GFP	BY4741, DED1-GFP::HphNT1, *cys4Δ::NatMx6*
cys3Δ; Cys4-GFP; Ded1-mCherry	BY4741, CYS4-GFP::KanMx6; DED1-mCherry::HphNT1, *cys3Δ::NatMx6*

marker, and a 50bp sequence homologous to downstream of their respective stop codons. These cassettes were introduced into yeast using standard yeast transformation protocols. Genomic DNA was extracted from resulting transformants and the loci were PCR amplified and sequenced to verify the presence of the correct mutation.

Preparation of yeast for microscopy

Sodium azide, glucose deprivation, and ethanol shock were carried out as described previously with methionine deprivation under similar conditions. Briefly, cells were grown in SD medium overnight at 30°C and then back diluted into fresh medium to an OD600 of 0.2 and grown at 30°C to log phase. For NaN_3 experiments, yeast cultures were treated with 0.5% NaN_3 or water for 30 minutes at 30°C prior to imaging. For glucose deprivation experiments, cells were collected and washed in 30°C pre-warmed medium lacking glucose followed by resuspension again in 30°C pre-warmed medium lacking glucose. Cells were then placed back at 30°C for 30 minutes and then imaged immediately prior to imaging. For ethanol shock, yeast cultures were collected and washed in 30°C pre-warmed SD medium with ethanol (SD EtOH 6%) as its sole carbon source followed by resuspension again in 30°C pre-warmed SD medium with ethanol. Cells were placed black at 30°C for 30 minutes and imaged immediately. For methionine deprivation experiments, cells were collected and washed with 30°C pre-warmed SD medium lacking methionine followed by resuspension again in 30°C pre-warmed SD medium lacking methionine. Cells were placed back at 30°C for 30 minutes and imaged immediately.

For diaxuic shift and stationary phase experiments, cells were grown in YPD overnight at 30°C, back diluted to OD_{600} 0.2 in fresh YPD medium, and then grown for 24 or 120 hours at 30°C. At these time points, 1mL of culture was harvested and then concentrated to 200 µls in the same medium prior to imaging.

Microscopy and image analysis

Imaged were acquired on a Zeiss Axiovert 200M fluorescent microscope equipped with a CSU-X1 spinning disk (Yokogawa), an iChromeMLE laser source (Toptica Photonics) and µManager version 1.4 software. For each acquisition, a 2µm Z-stack was taken with slices at 0.25µm intervals using the 40X. For a minimum of three biological replicates, images were taken per experiment until at least 100 cells was obtained. For all images, optimal Z-projections were obtained using ImageJ along with subsequent image analysis. Colocalization quanitification was determined manually as the percentage of the number of GFP foci overlapped with mCherry foci divided by the total number of GFP foci. The number of cells with foci was calculated manually.

Western blot analysis

Whole cell extracts were prepared via NaOH extraction as indicated in Kushnirov et al 2000. Briefly, cells were grown in YPD medium at 30°C to either log phase or 1 day time point. Next, 1 OD600 (log phase) or 2.5 OD600 (1 day) was spun down and resuspended in 0.1N NaOH. After incubation at RT for 5 min, cells were spun down and then resuspended in 2x Sample Buffer with protease inhibitors (Sigma Aldrich). Samples were boiled for 5 min at 95°C and incubated on ice for 3 mins prior to centrifugation once more. Supernatants were stored at -20°C or used immediately.

Whole cell extracts were resolved on 10% SDS-PAGE gels and subsequently transferred to nitrocellulose membrane using semi-dry conditions. Membranes were then incubated in blocking solution (5% milk in TBST 0.1%) for 1 hour. After TBST 0.1% washes, membranes were incubated in primary antibody overnight at 4°C (1:5000 rabbit anti-GFP; Torrey Pines, 1:10000 mouse anti-PGK1; Invitrogen). Primary antibody was removed and washed with TBST 0.1% prior to adding horseradish peroxidase-conjugated secondary antibody (1:10000 donkey anti-rabbit, 1:2500 sheep anti-mouse) in 5% blocking solution for 2 hours at RT. Membranes were then washed with TBST 0.1% and then incubated in Thermo Scientific Pierce ECL Western Blotting Substrate. Chemiluminescence was detected using FluorChem E system (Protein Simple). Quantification of protein levels was carried out using densitometry methods by comparing GFP signal to internal control signal (PGK1).

Recombinant Cys4 protein purification

1L of BL21(DE3) *E.coli* cells expressing WT or D501A 6xHis-SNAP::Cys4 plasmids were grown in Terrific Broth at 37°C until OD_{600} ~0.5 was reached. IPTG was then added and grown at 18°C for 16 hours to induce expression of Cys4 proteins. Cells were then centrifuged at 4750rpm for 10 minuntes at 4°C and pellets were resuspended in 7mLs of lysis buffer (50mM Tris pH 8.0, 500mM NaCl, 20mM Imidazole pH 8.0, 10mM BME, 1x protease inhibitors). Sonication was used to break open cells and cells were spun down at 14,000rpm for 30 min at 4°C. Lysates were added to Ni-NTA beads that were pre-equilibrated with lysis buffer. After overnight incubation with rocking, beads were pelleted at 500rpm for 2 minutes at 4°C and then washed with 100mLs of wash buffer (50mM Tris pH 8.0, 500mM NaCl, 40mM Imidazole pH 8.0, 10mM BME). After loading onto a column, beads were then slowly washed with an extra 50mLs of wash buffer. 15 mLs of elution buffer (50mM Tris pH 8.0, 500mM NaCl, 250mM Imidazole pH 8.0, 10mM BME) was added to elute 6xHis-SNAP::Cys4 protein. Collected fractions were then pooled together and dialyzed into reaction buffer (50mM Tris pH 8.0, 250mM NaCl, 1mM DTT). Following dialysis, Cys4 protein was passed through a gel filtration column and the collected fractions were pooled together. 10% glycerol was added to the protein prior to determining protein concentration via Bradford assay and flash freezing. Aliquots were stored at -80°C.

Phase separation reaction

50µl SNAP tag labeling reactions were performed using SNAP Surface 647 according to the manufacturers protocol (New England BioLabs). 450µl of reactions buffer was added to stop the reaction and was then reconcentrated to 50µl using Amicon centrifuge filters (ThermoFischer Scientific). 500nM 6xHis-SNAP(647)::Cys4 protein was incubated with 1µg/µl poly-L-lysine (Sigma Aldrich) for 15 minutes. Reactions were then spotted onto microscope slides and coverslips prior to imaging.

Acknowledgments

Appendix B is a manuscript in preparation and will be submitted for publication. Begovich, K., Wilhelm, J.E. “AdoMet binding regulates stress granule-indepdenent assembly and stress granule recruitment of Cys4.” The dissertation author is the primary experimenter and author on this paper.

References

Buchan, J.R., Yoon, J.-H., and Parker, R. (2011). Stress-specific composition, assembly and kinetics of stress granules in Saccharomyces cerevisiae. J. Cell Sci. *124*, 228–239.

Janošík, M., Kery, V., Gaustadnes, M., Maclean, K.N., and Kraus, J.P. (2001). Regulation of Human Cystathionine β-Synthase by *S* -Adenosyl- L -methionine: Evidence for Two Catalytically Active Conformations Involving an Autoinhibitory Domain in the C-Terminal Region [†]. Biochemistry *40*, 10625-10633.

Koutmos, M., Kabil, O., Smith, J.L., and Banerjee, R. (2010). Structural basis for substrate activation and regulation by cystathionine beta-synthase (CBS) domains in cystathionine β-synthase. Proc. Natl. Acad. Sci. *107*, 20958–20963.

Majtan, T., Pey, A.L., Fernández, R., Fernández, J.A., Martínez-Cruz, L.A., and Kraus, J.P. (2014). Domain Organization, Catalysis and Regulation of Eukaryotic Cystathionine Beta-Synthases. PLOS ONE *9*, e105290.

McCorvie, T.J., Kopec, J., Hyung, S.-J., Fitzpatrick, F., Feng, X., Termine, D., Strain-Damerell, C., Vollmar, M., Fleming, J., Janz, J.M., Bulawa, C., and Yue, W.W. (2014). Inter-domain Communication of Human Cystathionine β-Synthase. J. Biol. Chem. *289*, 36018–36030.

Protter, D.S.W., and Parker, R. (2016). Principles and Properties of Stress granules. Trends Cell Biol. *26*, 668–679.

Quazi, F., and Aitken, S.M. (2009). Characterization of the S289A,D mutants of yeast cystathionine β-synthase. Biochim. Biophys. Acta BBA - Proteins Proteomics *1794*, 892–897.

Takahara, T., and Maeda, T. (2012). Transient Sequestration of TORC1 into Stress Granules during Heat Stress. Mol. Cell *47*, 242–252.

Zhu, H., Blake, S., Chan, K.T., Pearson, R.B., and Kang, J. (2018). Cystathionine β-Synthase in Physiology and Cancer.